ADVANCED STEEL CONSTRUCTION

An International Journal

Volume 15 Number 4

December 2019

CONTENTS

Website: http://www.hkisc.org
ISSN 1816-112X
Science Citation Index Expanded, Materials Science Citation Index and ISI Alerting
Cover: Macao Athletic Training and Development Centre
e-copy of IJASC is free to download at "www.asejournal.com" in internet and mobile apps.

ADVANCED STEEL CONSTRUCTION

VOL.15, NO.4(2019)

ADVANCED STEEL CONSTRUCTION

an International Journal

ISSN 1816-112X

Volume 15 Number 4 *December 2019*

ISSN 1816-112X

Science Citation Index Expanded, Materials Science Citation Index and ISI Alerting

Advanced Steel Construction
an international journal

Cover: Macao Athletic Training and Development Centre
e-copy of IJASC is free to download at "www.ascjournal.com" in internet and mobile apps.

General Information
Advanced Steel Construction, an international journal

Aims and scope

The International Journal of Advanced Steel Construction provides a platform for the publication and rapid dissemination of original and up-to-date research and technological developments in steel construction, design and analysis. Scope of research papers published in this journal includes but is not limited to theoretical and experimental research on elements, assemblages, systems, material, design philosophy and codification, standards, fabrication, projects of innovative nature and computer techniques. The journal is specifically tailored to channel the exchange of technological know-how between researchers and practitioners. Contributions from all aspects related to the recent developments of advanced steel construction are welcome.

Subscription inquiries and change of address. Address all subscription inquiries and correspondence to Member Records, IJASC. Notify an address change as soon as possible. All communications should include both old and new addresses with zip codes and be accompanied by a mailing label from a recent issue. Allow six weeks for all changes to become effective.

The Hong Kong Institute of Steel Construction
HKISC
c/o Department of Civil and Environmental Engineering,
The Hong Kong Polytechnic University,
Hunghom, Kowloon, Hong Kong, China.
Tel: 852- 2766 6047 Fax: 852- 2334 6389
Email: *ceslchan@polyu.edu.hk* Website: *http://www.hkisc.org/*
ISSN 1816-112X
Science Citation Index Expanded, Materials Science Citation Index and ISI Alerting

ISSN 1816-112X

Science Citation Index Expanded, Materials Science Citation Index and ISI Alerting

Advanced Steel Construction
an international journal

VOLUME 15 NUMBER 4 December 2019

Technical Papers

Advanced Steel Construction – Vol. 15 No. 4 (2019) 306-315
DOI:10.18057/IJASC.2019.15.4.1

BENDING BEHAVIOR OF COLD-FORMED STEEL–CONCRETE COMPOSITE FLOORS

Xin-mei Yao[1], Xu-hong Zhou[1, 2, 3], Yu Guan[1], Yu Shi[2, 3, *]and Zi-qi He[2,3]

[1] *College of Civil Engineering, Chang'an University, Xi'an, China*
[2] *School of Civil Engineering, Chongqing University，Chongqing, China*
[3] *Key Laboratory of New Technology for Construction of Cities in Mountain Area (Ministry of Education), Chongqing University, Chongqing, China*
** (Corresponding author: E-mail: shiyu7811@163.com)*

ABSTRACT

In cold-formed steel framing constructions, cold-formed steel–concrete composite floors built with concrete slabs and cold-formed steel joists are a common floor system. To investigate the bending behavior of such a floor system, two floor specimens with alternative slab materials were evaluated. The test results indicated that varying the slab materials had no significant influence on the ultimate bending capacity; however, the stiffness of the composite floor with a concrete slab was much higher than that of the floor with a gypsum-based self-leveling underlayment slab. A finite element model was developed and validated with the test results to simulate the bending behavior of the floors using the ANSYS finite element software. Parametric investigations were conducted through the verified finite element models. The results showed that the web depth-to-thickness ratio, span-to-depth ratio of the joist, and steel strength significantly affected the ultimate bending capacity of the composite floors, whereas the effects of screw spacing and concrete slab thickness were negligible. Finally, a simplified method was proposed to evaluate the ultimate moment capacity of cold-formed steel–concrete composite floors. The results obtained from the proposed method were validated by both experimental and numerical investigations of two full-scale cold-formed steel–concrete composite floors built with concrete slabs and cold-formed steel joists.

ARTICLE HISTORY

Received: 10 October 2018
Revised: 28 April 2019
Accepted: 01 May 2019

KEYWORDS

Composite floor;
Bending behavior;
Cold-formed steel;
Experimental study;
Numerical analysis;
Simplified method

1. Introduction

It is well known that floor systems of buildings play a key role in bearing vertical loads and transferring them to wall panels and foundations. Cold-formed steel (CFS) composite floor systems comprising CFS joists and concrete composite slabs have been used extensively in CFS framing because of their high strength-to-weight ratio and non-combustibility. For example, CFS–concrete composite floors have been employed in the "Poly Canyon Village" project in California [1]. Although the mechanical performance of hot-rolled steel and concrete composite beams has been investigated comprehensively, research on the behavior of CFS–concrete composite floors due to the thinness of CFS members, which is different from that of hot-rolled steel, is scarce

Extensive experimental studies have been conducted on the composite action of CFS and concrete. Based on push-out tests of different shear connectors and bending tests of full-scale CFS–concrete composite beams, Hanaor [2] concluded that the ductility and capacity of composite beams with shear connectors were higher than those of the design assumptions. Experimental investigations conducted by Lakkavalli et al. [3] and Irwan et al. [4,5] indicated the advantages of installing shear transfers between CFS and concrete. It can be concluded that shear transfers employed within composite beams and floors are crucial for the composite action between the joists and concrete owing to the resistance slipping between the CFS and concrete slab, and hence, result in an improved loading moment capacity of the system. Therefore, a different type of shear transfer was used in the CFS–concrete composite floors in this study.

In recent years, innovative and practical floor systems have been investigated for determining the bending behavior of composite floor systems. A new composite beam system built with back-to-back CFS joists, reinforced concrete slab on corrugated cold-formed metal, and shear connectors was developed by Hsu et al. [6]. It exhibited better bending behavior for strength and ductility compared with non-composite beams. Four-point bending tests were performed on composite CFS and wood-based flooring systems by Kyvelou [7], and the benefits of the composite action in CFS flooring systems were first illustrated through practical exploitation. However, the bending behavior of a CFS–concrete composite floor comprising a CFS frame and concrete slab has not been studied, and research on CFS–concrete composite floors with different types of shear transfer, such as the Z tab shear transfer, is insufficient. In addition, the influence of slab materials, such as gypsum-based self-leveling underlayment (GSU) and fine aggregate concrete (FAC), on the performance of composite floors needs to be explored.

In this study, an experimental method for investigating the bending behavior of a CFS–concrete composite floor system is presented. Moreover, a numerical simulation approach is provided to analyze the influence of some parameters such as the web depth-to-thickness ratio and span-to-depth ratio of the joist, screw spacing, concrete slab thickness, and steel strength on the bending performance of such floor system. Furthermore, a simplified method for the calculation of the ultimate moment capacity of the floor is presented to provide a practical design reference and a calculation method for engineers involved in the design of CFS–concrete composite floors. The structure of this paper is as follows. After the introduction, section 2 presents the details, results, and analysis of the tests. Section 3 discusses the established finite element (FE) model and the analysis of the influences of key parameters on the bending performance of the CFS–concrete floor. In section 4, a simplified method for calculating the ultimate moment capacity of composite floors is presented. Finally, section 5 provides the primary conclusions.

2. Bending test program

2.1 Test specimen

The objective of this experimental study is to investigate the bending behavior of a CFS–concrete composite floor with different slab materials. The configurations of two composite floor specimens are summarized in Table 1. As indicated in the table, the slab material of BM-1 is GSU, whereas that of BM-2 is FAC. The floor configuration of BM-1 is illustrated in Fig. 1, and the width and length of BM-1 were 0.8 m and 3.6 m, respectively. The floor specimen comprises two primary parts: the CFS frame and composite slab. Fig. 1 shows that the CFS frame consists of three C-shape joists with dimensions of 254 × 40 × 13 × 1.5 mm spaced at 400 mm on center, and two U-shape tracks with dimensions of 254 × 40 × 1.5 mm connected to the flange at each end of the joists through self-tapping screws with a diameter of 4.8 mm (ST4.8 screws). A 50 × 1.0 mm (width × thickness) steel strap was fastened to the bottom flanges at the midspan of the joists using ST4.8 screws to avoid lateral torsion of the joists. Moreover, Fig. 1 shows that web stiffeners were fastened to both ends of the CFS joists through six ST4.8 screws to resist the web crippling of the joists at the supports.

The composite slab comprises a 0.75 mm thick YX-14-63-820 shallow CFS form deck, a 40 mm thick GSU solid slab, and Z tab shear transfers as shown in Fig. 2. As indicated in Fig. 3, the CFS form deck was connected to the joists through hexagon-head self-tapping screws with diameters of 5.5 mm (ST5.5 screws) spaced at 126 mm and 252 mm along the perimeter and in the field of the CFS form deck, respectively. Additionally, the Z tab shear transfers were fastened to the CFS form deck spaced at 252 mm along the length of the joists using ST5.5 screws. The GSU was poured on the CFS form-deck, which was brushed with a layer of interfacial agent to enhance the bond capacity between the GSU slab and the CFS form deck.

Table 1
Description of composite floor test specimens

Specimen	Material of slab	Configuration of shear transfer	Details of steel members (mm)
BM-1	GSU	Z tab shear transfer+ Interfacial agent	C-shape joist: C254×40×13×1.5; U-shape track: U254×40×1.5; Web stiffener: C100×35×12×1.5; Steel strapping: 50×1.0; Z tab shear transfer: 20×15×1.5; CFS form-deck: YX-14-63-820
BM-2	FAC		

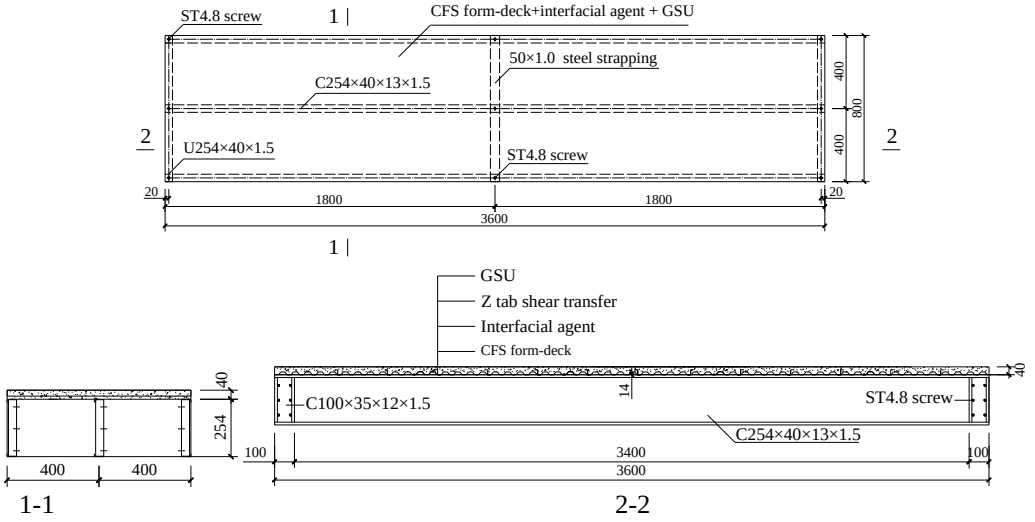

Fig. 1 Dimensions of specimen BM-1 (all dimensions in mm)

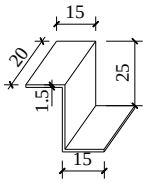

Fig. 2 Z tab shear transfer (all dimensions in mm)

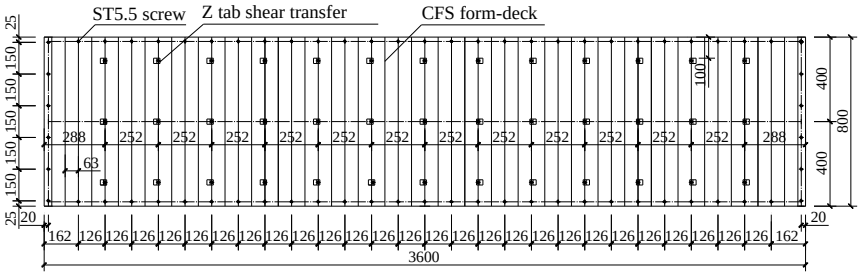

Fig. 3 Connection between Z tab shear transfer and CFS form-deck (all dimensions in mm)

2.2 Material properties

Table 2 lists the mechanical properties of CFS materials in the floor specimens tested following GB/T 228.1 [8], where E_s is the elastic modulus of steel. The average steel thickness of the CFS joists and form-deck were 1.5 mm and 0.75 mm, respectively. For the CFS joists and tracks, the average yield and tensile strengths were 318.4 MPa and 369.6 MPa, respectively, and the steel elastic modulus and Poisson's ratio were 2.09×10^5 MPa and 0.3, respectively. For the CFS form-deck, the average yield and tensile strengths were 356.3 MPa and 438.6 MPa, respectively, and the steel elastic modulus and Poisson's ratio were 2.00 × 105 MPa and 0.3, respectively. The properties of concrete tested according to GB 50081 [9] are presented in Table 3, where E_c is the elastic modulus of concrete. The average compressive strength of 100 × 100 × 100 mm GSU cubes at 28 days was 33.7 MPa with an elastic modulus of 2.17×10^4 MPa, while it was 31.17 MPa with an elastic modulus of 3.0×10^4 MPa for FAC cubes. The ultimate shear forces were 7.56 kN and 9.30 kN for the ST4.8 and ST5.5 screws, respectively.

Table 2
Properties of CFS

Material	Thickness (mm)	Average yield strength (MPa)	Average tensile strength (MPa)	Elastic modulus $E_s \times 10^5$ (MPa)
CFS joists and tracks	1.5	318.4	369.6	2.09
CFS form-deck	0.75	356.3	438.6	2.00

Table 3
Properties of concrete

Material	Cube size (mm)	Density (kg/m^3)	Average cube compressive strength (MPa)	Elastic modulus $E_c \times 10^4$ (MPa)
GSU	100×100×100	1969	33.70	2.17
FAC	100×100×100	2077	31.17	3.0

2.3 Test setup

Fig. 4 illustrates the test setup of the investigated composite floor, in which steel frames bolted to the concrete ground were used to support the floor specimens. The specimen was simply supported on hinge supports at either end of the joists. Steel plates were placed under the U-shaped tracks to prevent excessive concentrated stress. A hydraulic jack was used monotonically on the floor specimens using spreader beams with four concentrated forces for simulating a uniform gravity loading, as illustrated in Fig. 4(a). Before the tests, the expected ultimate load of the floors was calculated in accordance with the method proposed by Chien [10] to be approximately 120 kN. A load of 2.5% of the expected ultimate load was applied at 3 kN per step until the ultimate capacity was reached. Subsequently, a load of 1 kN per step was applied until failure occurred. Each step lasted for 3 min. The TDS-602 data acquisition system was used to record the applied load and displacements.

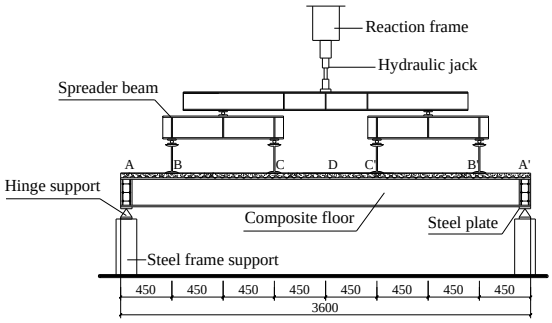

(a) Loading system

(b) Photograph of test setup

Fig. 4 Test setup of floor specimens

2.4 Experimental results and discussion

The BM-1 and BM-2 specimens were tested to investigate the bending behavior of the composite floor and explore the influence of the slab material on the bending performance of the composite floors. The failure characteristics, ultimate load, corresponding deflection of floors, and load–deflection curves are presented as follows.

2.4.1 Failure characteristics

Both specimens demonstrated similar failure characteristics in the tests. Here BM-1 was used as an example to illustrate the failure modes. When the applied load was approximately 53% of the ultimate load, webs of the boundary joists displayed shear buckling, as illustrated in Fig. 5(a). Furthermore, screw tilting was observed as illustrated in Fig. 5(b). When the load applied was 77% of the ultimate load, cracks were observed on the GSU slab. At the ultimate load, the specimens demonstrated disengagement of the CFS form-deck from the concrete slab on both end supports as shown in Fig. 5(c), torsional deformation of the joist webs as shown in Fig. 5(d), distortional buckling of the joists at the loading point (Fig. 5(e)), and bending deformation of the steel strapping as shown in Fig. 5(f).

(a) Shear buckling of joist web

(b) Screw tilting

(c) Disengagement of CFS form-deck from concrete slab

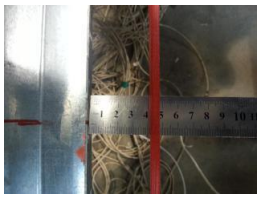

(d) Torsional deformation of joist web

(e) Distortional buckling of joist at loading point

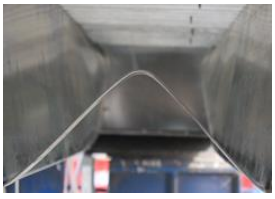

(f) Bending deformation of steel strapping

Fig. 5 Failure characteristics of BM–1

In the initial imperfections of the specimens before the tests, full-length cracks on the Z tab shear transfers along the floor length were observed. These were caused by the relative thinness of the concrete slab and abreast the regular arrangement of the Z tab shear transfers, thus weakening the bonding mechanism between the concrete slab and CFS form-deck, and consequently reducing the bending capacity of the composite floors. Therefore, a staggered arrangement of the Z tab shear transfers was suggested. In addition, the shear force between the concrete slab and CFS form-deck was transferred through the Z tab shear transfers and the interfacial agent; however, when the load was small, the lower shear resistance of the interfacial agent resulted in the earliest bond-slip failure between the concrete slab and CFS form-deck, from the support edge to the first row of the Z tab shear transfers. Subsequently, the bond-slip failure reduced at a distance closer to the loading point because of the large friction between the concrete slab and CFS form-deck resulting from the large compression at the loading point. With increasing applied load, the concrete slab failed at the loading point. This is attributable to the bond-slip failure occurring in the concrete slab, which hindered its operation with the CFS joists. Furthermore, the failure characteristics of the joists were overall bending deformation, torsional deformation, and interactive buckling of compressive CFS plate members.

2.4.2 Ultimate load

Table 4 presents the ultimate load P_u and the corresponding midspan vertical displacement Δ_u. As shown, BM-2 showed only a 2.8% increase in the ultimate load over BM-1, whereas the midspan vertical displacements of the central and boundary joists of BM-2 reduced by 30.6% and 27.4%, respectively, compared with those of BM-1. The results demonstrated that the change in slab material had little influence on the ultimate load, but affected the flexural stiffness of the composite floors significantly.

Table 4
Test results

Specimen	Location	P_u（kN）	Δ_u（mm）
BM-1	Central joist	113.06	25.94
	Boundary joist		30.37
BM-2	Central joist	116.32	17.98
	Boundary joist		22.05

A comparison of the load–deflection curves of BM-1 and BM-2 is illustrated in Fig. 6. As shown, the stiffness of BM-2 (with an FAC slab) was generally higher than that of BM-1(with a GSU slab). Furthermore, the specimens exhibited ductile failure rather than brittle failure. Fig. 7 illustrates the difference between the boundary and central joists of the composite floors. As shown in Fig. 7(a), the initial stiffness of the boundary and central joists of BM-1 was almost equal. However, when a load of 50 kN was applied, the stiffness of the boundary joist decreased compared to that of the central joist; consequently, the deformation of the boundary joist was larger than that of the central joist with increasing load. Regarding BM-2, as shown in Fig. 7(b), the stiffness of the central joist was larger at first compared to that of the boundary joist. When a load of 100 kN was applied, the stiffness degradation of the boundary joist was more evident than that of the central joist. As indicated in Table 4, the ultimate vertical deflection of the boundary joist was 5 mm larger than that of the central joist. This is attributable to the steel strapping that is transferring symmetric constraints from the two boundary joists to the central joist, thereby restricting the torsional and vertical deformations of the central joist.

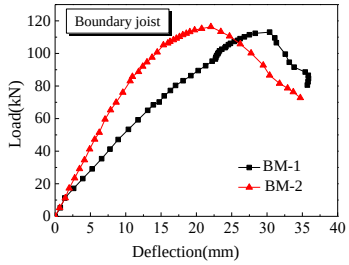

(a) Boundary joist

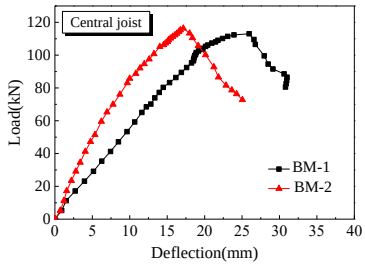

(b) Central joist

Fig. 6 Comparison of the load–deflection curves of BM-1 and BM-2

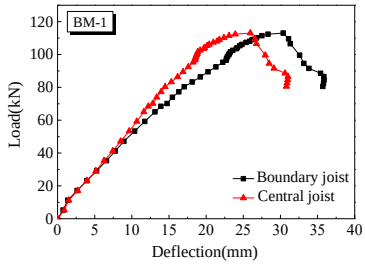

(a) BM-1

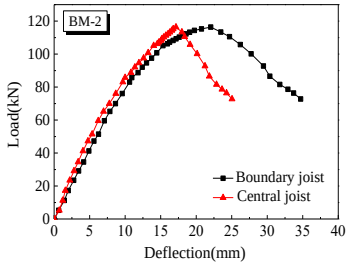

(b) BM-2

Fig. 7 Comparison of the load–deflection curves of boundary joist and central joist

Based on the failure characteristics of the concrete slab and the CFS joists of the specimens, the bending capacity of the composite floors is influenced by many factors, such as joist size, screw spacing, thickness of concrete slab, and steel strength. Therefore, the following analysis is based on specimen BM-1, and the influence of key parameters, including the web depth-to-thickness ratio, span-to-depth ratio of the joist, screw spacing, and steel strength, on the bending capacity of the CFS–concrete composite floor system, are investigated through numerical simulations.

3. Nonlinear FE analysis

3.1 Verification of FE method

The tested floors were simulated by the ANSYS FE software [11]. In the FE models, element shell181 was selected to simulate the steel members, as shown in Fig. 8(a). Element solid65 was found to be suitable for simulating the concrete slab. The self-tapping screws between the CFS joists and CFS form-deck were simulated by element beam188, as shown in Fig. 8(a). Except for the screws connecting the CFS joists and CFS form-deck, screw connections such as those between the joists and tracks, joists and web stiffeners, joists and steel strapping, and tracks and CFS form-deck, were simulated by coupling the two nodes at the screw connection and constraining the translation in the three degrees of freedom in the *x*, *y*, and *z* directions, because these connections exhibited no obvious failure features, as shown in Fig. 8(a). The overall model of the specimen is shown in Fig. 8(b). The contact pair (element target170 and element target174) was constructed by using the surface-to-surface contact elements for modeling the contact behavior such as for the contact between concrete slab and corrugated metal deck. Boundary conditions and loads were applied as shown in Fig. 8(b). The displacements along the *x* and *y* directions at the left support and along the *x*, *y*, and *z* directions at the right support were constrained. Uniformly distributed line loads were applied at the locations where the distribution beams were arranged, as illustrated in Fig. 8(b). The constitutive relation of the CFS used in the FE model was determined based on the test results.

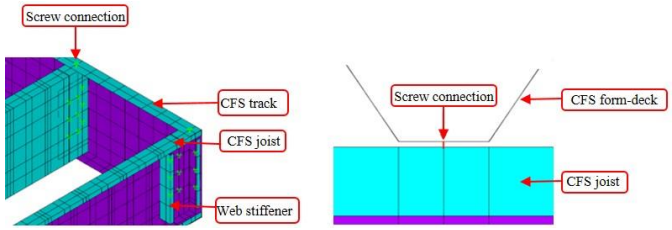

(a) Screw connection

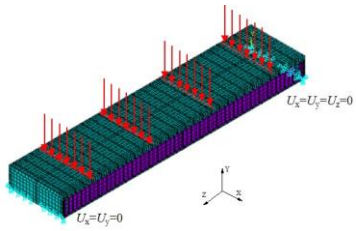

(b) Boundary conditions and loads of the specimen

Fig. 8 Finite element model of composite floor

Table 5 presents the comparison of the test results and FE analysis results on the ultimate bearing capacities and the corresponding deformations. In Table 5, P^*_u is the ultimate load obtained in FE analysis and Δ^*_u is the mid-span vertical displacement corresponding to the ultimate load obtained FE analysis. The ultimate capacities of BM-1 and BM-2 predicted by the FE models were only 2% and 3% higher than those obtained from tests, respectively. Generally, the FE results agree strongly with the experimental results, and further parametric investigations can be conducted using the validated FE models.

Table 5
Comparisons of finite element analysis and test results of specimens

Specimen	Ultimate bending capacity (kN)			Deflection (mm)		
	P_u	P^*_u	P^*_u/P_u	Δ_u	Δ^*_u	Δ^*_u/Δ_u
BM-1	113.06	115.79	1.02	25.96	24.93	0.96
BM-2	116.36	119.84	1.03	22.05	21.87	0.99

3.2. FE parametric analyses

3.2.1 Influence of web depth-to-thickness ratio and span-to-depth ratio of joist

It is widely known that the bending capacities of CFS members are affected by the web depth-to-thickness ratio and span-to-depth ratio of the joists [12, 13]. Consequently, the ultimate load is also influenced by these two factors. In this study, three alternative spans, namely 3,048, 4,064, and 5,080 mm, and five different web thicknesses, i.e., 2.55, 1.7, 1.27, 1.02, and 0.85 mm, were investigated. The details of the modeled specimens and results are presented in Table 6, where l is the span of the joist, and t is the thickness of josits. The comparisons are illustrated in Fig. 9, where C254-12-100 implies that the web depth of the joist h is 254 mm, span-to-depth ratio of the joist l/h is 12, and web depth-to-thickness ratio of the joist h/t is 100. As shown in Fig. 9, the variation in the web depth-to-thickness ratio substantially affected the ultimate load. The ultimate bending capacity reduced significantly as the web depth-to-thickness ratio increased. For specimens with a span-to-depth ratio of 12, when the web depth-to-thickness ratio increased from 100 to 150, 150 to 200, 200 to 250, and 250 to 300, the corresponding reductions in the ultimate capacity of the composite floor were 34.40, 37.46, 36.20, and 31.41%, respectively. Therefore, the ultimate capacity of the composite floor was influenced most significantly by the web depth-to-thickness ratio. Moreover, with increasing web depth-to-thickness ratio, the effect of the span-to-depth ratio was small and negligible. For example, when the web depth-to-thickness ratio was 100, the ultimate capacity of the specimen with a span-to-depth ratio of 12 was 31.7% higher than that of the specimen with a span-to-depth ratio of 16. However, when the web depth-to-thickness ratio was 300, the ultimate capacity only increased by 14.9%. This is because when the web depth-to-thickness ratio was 300, the web thickness of the joist was only 0.85 mm; therefore, failure of the floors occurred due to the lower buckling load of the CFS members. Thus, the span-to-depth ratio had little influence on the failure mechanism.

Table 6
Influence of web depth-to-thickness ratio and span-to-depth ratio of joist on the capacity of composite floor

Specimen	l (mm)	t (mm)	P^*_u (kN)
C254-12-100	3048	2.55	244.276
C254-12-150	3048	1.7	160.247
C254-12-200	3048	1.27	100.225
C254-12-250	3048	1.02	63.939
C254-12-300	3048	0.85	43.853
C254-16-100	4064	2.55	185.525
C254-16-150	4064	1.7	126.963
C254-16-200	4064	1.27	89.441
C254-16-250	4064	1.02	59.870
C254-16-300	4064	0.85	38.167
C254-20-100	5080	2.55	174.142
C254-20-150	5080	1.7	117.796
C254-20-200	5080	1.27	81.629
C254-20-250	5080	1.02	58.718
C254-20-300	5080	0.85	37.293

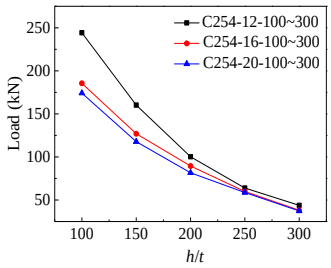

Fig. 9 Effect of web depth-to-thickness ratio on floors with different span-to-depth ratios

Fig. 10 illustrates the load–deflection curves for different span-to-depth ratios and web depth-to-thickness ratios. The ultimate deflection and initial slope of the load–deflection curves in Fig. 10(a) demonstrate that the bending stiffness and ductility of floors also reduced with increasing web depth-to-thickness ratio when the span-to-depth ratio was 12. This is attributable to the increase in the CFS joist thickness; a constant web depth of the joists can increase the section modulus and consequently increase the bending stiffness of the composite floor. However, as depicted in Fig. 9 and Fig. 10(b), the ultimate load and bending stiffness were not improved when the span-to-depth ratio was reduced from 20 to 16.

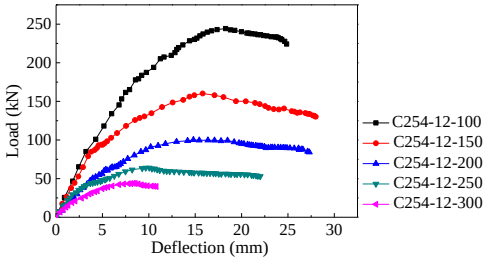

(a) Varying web depth-to-thickness ratio (l/h = 12)

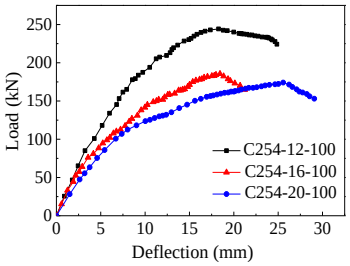

(b) Varying span-to-depth ratio (h/t = 100)

Fig. 10 Comparison of load–deflection curves for floors with different span-to-depth ratios and web depth-to-thickness ratios

3.2.2 Influence of screw spacing

As the test results indicated that the screw connections between the CFS joist and CFS form-deck were extremely important for the composite action of the floors, a parametric research was performed to obtain the influence of screw spacing on both the ultimate load and bending stiffness of CFS–concrete floors. Three values for spacing along the perimeter, i.e., 252, 126, and 63 mm, were considered when the spacing in the field was 252 mm. On the other hand, when the spacing along the perimeter was 126 mm, three values of spacing in the field, i.e., 315, 252, and 126 mm, were evaluated.

From the results presented in Table 7 and the load–deflection curves in Fig. 11, where C254-s63/252 indicates a joist height of 254 mm, screw spacing along the perimeter of 63 mm, and screw spacing in the field of 252 mm, it can be concluded that decreasing the screw spacing along the perimeter from 252 mm to 126 mm and subsequently from 126 mm to 63 mm resulted in a gradual increase in ultimate load, with enhancements in capacity of up to 3.0% and 4.3%, respectively. However, the initial bending stiffness exhibited no difference when only the screw spacing along the perimeter was varied. As shown in Fig. 11(b), reducing the screw spacing in the field from 315 mm to 252 mm and subsequently from 252 mm to 126 mm increased the ultimate load by up to 8.4% and 3.9%, respectively. When the screw spacing in the

field was 315 mm, the larger screw spacing resulted in a reduced number of screws between the CFS joists and the CFS form-deck, subsequently causing a sharp decline in the ultimate capacity of the floor. As presented in Table 7, only a little variation was observed for the capacities of composite floors with other values of screw spacing. Therefore, considering the load and construction simplicity, the screw spacing of s126/252 used in the test was deemed to be reasonable.

Table 7
Influence of screw spacing on the capacity of composite floor

Specimen	Screw spacing (mm)		P^*_u (kN)
	Perimeter	In the field	
C254-s252/252	252	252	116.324
C254-s126/252	126	252	119.794
C254-s63/252	63	252	124.945
C254-s126/126	126	126	124.142
C254-s126/315	126	315	110.499

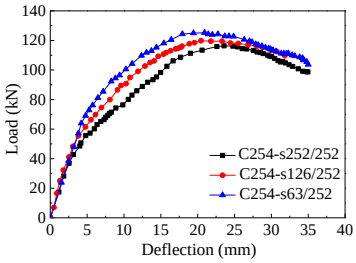

(a) Varying spacing along perimeter

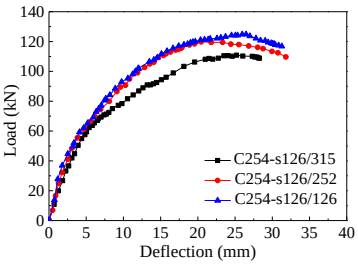

(b) Varying spacing in the field

Fig. 11 Comparison of load–deflection curves for floors with different values of screw spacing

3.2.3 Influence of concrete slab thickness

Owing to the large cracks on the concrete slab that occurred during the tests and the conclusion in [14] that a thicker slab may increase the bending resistance of a composite beam, five slab thicknesses in Table 8 are considered to better understand the influence of concrete slab thickness on the ultimate capacity of CFS–concrete composite floors. The concrete slab thickness is the distance from the valley of the shallow CFS form deck to the top surface of the concrete slab. The concrete properties adopted in the FE model were acquired from the results of the material tests discussed in subsection 2.2. As indicated in Table 8, the ultimate load increased with increasing slab thickness. For example, when the slab thickness was increased by 10 mm from 30 mm, the ultimate bearing capacities of the composite floors were increased by 23.40%, 6.50%, 0.33%, and 4.33%, respectively. As shown, enhancement in the ultimate load was apparent when the slab thickness increased from 30 mm to 40 mm, whereas varying the slab thickness from 40 mm to 70 mm exhibited a small impact. Fig. 12 shows the load–deflection curves of the specimens. Before the loading reached 60 kN, the slopes of all curves were similar, indicating that the influence of slab thickness on the initial stiffness of the floors was negligible. However, after 60 kN, the specimen with the slab thickness of 30 mm showed the most severe stiffness degradation. Therefore, the minimum concrete slab thickness is suggested to be 40 mm.

Table 8
Influence of concrete slab thickness on the capacity of composite floor

Specimen	Slab thickness (mm)	P^*_u (kN)
C254-o30	30	97.080
C254-o40	40	119.794
C254-o50	50	127.585
C254-o60	60	128.007
C254-o70	70	133.546

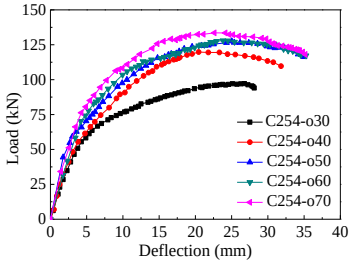

Fig. 12 Comparison of load–deflection curves for floors with different concrete slab thickness

3.2.4 Influence of steel strength of the joist

Specimens C254-Q235 and C254-Q318 were identical in all aspects but had different values of steel strength for their joists. The steel yield strength of C254-Q235 was 235 MPa, whereas that of C254-Q318 was 318 MPa. As presented in Table 9, increasing the steel yield strength resulted in an increase in the ultimate load, with enhancements in capacity of up to 18.1%. This is primarily due to the increase in the steel yield strength, which resulted in an increased bending section modulus of the CFS, thereby increasing the ultimate load of the composite floors. Additionally, the specimen with a higher steel yield strength of the joists achieved a higher initial stiffness, as shown in Fig. 13.

Table 9
Influence of steel strength of joists on the capacity of composite floor

Specimen	Steel yield strength（MPa）	P^*_u (kN)
C254-Q235	235	101.38
C254-Q318	318	119.79

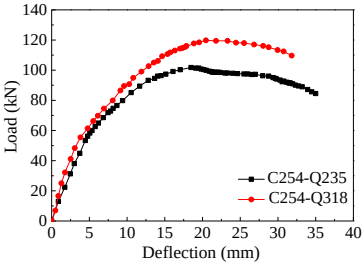

Fig. 13 Comparison of load–deflection curves for floors with different values of steel strength for joists

Hence, according to the above analyses, it can be concluded that the web depth-to-thickness ratio, span-to-depth ratio of the joists, and steel strength had significant influences on the ultimate capacity of the composite floor. Therefore, only these three factors were considered in the method for evaluating the bending capacity of composite floors in section 4.

4. Simplified method for calculating the ultimate moment capacity of CFS–concrete floors

A simplified method, the core of which comprises the segregation of the composite floor model and the determination of the corresponding comprehensive corrected coefficient of each component, has been developed for calculating the ultimate moment capacity of the CFS–concrete composite floor system.

4.1 Simplified calculation model

As reported in [15], the enhancement in ultimate moment capacity of composite floors is linearly proportional to the number of joists. Therefore, the CFS–concrete composite floor was simplified to a configuration of one T-shape composite beam and two inverted L-shape composite beams (hereinafter L-shape composite beam), as illustrated in Fig. 14. Hence, the ultimate moment capacity of the floor can be obtained from the summation of the ultimate moment capacity of the T- and L-shape beams. This subsection aims to validate this simplified method through an FE analysis.

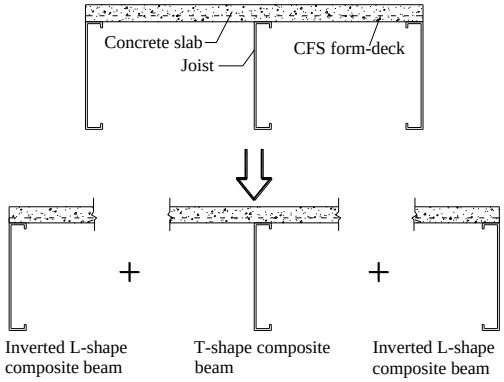

Fig.14 Equivalent diagram of composite floor

The FE models of the simplified T- and L-shape composite beams were developed by using the method detailed in subsection 3.1. The assumptions are as follows: 1. The floor slab at each cross section exhibits the same displacement in the *y* direction, e.g., points *a*, *b*, and *c* shown in Fig. 15(a) show the same deflection ($U_{ay}=U_{by}=U_{cy}$). 2. The composite floor has no deflection along the *x* direction, and the boundary conditions of the T-shape composite beam are as shown in Fig. 15(b).

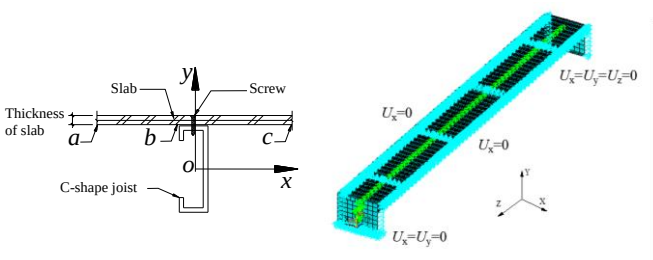

(a) Simplified T-shape model (b) Boundary conditions

Fig. 15 Simplified FE model of T-shape composite beam

The simplified FE model for the T-shape composite beam is shown in Fig. 15(b). Because no shear lag effects were observed in the tests, the slab width was modeled as equal to the joist spacing (i.e., 400 mm) [16]. Furthermore, overall models with different numbers of joists were developed, and comparisons of the ultimate moment capacities between the overall and simplified models are presented in Table 10. In Table 10, M_u is the ultimate moment capacity of the overall model, $M_{u\text{-}T}$ is the ultimate moment capacity of a single T-shape model, $M_{u\text{-}L}$ is the ultimate moment capacity of a single inverted L-shape model, $M_{u\text{-}S}$ is the ultimate moment capacity from simplified method and $M_{u\text{-}F}$ is the ultimate moment capacity from FE analysis.

Table 10
Comparisons of ultimate moment capacities between overall model and simplified model

$l\times b$ (mm)	T-shape beam n_1	Inverted L-shape beam n_2	$M_{u\text{-}T}$ (kN·m)	$M_{u\text{-}L}$ (kN·m)	$M_{u\text{-}S}$ (kN·m)	$M_{u\text{-}F}$ (kN·m)	$M_{u\text{-}S}/M_{u\text{-}F}$
3600×800	1	2	19.52	18.20	55.92	53.93	1.037
3600×1200	2	2			75.43	77.32	0.976
3600×1600	3	2			94.95	97.87	0.970
3600×2000	4	2			114.46	117.58	0.974

As indicated, the difference between the overall and simplified models is within 4%, thereby demonstrating the validity of this method in simplifying the composite floor to T-shape and inverted L-shape composite beams. Thus, the ultimate moment capacity of the CFS–concrete composite floor can be considered as the summation of the individual capacities of the T- and L-shape composite beams, which can be defined as Eq. (1).

$$M_u = n_1 M_{u\text{-}T} + n_2 M_{u\text{-}L} \tag{1}$$

where $M_{u\text{-}T}$ and $M_{u\text{-}L}$ are the ultimate moment capacities of the T- and L-shape composite beams, respectively; n_1 and n_2 are the number of T- and L-shape composite beams, respectively.

Moreover, a comprehensive corrected coefficient η was introduced to consider the effects of key factors, such as the web depth-to-thickness ratio, span-to-depth ratio of the joists, and steel strength. Therefore, the ultimate bending capacity of the T- and L-shape CFS–concrete composite beams can be calculated through Eqs. (2) and (3).

$$M_{u\text{-}T(L)} = \eta_{T(L)} M_{y\text{-}T(L)} \tag{2}$$

where η_T and η_L are the comprehensive corrected coefficients of the T- and L-shape composite beams, respectively; $M_{y\text{-}T}$ and $M_{y\text{-}L}$ are the elastic bending moment capacities of the T- and L-shape composite beams, respectively, which can be calculated using Eq. (3).

$$M_{y\text{-}T(L)} = W_{T(L)} f_y \tag{3}$$

where $W_{T(L)}$ is the bending modulus of the T- or L-shape composite beam [17], and f_y is the steel yield strength.

4.2 Evaluation of comprehensive corrected coefficient η

The comprehensive corrected coefficient η is affected by the web depth-to-thickness ratio, span-to-depth ratio of the joists, and steel strength. The influences of these parameters were investigated by extensive FE analyses on a selected T-shape composite beam. An FE model of the L-shape composite beam was also developed to examine the coefficient η_L. The method for all FE models was the same as that used in subsection 3.1, and only the yield strength of the steel joists was changed to 235 MPa or 345 MPa.

The values of the comprehensive corrected coefficient of the composite beam in which the yield strength of the steel joists was 235 MPa are presented in Table 11. On the other hand, Table 12 lists the values of the comprehensive corrected coefficients of the composite beam in which the yield strength of the steel joists was 345 MPa. The results presented in Tables 11 and 12 were obtained using two different steel strengths, namely 235 MPa and 345 MPa, respectively, and three web depths, i.e., 205, 254, and 305 mm. For each web depth, three span-to-depth ratios, namely 12, 16, and 20, and four web depth-to-thickness ratios, i.e., 100, 150, 200, and 250 were employed. $M_{u\text{-}T}$ and $M_{y\text{-}T}$ are the ultimate moment capacity and elastic bending moment capacity of the T-shape composite beam, respectively, whereas $M_{u\text{-}L}$ and $M_{y\text{-}L}$ are those of the inverted L-shape composite beam, respectively. Furthermore, $\eta_{T\text{-}235}$ and $\eta_{L\text{-}235}$ are the comprehensive corrected coefficients of the T and L-shape composite beams, respectively, in which the yield strength of the steel joists was 235 MPa; meanwhile, $\eta_{T\text{-}345}$ and $\eta_{L\text{-}345}$ represent those with a yield strength of 345 MPa, respectively.

As mentioned in Eq. (2),

$$\eta_{T\text{-}235} = \frac{M_{u\text{-}T}}{M_{y\text{-}T}} \tag{4}$$

and this is similar for $\eta_{L\text{-}235}$, $\eta_{T\text{-}345}$ and $\eta_{L\text{-}345}$.

Table 11
η of the composite beam with 235 MPa yield strength of steel joist

Details of steel joist (mm)					FE analysis M_u (kN·m)		Elastic theory M_y (kN·m)		$\eta_{T\text{-}235}$	$\eta_{L\text{-}235}$
Dimension of joist	l/h	h/t	l	t	$M_{u\text{-}T}$	$M_{u\text{-}L}$	$M_{y\text{-}T}$	$M_{y\text{-}L}$		
C205×41×14×t	12	100	2460	2.05	16.821	14.634	13.710	12.966	1.227	1.129
		150	2460	1.37	10.756	9.633	9.380	8.974	1.147	1.073
		200	2460	1.02	7.475	7.109	7.085	6.824	1.055	1.042
		250	2460	0.82	5.710	5.529	5.751	5.559	0.993	0.994
	16	100	3280	2.05	17.523	16.631	13.710	12.966	1.278	1.283
		150	3280	1.37	10.820	10.876	9.380	8.974	1.153	1.212
		200	3280	1.02	7.109	8.062	7.085	6.824	1.003	1.181
		250	3280	0.82	5.568	6.037	5.751	5.559	0.968	1.086
	20	100	4100	2.05	16.902	15.390	13.710	12.966	1.233	1.187
		150	4100	1.37	11.377	10.814	9.380	8.974	1.213	1.205
		200	4100	1.02	8.365	8.062	7.085	6.824	1.181	1.181
		250	4100	0.82	6.609	6.037	5.751	5.559	1.149	1.086
C254×41×14×t	12	100	3060	2.55	27.415	23.443	22.539	21.060	1.216	1.113
		150	3060	1.7	17.190	15.417	15.469	14.650	1.111	1.052
		200	3060	1.27	12.102	11.442	11.752	11.229	1.030	1.019
		250	3060	1.02	9.142	9.096	9.541	9.169	0.958	0.992
	16	100	4080	2.55	27.249	25.171	22.539	21.060	1.209	1.195
		150	4080	1.7	16.422	16.198	15.469	14.650	1.062	1.106
		200	4080	1.27	11.664	11.545	11.752	11.229	0.992	1.028
		250	4080	1.02	9.374	8.741	9.541	9.169	0.982	0.953
	20	100	5100	2.55	27.649	26.826	22.539	21.060	1.227	1.274
		150	5100	1.7	18.602	17.616	15.469	14.650	1.203	1.202
		200	5100	1.27	13.752	12.495	11.752	11.229	1.170	1.113
		250	5100	1.02	10.838	9.818	9.541	9.169	1.136	1.071
C305×41×14×t	12	100	3660	3.05	39.766	33.448	34.458	31.850	1.154	1.050
		150	3660	2.0	24.234	22.555	23.436	21.968	1.034	1.027
		200	3660	1.5	17.801	17.129	17.932	16.974	0.993	1.009
		250	3660	1.22	13.874	13.876	14.765	14.067	0.940	0.986
	16	100	4880	3.05	38.900	37.777	34.458	31.850	1.129	1.186
		150	4880	2.0	24.809	23.601	23.436	21.968	1.059	1.074
		200	4880	1.5	17.934	17.361	17.932	16.974	1.000	1.023
		250	4880	1.22	14.353	13.249	14.765	14.067	0.972	0.942
	20	100	6100	3.05	41.289	40.122	34.458	31.850	1.198	1.260
		150	6100	2.0	27.420	25.429	23.436	21.968	1.170	1.158
		200	6100	1.5	20.000	18.376	17.932	16.974	1.115	1.083
		250	6100	1.22	15.578	14.754	14.765	14.067	1.055	1.049

Table 12
η of the composite beam with 345 MPa yield strength of steel joist

Details of steel joist (mm)					FE analysis M_u (kN·m)		Elastic theory M_y (kN·m)		$\eta_{T\text{-}345}$	$\eta_{L\text{-}345}$
Dimension of joist	l/h	h/t	l	t	$M_{u\text{-}T}$	$M_{u\text{-}L}$	$M_{y\text{-}T}$	$M_{y\text{-}L}$		
C205×41×14×t	12	100	2460	2.05	23.538	20.337	20.127	19.034	1.170	1.068
		150	2460	1.37	15.131	13.717	13.771	13.175	1.099	1.041
		200	2460	1.02	10.944	10.354	10.401	10.018	1.052	1.034
		250	2460	0.82	8.815	8.093	8.442	8.162	1.044	0.992
	16	100	3280	2.05	23.112	20.101	20.127	19.034	1.148	1.056
		150	3280	1.37	14.546	13.505	13.771	13.175	1.056	1.025
		200	3280	1.02	10.703	10.354	10.401	10.018	1.029	1.034
		250	3280	0.82	8.653	8.093	8.442	8.162	1.025	0.992
	20	100	4100	2.05	22.991	20.548	20.127	19.034	1.142	1.080
		150	4100	1.37	15.431	13.863	13.771	13.175	1.121	1.052
		200	4100	1.02	11.495	10.389	10.401	10.018	1.105	1.037
		250	4100	0.82	8.385	8.209	8.442	8.162	0.993	1.006
C254×41×14×t	12	100	3060	2.55	38.126	31.797	33.089	30.918	1.152	1.028
		150	3060	1.7	24.663	22.216	22.710	21.508	1.086	1.033
		200	3060	1.27	17.789	16.865	17.253	16.485	1.031	1.023
		250	3060	1.02	14.214	13.083	14.008	13.461	1.015	0.972
	16	100	4080	2.55	36.185	31.794	33.089	30.918	1.094	1.028
		150	4080	1.7	23.479	22.131	22.710	21.508	1.034	1.029
		200	4080	1.27	17.528	16.931	17.253	16.485	1.016	1.027
		250	4080	1.02	14.152	13.745	14.008	13.461	1.010	1.021
	20	100	5100	2.55	37.455	32.842	33.089	30.918	1.132	1.062
		150	5100	1.7	24.894	22.540	22.710	21.508	1.096	1.048
		200	5100	1.27	18.515	16.999	17.253	16.485	1.073	1.031
		250	5100	1.02	13.806	13.498	14.008	13.461	0.986	1.003
C305×41×14×t	12	100	3660	3.05	53.436	47.507	50.587	46.759	1.056	1.016
		150	3660	2.0	34.463	33.155	34.406	32.250	1.002	1.028
		200	3660	1.5	26.530	25.410	26.326	24.919	1.008	1.020
		250	3660	1.22	21.187	19.814	21.676	20.652	0.977	0.959
	16	100	4880	3.05	53.064	47.507	50.587	46.759	1.049	1.016
		150	4880	2.0	33.489	33.674	34.406	32.250	0.973	1.044
		200	4880	1.5	26.474	25.741	26.326	24.919	1.006	1.033
		250	4880	1.22	21.076	20.687	21.676	20.652	0.972	1.002
	20	100	6100	3.05	55.945	47.507	50.587	46.759	1.106	1.016
		150	6100	2.0	35.918	33.155	34.406	32.250	1.044	1.028
		200	6100	1.5	27.015	25.410	26.326	24.919	1.026	1.020
		250	6100	1.22	20.183	19.814	21.676	20.652	0.931	0.959

For a more quantitative analysis, a regression analysis of the data from Tables 11 and 12 was conducted using the MATLAB® (The Mathworks Inc., USA) function "lsqcurvefit" to identify the relationship between the comprehensive corrected coefficient and independent variables such as web depth-to-thickness ratio, span-to-depth ratio of the joists, and steel strength. The equations are expressed as

$$\eta_{T\text{-}235} = 1.613 - 0.0295\sqrt{l/h} - 0.0287\sqrt{h/t} \tag{5}$$

$$\eta_{T\text{-}345} = 1.779 - 0.069\sqrt{l/h} - 0.0391\sqrt{h/t} \tag{6}$$

$$\eta_{L\text{-}235} = 1.5753 - 0.0255\sqrt{l/h} - 0.0312\sqrt{h/t} \tag{7}$$

$$\eta_{L\text{-}345} = 1.3755 - 0.029\sqrt{l/h} - 0.0333\sqrt{h/t} \tag{8}$$

4.3 Result validation of the proposed method

According to Eqs. (1) and (2), the ultimate moment capacity of the CFS–concrete composite floor, in which the yield strengths of the steel joists are 235 MPa and 345 MPa, respectively, can be calculated by Eqs. (9) and (10).

$$M_u = n_1\eta_{T\text{-}235}M_{y\text{-}T} + n_2\eta_{L\text{-}235}M_{y-L} \tag{9}$$

$$M_{\mathrm{u}} = n_1\eta_{\mathrm{T\text{-}345}}M_{\mathrm{y\text{-}T}} + n_2\eta_{\mathrm{L\text{-}345}}M_{\mathrm{y-L}} \tag{10}$$

In Eqs. (9) and (10), $M_{\mathrm{y\text{-}T}}$ and $M_{\mathrm{y\text{-}L}}$ can be obtained according to Eq. (3), whereas η_{T} and η_{L} can be calculated according to Eqs. (5) to (8). Additionally, a linear interpolation method can be adopted for other yield strengths. The proposed method can provide a simple calculation and design approach for designers to estimate the ultimate moment capacity of CFS–concrete composite floor systems.

For validating the proposed method, the elastic bending moment capacity of the composite beam was calculated according to Eq. (3). Values of the ultimate moment capacity obtained from the simplified method and FE analysis are listed and compared in Table 13. The calculated ultimate moment capacities based on Eqs. (9) to (10) were compared with those of specimens BM-1 and BM-2 in the test and FE analysis. The results are presented in Table 14, in which $M_{\mathrm{u\text{-}E}}$, $M_{\mathrm{u\text{-}F}}$, and $M_{\mathrm{u\text{-}S}}$ represent the ultimate moment capacity obtained from the test, FE analysis, and simplified method, respectively. The errors were all less than 9%, indicating that the results calculated by the suggested method agreed well with those obtained from the FE analysis. As indicated in Table 14, strong agreements were achieved among the ultimate moment capacities of both floors obtained from the proposed method, and the experimental and numerical investigations. According to the FE parametric analyses results of section 3.2, the influences of both screw spacing and concrete slab thickness were insignificant and not considered in the evaluation of the comprehensive corrected coefficient. However, if the effects of both screw spacing and concrete slab thickness were considerable, the comprehensive corrected coefficient should be investigated further. Therefore, the proposed method only applies to the CFS–concrete composite floor in which the screw spacing and concrete slab thickness have small effects on the ultimate moment capacity of CFS–concrete floors.

Table 13
Comparison of the ultimate moment capacity from simplified method and FE analysis

$l\times b$ (mm)	n_1	n_2	$\eta_{\mathrm{T}}M_{\mathrm{y\text{-}T}}$ (kN·m)	$\eta_{\mathrm{L}}M_{\mathrm{y\text{-}L}}$ (kN·m)	$M_{\mathrm{u\text{-}S}}$ (kN·m)	$M_{\mathrm{u\text{-}F}}$ (kN·m)	M_{uS} /$M_{\mathrm{u\text{-}F}}$
3600×800	1	2	19.18	18.62	56.42	53.928	1.046
3600×1200	2	2			75.6	77.32	0.978
3600×1600	3	2			94.78	97.87	0.968
3600×2000	4	2			113.96	117.58	0.969

Table 14
Comparison of the ultimate moment capacity from simplified method and FE analysis

Specimen	n_1	n_2	$\eta_{\mathrm{T}}M_{\mathrm{y\text{-}T}}$ (kN·m)	$\eta_{\mathrm{L}}M_{\mathrm{y\text{-}L}}$ (kN·m)	$M_{\mathrm{u\text{-}S}}$ (kN·m)	$M_{\mathrm{u\text{-}E}}$ (kN·m)	$M_{\mathrm{u\text{-}F}}$ (kN·m)	$M_{\mathrm{u\text{-}S}}/M_{\mathrm{u\text{-}E}}$	$M_{\mathrm{u\text{-}S}}/M_{\mathrm{u\text{-}F}}$
BM-1	1	2	19.18	18.62	56.42	50.88	52.11	1.11	1.08
BM-2						52.36	53.93	1.08	1.05

5. Conclusion

In this study, two composite CFS specimens were examined by full-scale bending tests to investigate the influence of slab materials on the bending performance of CFS–concrete composite floors at first. Subsequently, FE models of the tested floor were established, and the model was validated using the test results. Good agreements between the experimental and numerical results were achieved and the established FE model was subsequently adopted for parametric analyses. The influences of different parameters, such as web depth-to-thickness ratio, span-to-depth ratio of the joist, screw spacing, concrete slab thickness, and steel strength, on the ultimate load were investigated with various floor configurations. Consequently, based on the equivalent model of composite floors and the proposed equations for evaluating the comprehensive corrected coefficient for the simplified beam models, a simplified method for evaluating the ultimate moment capacity of CFS–concrete floors was proposed. The results obtained from the proposed method showed good agreements with those of both experimental and numerical investigations. The conclusions from the investigation are as follows:

(1) Varying the slab material had no significant effect on the ultimate load, but a higher stiffness was observed when the slab material was changed from GSU to FAC.

(2) The web depth-to-thickness ratio, span-to-depth ratio, and steel strength of the joists affected the ultimate load significantly and consequently the bending capacity of the floors. A higher web depth-to-thickness ratio resulted in a smaller ultimate bending capacity of the CFS–concrete floor. Meanwhile, a smaller span-to-depth ratio led to a higher ultimate bending capacity. Increasing the steel strength of the joists correspondingly increased the ultimate capacity of the CFS composite floors.

(3) Increasing the screw spacing and concrete slab thickness had little influence on the ultimate load; therefore, they were not taken into consideration in the proposed equations for calculating the ultimate moment capacity.

The composite action between the CFS joists and GSU subfloors, which is neglected in the current design standard owing to the difficulty in quantifying the influence of the composite action on the bending capacity of the floors, was considered in the simplified method. Finally, the proposed method was validated using the results of the experimental and numerical investigations, and therefore, can be applied in engineering practice.

Acknowledgments

The authors wish to acknowledge the support of the Natural Science Foundation of China (Grant No.: 51678060) and Fundamental Research Funds for the Central Universities (Grant No.:310828171011). Any opinions, findings, and conclusions or recommendations expressed herein are those of the authors and do not necessarily reflect the views of the sponsors.

References

[1] Steel Framing Alliance. Poly Canyon Village student housing. Steel Success Stories, 2010
[2] Hanaor A., “Tests of composite beams with cold-formed sections”, Journal of Construction Steel Research, 54(2), 245–264, 2000.
[3] Lakkavalli B.S. and Liu Y., “Experimental study of composite cold-formed steel C-section floor joists”, Journal of Construction Steel Research, 62(10), 995–1006, 2006.
[4] Irwan J.M., Hanizah A.H. and Azmi I., “Test of shear transfer enhancement in symmetric cold-formed steel-concrete composite beams”, Journal of Construction Steel Research, 65(12), 2087-2098, 2016.
[5] Irwan J.M., Hanizah A.H., Azmib I. and Koh H.B., “Large-scale test of symmetric cold-formed steel (CFS)–concrete composite beams with BTTST enhancement”, Journal of Construction Steel Research, 67(4), 720–726, 2011.
[6] Hsu C.T.T, Punurai S., Punurai W. and Majdi Y., “New composite beams having cold-formed steel joists and concrete slab”, Engineering Structures, 71, 187–200, 2014.
[7] Kyvelou P., Gardner L. and Nethercot D.A., “Testing and analysis of composite cold-formed steel and wood−based flooring systems”, Journal of Structural Engineering, 143(11), 1-16, 2017.
[8] GB/T 228.1-2010, “Metallic Materials-Tensile Testing-Part 1: Method of Test at Room Temperature”, 2011, Beijing, Standard Press of China. (in Chinese)
[9] GB/T 50081-2002, Standard for test method of mechanical properties on ordinary concrete, 2002, Beijing, China Architecture & Building Press. (in Chinese)
[10] Chien E. and Ritchie J.K., “Design and construction of composite floor systems”, 1984, Ontario, Canadian Institute of Steel Construction.
[11] Ansys Inc, “Element reference”, 2009b, Canonsburg, PA, Ansys Incorporation.
[12] Alhajri T.M., Tahir M.M., Azimi M., Mirza J., Lawan M. M. and Alenezi K.K., “Behavior of pre-cast U-shaped composite beam integrating cold-formed steel with ferro-cement slab”, Thin-Walled Structures, 102, 18-29, 2016.
[13] Xu L., Sultana P. and Zhou X.H., “Flexural strength of cold-formed steel built-up box sections”, Thin-Walled Structures. 47(6–7), 807-815, 2009.
[14] Hou H.T., Liu X., Qu B., Ma T.X., Liu H.N., Feng M.Y. and Zhang B., “Experimental evaluation of flexural behavior of composite beams with cast-in-place concrete slabs on precast prestressed concrete decks”, Engineering Structures, 126, 405-416, 2016.
[15] Zhou X.H. and Jia Z.W., “Experimental study on flexural capacity of cold-formed steel joists and concrete composite floor”, Journal of Building Structures, 7(31), 13-22, 2010. (in Chinese)
[16] Pinelopi K., Leroy G. and Nethercot D.A., “Design of composite cold-formed steel flooring systems”, Structures, 12, 242-252, 2017.
[17] GB 50017-2017, Standard for design of steel structures, 2017, Beijing, China Architecture & Building Press. (in Chinese).

Advanced Steel Construction – Vol. 15 No. 4 (2019) 316–322
DOI:10.18057/IJASC.2019.15.4.2

INFLUENCE OF COLD-FORMED ANGLE ON HIGH STRENGTH STEEL MATERIAL PROPERTIES

Anh Tuan Tran [1, *], Lars Bernspång [1], Milan Veljkovic [2], Carlos Rebelo[3] and Luís Simões da Silva [3]

[1] *Luleå University of Technology, Sweden*
[2] *Delft University of Technology, The Netherlands*
[3] *ISISE, University of Coimbra, Portugal*
** (Corresponding author: E-mail: trananhtuangtvt@gmail.com)*

ABSTRACT

This paper describes a study of the S650 high strength steel material properties including the effect of cold-formed angle. Coupon specimens with different cold-formed angles (90°, 100°, 120°, 140°, 160° and 180°) and different thicknesses (4 mm and 6 mm) were examined. Relationships between cold-formed angle and yield stress as well as tensile stress of the material were determined, based on the tensile coupon test results. Yield and tensile stresses assessed by considering the influence of the cold-formed angles were compared with those without considering this influence. Analyses revealed that both yield and tensile stresses decreased with increasing cold-formed angle. Ductile-damage material models available in the finite element analysis software ABAQUS were used to simulate tensile coupon tests. The experimental and numerical results showed good agreements.

ARTICLE HISTORY

Received: 19 March 2018
Revised: 20 April 2019
Accepted: 05 May 2019

KEYWORDS

High strength steel material;
Cold-formed angle;
Tensile coupon test;
Ductility;
Experimental investigation;
Finite element analysis;

1. Introduction

Cold-formed steel members are used increasingly in industrial and civil construction. Their use allows optimizing member cross sections and shapes, thereby reducing the amount of steel used as well as the weight of the structures and, consequently, reducing harmful effects on the environment. Cold-formed members are manufactured by either cold rolling method or press braking method. In the cold rolling method, the cold-formed member is obtained from passing flat steel sheet through a series of deformation stages. In the press braking method, the cold formed member is produced by bending a flat steel sheet along its length. The press braking method yields various cross sections and is therefore more popular than the cold rolling method.

Cold forming has significant effect on ductility and yield and tensile stresses of steel materials. In EN 1993-1-3 [1], influence of cold forming is considered by increasing average the yield stress of the whole cross-section. The average yield stress depends on the number of 90° bends in the cross-section. Afshan et al. [2] determined the material properties of S355 carbon steel via tensile coupon tests. Flat coupon specimens, 90° corner coupon specimens of the square hollow sections and rectangular hollow sections as well as circular coupon specimens of the circular hollow sections were investigated. The investigated cross sections had thicknesses of 5 mm and 6 mm. The Ramberg - Osgood parameters from the tensile tests were also presented in the study. In a previous study [3], the properties of high strength steel were determined using tensile coupon tests. These tests were performed on corner coupon specimens and flat coupon specimens that were extracted from the hot finished and cold formed square hollow sections and rectangular hollow sections. The ratio of the yield stresses and tensile stresses of the corner and flat specimens were also determined. The stress-strain curves of flat and corner coupon specimens of S460, S500, and S690 materials also were compared. Ma et al. [4] investigated, via experiments, cold formed high strength steel materials with 0.2% offset yield stresses of 700 MPa, 900 MPa, and 1100 MPa. A total of 66 tensile coupon tests was performed and various coupon specimens were considered, namely the: flat coupon, corner coupon, and curved coupon, which were extracted from the square hollow sections, rectangular hollow sections, and circular hollow sections. A new constitutive model, which uses the Ramberg - Osgood expression, was developed based on the experimental results. These results revealed that cold forming has significant effect on the material strength. In fact, the strength in the corner part of coupon specimens with 90° bends, increased by up to 34% with effect of cold forming. Shi et al. [5] performed 46 tensile coupon tests on high strength steel materials that have nominal yield stresses of 500 MPa, 550 MPa, and 690 MPa. The coupon specimens were grouped into two categories, namely those with thicknesses of (i) <16 mm and (ii) >16 mm. Flat coupon specimens were tested at different load rates, different compliances, and different strain rates. The experimental results were used to develop a nonlinear constitutive model and a revised multi-linear constitutive model. Tran et al. [6] investigated the material strengths of the S650 high strength steel using 18 tensile coupon tests. The coupon specimens were extracted from the polygonal and circular cold-formed high strength steel sections.

This paper describes experimental and numerical studies of the S650 high strength steel material properties with effect of cold-formed angle using thirty tensile coupon tests. Tensile coupon specimens with different cold-formed angles (90°, 100°, 120°, 140°, 160° and 180°) and different thicknesses (4 mm and 6 mm) were considered. Relationships between the cold-formed angles and yield stress as well as tensile stress of the material were investigated. The yield and tensile stresses determined by considering the influence of the cold-formed angle were compared with those determined without considering this influence. Ductile-damage material models in the commercial finite element analysis (FEA) programme ABAQUS [14] were used to simulate tensile coupon tests and then, the experimental and FEA results were compared.

2. Experimental investigation

2.1. Coupon specimens

In order to investigate the influence of cold-formed angles on the properties of high strength steel material, thirty coupon specimens with different cold-formed angles (90°, 100°, 120°, 140°, 160° and 180°) and different thicknesses (4 mm and 6 mm) were examined. Number and thicknesses of the coupon specimens were considered as limitation in this study. The coupon specimens were produced using a three-step process. In the first step, L-section profiles were produced from the high strength steel plates using the press braking method, Fig. 1.

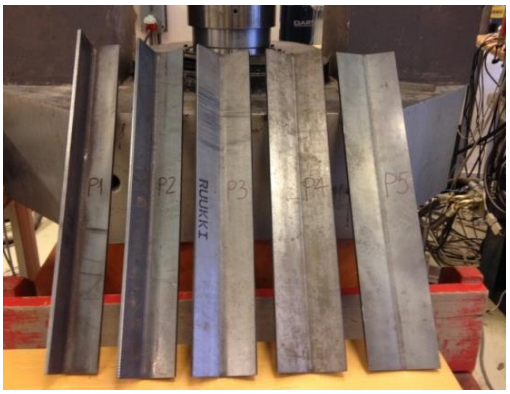

Fig. 1 L section profiles with different cold-formed angles

In the second step, a water jet was used to cut the coupon specimens from the profiles with an extra 5 mm on each side to avoid any heating of the coupon specimens. In the last step, both sides of the coupon specimens were made perfectly perpendicular to the specimen surface and both ends of the specimens were then flattened to help clamping specimens during the tests, Fig. 2. Chen and Young [7] also flattened the ends of corner coupon specimens for tensile coupon tests to study the corner properties of cold-formed steel sections at elevated temperatures.

Fig. 2 Coupon specimens

Fig. 3 shows general dimensions of the tensile coupon specimen. Total lengths (Lt) of the specimens were approximately 596 mm. The flattened part lengths (Lf) at both ends were used to help gripping the specimens during the tensile tests and were designed so that flattening does not affect the middle parts of the coupon specimens. The large radii (R2) were used to help failure sections occurred at middle of the specimens and were approximately 1513 mm and 2113 mm for the 4 mm and 6 mm thick coupon specimens, respectively.

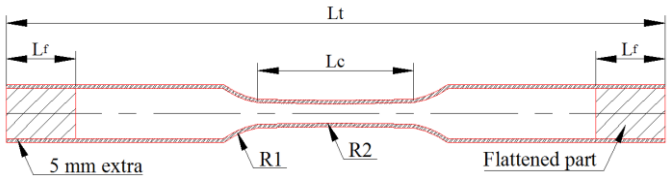

Fig. 3 General dimensions of the corner coupon specimen

Fig. 4 shows a typical cross section of the coupon specimens. Considered dimensions are inner radius (R3), outer radius (R4), width of the inner curves (B1), width of the outer curves (B2), and thickness (t). These dimensions were measured three times by using a digital caliper device with 0.01 mm of precision and used to define the area of the cross-section.

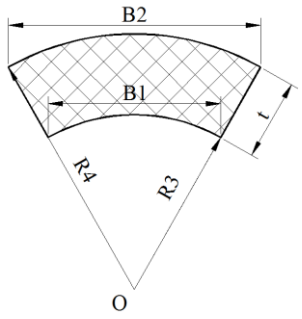

Fig. 4 Typical cross section of a corner coupon specimen

Tables 1 and Table 2 show the measured dimensions of cross sections of the 4 mm thick and 6 mm thick coupon specimens, respectively. The areas of the cross sections are also presented in these Tables. The following nomenclature are adopted for the specimens: angle of coupon specimen {C1(90°), C2(100°), C3(120°), C4(140°), C5(160°) and F(180°)} - thickness {4 mm and 6 mm}-test number in the test series {S1; S2; S3}.

Table 1
Dimensions of cross sections of the 4 mm thick coupon specimens

Specimen	Angle	B1 (mm)	B2 (mm)	t (mm)	A (mm²)
C1-4-S1	90°	8.49	14.14	4.01	50.39
C1-4-S2	90°	8.40	14.22	4.01	50.36
C1-4-S3	90°	8.45	14.09	4.02	50.30
C2-4-S1	100°	7.69	12.82	4.02	44.74
C2-4-S2	100°	7.71	12.86	3.99	44.68
C2-4-S3	100°	7.66	12.91	4.00	44.68
C3-4-S1	120°	6.01	10.01	3.99	33.51
C3-4-S2	120°	6.05	10.03	3.96	33.37
C3-4-S3	120°	6.08	10.02	4.03	33.99
C4-4-S1	140°	11.62	14.36	4.00	55.34
C4-4-S2	140°	9.86	13.47	4.03	48.94
C4-4-S3	140°	7.10	9.58	4.01	34.63
F-4-S1	180°	10.90	10.90	4.10	44.60
F-4-S2	180°	10.60	10.60	4.10	43.20
F-4-S3	180°	10.80	10.80	4.10	44.40

Table 2
Dimensions of cross sections of the 6 mm thick coupon specimens

Specimen	Angle	B1 (mm)	B2 (mm)	t (mm)	A (mm²)
C1-6-S1	90°	12.73	21.21	6.00	113.10
C1-6-S2	90°	12.70	21.26	5.96	112.39
C1-6-S3	90°	12.71	21.18	6.02	113.23
C2-6-S1	100°	11.57	19.28	6.01	100.59
C2-6-S2	100°	11.62	19.31	6.03	101.31
C2-6-S3	100°	11.60	19.26	6.03	101.03
C3-6-S1	120°	9.02	15.01	6.02	75.75
C3-6-S2	120°	9.05	15.08	6.02	76.10
C3-6-S3	120°	9.00	15.01	6.00	75.41
C5-6-S1	160°	11.00	13.09	6.00	73.13

C5-6-S2	160°	9.09	11.18	5.98	61.28
C5-6-S3	160°	6.62	8.71	6.02	46.60
F-6-S1	180°	11.10	11.10	6.01	66.7
F-6-S2	180°	11.10	11.10	6.00	66.4
F-6-S3	180°	11.00	11.00	6.01	66.1

2.2. Test set-up and instruments

Dartec testing machine with maximum capacity of 250 kN was used to perform the tensile coupon tests under laboratory temperature and humidity conditions. Displacements of the tensile coupon specimens during the tests were measured using an extensometer with 50 mm length gage allowing ±12.5 mm (±25%) clearance in elongation. Fig. 5 illustrates the typical set up for the tensile coupon tests. The tensile coupon tests were carried out by displacement control method. EN 10002-1 [8] recommends rate limitations at crossheads for tensile coupon tests. For example, maximum and minimum stress rates of 6 MPa/s and 60 MPa/s, respectively, are recommended for testing within the elastic range and at stresses up to the yield stress. Maximum strain rates of 0.25% strain/s and 0.8% strain/s are recommended for testing within the plastic range at stresses up to the proof stress and greater than the proof stress, respectively. In this study, the tensile coupon tests were performed at a uniform crosshead displacement of 0.02 mm/s.

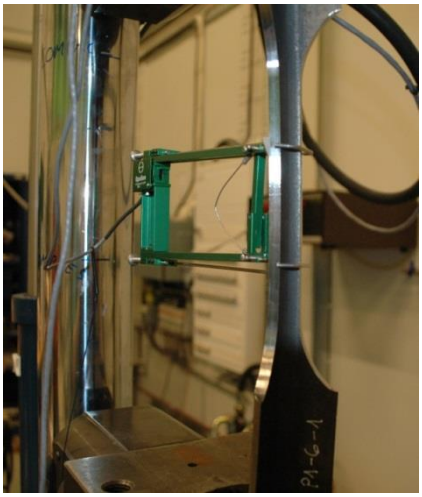

Fig. 5 Set-up for the tensile coupon test

3. Experimental results

Results of the tensile coupon tests are summarized in Table 3 to Table 5, which show the key parameters such as the yield stress σ_y, tensile stress σ_u, yield strain ε_y, tensile strain ε_u and failure strain ε_f. Cold-formed angles of the coupon specimens are also presented in those tables. It should be noted that flat coupon specimens are named as 180° cold-formed angles in this study. In some cases, the failure sections occurred outside the gauge lengths and, hence, those values (C1-4-S2, C4-4-S1 and C5-6-S1, C5-4-S1, S2, S3, C4-6-S1, S2, S3) were not recorded.

Cold-formed angle significantly affects material properties of the S650 high strength steel. Average tensile stress of the 4 mm thick coupon specimens with 90° cold-formed angle is 7.7% higher than those of the specimens with 140° cold-formed angles. Average tensile stress of the 6 mm thick coupon specimens decreases from 905 MPa to 884 MPa when cold-formed angles increase from 90° to 160°. However, average strains at fracture significantly increase with increasing cold-formed angles. Average fracture strain of the 4 mm thick coupon specimens increases from 7.17% to 8.32% with increasing cold-formed angles (from 90° to 140°). Average fracture strain of the 6 mm thick coupon specimens increases from 9.15% to 11.02% with increasing cold-formed angles (from 90° to 160°). Results reveals the similar shape of the engineering stress-engineering strain curves of the 6 mm thick coupon specimens with different cold-formed angles (90°, 100°, and 160°), Fig. 6.

Table 3
Key material properties determined from the tensile coupon tests of the flat coupon specimens

Specimen	Angle	σ_y (N/mm²)	ε_y (%)	σ_u (N/mm²)	ε_u (%)	ε_f (%)
F-4-S1	180°	762	0.60	802	10.6	19.2
F-4-S2	180°	763	0.60	807	8.6	19.1
F-4-S3	180°	762	0.60	806	8.5	19.0
F-6-S1	180°	801	0.40	845	5.7	14.4
F-6-S2	180°	793	0.40	843	6.0	14.8
F-6-S3	180°	791	0.40	843	5.9	14.9

Table 4
Key material properties determined from the tensile coupon tests of the 4 mm thick coupon specimens

Specimen	Angle	σ_y (N/mm²)	ε_y (%)	σ_u (N/mm²)	ε_u (%)	ε_f (%)
C1-4-S1	90°	889	0.62	929	1.18	7.24
C1-4-S2	90°	-	-	-	-	-
C1-4-S3	90°	925	0.64	951	1.24	7.09
C2-4-S1	100°	932	0.64	948	1.02	7.06
C2-4-S2	100°	927	0.64	948	1.12	6.98
C2-4-S3	100°	914	0.64	944	1.16	7.36
C3-4-S1	120°	837	0.60	895	1.25	7.34
C3-4-S2	120°	865	0.61	917	1.17	7.04
C3-4-S3	120°	859	0.61	898	1.15	6.97
C4-4-S1	140°	-	-	-	-	-
C4-4-S2	140°	839	0.60	876	1.51	8.97
C4-4-S3	140°	831	0.60	859	1.07	7.66

Table 5
Key material properties determined from the tensile coupon tests of the 6 mm thick coupon specimens

Specimen	Angle	σ_y (N/mm²)	ε_y (%)	σ_u (N/mm²)	ε_u (%)	ε_f (%)
C1-6-S1	90°	782	0.57	896	1.50	9.39
C1-6-S2	90°	830	0.60	923	1.46	8.85
C1-6-S3	90°	874	0.62	896	1.22	9.20
C2-6-S1	100°	843	0.60	898	1.37	9.48
C2-6-S2	100°	861	0.61	893	1.31	9.69
C2-6-S3	100°	853	0.61	890	1.37	9.41
C3-6-S1	120°	878	0.62	916	1.33	10.31
C3-6-S2	120°	883	0.62	917	1.32	10.41
C3-6-S3	120°	845	0.60	905	1.69	10.88
C5-6-S1	160°	-	-	-	-	-
C5-6-S2	160°	778	0.57	867	1.67	11.52
C5-6-S3	160°	826	0.59	881	1.34	10.52

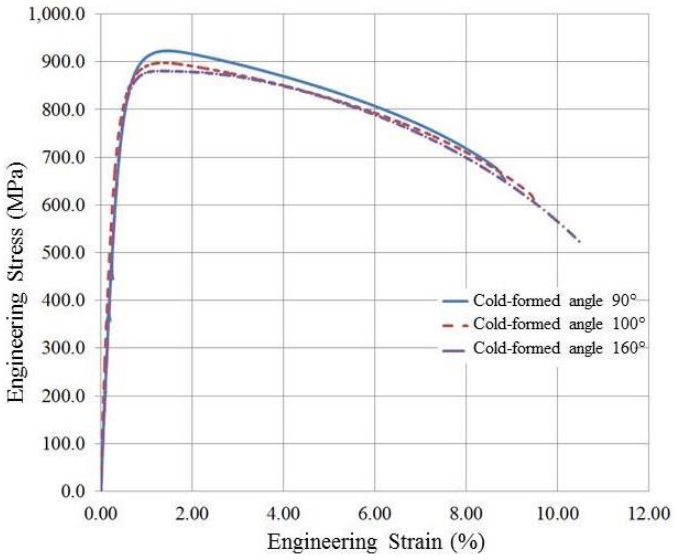

Fig. 6 Engineering stress-strain curves of the 6 mm thick coupon specimens with different cold-formed angles

4. Proposed design rules

4.1. Influence of cold-formed angle on strength of material

Figs. 7 and 8 show the relationship between cold-formed angle and the yield stresses and tensile stresses of the material S650. Tensile coupon test results performed by Wang et al. [13] for high strength steel materials S500 and S960 at the flat parts and corner (90°) parts are also shown in these figures. Trend lines are created based on the tensile coupon test results. The trend lines of different high strength materials S500, S650 and S960 show a similar trend of increasing yield stress and tensile stress as the effect of cold-formed angle increases. It should be noted that flat coupon specimen is named as 180° cold-formed angle specimen. Based on the trend lines, the effects of cold-formed angle on yield and tensile stresses may be calculated using Eq. 1 and Eq. 2 respectively.

$$\sigma_y = -1.258\alpha + 1007 \quad (1)$$

$$\sigma_u = -1.085\alpha + 1027 \quad (2)$$

In these equations σ_y , σ_u , and α are yield stress, tensile stress and cold-formed angle respectively.

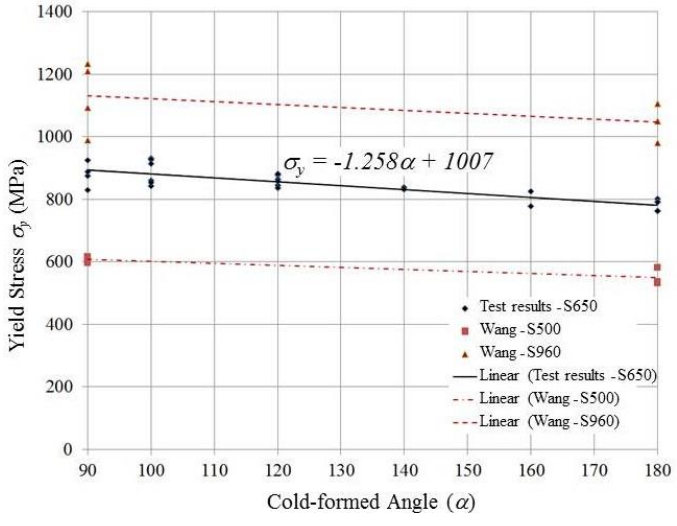

Fig. 7 Relationship between the yield stress and cold-formed angle

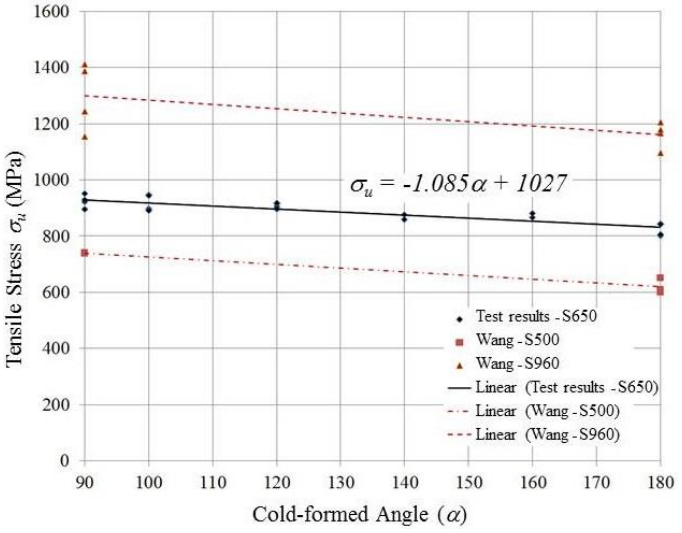

Fig. 8 Relationship between the tensile stress and cold-formed angle

In order to investigate effect of cold-formed angle on the original material strength, yield stress and tensile stress at corner parts of the tensile coupon specimens were compared to those at flat parts. Table 6 shows the ratios between yield stresses and between tensile stresses at the corner parts and the flat parts, as well as thicknesses and angles of the tensile coupon specimens. The comparisons show that cold-formed angle has significant effect on tensile and yield stresses of the S650 high strength steel material. Trend lines based on analyses are presented in Figs. 9 and 10. Relationship between yield and tensile stresses at corner parts and at flat parts of the tensile coupon specimens may be expressed as following function:

$$\sigma_{corner} = \sigma_{flat}(-0.001\alpha + 1.2) \quad (3)$$

Table 6
Stress comparison between the material with effects of cold-formed angle and its base material

Specimen	Angle	Thickness (mm)	$\frac{\sigma_{y,corner}}{\sigma_{y,flat}}$	$\frac{\sigma_{u,corner}}{\sigma_{u,flat}}$
C1-4-S1	90°	4	1.17	1.15
C1-4-S2	90°	4	-	-
C1-4-S3	90°	4	1.21	1.18
C2-4-S1	100°	4	1.22	1.18
C2-4-S2	100°	4	1.22	1.18
C2-4-S3	100°	4	1.20	1.17
C3-4-S1	120°	4	1.10	1.11
C3-4-S2	120°	4	1.13	1.14
C3-4-S3	120°	4	1.13	1.12
C4-4-S1	140°	4	-	-
C4-4-S2	140°	4	1.10	1.09
C4-4-S3	140°	4	1.09	1.07
C1-6-S1	90°	6	0.98	1.06
C1-6-S2	90°	6	1.04	1.09

C1-6-S3	90°	6	1.10	1.06
C2-6-S1	100°	6	1.06	1.06
C2-6-S2	100°	6	1.08	1.06
C2-6-S3	100°	6	1.07	1.05
C3-6-S1	120°	6	1.10	1.09
C3-6-S2	120°	6	1.11	1.09
C3-6-S3	120°	6	1.06	1.07
C5-6-S1	160°	6	-	-
C5-6-S2	160°	6	0.98	1.03
C5-6-S3	160°	6	1.04	1.04

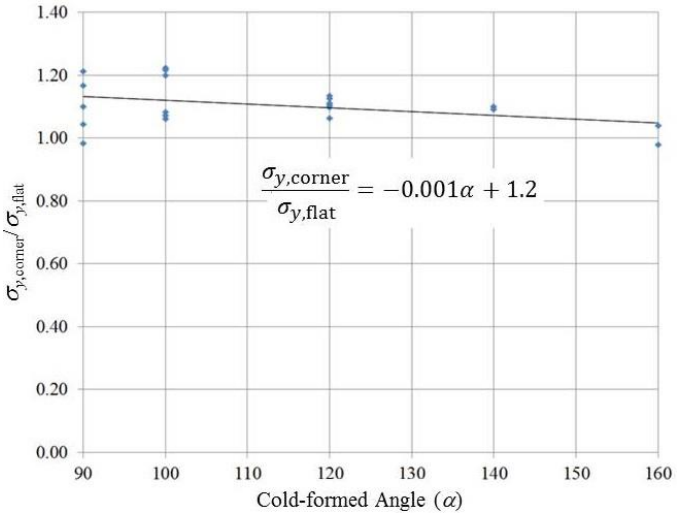

Fig. 9 Relationship between yield stress ratio and cold-formed angle

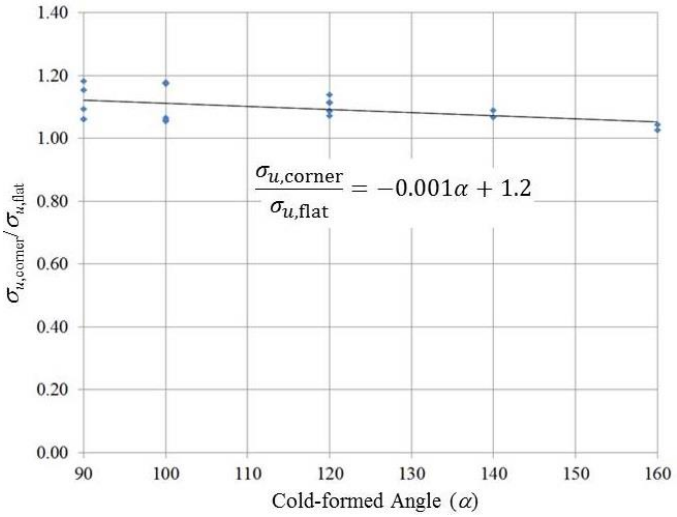

Fig. 10 Relationship between tensile stress ratios and cold-formed angles

4.2. Influence of cold-formed angle on ductility of material

According to EN 1993-1-12 [9], S460 to S700 steel materials should fulfil the following requirements $\sigma_u / \sigma_y \geq 1.05$, $\varepsilon_u \geq 15\varepsilon_y$, elongation at failure: $\varepsilon_f \geq 10\%$ where ε_u and ε_y are the tensile strain, and yield strain, respectively. ASTM-A514 [10] code specifies that high yield stress, quenched and tempered alloy steel plate, suitable for welding, must satisfy the following tensile and hardness requirements: at thicknesses of up to 65 mm (tensile stress: 760 MPa – 895 MPa, minimum yield stress measured at 0.2% offset: 690 MPa, minimum elongation: 18%); at thicknesses 65 mm – 150 mm (tensile stress: 690 MPa – 895 MPa, minimum yield stress measured at 0.2% offset: 620 MPa, minimum elongation: 16%). ASTM-A709 [11] specifies four yield stress levels (250 MPa, 345 MPa, 485 MPa, and 690 MPa) for seven grades (250, 345, 345S, 345W, HPS 345W, HPS 485W, and HPS 690W) of structural steel designated for bridges. At plate thicknesses of up to 100 mm, grades 250, 345, 345W, and 485W exhibit minimum elongations of 23%, 21%, 21%, and 19%, respectively. Moreover, for plate thicknesses smaller 65 mm and 65 mm – 100 mm, the 690W grade exhibits minimum elongations of 18% and 16%, respectively. It should be noted that the ductility requirements in the codes are applied to flat coupon specimens without considering the influence of cold forming.

Results of ductility analyses performed on the S650 high strength steel material, including influence of cold-formed angle, are presented in Fig. 11 to Fig. 13. The analyses show gathering of the results. It could prove quality of the coupon tensile tests. All results are outside of EN 1993-1-12 scope [9]. However, it emphasizes that the results are obtained with effects of cold-formed angle.

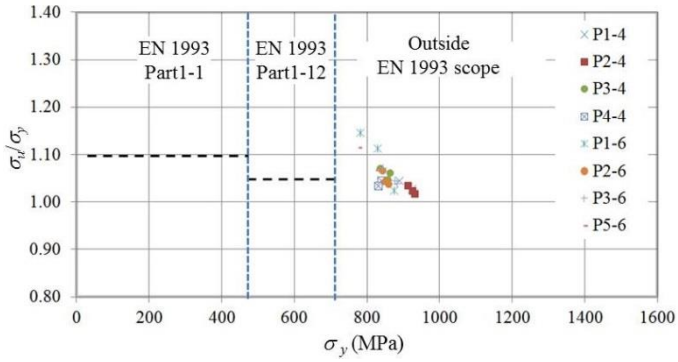

Fig. 11 Relationship between tensile stress and yield stress with effect of the cold-formed angles

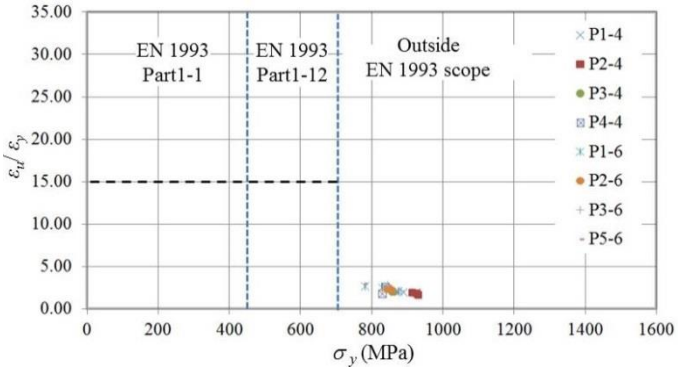

Fig. 12 Relationship between tensile strain and yield strain with effect of the cold-formed angles

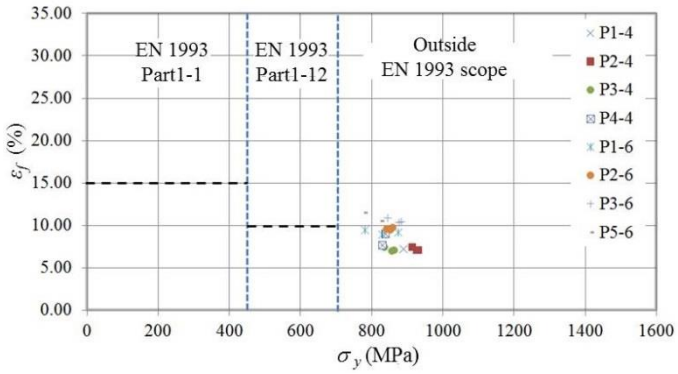

Fig. 13 Elongation at failure with effect of the cold-formed angles

Ductility factors were determined by statistical and 95% probability analyses. The corresponding probability density function (pdf) [12] is given as

follows:

$$f\left(x|\mu,\sigma\right)=\frac{1}{\sigma\sqrt{2\pi}}e^{\frac{-(x-\mu)^2}{2\sigma^2}} \quad , \quad -\infty<x<\infty \tag{4}$$

Where σ is a non-negative scalar value, μ is a scalar value. Fig. 14 to Fig. 16 present probability distributions of σ_u/σ_y, $\varepsilon_u/\varepsilon_y$ and ε_f respectively. The probability distributions were determined based on the results of the tensile coupon tests. The 95% probability was used to determine ductility factors of the S650 high strength steel material including influence of cold-formed angle. The following ductility factors with effects of cold-formed angle are recommended:

- $\sigma_u/\sigma_y \geq 1.0$ (5)

- elongation of failure $\varepsilon_f \geq 6.3$ (6)

- $\varepsilon_u \geq 1.8\varepsilon_y$ (7)

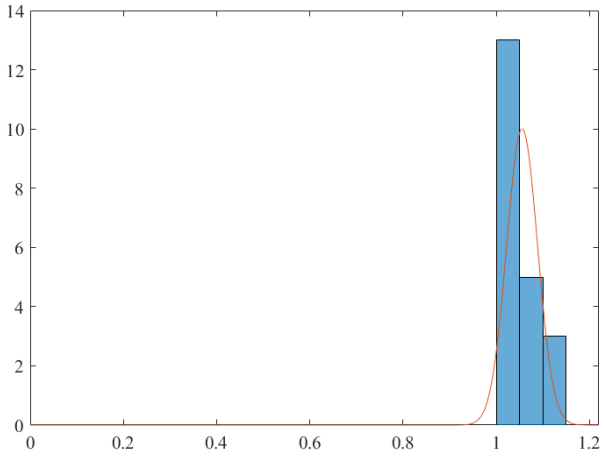

Fig. 14 Probability distribution of σ_u/σ_y

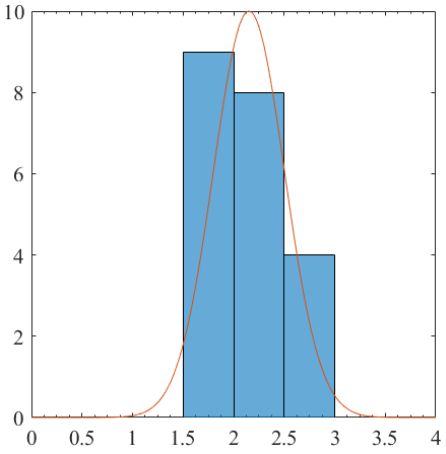

Fig. 15 Probability distribution of $\varepsilon_u/\varepsilon_y$

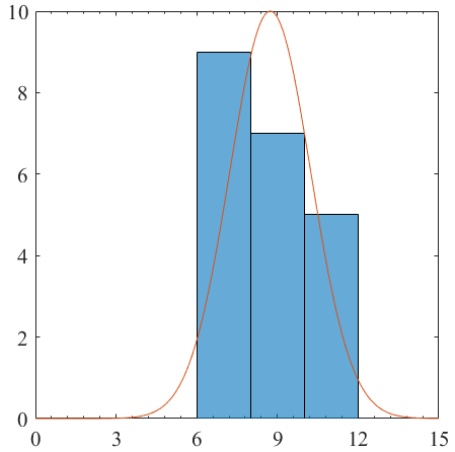

Fig. 16 Probability distribution of ε_f

4.3. Ductile damage analysis

In finite element analysis, the engineering stress (σ_{eng}) and engineering strain (ε_{eng}) are converted to the true stress (σ_{tr}), true strain (ε_{tr}), and true plastic strain (ε_{tr}^{pl}) by using following Equations:

$$\varepsilon_{tr}=\ln(1+\varepsilon_{eng}) \tag{8}$$

$$\sigma_{tr}=\sigma_{eng}(1+\varepsilon_{eng}) \tag{9}$$

$$\varepsilon_{tr}^{pl}=\varepsilon_{tr}-\frac{\sigma_{tr}}{E} \tag{10}$$

In ABAQUS [15], Eq. 8 to Eq. 10 are used to define plastic curves based on the assumption that material is undamaged and exhibits perfect plastic behavior. Equations describing the onset of damage and damage evolution are used to create material curves where material damage is considered. The equivalent plastic strain at the onset of damage is defined as a function of the stress triaxiality and the strain rate, and is given as follows:

$$\bar{\varepsilon}_D^{pl}(\eta,\bar{\varepsilon}^{pl})$$

Where η and $\bar{\varepsilon}^{pl}$ are the stress triaxiality and the equivalent plastic strain rate, respectively. Overall damage variable is D = 0 at onset of damage and reaches D = 1 at failure point.

In this study, ductile damage material models were considered for FE analyses of the tensile coupon tests. Fig. 17 shows the meshes of the 6 mm coupon models with cold formed angles of 90°, 100°, and 160°. Elements (size: 1.5 mm) with 8-node linear brick and reduced integration with hourglass control (C3D8R) were used for these analyses. The computation time was reduced by considering only a half of the models. Furthermore, symmetry boundary conditions were applied.

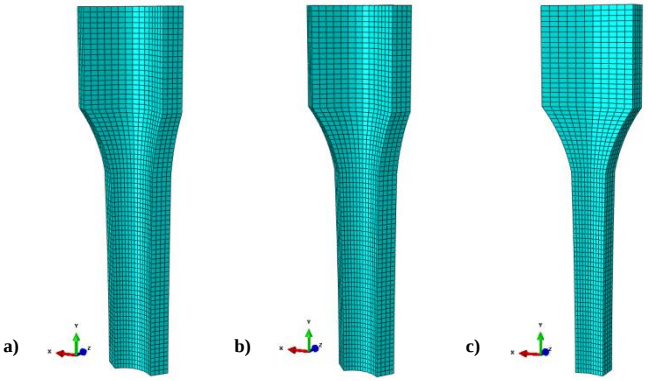

Fig. 17 Meshes of the coupon models with cold-formed angles of: a) 90°, b) 100° and c) 160°

Fig. 18 shows the distribution of Von Mises stresses in the coupon models with cold-formed angles of 90°, 100°, and 160° at the rapture points. Cold-formed angle has significant effect on the stress distribution in the models. Considering the stress distributions at corner parts of the models, the stresses are spread farther along the length of the models and are closer to the end of the model with a 90° cold-formed angle than in the model with 160° cold-formed angle. At the rapture point, thicknesses of the models with 90° and 160° cold-formed angles are significantly reduced 35% and 38%, respectively and their widths considerably decrease by 17% and 29%, respectively.

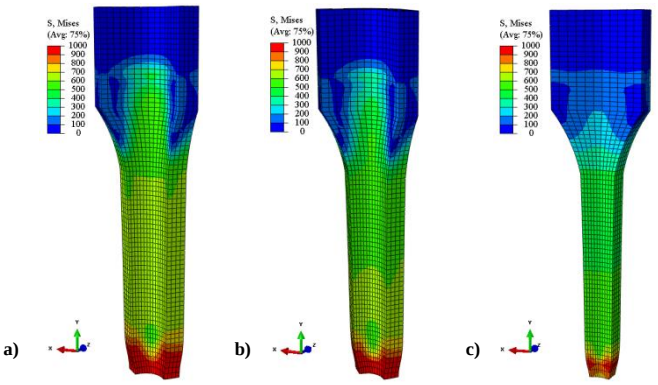

Fig. 18 Stress distribution in coupon models with cold-formed angles of: a) 90°, b) 100° and c) 160° at the rapture point

Fig. 19 and Fig. 20 reveal the good agreement between the experimental and FEA curves of the 6 mm thick coupon specimens with 100° and 160° cold-formed angles, respectively. At rapture point of the specimen with a cold formed angle of 100°, the stress and strain experimentally obtained differ by 1.8% from the respective FEA-determined values. Similarly, the stress and strain differ by 5.6% and 3.6%, respectively, in the case of the specimen with 160° cold-formed angle.

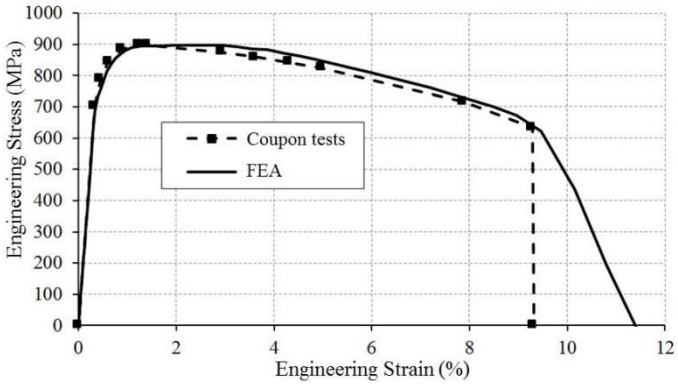

Fig. 19 Stress-strain curves obtained from the experiment and FEA of the 6 mm thick coupon specimen with 100° cold-formed angle

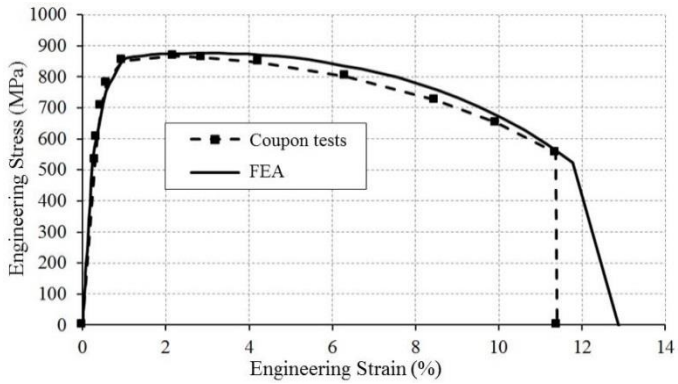

Fig. 20 Stress-strain curves obtained from the experimental and FEA of the 6 mm thick coupon specimen with 160° cold-formed angle

5. Conclusions

The influence of cold-formed angle on properties of the S650 high strength steel material was assessed using tensile coupon tests and numerical simulations. Coupon specimens with different cold-formed angles (90°, 100°, 120°, 140°, 160° and 180°) and different thicknesses (4 mm and 6 mm) were tested. Based on the experimental and FEA results, following conclusions can be drawn:

- The experimental results indicate that cold-formed angle has significant effect on properties of the S650 high strength steel material. The yield stress and tensile stress decrease by 9.4% and 10.3%, respectively, with increasing (from 90° – 180°) cold-formed angles.
- Based on the tensile coupon test results, relationships between the cold-formed angles and yield stress as well as tensile stress of the S650 high strength steel material are described in Eq. 1 and Eq. 2. Stress relationship between the material with effect of cold-formed angle and its base material is presented in Eq. 3.
- It is clear from the results that cold-formed angle has considerable influence on ductility of the S650 high strength steel material. Ductility factors including the effect of cold-formed angle are recommended in Eq. 5 to Eq. 7.
- Ductile-damage material models in the ABAQUS software was used to simulate tensile coupon tests. The experimental and FEA results show good agreements. At the rapture point of the 6 mm coupon specimen with 100° cold-formed angle, the experimentally determined stress and strain differ by 1.8% from the FEA results.

Acknowledgements

The authors wish to thank the Research Fund for Coal and Steel for financially supporting the research in this paper through the Research Project HISTWIN 2 (RFSR-CT-2010-00031).

References

[1] EN 1993-1-3, “Design of steel structures, Part 1-3: General rules – Supplementary rules for cold-formed members and sheeting”, Brussels, Belgium: European Committee for Standardization, 2006.
[2] Afshan S., Rossi B. and Gardner L., “Strength enhancement in cold-formed structural sections – Part I: Material testing”, Journal of Constructional Steel Research, 83, 177–188, 2013.
[3] Schillo N., Theofanous M., Gardner L. and Feldmann M., “Material properties and local buckling behavior of high strength steel hollow sections”, Proceeding of 7th European conference on Steel and Composite Structures, Napoli, Italy, 10–12 September 2014.
[4] Ma J.L., Chan T.M. and Young, B., “Material properties and residual stresses of cold-formed high strength steel hollow sections”, Journal of Constructional Steel Research, 109, 152–165, 2015.
[5] Shi G., Zhu X. and Ban H., “Material properties and partial factors for resistance of high strength steels in China”, Journal of Constructional Steel Research, 121, 65–79, 2016.
[6] Tran A.T., Veljkovic M., Rebelo C. and Simões da Silva L., “Resistance of cold-formed high strength steel circular and polygonal sections - Part 1: Experimental investigations”, Journal of Constructional Steel Research, 120, 245–257, 2016.
[7] Chen J. and Young B., “Corner properties of cold-formed steel sections at elevated temperatures”, Thin-Walled Structures, 44, 216–223, 2006.
[8] EN 10002-1, “Metallic materials – Tensile testing, Part 1: Method of test at ambient temperature”, Brussels, Belgium: European Committee for Standardization, 2001.
[9] EN 1993-1-12, “Design of steel structures, Part 1-12: Additional rules for the extension of EN 1993 up to steel grades S700”, Brussels, Belgium: European Committee for Standardization, 2007.
[10] ASTM-A514, “Standard specification for high-yield-strength, quenched and tempered alloy steel plate, suitable for welding”, Am. Soc. Test Mater, 2013.
[11] ASTM-A709, “Standard specification for structural steel for bridges”, Am Soc. Test Mater, 2013.
[12] MATLAB R2015b, The MathWorks, Inc., Natick, Massachusetts, United States.
[13] Wang J., Afshan S., Schillo N., Theofanous M., Feldmann M. and Gardner, L., “Material properties and compressive local buckling response of high strength steel square and rectangular hollow sections”, Engineering Structures, 130, 297–315, 2017.
[14] Abaqus 6.12-1, Simulia Dassault Systmes, 2012.
[15] Abaqus/Standard user’s manual, Version 6.12.

Advanced Steel Construction – Vol. 15 No. 4 (2019) 323–328
DOI:10.18057/IJASC.2019.15.4.3

EXPERIMENTAL AND NUMERICAL INVESTIGATION ON UPHEAVAL BUCKLING OF FREE-SPAN SUBMARINE PIPELINE

Zhi-hua Chen[1], Jian-guo Yang[1] and Zhan-sheng Liu[2, *]

[1] *State Key Laboratory of Hydraulic Engineering Simulation and Safety, Tianjin University, Tianjin, China*
[2] *Department of Civil Engineering, Beijing University of Technology, Beijing, China*
** (Corresponding author: E-mail: lzs4216@163.com)*

ABSTRACT

Submarine pipeline is widely used for the transportation of oil and gas in offshore exploration and production. The free span of pipeline is inevitable because of the complex seabed conditions, which may result in the upheaval buckling failure under the service conditions. In this paper, several experimental tests on scale models of submarine pipelines was carried out. The test results show that the length of the free span is closely related with the buckling of the pipeline. The upheaval buckling of pipelines is induced by the high compressive stress due to thermal action and triggered by the initial curvature due to self-weight. Thus, the traditional analysis and design method with effective length method cannot be used. Based on the experimental results, a simple and effective finite element model is developed and verified for parametric study. The numerical simulation results show that the diameter, length of free span and the self-weight of the pipeline will influence the buckling resistance of the pipeline system. The proposed finite element model can be used for the practical design of submarine pipelines.

ARTICLE HISTORY

Received: 24 September 2018
Revised: 02 May 2019
Accepted: 06 May 2019

KEYWORDS

Submarine pipeline;
Upheaval buckling;
Free span;
Scale model experiment;
Numerical simulation

1. Introduction

After nearly a hundred years of exploitation of land-based oil, the storage capacity of oil fields on land has been rapidly reduced. Therefore, the main exploitation of oil has turned to the ocean in recent years. The submarine pipeline system is the common way for oil and gas transportation in the marine oil and gas exploration because of easy construction, low cost and high reliability. Up to the year 2006, the total length of the submarine pipelines in the world had exceeded 175,000 kilometers, which is around 4.4 times of the Earth's equator. The service environment of the submarine pipelines is complex as the internal waves, ocean currents, earthquakes, and many other natural disasters may lead to the failure of the pipelines. In the event of the oil and gas leak in the pipeline, it will cause huge disasters to the marine ecological environment and bring significant losses in the development of the social economy [1] .

Generally, the crude oil needs to be transported at high pressure and high temperature because of its high viscosity and high freezing point. With the increase of the pressure and temperature, the stress of the pipeline will be increased. Most importantly, the pipeline may be buckled under high compressive stress and with lack of terrain constraint of the seabed. For this reason, extensive research has been conducted on the failure mechanisms of submarine pipeline system, which can be can be summarized into three approaches. The first is the theoretical research on the buckling of the submarine pipelines. As early as the 1980s, Hobbos et al. [2, 3] developed a buckling critical load calculation formula for the ideal straight pipeline based on the small rotation and line elasticity hypothesis. This formula has been applied to investigate the thermal buckling of semi-infinite long pipeline [4]. Various theoretical buckling models of pipelines under the complex service conditions have been developed in the past three decades [5-8]. The second is the numerical simulation on the buckling of the submarine pipelines. Commercial software such as ABAQUS has been widely used to analyze the buckling of the submarine pipelines [9, 10]. Because of the inevitable model simplification in both of the theoretical analysis and numerical simulation, the experimental work is necessary to support and verify the theoretical and numerical simulation results. The third is the experimental tests on the buckling of the submarine pipelines. For example, Miles et al. [11] investigated the lateral buckling using an elastic rod and an attenuation formula of the lateral buckling was derived. Feng et al. [12] used the optical fiber sensor to measure the strain distributions of the submarine pipeline during the pre-buckling and post-buckling responses. The reliability of the optical fiber measurement method in this application has been verified. In general, the experimental study on the submarine pipelines were based on the scale model but not the full-scale model. The section dimensions, loading modes, test objects and other factors may affect the test results. Thus, only the experimental work on the buckling of the submarine pipelines is insufficient.

From the above, a simple and effective analysis and design approach for submarine pipelines is still limited. The high temperature in the pipelines not only induce thermal stress but also change the material properties. Therefore, the conventional design method based on the effective length method cannot be used. Hence, the use of both experimental and numerical tests is an effective and reliable method to investigate the actual behaviors of submarine pipelines. It is noted that the pipelines with free spans are very common in the submarine structures and upheaval buckling failures may be induced [13]. In this paper, the experiment tests using scale model has been were conducted. Further, an numerical simulation model is proposed and verified by the experimental test results. Finally, the factors related to the upheaval buckling of the pipelines with free spans are discussed and some recommendations are provided.

2. Experimental test of scale model

2.1. Scale Model and Test Setup

Submarine pipelines are commonly made of X65 or the higher grade steels in the practical engineering application. Compared to the aluminum alloy, the steel possesses the larger self-weight, higher elastic modulus, and lower thermal conductivity. If the steel specimen is adopted in the experimental test, the buckling failure mode can not be observed due to limited capacity of the facilities. Therefore, the pipeline specimen made of 6061T6 aluminum alloy was tested instead of steel pipeline in this paper [15]. The material properties of aluminum 6061T6 are shown in Table 1. The dimensions of the aluminum pipeline specimen are given as follows: the diameter is 70 mm, the wall thickness is 2 mm, and the length is 9000 mm.

Table 1
The material properties of 6061T6 aluminum

Average density (kg/m3)	Melting point (℃)	Linear expansion coefficient (℃-1)	Specific heat (cal/g)	Thermal conductivity (cal cm s ℃)	Resistivity (μΩ cm)	Elastic modulus (GPa)
2700	658	24×10^{-6}	0.225	0.52	2.84	68.5

The illustration of the experimental setup is shown in Fig. 1, which includes the oil heating pump, the seabed simulated by sand, and the fixed end. The temperature load was applied to the pipeline specimen by the oil heating pump. The oil flow is heated up from the room temperature while the temperature rising process was paused every 10 ℃. When the deformation of the specimen was stable in the pause step, the strain, displacement, and other parameters were recorded. The temperature rising process was continued until the buckling failure was observed in the aluminum pipeline.

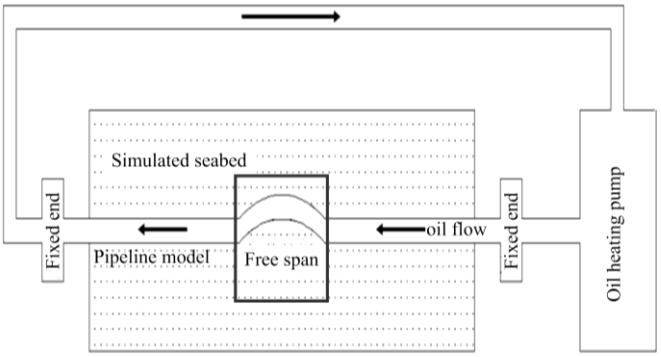

Fig. 1 The illustration of the experimental setup

The two ends of the pipeline specimen should be in a line and fixed at the edge, which can minimize the bending moment induced during the temperature loading process. Since the simulated seabed was made of fine sand, the depression would be formed on the simulated seabed by the sinking of the pipeline. In order to remove this influence, the sand on both sides of the lower part of the pipeline model was removed. The angle bars were added at the ends of the free span to simulate the hard contact, which can prevent the changes of boundary conditions because of the slippage of the sand in the deformation process of the pipeline model. The main purpose of this paper is to investigate the upheaval buckling. Thus, the articulated connection was selected between the ends of the pipeline model and the fixed ends. Two steel bars were welded at both sides of the pipeline model to limit the lateral displacement of the pipeline model. Fig. 2(a) shows the overall setup of experimental setup while Fig. 2(b) shows the connection between the end of the specimen and the fixed end of seabed.

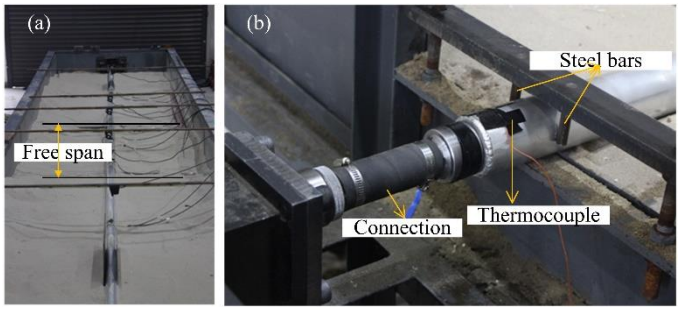

Fig. 2 Experimental test photos: (a) Overall setup; (b) End connection details

As the temperatures, strains, displacements at the different locations of the specimen were different, five displacement measurement points were arranged along the pipeline, as seen in Fig. 3. The range of the displacement transduser used in this experimental test was 500 mm with the sensitivity of 0.5 mm. The high-temperature strain gauges were adhered on the middle point (point 3 in Fig. 3) to measure both the axial strain and the bending strain.

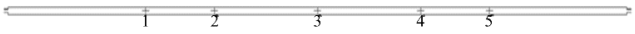

Fig. 3 The arrangement of five displacement measurement points

The high compressive stress due to temperature will lead to the buckling of the pipeline specimen. Thus, five temperature measurement points were arranged along the pipeline as indicated in Fig. 4. Point 1 was located on the oil inlet and point 5 was located on the oil outlet. The thermocouples with the temperature acquisition frequency of 1 time/s were used to measure the temperature.

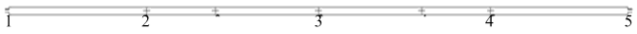

Fig. 4 The arrangement of five temperature measurement points

Three groups of specimens have been tesed to study the influence of free span length, which are listed in Table 2. The mean values of the test results for each group were taken as the reliable results. The curves of the temperature loading history are plotted in Fig. 5. T1 to T5 represent the temperatures of five temperature measurement points. It can be seen that the temperature has a certain loss along the oil flow path, which is the same as the observations in practical engineering. Moreover, as the length of the free span increases, the temperature loss decreases.

Table 2
The specimens in experimental test

Group	1	2	3
Length of free span (m)	2	3	4
Number of pipeline specimen	3	3	3

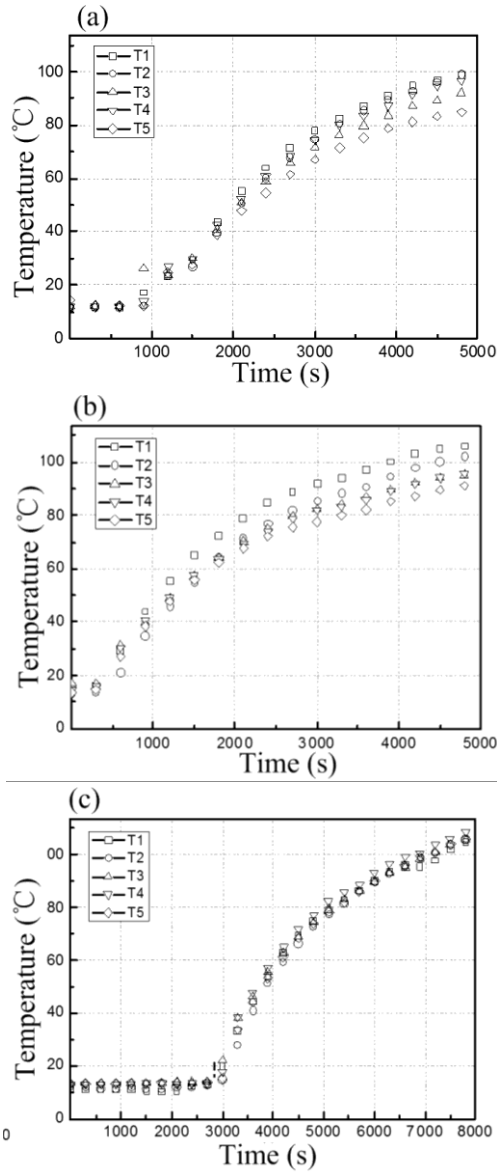

Fig. 5 The curves of the temperature loading history with different length of free span: (a) Length = 2 m; (b) Length = 3 m; (c) Length = 4 m

2.2. Experimental results and discussion

As shown in Fig. 6(a), the self-weight of the free span induces the initial geometrical imperfection of the pipeline specimen, which will lead to upheaval buckling failure of the pipeline under compression. In the process of the oil temperature increase, due to the axial constraints at both ends and lack of lateral constrains at the free span, the pipeline model was displaced vertically and

finally failed due to the buckling. Also, because of the constraints of the steel angles, the pipeline specimen exhibited a wave-shaped buckling mode, seen in Fig. 6(b).

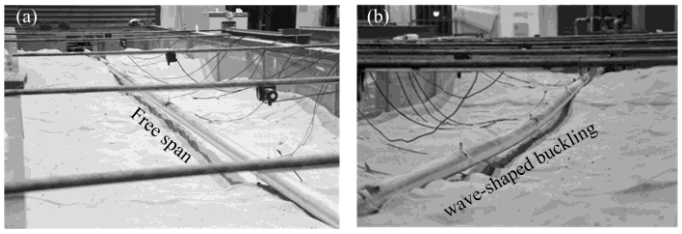

Fig. 6 Typical specimen in test: (a) Initial state; (b). Buckling failure mode

The mean values of the vertical displacement on the middle point of the pipeline model of each specimen group are plotted in Fig. 7. The maximum vertical displacement of the pipeline model with 2 m free span was only 8 mm and the buckling phenomenon seems not obvious. For the pipeline model with 3 m free span, the increase of the vertical displacement was linear in the loading process and the increase rate decreased after the buckling occured. When the length of the free span was 4 m, the increase rate of the vertical displacement was higher and the maximum vertical displacement was up to 85 mm. The buckling rate is higher and the critical temperature is the lowest. The main reason for the above-mentioned phenomenon is the use of the steel angle at the ends of the free span which provided sufficiently rigid boundary. When the length of the free span is small, the thermal displacement of the pipeline model is small due to the restraint of the steel angle. When the free span is longer, the initial geometrical imperfection induced by the self-weight of the free span becomes important and will trigger the buckling. Although the steel angle provides rigid boundary and the pipeline specimen is almost straight before appling thermal load, the initial curvature of the pipeline induced by the gravity load results in the clear upheaval buckling failure.

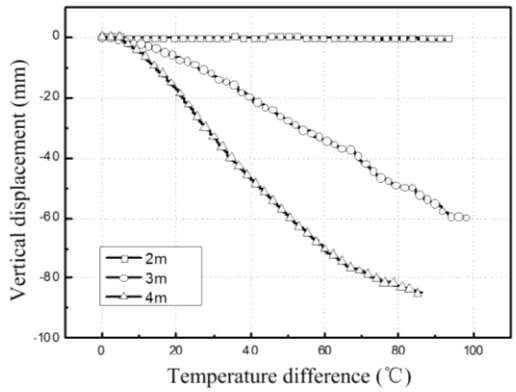

Fig. 7 Temperature versus vertical displacement curves from test

The axial force of the middle point of the pipeline model was calculated by the formula of $F = \varepsilon A$, in which A is the cross-sectional area of the pipeline while ε is the axial strain measured by the strain gauge. The mean value of the axial force of each specimen group was calculated. Fig. 8(a) shows the relationship between the axial force and the temperature difference. For the pipeline with 2 m free span, because the axial constraint of the ends had a certain gap, the deformation of the middle point of the pipeline model was rapid and the axial force increased fast before the temperature difference of 20 ℃. When the gap was offset, the axial force changed slowly between the temperature differences from 20℃ to 60℃. When the temperature is higher than 60℃, the axial force continuously increased and induced buckling failure after 90℃. For the pipeline with a free span of 3 m, the tensile axial force occurred at the initial stage of the temperature loading, which tightened the pipeline model and fixed ends. With the increase of temperature, the tensile axial force was changed to compressive axial force. When the axial force was increased up to 230 kN at the temperature difference of 90℃, the pipeline was buckled. For the specimens with free span of 4 m, the axial force changed with a fluctuation. The axial force increased linearly after the temperature difference of 20℃. Fig. 8(b) is the relationship between the axial force and the vertical displacement of the middle point of the pipeline model. For the pipeline model with 2 m free span, because of the short length and the large diameter of the pipeline model, the small initial curvature at free span resulted in the small displacement which was near to zero.

For the pipeline model with 3 m free span, the specimen was buckled when the vertical displacement reached 40 mm with the axial force of 150 kN. The axial force increased slowly in post-buckling range, but the vertical displacement continuously increased. When the free span of the specimen was 4 m, the pipeline model was buckled when the vertical displacement reached 10 mm with the axial force of 75 kN.

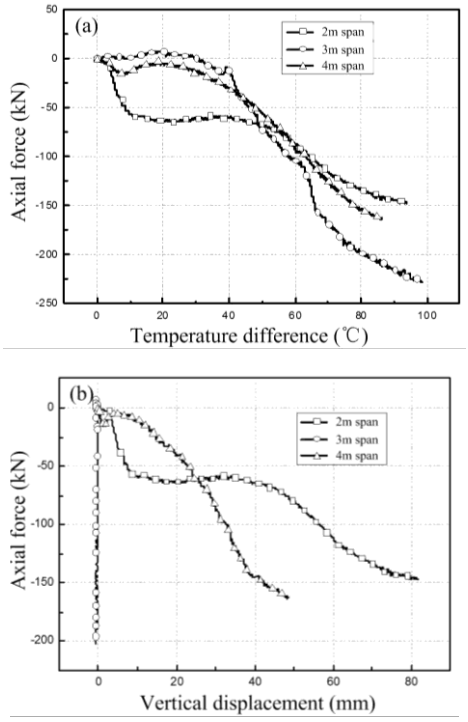

Fig. 8 Axial forces from test: (a) axial force vs. temperature difference; (b)axial force vs. vertical displacement

3. Numerical simulation study

3.1. Numerical simulation model

In this paper, the commercial software ABAQUS was used to establish the finite element model. The specific modeling and analysis process are described as follows:

(1) The element types used in the model was based on the structural behaviors the objects [16]. The submarine pipeline is a typical slender structure, in which the dimension in one direction is much larger than that in the other two directions. Therefore, the beam element (B21) was selected to simulate the response of the pipeline. For each model, 300 bean elements are used to model the pipeline. The seabed was simulated by the rigid contact surface (R2D2). The contact model between the pipeline model and the seabed was set as the hard contact. For each model, 300 rigid elements are used to model the seabed. And the frictional behavior was represented by the Coulomb friction model.

(2) The length of the pipeline model was evaluated. Because of the obvious localized feature of the submarine pipeline buckling, the buckling behavior generally affects a small part of the total length of the pipeline [14]. Therefore, it is not necessary to establish the finite element model with the total length of the pipeline. In this paper, the length of the pipeline model was selected as 50 times the length of the free span.

(3) The constraints at both ends of the pipeline model were determined. The submarine pipeline would have an elongation tendency under the action of the internal temperature. As the frictional force of the seabed soil accumulates in the axial direction, the pipe anchoring section is finally formed. Because two ends of the anchoring section have no axial displacement, the constraints at both ends of the pipeline model were determined as articulated connection.

(4) The loading type was determined. The main reason for the pipeline buckling is the axial force generated by the expansion effect. Therefore, the pressure induced by the increase of temperature was the loading type in this paper.

(5) The analysis steps and method were determined. The simulation work was mainly divided into two load steps. Firstly, the self-weight was applied on the model, which is a general static analysis step. Second, a temperature action was applied to the pipeline, involving a time-history of thermal analysis.

3.2. Verification of the numerical model

Based on the parameters of the scale models in experimental test, the numerical simulation models were established according to section 3.2 and then they were verified by the test results presented in section 2.2. Fig. 9 shows the comparison of axial force-temperature curves obtained by experimental and numerical simulation. It can be seen from Fig. 9 that the basic trend of the curves from simulation and experiment are the same. The critical buckling force derived by the numerical simulation is slightly smaller than that observed from the experimental test. The reason may be due to the use of fully restrained boundary conditions in numerical simulation while the support conditions of the pipeline specimens in the experimental test were semi-rigid. In general, the numerial results shows in good agreement with the test and therefore the proposed FE model will be used for further parametric study on the responses of pipelines under more conditions.

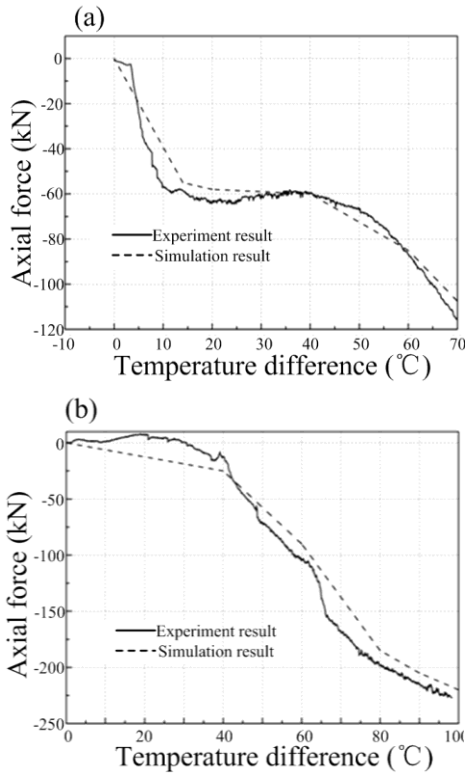

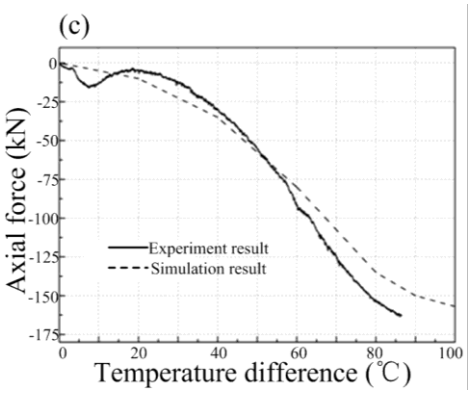

Fig. 9 The axial force-temperature curves with different length of free span: (a) Length = 2 m; (b) Length = 3 m; (c) Length = 4 m

4. Parametric study

Unlike the specimens tested in section 2 which were made of aluminum 6061T6, the material of the pipeline in FE model is steel to represent the actual conditions in practical engineering. The elastic modulus is 207 GPa while the linear expansion coefficient is 11×10-6. The main parameters of the pipelines in numerical simulation study are listed in Table 3.

Table 3
The main parameters of pipelines in numerical simulation study

Diameter (mm)	254, 273, 323, 355, 381
Wall thickness (mm)	12
Length of the free span (m)	20, 24, 28, 32, 36, 40
Self-weight (N/mm)	0.6, 0.8, 1.0, 1.2, 1.4

The first step was the static analysis of the pipeline subjected to self-weight only. The second step is thermal analysis by increasing the temperature until the failure is observed.

Fig. 10 shows the displacement and the von Mises stress contours of the pipeline model under 100℃ with the parameters of 254 mm diameter, 12 mm wall thickness, 0.6N/mm self-weight, and 20 m free span. Because the upheaval buckling is a local behavior of the pipeline model, only a part of the pipeline model including the buckling failure is shown in Fig. 10. Obviously, there is no vertical displacement of the section of the pipeline model away from the free span. Because the self-weight of the free span results in the deflection of the free span and the warping of two sides of the free span, the free span acts as an initial vertical defect in the loading process which leads to the upheaval buckling of the pipeline model. The buckling shape of the pipeline model includes two peaks and one trough. The stress at the peak and the trough are larger. The maximum vertical displacement of the trough is smaller than that of the peak.

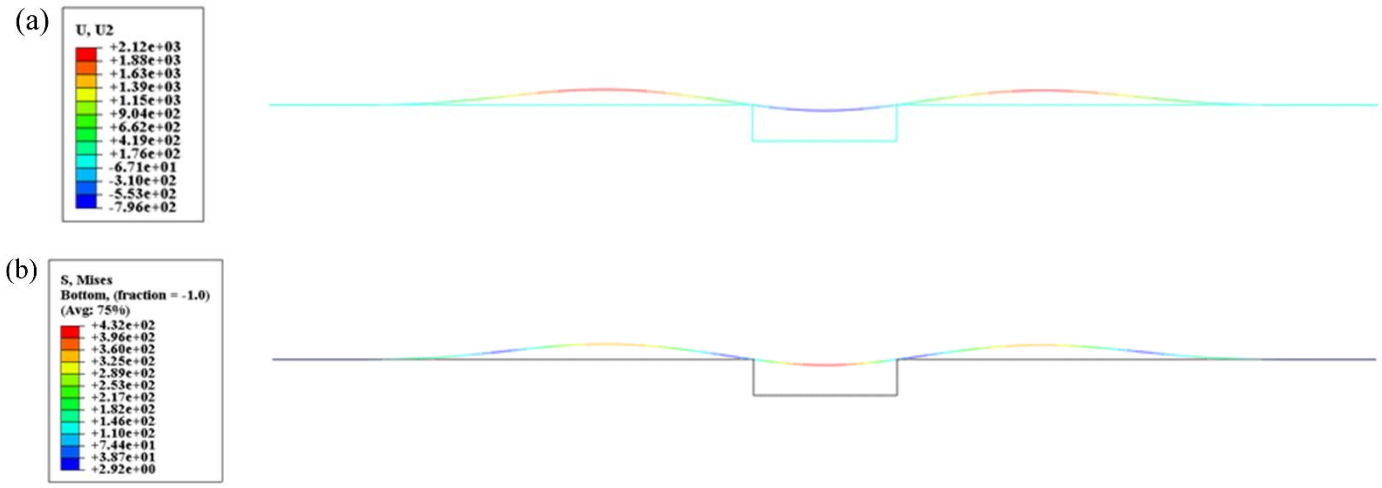

Fig. 10 Typical specimen in test: (a) Initial state; (b). Buckling failure mode

Fig. 11 shows the whole process of the vertical buckling of the pipeline model with the parameters of 381 mm diameter, 12 mm wall thickness, 1.0 N/mm self-weight, and 32 m free span. As shown in Fig. 11(a), the structural self-weight induced the small initial vertical displacement at the free span and the small warping of two sides of the free span before the increase of temperature. In the early stage of buckling development, the vertical displacement of the free span is always greater than that of two-sided warping section. The influence range of the buckling section appears as a symmetrically extended state on both sides. When the temperature rises to the buckling critical value, the vertical displacement of the buckling section develops rapidly. The vertical displacement of two-sided warping section gradually exceeds that of the free span, which becomes the main buckling section. The increase of the buckling displacement of the free span slows down. Fig. 11(b) shows the development of the combined stress. Obviously, the stress development of the buckling also shows a symmetric distribution and gradually expands outward as the temperature rises. Before the buckling occurs, the stress level of the pipeline model is low. There are two compressive stress peaks at two sides of the free span and one tensile stress peak in the middle of the free span. After the buckling occurs, the stress shows a waveform distribution. There are three tensile stress peaks and two compressive stress peaks, in which the tensile stress peaks on both sides appear near the initial point of bending of the pipeline model. The tensile stress peak in the middle point of the pipeline model corresponds to the location of the maximum vertical displacement of the free span. Two compressive stress troughs occur on both sides in Fig. 11(b). It is worth noting that after the buckling occurs, the individual stress peaks propagate rapidly symmetrically along both sides of the pipeline model.

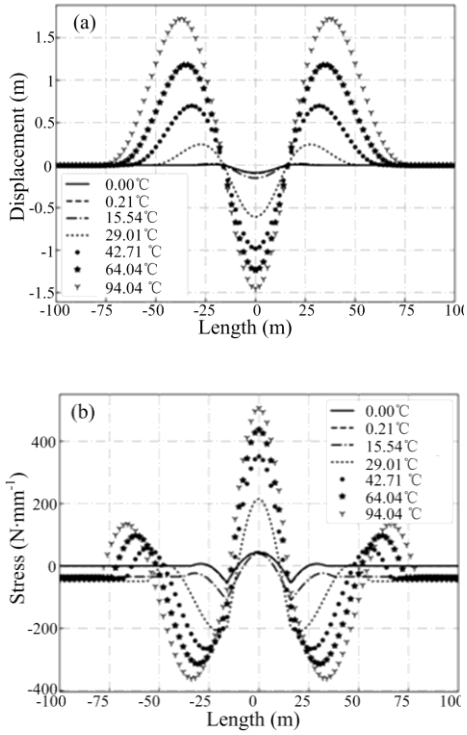

Fig. 11 Simulation results along the pipeline: (a)Displacement distribution; (b) Stress distribution

The axial force and the vertical displacement of the middle point of the pipeline model were used to investigate the influence of the free span length, the diameter, and the self-weight on the buckling mode. Fig. 12 shows the influence of the length of the free span on the buckling of the pipeline model. In this simulation test groups, the diameter is 381 mm and the thickness of the wall is 12mm. As shown in Fig. 12(a), there are two main development modes of buckling displacement: when the length of the free span is small, the vertical displacement of the pipeline model is small before the buckling; while after the buckling occurs, the displacement of the pipeline model develops rapidly to reach a new equilibrium state. Then the displacement continues to increase slowly with the increase of temperature. Meanwhile, there is a certain dynamic effect during the temperature rise process, which has the characteristics of jumping buckling. When the length of the free span is longer, the initial deflection of the pipeline model is larger with slow development of displacement. Fig. 12(b) shows the development of the axial force of the middle point of the pipeline model. Obviously, the critical bending axial force gradually decreases as the length of the free span increase. The main development modes of buckling axial force can be classified into two categories: when the length of the free span is small, there is a significant critical buckling axial force. The axial force decreases rapidly after the critical buckling axial force. When the length of the free span is longer, there is no obvious critical buckling axial force and the axial force change slowly with the temperature rise.

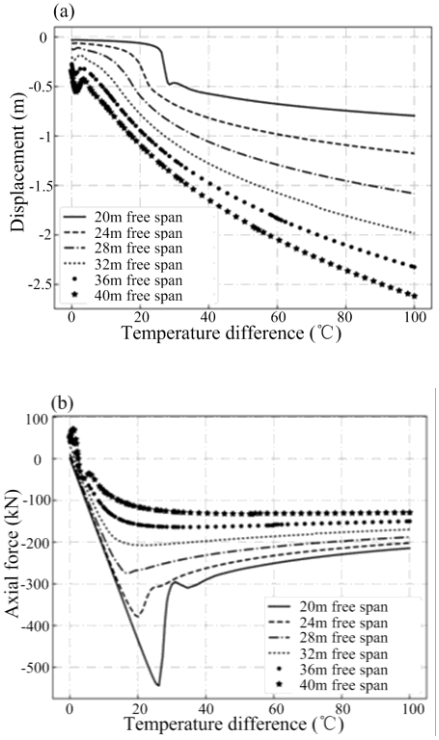

Fig. 12 Displacements and axial forces related to length of free span: (a) Displacement-temperature curves; (b) Axial force-temperature curves

Fig. 13(a) is the relationship between vertical displacement of the middle point of the pipeline and the temperature difference under different diameters; while Fig. 13(b) is the relationship between axial force of the middle point of the pipeline and the temperature difference under different diameters. In this simulation groups, the length of the free span is 32 m and the thickness of the wall is 12mm. The different diameters also would result in two vertical buckling models. When the diameter is small, the buckling displacement develops gently and there is no obvious critical buckling force. After the critical axial force, the axial force of buckling section drops gently. When the diameter of the pipeline is larger, there is a sudden change in the buckling displacement, and there is a significant critical buckling axial force. After breaking the critical value, the axial force of the buckling section decreases rapidly, accompanied with a dynamic effect.

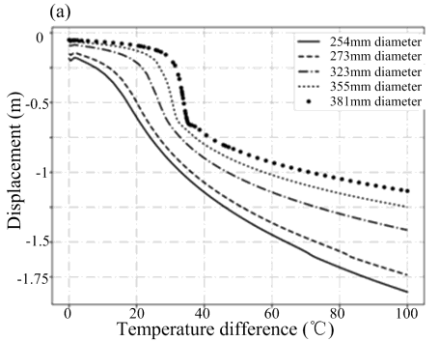

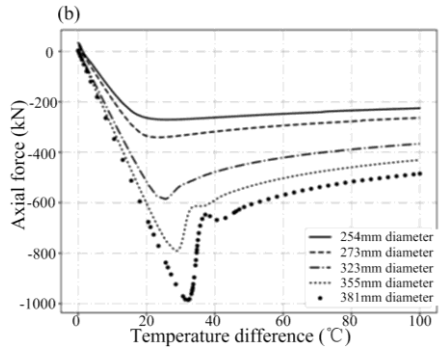

Fig. 13 Displacements and axial forces related to diameter of pipeline: (a) Displacement-temperature curves; (b) Axial force-temperature curves

Fig. 14 shows the effect of the self-weight on the buckling modes of the pipeline model. In this simulation groups, the diameter is 381 mm, the length of the free span is 32 m and the thickness of the wall is 12mm. Compared to the influence of the length of the free span and the diameter, the effect of the self-weight on the buckling of the pipeline model is small. As the self-weight of the pipeline model increases, the final post-buckling displacement of the pipeline model increases, the critical buckling temperature corresponding to the buckling of the pipeline model also increases, and the post-buckling axial force increases.

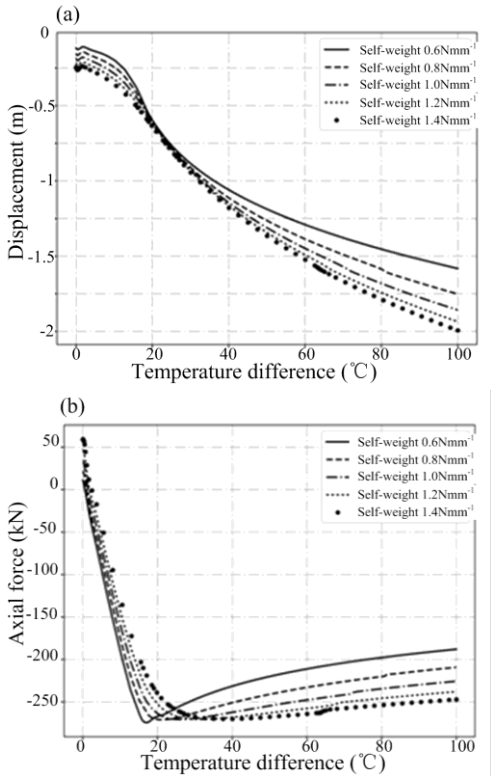

Fig. 24 Displacements and axial forces related to self-weight of pipeline: (a) Displacement-temperature curves; (b) Axial force-temperature curves

5. Conclusions

Submarine pipelines have been extensively used in the transportation of oil and gas. However, the pipeline is prone to upheaval buckling failure under the service conditions. There is still lack of reliable design method for the submarine pipelines as the conventional design method is mainly based on effective length method with the assumption of initially undeformed configuration. In this paper, several experimental tests on scale models of submarine pipelines have been conducted and a simple and effective finite element (FE) model is proposed and verified by the test results. Further, the proposed FE model is used for parametric study. The influence of free-span length, diameter and wall thickness of pipeline has been investigated.

In summary, the following conclusions can be drawn from this paper.

1. The upheaval buckling of pipelines is induced by the high compressive stress due to thermal action and triggered by the initial curvature due to self-weight.

2. A simple and effective finite element model is developed and verified by the test results. Parametric study has been conducted to investigate the influence of several factors such as free-span length, the diameter and wall thickness of the pipeline.

3. The simulation results show that the pipeline has two vertical buckling modes. When the diameter of the pipe is large or the length of the free span is small, the jump buckling of the pipe will occur, which should be avoided in actual engineering. When the pipe diameter is small or the free span is large, the buckling process of the pipe is relatively gentle and should be carefully evaluated to ensure the safety of the pipe in the buckling state.

4. The length of the free span and the diameter of the pipe are the two most important factors affecting upheaval buckling behavior. As the diameter increases and the length of the free span decreases, the critical bending crankshaft force of the pipe increases.

5. The proposed FE model is simple and effective for practical design of submarine pipelines.

Acknowledgement

The authors are grateful for the support provided by the National Basic Research Program of China under Grant No. 2014CB046801.

References

[1] Zhu Y., Qian X., Liu Z., et al., “Analysis and assessment of the Qingdao crude oil vapor explosion accident: lessons learnt”, Journal of Loss Prevention in the Process Industries, 33, 289-303, 2015.
[2] Hobbs R.E., “In-service buckling of heated pipelines”, Journal of Transportation Engineering, ASCE, 110(2), 175-189, 1984.
[3] Hobbs R.E., “Pipeline buckling caused by axial loads”, Journal of Constructional Steel Research, 1(2), 2-10, 1981.
[4] Hobbs R.E. and Liang F., “Thermal buckling of pipelines closed to restraints”, International Conference on Offshore Mechanics and Arctic Engineering, 1(5), 121-127, 1989.
[5] Miles D.J. and Calladine C.R., “Lateral thermal buckling of pipelines on the sea bed”, Journal of applied mechanics, 66(4), 891-897, 1999.
[6] Bokaian A., “Thermal expansion of pipe-in-pipe systems”, Marine Structure, 1(17), 475-500, 2004.
[7] Hong Z., Liu R., Liu W., et al., “Study on lateral buckling characteristics of a submarine pipeline with a single arch symmetric initial imperfection”, Ocean engineering, 108(21-32), 2015.
[8] Wang Y., Zhang X., Zhao Y., et al., “Perturbation analysis for upheaval buckling of imperfect buried pipelines based on nonlinear pipe-soil interaction”, Ocean Engineering, 132(92-100), 2017.
[9] Peek R. and Yun H., “Flotation to trigger lateral buckles in pipelines on a flat seabed”, Journal of Engineering Mechanics, 133(4), 442-451, 2007.
[10] Liu, R., Xiong, H., Wu, X., et al., “Numerical studies on global buckling of subsea pipelines”, Ocean Engineering, 78(1), 62-72, 2014.
[11] Miles D.J. and Calladine C.R., “Lateral thermal buckling of pipelines on the sea bed”, Journal of applied mechanics, 66(4), 891-897, 1999.
[12] Feng X., Wu W., Li X., et al., “Experimental investigations on detecting lateral buckling for subsea pipelines with distributed fiber optic sensors”, Smart Structures & Systems, 2(15), 245-258, 2015.
[13] Furnes G.K. and Berntsen J., “On the response of a free span pipeline subjected to ocean currents”, Ocean engineering, 30(12), 1553-1577, 2003.
[14] Standard O., “Submarine Pipeline Systems. DNV-OSF101”, DNV, 2000.
[15] Yu J.X., An S.Y., Sun Z., et al. Envisage and analysis of sea trial on deep-water pipeline's resistance to external pressure, Ocean Engineering, 2018.
[16] Yu J.X., Li Z.B., Du Z.F., et al. Theoretical calculation method of the nonlinear buckling of deepsea pipes, The Ocean Engineering, 2013.

Advanced Steel Construction – Vol. 15 No. 4 (2019) 329–337
DOI:10.18057/IJASC.2019.15.4.4

DYNAMIC RESPONSE ANALYSIS METHOD FOR THE PEAK VALUE STAGE OF CONCRETE-FILLED STEEL TUBE BEAMS UNDER LATERAL IMPACT

Xiang-jie Kang [1], Yan-hui Liu [1,*], Lei Zhao [2], Zhi-xiang Yu [1,3], Shi-chun Zhao [1,3] and Heng Tang [1]

[1] *School of Civil Engineering, Southwest Jiaotong University, Chengdu, China*
[2] *Department of Civil and Environmental Engineering, The Hong Kong Polytechnic University, Hong Kong, China*
[3] *National Engineering Laboratory for prevention and control of geological disasters in land transportation, Chengdu, China*
** (Corresponding author: E-mail: liuyanhui00@126.com)*

ABSTRACT

This paper proposes a dynamic response analysis method of concrete-filled steel tube (CFST) beams at the peak value stage under lateral impact load. Targeted calculation of the peak value stage, finite element analysis (FEA) was carried out to determine the calculation model suitable for the analysis of the peak value stage and the simplified trend curve of beam acceleration at the impact point. Then, an analysis method for calculating the dynamic response of a fixed-fixed supported CFST beam is proposed, which consists of the travelling hinge theorem and a prediction model of the simplified trend curve. The predicted simplified trend curve is applied to replace the motion constraint assumption of the impactor and beam in the travelling hinge model. In the meantime, the elastoplastic behaviour of the CFST beams is considered in the analysis process. Through the comparison of experimental results and analysis results, this analysis method can predict the time history curves of the acceleration and impact force of CFST beams reasonably.

ARTICLE HISTORY

Received: 25 January 2019
Revised: 01 May 2019
Accepted: 19 May 2019

KEYWORDS

Lateral impact;
Dynamic response;
Concrete filled steel tube;
Calculation method;
Peak value stage

1. Introduction

Due to the functional requirements of a structure, it is inevitable to analyse the dynamic response of structural members under ultimate loads. The lateral impact is one of the dynamic loads that cannot be ignored, which can cause serious damage and even the collapse of bridges and buildings [1,2]. Therefore, the impact resistance of structures has been studied by using several experiments and numerical simulations [3-9]. According to the impact load measured from lateral impact tests, the dynamic response process of a beam can usually be divided into three stages: the peak value stage, the platform stage, and the unloading stage [10]. The peak value stage appears earliest in the dynamic response process, which determines the initial state of the following stage. Moreover, the maximum value of the impact load also appears at the peak value stage. Consequently, it is of significance to gain insight into the peak value stage in the process of analysis and design.

The difficulty of calculation at the peak value stage consists in the estimation of the beam resistance. When the impact occurs rapidly, the resistance of the beam at the peak value stage may be completely provided by inertial force. The dynamic bending moment and the shear force in a structural member can only be balanced with the inertial resistance of the beam and the impact force of the impactor [11,12]. As a result, the beam supports have no significant influence on the impact process [13]. Correspondingly, the dynamic equilibrium equation is different from that of the static case due to their different boundary conditions. The method which can describe this inertial resistance process is the travelling hinge theorem [14], which has been used by Parkes [15,16] to determine the dynamic responses of rigid plastic beams under lateral impact loads. In the calculation process, the travelling plastic hinge is used to replace the function of the supports. The impact force of the impactor can only be balanced with the inertial resistance of the beam before travelling hinge reaches the support constraint.

Nevertheless, the travelling hinge theorem has not yet been adopted to calculate the dynamic responses of structural members at the peak value stage, because this model assumes that the motion of both the impactor and beam are the same in the impact area. This motion constraint assumption is different from the actual phenomenon occurring at the peak value stage. However, Pham et al. [17,18] show that the position of a plastic hinge could significantly affect the dynamic response of the structural beam because there is a possibility that the plastic hinge of one structural beam may not reach the support constraint during the dynamic response process. Therefore, when calculating the dynamic response of a structural member, it is necessary to describe the travelling process of the plastic hinge.

The concrete-filled steel tube (CFST) beam exhibits a high bearing capacity and good ductility; therefore, it has become the common form of structural members [19-22]. The CFST beam dynamic response process obtained from lateral impact tests [23-26] also includes the peak value stage, the platform stage, and the unloading stage. However, there are several methods for calculating the platform stages in CFST beams [27-30], whereas those for the peak value stage are rare. Only the analytical calculation performed by Wang et al. [31] includes the peak value stage. A transient force (P)-local indentation (δ) curve, which expresses a quality similar to contact stiffness, was introduced to describe the interaction between the impactor and beam. Although this method still does not obtain the accurate dynamic response of the beam at the peak value stage [31], it includes all three stages of the dynamic response process. The reason for the error occurring at the peak value stage may involve overlooking the motion of the plastic hinge. Overall, difficulties still exist in the calculation of the peak value stage of CFST beams.

This study is an attempt to address these difficulties in the calculation of the dynamic response of CFST beams at the peak value stage. Thus, finite element analysis (FEA) was conducted to investigate the dynamic behaviour of fixed-fixed supported CFST beams under lateral impact loads, and five lateral impact tests were adopted to verify the FEA results. Based on these results, an analysis calculation model suitable for the peak value stage as well as a simplified trend curve of the impact point acceleration was determined. Then, the dynamic responses of CFST beams at the peak value stage were calculated on the basis of the travelling hinge theorem and the prediction model of the simplified trend curve.

2. Dynamic response at the peak value stage

2.1. Test description

Five lateral impact tests were carried out to obtain the dynamic response of CFST members under lateral impact at the peak value stage. The outer diameter (D) of the CFST beams is 114 mm, and the thicknesses of the steel tubes, which are made of mild steel, are 2.0 mm and 3.5 mm. Additionally, the geometric size ratio of the experimental members to the actual structural member is 1:10.

Standard tensile tests were conducted to measure the steel tube properties. The average static tensile strengths (f_y) of the 2.0 mm and 3.5 mm steel tubes are 338 MPa and 323 MPa, respectively. The elastic modulus (E_s) of the 2.0 mm and 3.5 mm steel tubes are 198 GPa and 201 GPa, respectively, and the corresponding elongation values are 21.68% and 21.57%, respectively. The density of the steel is 7850 kg/m^3. Besides, nine concrete cube blocks with a side length of 150 mm were made to measure the concrete properties. The average cubic compressive strength (f_{cu}) of the concrete block is 55 MPa, the elastic modulus (E_c) is 35.25 GPa, and the density is 2450 kg/m^3.

One gravity-driven impact device, composed of a rigid hammer, a mass block, and a sliding track, was used for generating the impact load, as shown in Fig. 1. The total mass of the impactor (m), including the rigid hammer and mass

block, was 270 kg. The impact heights of the test were selected to be 3 m, 5 m, and 7 m based on the effective impact length (*H*) of the slipway, and the corresponding initial impact velocities were 7.67 m/s, 9.90 m/s, and 11.72 m/s, respectively. The size of the hammer at the impact contact surface was 30 mm*80 mm. The boundary conditions employed in the test were also shown in Fig. 1. Both ends of the beam were fixed, with the effective support length (L_E) of the member being 900 mm. According to the provisions of BS EN 1991-1-7:2006 [32], the distance between the impact point and the support was 1.8m when the impact action was caused by a derailed train. For general structural members with a length of 6-10m, the corresponding range of the impact point position was 0.18-0.3 span. Therefore, the impact point position of the test was located at 2/9 span, as shown in Fig. 1. The impact point was near the support *N*, at a distance of 200 mm; whereas the distance between the centre of the impact point and the support *F* was 700 mm.

During the test process, the impactor was raised along the slipway to a predetermined impact height, so that the impactor was able to achieve the designed initial impact velocity. A force sensor used to measure the impact load was installed behind the rigid hammer, and the accuracies of the FEAs and theoretical calculations were evaluated by the obtained impact-force time history curve. The dynamic response of the beam was recorded with a high-speed camera, the range of which is shown in Fig. 1. The impact point deflection of the member was extracted from the high-speed camera video.

Table 1
Details of the impact test specimens

Specimen	*m* (kg)	V_{I0} (m/s)	E_i (kJ)	*D* (mm)	L_E (mm)	T_b (mm)	f_y (MPa)	f_{cu} (MPa)
YG1	270	7.67	7.94	114	900	2.0	338	55
YG2	270	9.90	13.23	114	900	2.0	338	55
YG3	270	11.72	18.54	114	900	2.0	338	55
YG4	270	11.72	18.54	114	900	3.5	323	55
YG5	270	9.90	13.23	114	900	3.5	323	55

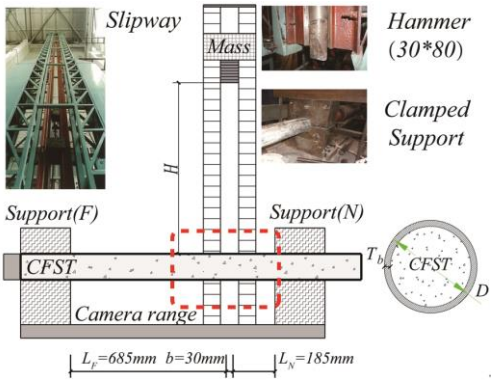

Fig. 1 Test information

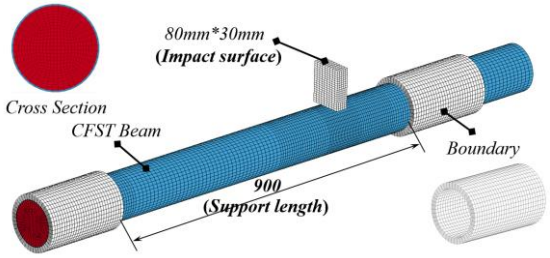

Fig. 2 FEA model

2.2. Finite element analysis

2.2.1 Description of the FEA model

The deformation modes of CFST beams at the peak value stage were supplemented by the FEAs as well as the change trends of velocity and acceleration at the impact point. The deformation mode is related to the calculation model, with the trend curve of acceleration being a supplementary condition in the analysis calculation.

The drop-weight impact test was simulated for the CFST beams based on the explicit criterion in LS-DYNA [33]. Fig. 2 shows a general FEA model of the CFST member in the simulation analysis. The drop hammer, steel tube, and core concrete were modelled using 8-node solid elements with reduced integration. The mesh convergence study was conducted to determine the appropriate mesh density and ensure the efficiency of the simulation. The maximum size of the solid elements in the simulation models is 11.5 mm.

The material properties of the steel followed the ideal elastic-plastic model (MAT_3 in LS-DYNA), in which the elongation determined the failure strain (FS) of eroding elements. Additionally, the properties of concrete followed the concrete damage model (MAT_72R3 in LS-DYNA) developed by Malvar et al. [34]. This concrete model has also been successfully applied to analyse the behaviours of CFST beams under lateral impact [23,27,31], which includes three independent surfaces (the initial yield surface, the maximum failure surface, and the residual failure surface) to describe the elastic-plastic response of the concrete [33,34].

During the dynamic response process, the strength of steel and concrete increases with the increase of the strain rate, which needs to be considered in FEA and other analysis calculations. The influence of the strain rate on the yield strength of steel is described by the Cowper-Symonds model [35], as shown in Eq. (1):

$$DIFs = \frac{\sigma_{dy}}{\sigma_{sy}} = \left[1 + \left(\frac{\dot{\varepsilon}}{C}\right)\right]^{\frac{1}{P}} \tag{1}$$

where σ_{dy} represents the yield strength of the steel tube under the strain rate $\dot{\varepsilon}$; σ_{sy} represents the yield strength of a steel tube; and *C* and *P* are the strain rate parameters with values 6844 s^{-1} and 3.91, respectively [1,10].

The influence of the strain rate on the dynamic compressive strength of concrete can be found in the CEB-FIP model code [36], as shown in Eq. (2):

$$DIF = \frac{f_{cd}}{f_{cs}} = \begin{cases} (\dot{\varepsilon} / \dot{\varepsilon}_{sc})^{1.026\alpha_s} & \dot{\varepsilon} \le 30s^{-1} \\ \gamma_s (\dot{\varepsilon} / \dot{\varepsilon}_{sc}) & \dot{\varepsilon} > 30s^{-1} \end{cases} \tag{2}$$

where f_{cd} represents the dynamic compressive strength of concrete at the strain rate $\dot{\varepsilon}$ within the range of $30\times10^{-6}s^{-1}$ to $300\ s^{-1}$; f_{cs} represents the static compressive strength of concrete at the strain rate $\dot{\varepsilon}_{sc}$ ($\dot{\varepsilon}_{sc} = 30\times10^{-6}s^{-1}$); $\log\gamma_s = 6.156\alpha_s - 2$; $f_{co} = 10MPa$; $\alpha_s = (5+9f_{cs}/f_{co})^{-1}$.

The influence of the strain rate on the dynamic tensile strength of concrete is also given in the CEB-FIP model code [36], as shown in Eq. (3):

$$DIF = \frac{f_{td}}{f_{ts}} = \begin{cases} (\dot{\varepsilon} / \dot{\varepsilon}_{st})^{1.016\delta_s} & \dot{\varepsilon} \le 30s^{-1} \\ \beta_s (\dot{\varepsilon} / \dot{\varepsilon}_{st})^{1/3} & \dot{\varepsilon} > 30s^{-1} \end{cases} \tag{3}$$

where f_{td} is the dynamic tensile strength of concrete at the strain rate $\dot{\varepsilon}$ within the range of $30\times10^{-6}s^{-1}$ to $300\ s^{-1}$; f_{ts} is the static tensile strength of concrete at the strain rate $\dot{\varepsilon}_{st}$ ($\dot{\varepsilon}_{st} = 3\times10^{-6}s^{-1}$); $\log\beta_s = 7.11\delta_s - 2.33$; and $\delta_s = 1/(10+6f_{cs}/f_{co})$.

Both the impact hammer and supports are simplified in the FEA model, as shown in Fig. 2. Specifically, the supports are simplified to hollow cylinders with all degrees of freedom constrained, while the impactor is simplified as a rectangular block. The impact contact surface size and the total mass of the impact block in the FEA model are the same as those in the tests. Both the support and the impact block are rigid bodies, corresponding to the MAT_15 model in LS-DYNA.

The parameters of the CFST beams are consistent with those of the tests. A continuous node mode is used to describe the contact relationship between the

concrete and the steel tube, while their relative slip is not considered in the FEA model. Automatic node-to-surface contact is adopted as the contact relationship of the CFST beam and the supports as well as between the CFST member and the block, for which the dynamic friction coefficients are 0.2 and 0, respectively. Additionally, the penalty scale factors, SFS and SFM, are equal to 2.0. The initial impact velocities of the impactor were determined according to the tests. Besides, a stiffness-type hourglass control was used to eliminate the zero-energy modes.

2.2.2 Verification of the FEA model

Fig. 3 shows the general FEA result. The dynamic response modes of the CFST beams were bending deformation and fracture, with reasonable CFST beam damage and deformation being obtained via the establishment FEA model.

The impact-force time history curves obtained from the FEAs are shown in Fig. 4. The comparisons between the predicted and experimental peak values (P_{max}), plateau values (P_{stable}) and load durations (t) of the impact forces (F) are shown in Table 2. The subscripts *FE* and *TE* in Table 2 refer to the FEA and the experimental results, respectively. The mean values of $P_{max,FE}/P_{max,TE}$, $P_{stable,FE}/P_{stable,TE}$ and t_{FE}/t_{TE} ratios are 0.97, 1.05 and 1.01, respectively, and the corresponding standard deviations are 0.049, 0.037, and 0.061. The maximum deflections of the impact point (W_{bmax}) obtained from the FEAs and the tests are also summarised in Table 2. The mean value and standard deviation of the $W_{bmax,FE}/W_{bmax,TE}$ ratio are 1.01 and 0.054, respectively. Therefore, the results of the dynamic response of CFST beams obtained from the FEAs are consistent with those from the 2/9 span tests.

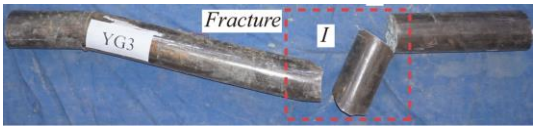

(a) Test Result

(b) FEA Result

Fig. 3 Damage condition

Table 2
Summary of the FE simulation results

Specimen	P_{max} (kN)			P_{stable} (kN)			W_{bmax} (mm)			*Total duration t* (ms)		
	FEA	TEST	FE/TE	FEA	TEST	FE/TE	FEA	TEST	FE/TE	FEA	TEST	FE/TE
YG1	370.3	410.9	0.90	210.6	193.8	1.09	30.9	32.2	0.96	14.0	13.3	1.05
YG2	469.0	449.6	1.04	193.2	186.1	1.07	93.7	91.4	1.03	44.4	42.5	1.04
YG3	529.3	527.1	1.00	199.2	201.6	0.96		Fracture			Fracture	
YG4	619.4	651.2	0.95	312.4	286.8	1.09	49.5	49.5	1.00	12.6	13.1	0.96
YG5	517.3	542.6	0.95	309.3	294.6	1.05	35.5	33.3	1.06	11.3	11.7	0.97
Mean Error			0.97			1.05			1.01			1.01
Std. Dev.			0.049			0.037			0.054			0.061

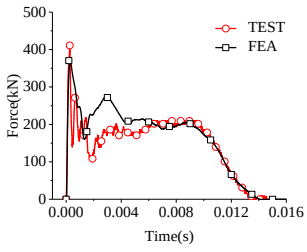

(a) YG1

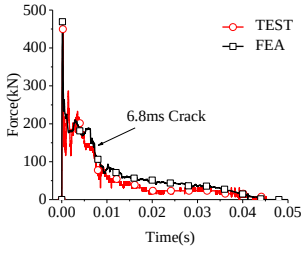

(b) YG2

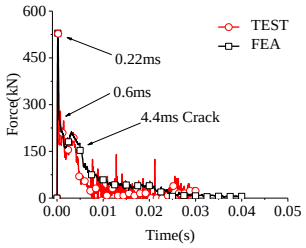

(c) YG3

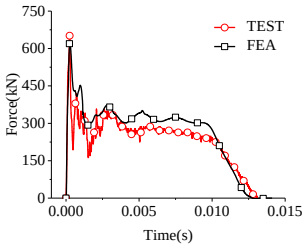

(b) YG4

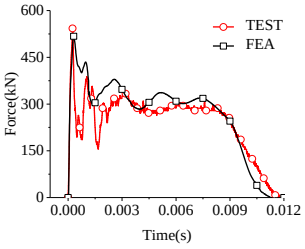

(e) YG5

Fig. 4 Impact-force time history curves

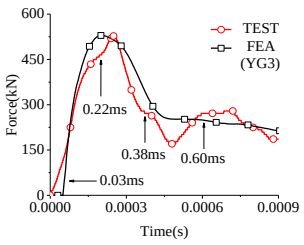

(a) Impact force

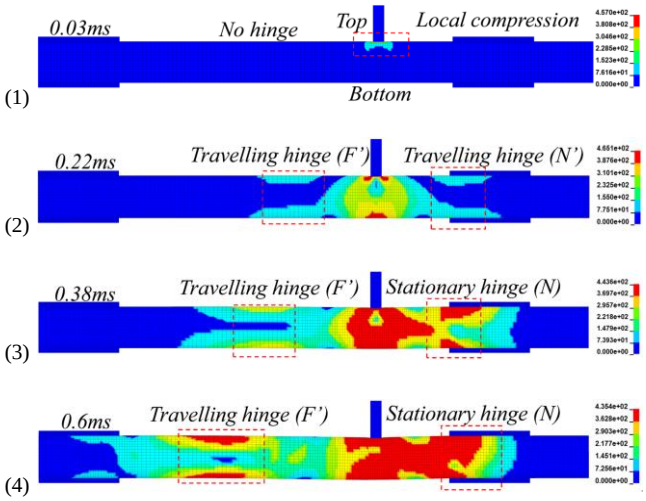

(b) Stress distribution

Fig. 5 Stress distribution during the peak value stage

2.3. Deformation mode

Fig. 5 shows the propagation process of stress waves at the peak value stage, which is applied to analyse the force mechanism of CFST members. From the Von-Mises stress distributions of the beam (YG3), there are two deformation modes for CFST beams at the peak value stage which are the local compression mode and the local bending deformation mode.

The local compression stage is shown in Fig. 5 (b-1). At this stage, the stress wave propagated from the top to the bottom point, and the stress value at the bottom point of the CFST member was always zero. From this phenomenon, it is considered that the bottom of the CFST member cross-section remains stationary, and the whole deformation of the cross-section does not occur. Therefore, only local compressive deformation occurs in CFST members at this stage. After the stress wave spreads to the bottom of the CFST beam, the member cross-section exhibits the bending deformation.

The bending deformation stage is shown in Fig. 5 (b-2) to (b-4). The main feature of this stage is that there are two travelling stress-concentrated regions (i.e., travelling hinges) outside the impact point. The middle of the stress-concentrated region displayed a low-stress level, while the top and bottom of the region displayed high- stress levels; which is a typical bending stress distribution. Therefore, it was determined that the deformation mode of the CFST beam is a bending mode. The stress distribution also proved that the deformation of the CFST beam is local since there were stress-less regions between the supports and the stress-concentrated regions. The stress-concentrated regions gradually extended from the impact area to the constraints, as shown in Fig. 5 (b-2) to (b-4), a process that can be described by the travelling hinge theory [14-16, 37]. The stress-concentrated region is similar to the travelling hinge, with the stress level of the travelling hinge increasing during its travelling process, resulting in it eventually reaching a plastic state from an elastic state, as seen in Fig. 5 (b-4). Thus, the elastoplastic behaviour of CFST beams is an additional factor that requires consideration in analysis calculations.

2.4. Velocity and acceleration

Fig. 6 displays the velocity time history and acceleration time history curves for the YG3 case, with W_b, V_b and a_b as the displacement, velocity and acceleration variables of the CFST member at the impact point, respectively. Additionally,. W_I, V_I and a_I are the displacement, velocity and acceleration variables of the impactor, respectively. The above parameters are also marked in Fig. 6 (c).

The impact velocity (Velocity) versus time (Time) curves are showed in Fig. 6(a), including V_I and V_b. From the V_I curve, the velocity of the impactor decreases continuously at the peak value stage which indicates that the impactor is always in the state of deceleration. In contrast, the V_b curve witnesses an increase during the initial period, which indicates that the CFST beam is in the state of acceleration, then it falls gradually. Thus, the peak value stage can be further divided into the acceleration process (*OLV*) and the deceleration process (after point *V*) based on the state of the CFST beam. The demarcation point of the two processes is represented by point *V*, as shown in Fig. 6 (a). From the V_b curve, It is also observed the fact that the acceleration process is characterized by the approximate linear increment. Based on this feature, it can be assumed that the value of a_b is approximately a constant during the acceleration process. Besides, as the V_b and V_I curves stay close and share the similar trend in the deceleration process, it can be assumed that $V_I \equiv V_b$ in this process, which is also a general supplementary condition in the analysis calculations [15-16, 27-30], while not suitable at the peak value stage.

The supplementary condition of the acceleration process is suggested to be the simplified acceleration time history curve (i.e., the simplified trend curve), as shown in Fig. 7. The simplified trend curve in the acceleration process can be divided into three stages in which: *OL* represents the local compression stage, *LV* indicates the constant acceleration stage of bending deformation, and *VA* denotes the transition stage. Point *O* is the initial time of the impact process; point *L* is defined as the end time of the local compression process; point *V* is the time when $V_I = V_b$ for the first time (although $a_I \neq a_b$ at this time), and point *A* is the time when $V_I \equiv V_b$ ($V_I = V_b$ and $a_I = a_b$). The constant acceleration stage is the main component of the simplified trend curve, corresponding to the linear change process of the V_b curve. The function of the local compression stage is to determine the parameters of the simplified curve. Since the CFST beam was already in the constant acceleration state when the local compression stage ended (*L* moment) (Fig. 6 [a] and [b]), time and the value of a_b at the *L* moment were used as the representative values to determine the curve. Finally, the transition stage was applied to ensure that $V_I \equiv V_b$ at *A* time. Point *V* and point *A* were determined by the relative motion states of the impactor and CFST beam.

The ideal simplified trend curve and the corresponding velocity time history curve are also displayed in Fig. 6(a) and (b). Compared with the FEA result (a_b FEA), although the trend of the simplified curve at the *VA* stage is slightly different from that of the FEA result, the general trends of the two curves in the acceleration process appear to be similar.

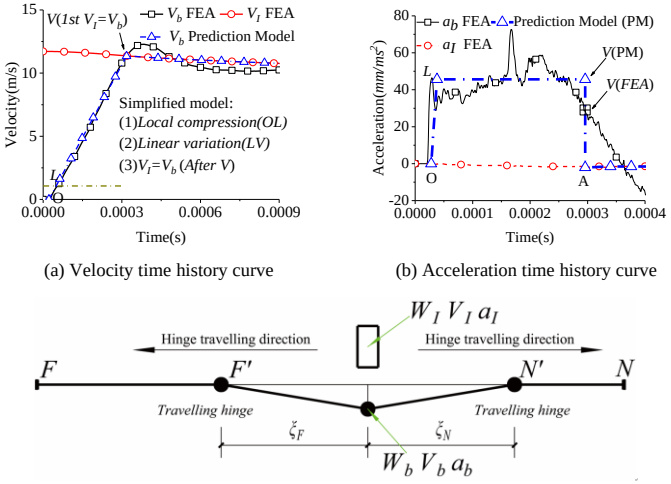

(a) Velocity time history curve (b) Acceleration time history curve

(c) General impact process

Fig. 6 Velocity and acceleration

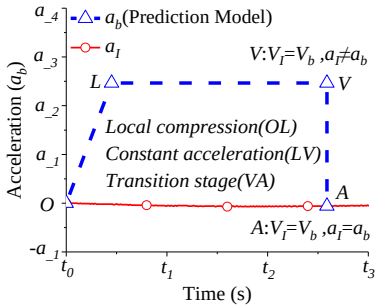

Fig. 7 Simplified acceleration curve

3. Analysis method of the peak value stage

3.1. Analysis process

There are two stages in the analysis and calculation process: local compression stage and bending deformation stage. The calculation of the local compression stage was performed to predict the parameters of the simplified trend curve (prediction model), as shown in Figure 7. Then, the bending deformation stage could be calculated based on the travelling hinge theorem, wherein the prediction model provides the supplementary condition for solving the equations.

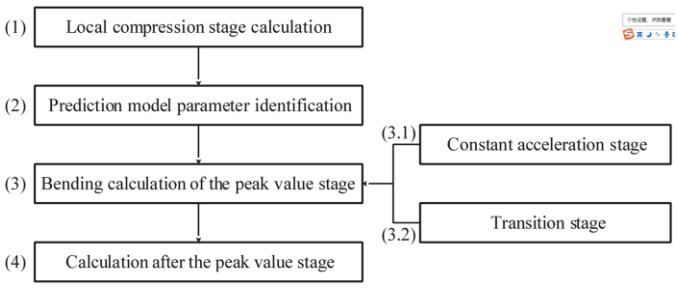

Fig. 8 Calculation process

The calculation process was divided into four stages according to the proposed prediction model, as shown in Fig. 8.

Step 1: Local compression stage calculation.

Step 2: Prediction model parameter identification.

Step 3: Bending deformation calculation at the peak value stage (based on the prediction model).

Step 4: Bending deformation calculation after the peak value stage (based on the $V_I \equiv V_b$ assumption).

On the basis of the prediction model, Step 3 can also be subdivided into the constant acceleration stage (Step 3.1) and the transition stage (Step 3.2).

3.2. Prediction of the acceleration curve

3.2.1 Calculation of the local compression process

The parameters of the prediction model were determined by the value of a_b (a_{bL}) and time (t_L) at the end of the local compression stage. Therefore, the a_b curve of the peak value stage could be predicted by the calculation of the local compression stage.

The propagation process of the impact at the local compression stage (*OL*) is shown in Fig. 9, which shows that the stress wave propagates from the contact point (*CP*) to the bottom of the beam (*BP*), and before it reaches point *BP*, the bottom of the beam is in a static and stress-less state. Thus, it can be concluded that the beam cannot generate bending deformation, and the local compression model is recommended for calculation during this process.

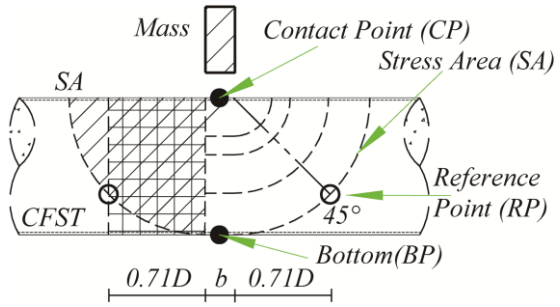

Fig. 9 Local compression model

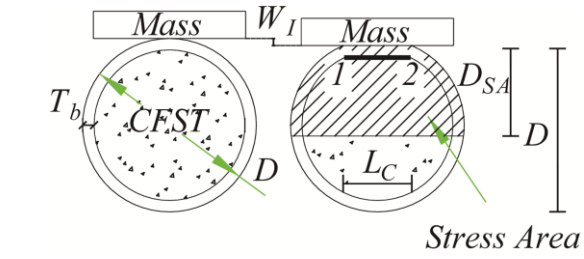

(a) Cross-section

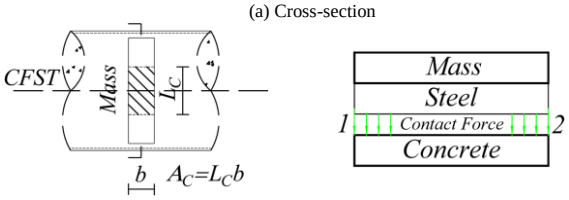

(b) Contact area (c) Contact force

Fig. 10 Calculation of the local compression process

Fig. 10 displays the calculation model of the local compression stage. The contact force is assumed to be controlled by the core concrete material, as shown in Fig. 10 (c). The force balance equation between steel and concrete was established, as given in contact mechanics [38]:

$$ma_I + DIF \times f_{cc} \times A_C = 0 \tag{4}$$

where A_C is the contact area; f_{cc} is the concrete strength with consideration to the lateral confining pressure; *DIF* is the dynamic increase factor of the concrete material given in the CEB90 model code[36].

The value of f_{cc} [39,40] is calculated by Eq.(5):

$$f_{cc} = f_c + k\sigma_3 \tag{5}$$

where f_c is the characteristic concrete strength, taken as 0.67 of the cubic strength of concrete for normal-strength concrete [1,10]; k is an empirical coefficient [39,40]; and σ_3 is the confining pressure around the concrete core, which can be estimated according to the local transverse strain of the concrete.

$$\sigma_3 = E_c\varepsilon_3 \le f_c \tag{6}$$

where E_c is the elastic modulus of concrete; ε_3 is the transverse strain of concrete at the impact point region; the transverse direction is the axial direction of the beam. The value of ε_3 can be calculated by the definition of Poisson's ratio, as shown in Eq. (7):

$$\nu = \frac{\varepsilon_3}{\varepsilon_{c3}} \tag{7}$$

where ν represents Poisson's ratio and ε_{c3} is the local compressive strain of concrete. The value of ε_{c3} is conservatively estimated by Eq. (8).

$$\varepsilon_{c3} = \frac{W_I}{\alpha(D-2T_b)} \tag{8}$$

where D is the diameter of the beam; T_b is the thickness of the steel tube; W_I is the displacement of the impactor. Additionally, α is the stress distribution coefficient with a suggested value of 0.71.

$D-2T_b$ in Eq. (8) is a conservative approximation of D_{SA}. D_{SA} is the height of the stress area, as shown in Fig. 10 (a), and α is the coefficient related to the stress distribution. From Fig. 9, the shape of the stress distribution in CFST members is approximately semi-circular. Thus, the impact point region with width *b* is subjected to the transverse constraint of the surrounding concrete. Moreover, the transverse constraint level of concrete at different section heights is not the same. If the effect of transverse constraint is ignored, $\alpha = 1$. When considering this effect, a reference point (i.e., point *RP*) can be used to estimate the average influence of the transverse constraint. The recommended point *RP* is the intersection point between the 45° line and the stress area edge, as shown in Fig. 9. Thus, the value of α is 0.71 ($\sin 45^\circ$). Additionally, the initial state of the bending deformation stage can also be obtained from the point *RP*. A rectangular stress area determined by the reference point can be equivalent to the semi-circular stress area, as seen in Fig. 9.

Then, the local compression strain rate (ε') used to estimate the *DIF* can also be calculated by Eq. (9).

$$\varepsilon' = \frac{V_I}{\alpha(D-2T_b)} \tag{9}$$

where V_I is the velocity of the impactor.

Besides, A_C is the contact area, and its value is calculated by Eq. (10):

$$A_C = L_C b \tag{10}$$

where b is the width of the hammer; L_C is the contact length displayed in Fig. 10(b). For circular cross-sections, L_C is calculated based on geometric relationships [38]:

$$L_C = 2\sqrt{W_I D} \tag{11}$$

3.2.2 Termination time of local compression stage

The local compression stage was terminated when the stress wave reached point *BP*. It was assumed that D_{SA} in Fig. 10(a) represented the maximum vertical distance between the stress area and the contact point. Thus, when $D_{SA} = D$, the local compression stage was terminated. At the time of $D_{SA} = D$, the vertical propagation distances of the stress wave in the steel and concrete are $2T_b$ and $D-2T_b$, respectively. Therefore, according to the formula for the elastic stress wave velocity [41], the termination time of the local compression stage (t_L) can be estimated as:

$$t_L = \frac{2T_b}{\sqrt{E_s/\rho_s}} + \frac{D-2T_b}{\sqrt{E_c/\rho_c}} \tag{12}$$

where E_s and E_c are the elastic modulus values of steel and concrete, respectively; ρ_s and ρ_c are the densities of steel and concrete, respectively.

3.2.3 Acceleration prediction

The stress area (*SA*) of the CFST member at time *L* (i.e., the termination time of the local compression stage) is shown in Fig. 9. According to the reference point (*RP*), the empirical acceleration distribution is shown in Fig. 11. In this empirical distribution, the acceleration value of the impact point region

with width b is a_b, and the position of zero acceleration point is 0.71D away from the boundary of the impact point region. It is assumed that the acceleration distribution is linear between the zero acceleration point and the edge of the impact point area.

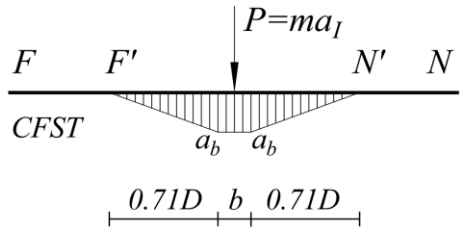

Fig. 11 The initial distribution of the acceleration during the bending stage

Therefore, the acceleration value of the beam impact point at time L (a_{bL}) is calculated as follows:

$$a_{bL} = -\frac{ma_{IL}}{\rho_l(b+0.71D)} \tag{13}$$

where ρ_l is the beam mass per unit length; a_{IL} is the acceleration of the impactor at time L obtained from Eq. (4).

Furthermore, the velocity of the beam impact point (V_{bL}) at time L was obtained by momentum conservation:

$$V_{bL} = \frac{m(V_{I0} - V_{IL})}{\rho_l(b+0.71D)} \tag{14}$$

where V_{IL} is the velocity of the impactor at time L obtained from Eq. (4).

The average deflection of the beam impact point at time L (W_{bL}) can be calculated using Eq. (15).

$$W_{bL} = 0.5V_{bL}t_L \tag{15}$$

In Eq. (13), a_b is a positive value, indicating that the velocity of the member gradually increases, whereas a_I is always negative, indicating that the impactor velocity continues to decrease.

3.3. Bending stage calculation

3.3.1 Bending equilibrium equation

The diagram used in the calculation of the impact process based on the travelling hinge model is shown in Fig. 6(c), in which F' and N' represent the travelling hinges. When a travelling hinge reaches the supported end of the beam, it immediately transforms into a stationary hinge. Equations for the travelling hinge model based on the assumption that $V_I \equiv V_b$ has been provided in the literature [15,16,37]. If the impactor and the member are independent, the original equation can be altered to Eqs. (16)-(18).

$$ma_I + \frac{1}{2}\rho_l a_b(\xi_F + \xi_N) + \frac{1}{2}\rho_l V_b(\xi_F' + \xi_N') + Q_F + Q_N = 0 \tag{16}$$

$$M_F + M_I = \frac{\rho_l a_b \xi_F^{\,2}}{6} + \frac{\rho_l V_b \xi_F \xi_F'}{3} + Q_F \xi_F \tag{17}$$

$$M_N + M_I = \frac{\rho_l a_b \xi_N^{\,2}}{6} + \frac{\rho_l V_b \xi_N \xi_N'}{3} + Q_N \xi_N \tag{18}$$

where ξ_F and ξ_N represent the location of the travelling hinges; ξ_N' and ξ_F' represent the corresponding travelling hinge velocities; M_I is the bending moment value of the stationary hinge at impact point I; M_N and M_F are the bending moment values of the corresponding travelling hinges; Q_N and Q_F are the shear force values of hinges N and F, respectively; and the subscripts F and N represent the supports corresponding to the travelling hinges F' and N'.

L_N and L_F denote the distance from impact point I to the supports N and F, respectively. Before a travelling hinges reaches the support ($\xi_N < L_N$ or $\xi_F < L_F$), the travelling hinge shear force is ignorable ($Q_N = 0$ or $Q_F = 0$); however, the travelling hinge velocity is not zero ($\xi_N' \neq 0$ or $\xi_F' \neq 0$). Conversely, if $\xi_N = L_N$ or $\xi_F = L_F$, $Q_{N(F)} \neq 0$ and $\xi_{N(F)}' = 0$.

3.3.2 Elastoplasticity of a travelling hinge

As steel and concrete are both elastic-plastic materials, the travelling hinge of a CFST beam is not rigid-plastic. Eqs. (19) and (20) illustrate an approximation method for estimating the elastoplastic deformation of a travelling hinge:

$$M_N = M_I = K\theta_N \le M_y \tag{19}$$

$$M_F = K\theta_F \le M_y \tag{20}$$

$$\theta_N = W_b/\xi_N \tag{21}$$

$$\theta_F = W_b/\xi_F \tag{22}$$

where M_y is the dynamic yield bending moment of the beam; θ_N and θ_F are the rotation angles of the travelling hinges; and K is the dynamic rotational stiffness.

$$K = DIF_\theta \times K_\theta \tag{23}$$

where DIF_θ is the dynamic increase factor related to the rotational velocity of the hinge, and K_θ is the static rotational stiffness calculated as follows:

$$K_\theta = \frac{K_\phi}{l_p} \tag{24}$$

where K_ϕ is the flexural rigidity of a CFST beam according to the AIJ1997 code [42], and l_p is the equivalent length of the hinge region with a value of $0.5D$.

$$K_\phi = E_S I_S + 0.2E_C I_C \tag{25}$$

where, I_S and I_C are the inertia moments of the steel tube and core concrete sections, respectively.

Eqs. (19) and (20) are optimisations of the $M_N = M_I = M_F = M_y$ assumption (i.e., the rigid-plastic model). The $M_N = M_I$ assumption is based on both the 2/9 span tests and FEA results, as shown in Fig. 3 and Fig. 5. Similar estimation methods of the θ value can also be found in the calculation of Qu [27].

Since the steel tube provides the main flexural capacity, DIF_θ is estimated as follows:

$$DIF_\theta = 1 + \left(\frac{\theta'}{C}\right)^{\frac{1}{P}} \tag{26}$$

where C and P are the strain rate parameters: C=6844 and P=3.91[1,7]. Additionally, θ' is the rate of the rotation angle [23].

$$\theta' = \frac{V_b}{\xi_N} \tag{27}$$

Then, the dynamic yield bending moment of the beam (M_y) can be calculated as follows:

$$M_y = DIF_\theta \times M_u^s \tag{28}$$

where M_u^s is the static yield bending moment of the beam that can be calculated by the formula presented by Han [43].

3.3.3 Calculation of bending stage

(1) Step 3.1

The unknown variables of the three equilibrium equations (16)-(18) include W_I, W_b, ξ_F and ξ_N. The prediction model provided the acceleration value of the beam (a_b) to determine its deflection (W_b). Thus, the equations can be solved.

The initial travelling hinge position (ξ_0) is shown in Figs. 9 and 11.

$$\xi_0 = 0.71D \tag{29}$$

The supplementary condition for the equilibrium equations is as follows:

$$a_b(t) = a_{bL} \tag{30}$$

The calculation process begins at time L (i.e., the termination time of the local compression stage), and the termination condition of the calculation process is the first occurrence of $V_I = V_b$.

(2) Step 3.2

The transition stage (*VA*) in the prediction model is shown in Fig. 7, with the times corresponding to point *V* and point *A* being equal. During the calculation, the basic assumption is $a_I = a_b$, and the parameters other than Q_N, Q_F, ξ_N' and ξ_F' maintain their values at *V* time. By introducing $a_I = a_b$ into Eqs. (16)-(18), the acceleration value corresponding to point *A* can be obtained.

(3) Step4

The deformation mode of the beam after the peak value stage is also a bending-type. Hence, Eqs. (16)-(18) can still be applied for the calculation of this stage. However, the supplementary condition changes from the prediction model to the equation $V_I \equiv V_b$.

3.4. Analysis Results

The dynamic response of the CFST beam at the peak value stage under lateral impact was predicted using the proposed analysis method, and the accuracy of which was then verified by the 2/9 span tests employed in this study and five other 1/2 span tests [1,10]. The rationality of the calculated results was evaluated by the acceleration and impact-force time history curves.

3.4.1 Acceleration time history curve

Fig. 12 presents the acceleration time history curve at the impact point *I* obtained from the prediction model. The calculated acceleration value of the beam in the constant acceleration stage was $a_{b,LV}$, and the results are summarized in the table of Fig. 12. The corresponding average value of FEA was assigned as $a_{b,FEAmean}$. As shown in the table of Fig. 12, the mean value of the $a_{b,LV} / a_{b,FEAmean}$ ratio was 0.987, and its standard deviation was 0.0504. The maximum calculation error appeared in the YG1 case, for which the value of the $a_{b,LV} / a_{b,FEAmean}$ ratio was 0.899. This error also led to a low calculated value of impact force in the YG1 case.

The shortcomings of the prediction model can be observed clearly in Fig. 12. The FEA results show that the impact point acceleration of the CFST beam decreases after the constant acceleration stage (point *V*), and gradually approaches the acceleration value of the impactor. However, the prediction model (*VA*) assumes that this process is completed immediately. The calculation error in the acceleration at this stage is evident, and its influence was discussed in the following section according to the impact-force time history curves.

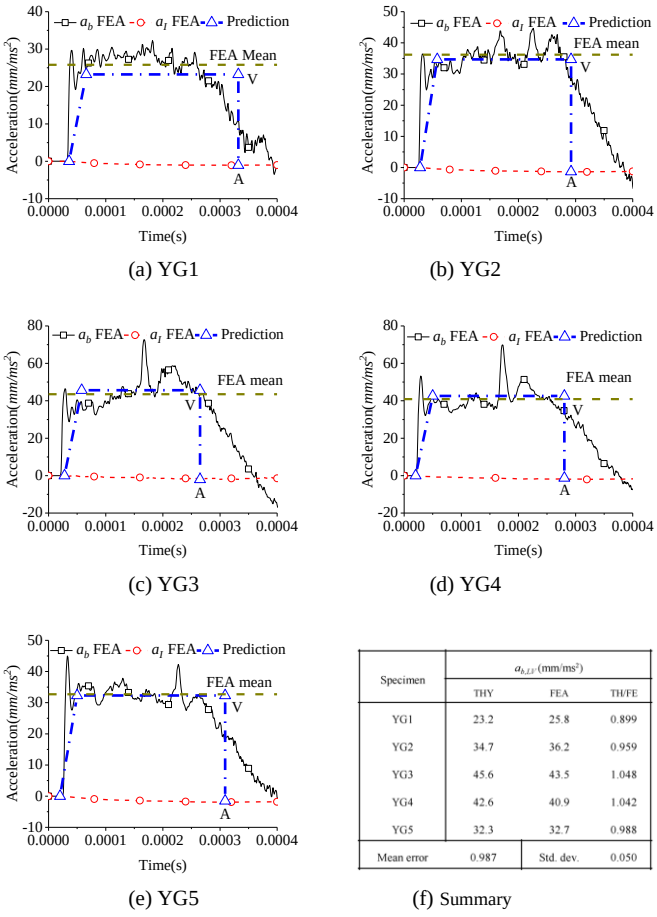

(a) YG1 (b) YG2

(c) YG3 (d) YG4

(e) YG5

Specimen	$a_{b,LV}$ (mm/ms²)		
	THY	FEA	TH/FE
YG1	23.2	25.8	0.899
YG2	34.7	36.2	0.959
YG3	45.6	43.5	1.048
YG4	42.6	40.9	1.042
YG5	32.3	32.7	0.988
Mean error	0.987	Std. dev.	0.050

(f) Summary

Fig. 12 Calculation results of prediction models

Table 3
Details of the analysis calculations

Specimen	m (kg)	V_{I0} (m/s)	D (mm)	T_b (mm)	f_c (MPa)	k[39,40]	E_c (MPa)	f_y (MPa)	M_y (kN·m)	*Impact point*	$P_{max,TH}$ (kN)	$P_{max,TE}$ (kN)	| *1-TH/TE* |
YG1	270	7.67	114	2	36.85	4.1	35250	338	9.63	2/9span	364.3	410.9	11.33%
YG2	270	9.90	114	2	36.85	4.1	35250	338	9.63	2/9span	436.4	449.6	2.93%
YG3	270	11.7	114	2	36.85	4.1	35250	338	9.63	2/9span	498.4	527.1	5.44%
YG4	270	11.7	114	3.5	36.85	4.1	35250	323	15.36	2/9span	636.3	651.2	2.28%
YG5	270	9.90	114	3.5	36.85	4.1	35250	323	15.36	2/9span	565.3	542.6	4.18%
CC1[1]	465	9.21	180	3.65	50.32	3	36800	247	35.26	1/2span	870.0	811.1	7.27%
CC2[1]	920	6.40	180	3.65	50.32	3	36800	247	35.26	1/2span	666.3	624.8	6.65%
CC3[1]	465	9.67	180	3.65	50.32	3	36800	247	35.26	1/2span	901.9	787.9	14.47%
DBF14[10]	230	3.90	114	1.7	32.63	4.1	32500	232	6.11	1/2span	148.2	160.5	7.66%
DBF17[10]	230	4.40	114	1.7	32.63	4.1	32500	232	6.11	1/2span	175.5	168.5	4.18%
Mean Error													6.64%
Std. Dev.													0.035

3.4.2 Impact-force time history curve

The impact-force time history curves of the 2/9 span tests obtained from the analysis method are shown in Fig. 13. The calculation parameters and results of the 1/2-span cases are summarized in Table 3.

Compared with the impact force peak values from the verification tests ($P_{max,TE}$), the mean error of the analysis calculation ($P_{max,TH}$) was 6.64%, and the standard deviation was 0.035. One of the cases exhibiting a larger error was YG1, in which the calculation value was 11.33% lower than the experimental value. The reason for this error may be that the influence of the steel tube was not considered in determining the parameters of the prediction model in Eq. (4). Therefore, the calculated results of beam acceleration (a_b) and the impact force were lower than those of the test. In addition, the greatest calculation error occurred in the case of CC3, in which the calculated value was 14.47% higher than the test value. A particular case led to this deviation, which involved the impact force peak values of the tests decreasing with rising impact velocity, as seen in CC1 and CC3. Although the theoretical method cannot reasonably describe this phenomenon, it can be inferred that it may be related to local damage of the CFST beam. Additionally, it can be further found from the impact-force time history curves that the *VA* process in the prediction model is acceptable, as shown in Fig. 13. This approximation method does not yield significant errors in the calculation results.

After the *A* time in Fig. 13, the impact-force platform value can be calculated based on the $V_I \equiv V_b$ assumption, and the calculation results consistent with the tests were obtained from the original travelling hinge theorem. However, since the $V_I \equiv V_b$ assumption was employed, the fluctuations of the impact force curves could not be described. The calculation process employed in this paper terminated after all the travelling hinges transformed into stationary hinges ($L_F = \xi_F$). It can be found from the curves after A time that the actual constraint length of the CFST beam at the early platform stage may be less than the distance from the impact point to the supports.

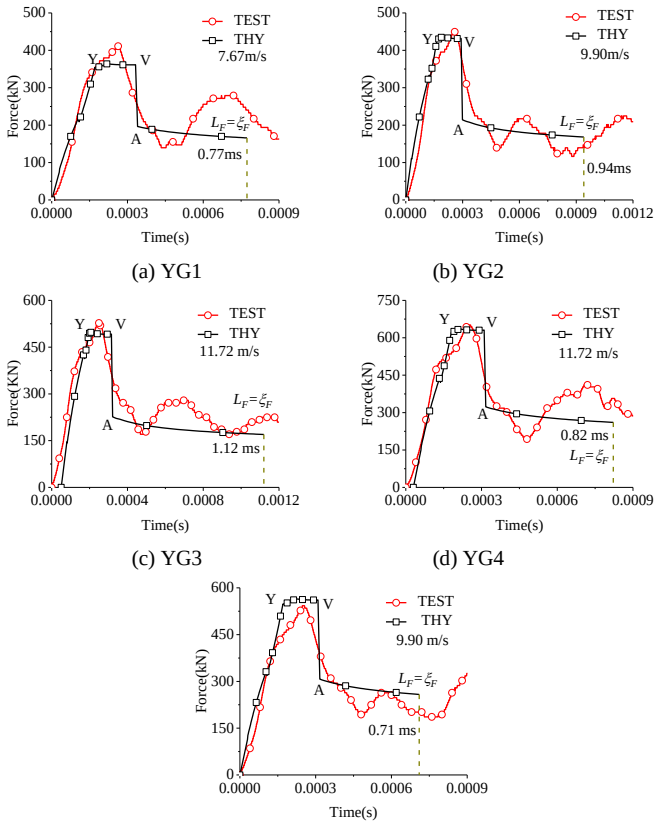

Fig. 13 Analysis calculation results

4. Conclusion

In this paper, an analysis method was presented to predict the dynamic response of CFST beams under the lateral impact process at the peak value stage. The rationality of the method was verified by the acceleration time history curve of FEAs and the impact-force time history curve of lateral impact tests. The following conclusions were obtained from the research of this paper.

(1) A simplified trend curve of the acceleration at the impact point of a CFST beam is proposed based on the FEA results. The curve can be a new supplementary solution condition in the calculation of the peak value stage. The simplified trend curve divides the peak value stage into the local compression stage, the constant acceleration bending stage, and the transition stage.

(2) The parameters of the simplified trend curve can be predicted by the calculation of the local compression stage. The influencing factors of the prediction model include impactor mass, impactor velocity, contact surface size, and concrete strength and strain rate.

(3) The dynamic responses of CFST beams at the peak value stage were accurately predicted. This analysis calculation depended on the prediction model of the simplified trend curve and the travelling hinge theorem. The elastoplastic behaviour of CFST beams was also considered during the calculation.

Based on the proposed simplified trend curve and the travelling hinge theorem, a dynamic response analysis method for the peak value stage of CFST beams under lateral impact can be established. This method provided the predictions for the dynamic response of CFST beams reasonably. However, the transition stage in the simplified trend curve is marginally different from the FEA results, and the current work cannot simplify this stage more accurately. Therefore, more research is needed to further optimise the simplified trend curve.

Acknowledgement

The authors are grateful for the financial support of the National Key Research and Development Program of China (Grant No. 2016YFC0802205), the National Natural Science Foundation of China (Grant Nos. 51378427, 51678504), and the Department of Science and Technology of the Sichuan Province (Grant No. 2018JY0029).

Notation

a_{IL}	Acceleration value of the impactor at time *L*	a_I	Acceleration of the impactor
V_{IL}	Velocity of the impactor at time *L*.	V_I	Velocity of impactor
t_L	Termination time of the local compression stage	w_i	Displacement of impactor
a_{bL}	Acceleration value of the beam at time *L*	a_b	Acceleration of the beam impact point
V_{bL}	Velocity of the beam impact point at time *L*	V_b	Velocity of the beam impact point
W_{bL}	Deflection of the beam impact point at time *L*	w_s	Displacement of the beam impact point
σ_3	Confining pressure around the concrete core	ν	Poisson's ratio
ε_3	Average transverse strain of concrete	A_C	Contact area
ε_{c3}	Compressive strain of concrete	D	Diameter of the beam
f_c	Characteristic concrete strength	T_b	Thickness of the steel tube
ε'	local compression strain rate	b	Width of the hammer
α	Stress distribution coefficient	E_c	Elastic modulus of concrete
k	Empirical coefficient	E_s	Elastic modulus of steel
M_y	Dynamic yield bending moment of the beam	ρ_c	Density of concrete
M_I	Bending moment value at impact point *I*	ρ_s	Density of steel
M_N	Bending moment values of the travelling hinge *N*	L_C	Contact length
M_F	Bending moment values of the travelling hinge *F*	ρ_l	Beam quality per unit length
M_u^s	Static yield bending moment of the CFST beam	ξ_N	Location of the travelling hinge *N*
θ_N	Rotation angles of the travelling hinge *N*	ξ_F	Location of the travelling hinge *F*
θ_F	Rotation angles of the travelling hinge *F*	ξ_N'	Velocity of the travelling hinge *N*
L_N	Distances from impact point *I* to the support *N*	ξ_F'	Velocity of the travelling hinge *F*
L_F	Distances from impact point *I* to the support *F*	ξ_0	Initial travelling hinge position
K_ϕ	Flexural rigidity of CFST members	Q_F	Shear force values of hinge *F*
K_θ	Static rotational stiffness	Q_N	Shear force values of hinge *N*
K	Dynamic rotational stiffness	C	Strain rate parameter
I_S	Inertia moment of steel tube section	P	Strain rate parameter
I_C	Inertia moment of core concrete section	l_p	Equivalent length of the hinge region
f_{cc}	Concrete strength in consideration of lateral confining pressure	DIF	Dynamic increase factor of concrete
DIF_θ	Dynamic increase factor related to the rotational velocity of the hinge		

References

[1] Han L.H., Hou C.C., Zhao X.L. and Rasmussen K. J., "Behaviour of high-strength concrete filled steel tubes under transverse impact loading", Journal of Constructional Steel Research, 92, 25-39 ,2014.

[2] Mindess S. and Bentur A., "A preliminary study of the fracture of concrete beams under impact loading, using high speed photography", Cement and Concrete Research, 15(3), 474-484, 1985.

[3] Yu Z.X., Zhao L., Liu Y.P., Zhao S. C., Xu H. and Chan, S. L., "Studies on flexible rockfall barriers for failure modes, mechanisms and design strategies: a case study of Western China", Landslides, 16(2), 347-362, 2019.

[4] Yu Z. X., Qiao Y. K., Zhao L., Xu H., Zhao S. C. and Liu Y. P., "A simple analytical method for evaluation of flexible rockfall barrier part 1: working mechanism and analytical solution", Advanced Steel Construction, 14(2), 115-141, 2018.

[5] Yu Z. X., Qiao Y. K., Zhao L., Xu H., Zhao S. C. and Liu Y. P., "A simple analytical method for evaluation of flexible rockfall barrier part 2: application and full-scale test", Advanced Steel Construction, 14(2), 142-165, 2018.

[6] Xu H., Gentilini C., Yu Z.X., Qi X. and Zhao S.C., "An energy allocation based design approach for flexible rockfall protection barrier", Engineering Structures, 173, 831-852, 2018.

[7] Liu C., Yu Z. X. and Zhao, S. C., "Quantifying the impact of a debris avalanche against a flexible barrier by coupled DEM-FEM analyses", Landslides, 2019.

[8] Yu Z. X., Zhao L., Guo L. P., Liu Y. P., Yang C. and Zhao, S. C., "Full-Scale Impact Test and Numerical Simulation of a New-Type Resilient Rock-Shed Flexible Buffer Structure", Shock and Vibration, 2019.

[9] Yu Z. X., Yan S.W., Xu H. and Zhao S. C., "Mechanical behavior of piston rod point-supported flexible buffer system", China Civil Engineering Journal, 11, 61-69, 2018. (in Chinese)

[10] Wang R., Han L.H. and Hou C.C., "Behavior of concrete filled steel tubular (CFST) members under lateral impact: Experiment and FEA model", Journal of Constructional Steel Research, 80(1), 188–201, 2013.

[11] Cotsovos D.M., "A simplified approach for assessing the load-carrying capacity of reinforced concrete beams under concentrated load applied at high rates", International Journal of Impact Engineering, 37(8), 907-917, 2010.

[12] Saatci S. and Vecchio F.J., "Effects of shear mechanisms on impact behavior of reinforced concrete beams", ACI Structural Journal, 106(1), 78-86, 2009.

[13] Pham T.M. and Hao H., "Prediction of the impact force on reinforced concrete beams from a drop weight", Advances in Structural Engineering, 19(11), 1710-1722, 2016.

[14] Lee E.H. and Symonds P.S., "Large plastic deformations of beam under transverse impact", Journal of Applied Mechanics-Transactions of the ASME, 19(3), 308-314, 1952.

[15] Parkes E.W., "The permanent deformation of a cantilever struck transversely at its tip", Proceedings of the Royal Society of London. Series A. Mathematical and Physical Sciences, 228(1175), 462-476,1955.

[16] Parkes E.W., "The permanent deformation of an encastre beam struck transversely at any point in its span", Proceedings of the Institution of Civil Engineers, 10(3), 277-304, 1958.

[17] Pham T.M. and Hao H., "Effect of the plastic hinge and boundary conditions on the impact behavior of reinforced concrete beams", International Journal of Impact Engineering, 102, 74-85, 2017.

[18] Pham T.M. and Hao H., "Plastic hinges and inertia forces in RC beams under impact loads", International Journal of Impact Engineering, 103, 1-11, 2017.

[19] Liu S.W., Liu Y.P. and Chan S.L., "Advanced analysis of hybrid steel and concrete frames: Part 1: Cross-section analysis technique and second-order analysis", Journal of Constructional Steel Research, 70, 326-336, 2012.

[20] Liu S.W., Chan T.M., Chan S.L. and So D. K. L., "Direct analysis of high-strength concrete-filled-tubular columns with circular & octagonal sections", Journal of Constructional Steel Research, 129, 301-314, 2017.

[21] Yang C., Yu Z. X. and Sun Y.P., "Axial residual capacity of circular concrete-filled steel tube stub columns considering local buckling", Advanced Steel Construction, 14(3), 496-513, 2018.

[22] Du Z.L., Liu Y.P., He J.W. and Chan S. L., "Direct analysis method for noncompact and slender concrete-filled steel tube members", Thin-Walled Structures, 135, 173-184, 2019.

[23] Aghdamy S., Thambiratnam D.P., Dhanasekar M. and Saiedi S., "Computer analysis of impact behavior of concrete filled steel tube columns", Advances in Engineering Software, 89, 52-63, 2015.

[24] Aghdamy S., Thambiratnam D.P., Dhanasekar M. and Saiedi S., "Effects of structure-related parameters on the response of concrete-filled double-skin steel tube columns to lateral impact", Thin-Walled Structures, 108, 351-368, 2016.

[25] Yousuf M., Uy B., Tao Z. and Remennikov A., "Transverse impact resistance of hollow and concrete filled stainless steel columns", Journal of Constructional Steel Research, 82, 177-189, 2013.

[26] Yousuf M., Uy B., Tao Z., Remennikov A. and Liew J. R., "Impact behaviour of pre-compressed hollow and concrete filled mild and stainless steel columns", Journal of Constructional Steel Research, 96, 54-68, 2014.

[27] Qu H.Y., Li G., Chen S., Sun J. and Sozen M. A., "Analysis of circular concrete-filled steel tube specimen under lateral impact", Advances in Structural Engineering, 14(5), 941-952, 2011.

[28] Deng Y. and Tuan C.Y., "Design of concrete-filled circular steel tubes under lateral impact", ACI Structural Journal, 110(4), 691-701, 2013.

[29] Bambach M.R., "Design of hollow and concrete filled steel and stainless steel tubular columns for transverse impact loads", Thin-Walled Structures, 49(10), 1251-1260, 2011.

[30] Shakir A.S., Guan Z.W. and Jones S.W., "Lateral impact response of the concrete filled steel tube columns with and without CFRP strengthening", Engineering Structures, 116, 148-162, 2016.

[31] Wang Y., Qian X., Liew J.Y.R. and Zhang, M. H., "Impact of cement composite filled steel tubes: An experimental, numerical and theoretical treatise", Thin-Walled Structures, 87(1), 76-88, 2015.

[32] European Committee for Standardization (CEN)., Eurocode 1: Actions on structures, part 1-7: General actions -Accidental actions, London, UK, 2006.

[33] Hallquist J.O., LS-DYNA keyword user manual-nonlinear dynamic analysis of structures, Livermore Software Technology Corporation, Livermore, CA, 2006.

[34] Malvar L.J., Crawford J.E., Wesevich J.W. and Simons D., "A plasticity concrete material model for DYNA3D", International Journal of Impact Engineering, 19(9-10), 847–873, 1997.

[35] Cowper G.R. and Symonds P.S., Strain-hardening and strain-rate effects in the impact loading of cantilever beams, Brown Univ, Providence Ri, 1957.

[36] Comité Euro-International du Béton., CEB-FIP Model Code 1990, Redwood Books, Trowbridge, Wiltshire, UK, 1993.

[37] Jones N., Structural impact, Cambridge University Press, 1997.

[38] Popov V.L., Contact Mechanics and Friction, Springer Berlin Heidelberg, Berlin,2010.

[39] Richart F.E., Brandtzaeg A. and Brown R.L., A study of the failure of concrete under combined compressive stresses, University of Illinois, Engineering Experimental Station, Bulletin, 1928.

[40] Ansari F. and Li Q., "High-strength concrete subjected to triaxial compression", ACI Materials Journal, 95(6), 747-755, 1998.

[41] Meyers M.A., Dynamic Behavior of Materials, John wiley & sons, New York, 1994.

[42] Architectural Institute of Japan (AIJ)., Recommendations for design and construction of concrete filled steel tubular structures, Tokyo, Japan, 1997.

[43] Han L.H., "Flexural behaviour of concrete-filled steel tubes", Journal of Constructional Steel Research, 60(2), 313-337, 2004.

Advanced Steel Construction – Vol. 15 No. 4 (2019) 338–348
DOI:10.18057/IJASC.2019.15.4.5

TENSILE FORCE AND BENDING MOMENT DEMANDS ON HEADED STUD FOR THE DESIGN OF COMPOSITE STEEL PLATE SHEAR WALL

Yi Qi [1, 2, *], Qiang Gu [1], Guo-hua Sun [1], Bao-cheng Zhao[1] and Hua-fei Wang[3]

[1] *School of Civil Engineering, Suzhou University of Science and Technology, Suzhou, China*
[2] *Jiangsu Province Key Laboratory of Structure Engineering, Suzhou University of Science and Technology, Suzhou, China*
[3] *College of Civil and Transportation Engineering, Hohai University, Nanjing 210098, China*
** (Corresponding author: E-mail: qiyi7711@126.com)*

ABSTRACT

The composite steel plate shear wall (C-SPW), composed of infill steel plate and reinforced concrete encasements, is widely used as a lateral load resisting system in high-rise buildings. The reinforced concrete encasement is connected to one or both sides of the infill steel plate using headed studs. Previous investigations have mainly focused on the seismic behaviour of C-SPWs and the bending failure of the connector, as explored in some experimental studies, are found before C-SPW achieve its target drift ratio. However, the behaviour of the headed stud, which plays an important role in the performance of C-SPWs, has been largely neglected. In this paper, a study of the tensile force and bending moment demands on headed studs in the design of C-SPWs is performed by using the finite element method. As the theoretical basis, the development, distribution and formation mechanisms of stud tension and bending moment are analysed. The effects of the headed stud diameter, number of headed studs, infill steel plate thickness, concrete panel thickness and panel aspect ratio on the stud performance are investigated. Based on this, available formulas for the tension and bending moment demands on headed studs in the design of C-SPWs are proposed.

ARTICLE HISTORY

Received: 8 October 2018
Revised: 01 May 2019
Accepted: 13 June 2019

KEYWORDS

composite steel plate shear wall;
stud tension;
stud bending moment;
finite element analysis;
nonlinear buckling

1. Introduction

Composite steel plate shear walls (C-SPWs), which incorporate significant ductility, stiffness and energy dissipation capacity, are widely used as lateral load resisting systems in structural designs. In C-SPWs, the reinforced concrete encasement attached to one or both sides of the infill steel plate using headed studs is required to prevent the infill steel plate from buckling before yielding. As a result, the desired load-resisting mechanism of shear yielding in the infill steel plate can be realized. In cases of large story drift, infill steel plate elasto-plastic buckling behaviour may occur. Tension and bending of the headed studs become evident resulting from the relative out-of-plane deformation experienced between the infill steel plate and concrete encasements. To meet the expected ductility, shear resistance and energy dissipation of C-SPWs in instances of earthquake, the tensile force and bending moment demands on the headed studs in the design of C-SPWs are important issues that must be thoroughly explored. However, of the many available studies on C-SPWs, most focus on its seismic behaviour, with some experimental works finding that the correlative failure of connectors between the infill steel plate and concrete encasement occurs before the C-SPW reaches its expected drift ratio. In contrast, studies of the headed stud for the design of C-SPWs have not yet been undertaken.

One study of stud tension was proposed by Zhao and Astaneh-Asl [1, 2], where the headed stud was required to resist a tensile force induced by elasto-plastic local buckling of an infill steel plate. The test results of a one-story C-SPW captured by Arabzade et al. revealed that some of the bolts used to connect the concrete panel to the infill steel plate failed due to shear and bending resulting from inelastic buckling of the infill steel plate [3]. In an experimental investigation of C-SPWs with light-weight concrete panel bolted to the steel plate, Rassouli et al. reported significant bolt bending after inelastic local buckling of the steel plate [4]. AISC 341-10 contains several provisions for the design of C-SPWs: the minimum concrete panel thickness must be 100 mm when a concrete panel is provided on both sides of the steel plate and, otherwise, must be 200 mm when a concrete panel is provided on only one side of the steel plate; in addition, the reinforcement ratio in both directions shall not be less than 0.25% [5].

Studies on the effects of design parameters on the seismic behaviour of C-SPWs have also been reported. Rahai and Hatami, Shafaei et al. and Rahnavard et al. performed numerical or experimental studies on the effects of important design parameters (e.g., stud spacing, concrete panel thickness, etc.) on the seismic behaviour (e.g., maximum lateral resistance, out-of-plane displacement of the steel plate, maximum interstory drift, energy dissipation, etc.) of C-SPWs [6-8]. Dey and Bhowmick investigated the contributions of the infill steel plate, concrete panels and boundary columns to lateral resistance using nonlinear numerical analysis [9]. Using the Rayleigh-Ritz method, Smith et al. [10] and Arabzade et al. [11] proposed the local buckling coefficient for a unilaterally constrained rectangular plate under pure shear.

Various improvements to the structural elements in C-SPWs have been explored by researchers. An experimental study of the C-SPW in a composite frame under cyclic loading was conducted by Guo et al. [12]. A buckling-restrained steel plate shear wall (BR-SPW) was tested by Guo and Dong [13, 14]. A comparison between the seismic behaviours of BR-SPWs and C-SPWs were made. A novel BR-SPW with inclined slots in the infill steel plate was theoretically and numerically analysed by Jin and Ou et al. [15]. A novel partially connected BR-SPW was theoretically and experimentally investigated by Wei et al. [16]. Compared to the traditional C-SPW, the aforementioned studies demonstrated that the corresponding improvements were beneficial to the structure's performance.

Few studies have explored the bearing capacity of headed studs in composite structures. Pallarés et al. comprehensively investigated the bearing capacity of headed studs under tension and combined tension and shear [17]. Lin et al. experimentally and numerically studied the behaviour of headed stud connections between concrete slabs and steel girders subjected to transverse bending moments [18]. The nominal tensile strengths of headed studs in composite structures are specified in ACI 318-11 [19], ACI 349-06 [20] and PCI 6th Edition [21].

Having a vital role to play in the behaviour of C-SPWs, the resistance demand on a headed stud should thus be treated as an important issue in the C-SPW design. The shear force demand on a headed stud and the concrete panel thickness demand for the design of C-SPWs was addressed previously by the authors [22, 23]. To date, however, there have been few studies of the tension or bending of headed studs due to the buckling of steel plates in the inelastic range of C-SPWs following the available design provisions or recommendations. In this paper, an investigation of the tensile force and bending moment demands on studs in seismic design of C-SPWs is conducted using the finite element method. This C-SPW consists of infill steel plate, cast-in-place reinforced concrete encasements with equal thickness on both sides of the steel plate as well as headed studs anchoring the concrete encasements to the steel plate. A validated finite element model incorporating an effective C-SPW behaviour prediction is established using ABAQUS /Standard [24]. Utilizing this validated finite element model, specific results regarding the nonlinear responses of headed studs in a C-SPW design under lateral loading are achieved. The finite element analyses are conducted for 27 specimens under monotonic lateral loadings with five variable design parameters including concrete panel thickness, infill steel plate thickness, panel aspect ratio (the ratio of the panel height to width) as well as the number of studs. The formation mechanisms of stud tension and bending moment are studied based on the interaction of the headed studs, infill steel plate and concrete panels, and the development and distribution of stud tension and bending moment are analysed. Fitting the collected tensile force and bending moment values of the headed studs when the drift ratios of C-SPWs reach 2.5%, available formulas for the tension and bending moment demands on headed studs in the design of C-SPW are proposed, respectively.

2. Finite element model of C-SPW

In the seismic design of this lateral load resisting system, which consists of a C-SPW and a boundary steel frame, the system is treated as C-SPWs entailing columns and beams, which are taken as a web plate, flange and stiffeners of a cantilever beam, respectively. Hence, the C-SPW undergoes shear deformation. To investigate the behaviours of headed studs in a C-SPW under shear loading, an in-plane shear load is applied to the infill steel plate, and a steel frame is introduced to the C-SPW to provide a boundary restriction without lateral resistance. In the finite element model (FEM) of the C-SPW, its boundary frame remains elastic with a hinged beam-column connection and simply supported base. Next, a monotonic lateral displacement is applied to the top beam. A finite element model of the C-SPW established using ABAQUS, which enables the inclusion of a hinged boundary frame and effectively takes into account the interactions between the infill steel plate, concrete panels, boundary frame and headed studs, as previously proposed and validated by the authors [22]. This FEM is employed to investigate the tensile force and bending moment on headed studs in this paper. The C-SPW evaluated here is characterized by cast-in-place reinforced concrete encasements attached to both sides of an infill steel plate, no gap between the concrete edges and a hinged single-bay one-story boundary steel frame. It should be mentioned that to avoid repetition, details regarding the element types, constitutive relationships governing materials, boundary conditions and validation of the FEM that can be found in [22] and are otherwise omitted here. The material properties as well as the interactions between finite elements are summarized below.

The plastic damage model, derived from Lubiner et al. [25] and Lee et al. [26], is utilized to depict the behaviour of the concrete material. The perfect elasto-plastic model is employed to model the constitutive relationships of the infill steel plate and reinforcing bar. The constitutive relationship of the headed stud is characterized by a bilinear hardening model with a hardening stiffness assumed to be 2% of the elastic stiffness. The material property of the boundary steel frame is assumed to maintain its elasticity in the finite element analysis.

Element types that include the infill steel plate, concrete panel, headed stud and reinforcing bar were reported in either prior finite element models of the C-SPW [8, 9] or steel-plate composite shear wall [27-29], which has a similar construction to that of the C-SPW. Herein, a 4-node reduced integration shell element (S4R) is utilized to model the infill steel plate; an 8-node reduced integration solid element (C3D8R) is utilized to model the concrete panel; a 2-node linear beam element (B31) is utilized to model the headed stud; and a truss element (T3D2) is utilized to model the reinforcing bar. The boundary frame is simulated by coupling the shell element S4R to the beam element B31, where B31 enables the interaction between the boundary frame and infill steel plate and S4R enables the interaction between the boundary steel flanges and concrete panels. Because the steel frame provides elastic boundary restriction but no lateral stiffness to the C-SPW, tying its shell elements to the centroidal axis of the beam elements only slightly influences the inertia moment of the beam cross section as well as the axial force capacities of the beams and columns, thereby having no effect on the performance of the C-SPW.

The bonding action between the steel plate and cast-in-place concrete is commonly assumed to have a coefficient of friction [8, 29-31]. To model this bond action more practically, nonlinear spring elements (SPRING2) are adopted. A "hard" contact relationship without a friction effect is employed between the edges of the concrete panels and boundary steel flanges. The welded and embedded connections are realized by coupling all degrees of freedom of the overlap nodes.

Following the design provisions and recommendations of C-SPWs [1,2,5], five groups comprising 27 FEM specimens are established and analysed. The invariant information pertaining to each specimen is described in the following. The cross sections of the beams and columns are W530×219 and W360×818, respectively. The nominal yield strength and ultimate strength of the headed studs are 240 MPa and 400 MPa, respectively. For the infill steel plate, Young's modulus is 206 GPa; Poisson's ratio is 0.3; the nominal yield strength is 235 MPa; and the height h is set as 3000 mm. For the concrete panel, the cubic nominal tensile strength and cubic nominal compressive strength of concrete are taken as 2.01 MPa and 20.1 MPa, respectively; Young's modulus is taken as 30 GPa; Poisson's ratio is 0.2; the reinforcement ratio is 0.75%; and the nominal yield strength of the reinforcing bar is 300 MPa.

In order to make the parametric study comprehensive, the design parameters are allowed to vary beyond the relevant requirements or recommendations. These variable parameters are listed in Table 1, where d_{st} is the stud diameter; t_s is the infill steel plate thickness; t_c is the overall thickness of the concrete panels (the thickness of the concrete plate on each side is the same); the panel aspect ratio, defined as the ratio of the height h to width l of the shear wall, is denoted as α; and the number of headed studs on one side of the infill steel plate is represented as $n_x \times n_y$, where n_x and n_y are the number of stud columns and rows, respectively. The stud diameters are taken as 16 mm and 22 mm. Infill steel plate thicknesses of 10 mm, 15 mm and 20 mm are used. The overall concrete panel thicknesses that enable infill steel plate buckling in the inelastic range are set as 100 mm, 140 mm and 200 mm. The stud spacings, calculated as $s_{st} = l/n_x = h/n_y$, which are able to prevent local buckling of the infill steel plate are set as 750 mm, 600 mm, 500 mm and 300 mm. Representative aspect ratios (the ratios of height to width) of one-story shear walls in engineering practice are considered to be 1.0 and 0.5.

3. The behaviour of the structural elements

The behaviour of the structural elements of specimen N5-B under lateral loading is analysed to provide a mechanistic study of the tensile force and bending moment of the headed stud. The shear force developments in the C-SPW, infill steel plate and concrete panel are illustrated to analyze the performance of these members in the pre- and post-buckling of infill steel plate as well as the drift ratio corresponding to the onset of elasto-plastic bucking of the infill steel plate. It should be noted that the interaction between the infill steel plate, concrete panels and headed studs was presented in detail by the authors in [22]. Due to space limitations, this investigation focuses on the post-buckling phase. After infill steel plate buckling, the stud responses are governed by tension and bending, which results from the large relative out-of-plane deformation between the infill steel plate and concrete panels. The developments of stud tension and bending moment are analysed, allowing the critical drift ratio and critical stud locations to be obtained. The distributions of the tensile forces and bending moments in the stud group are plotted using vectors, in which the transfer mechanics of the tension and bending moment in the stud can be deduced based on the correlative responses of the infill steel plate and concrete panels.

The location of the headed stud is represented by HS-*i*-*j*-A or HS-*i*-*j*-B, where i is the numbering of the stud column from left to right; j is the numbering of the stud row from top to bottom; "A" is the side of the infill steel plate in the positive direction of the Z-axis and "B" is the other side.

3.1. Development of shear force and deformation

The shear force-drift ratio curves of specimen N5-B are shown in Fig. 1, where V, V_s and V_c are the shear forces of the C-SPW, infill steel plate and concrete panel, respectively. It can be observed that the shear force developments of the C-SPW and steel plate are divided into two phases, i.e., the pre- and post-buckling phases. The lateral resistance of the C-SPW is primarily governed by the infill steel plate. In pre-buckling, both elastic and yielding phases of the infill steel plate are involved. In the elastic phase, all curves ascend linearly, and the maximum shear force of the concrete panel appears, while the infill steel plate remains elastic. In the yielding phase, the shear force-drift ratio curve of the C-SPW, V-θ, reaches the maximum value V_y =6660.7 kN, and then slowly declines; a plateau develops in the V_s-θ curve as shear yield occurs in the infill steel plate; and the V_c-θ curve gradually declines resulting from significant degradation of the concrete. In the post-buckling phase, the V-θ and Vs-θ curves sharply drop due to the inelastic buckling of the infill steel plate; then, the rate of decrease of both curves tends to decrease due to the lateral resistance of the diagonal tension field in the infill steel plate. The critical drift ratio, denoted as θ_b, is 1.36%.

The out-of-plane deflection development of the infill steel plate is illustrated in Fig. 2. The curve of steel plate deflection-drift ratio, D_{sp}-θ, is minimal in the pre-buckling phase; after the onset of buckling in the infill steel plate, the deflection suddenly ascends, followed by gradual slowing of this increasing trend. This remarkable increase in the deflection behaviour is triggered by buckling of the infill steel plate. Owing to the restraint from the concrete panels, the increasing trend is abated. The beginning of the increase in deflection corresponds with the decrease of the shear forces in the C-SPW and infill steel plate, which demonstrates that the critical drift ratio θ_b occurs at the commencement of infill steel plate buckling.

Table 1
Finite element specimen details.

Groups	Specimens	d_{st}（mm）	$n_x \times n_y$	t_s（mm）	t_c（mm）	α
N4	N4-B	16	4×4	15	140	1
	N4-D22	22	4×4	15	140	1
	N4-TS10	16	4×4	10	140	1
	N4-TS20	16	4×4	20	140	1
	N4-TC50	16	4×4	15	100	1
	N4-TC100	16	4×4	15	200	1
N5	N5-B	16	5×5	15	140	1
	N5-D22	22	5×5	15	140	1
	N5-TS10	16	5×5	10	140	1
	N5-TS20	16	5×5	20	140	1
	N5-TC50	16	5×5	15	100	1
	N5-TC100	16	5×5	15	200	1
N6	N6-B	16	6×6	15	140	1
	N6-D22	22	6×6	15	140	1
	N6-TS10	16	6×6	10	140	1
	N6-TS20	16	6×6	20	140	1
	N6-TC50	16	6×6	15	100	1
	N6-TC100	16	6×6	15	200	1
N10	N10-B	16	10×10	15	140	1
	N10-D22	22	10×10	15	140	1
	N10-TS10	16	10×10	10	140	1
	N10-TS20	16	10×10	20	140	1
	N10-TC50	16	10×10	15	100	1
	N10-TC100	16	10×10	15	200	1
L6	L6-B	16	5×10	15	140	0.5
	L6-TS10	16	5×10	15	140	0.5
	L6-TS20	16	5×10	15	140	0.5

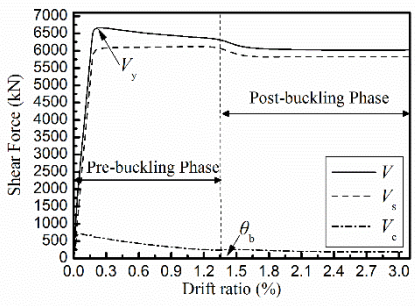

Fig. 1 Shear force-drift ratio curves of N5-B

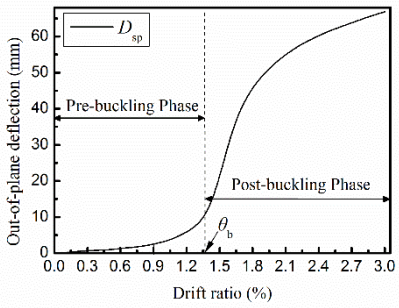

Fig. 2 Infill steel plate deflection-drift ratio curve of N5-B

3.2. Developments of tension and bending moment in the stud

In this section, the tensile force- and bending moment-drift ratio relationships of the representative studs in N5-B are analysed. The effects of design parameters on the stud tension and bending moment are discussed in the next chapter. As shown in Fig. 3, it is observed that the curves of HS-1-5-B and HS-5-1-B exhibit small peak values in the pre-buckling phase, which indicates that the infill steel plate and concrete panels have begun to separate at the wall corners. At the critical drift ratio θ_b =1.36%, the curves start to increase due to buckling of the infill steel plate. The increase of this curve in the post-buckling phase of the steel plate is divided into two stages, where the first is defined as Increase Stage 1 exhibiting a rapid rate of increase, and the second is defined as Increase Stage 2 incorporating a relatively slow rate of increase. This pattern has correspondence with the out-of-plane deflection of the infill steel plate. The tensile forces of critical tensile studs are almost identical.

As shown in Fig. 4, the representative bending studs in N5-B exhibit similar development patterns. In the pre-buckling phase, small peak values are found in some of the curves, resulting from relative in-plane shear deformation between the infill steel plate and concrete panels. At the critical drift ratio θ_b =1.36%, the curves start to rise. Two stages are observed in the post-buckling phase, as illustrated in Fig. 4. In the Increase Stage, the stud bending moments increase linearly. In the Plateau Stage, the curve holds approximately constant, and the curve appears to plateau. The bending moments of the critical bending studs are almost identical.

It can be concluded that the tension and bending moment stud becomes evident in the post-buckling phase. The critical drift ratio θ_b can be determined from the second inflection point in the stud tension- and bending moment-drift

ratio curves. The locations of the critical stud with relatively large tensile forces and bending moments are accordingly recorded according to these curves. The relationship between the locations of the critical studs and buckling half-wave of the infill steel plate are discussed below.

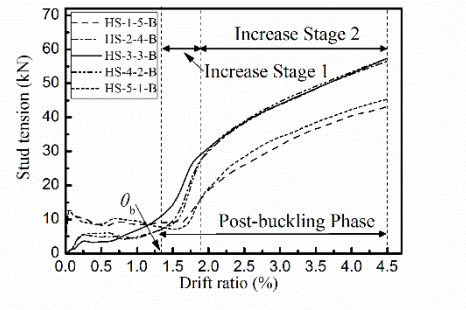

Fig. 3 Stud tension developments of N5-B

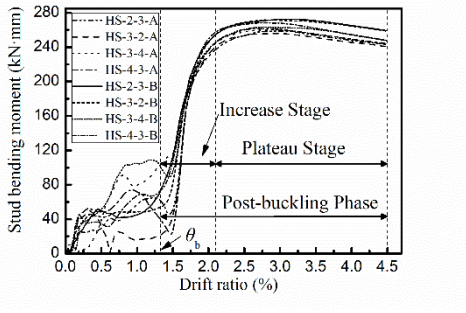

Fig. 4 Stud bending moment developments of N5-B

3.3. Distributions of stud tension and bending moment

The buckling mode of the infill steel plate and the distributions of stud tension and bending moment are illustrated in Figs. 5 and 6, respectively. These distributions are displayed using vectors, where the direction of the stud bending moment transferred through the concrete panel is defined by the right-hand rule (bending moments of studs on the "A" side of the infill steel plate are displayed representatively). As shown in Fig. 5, a single buckling half-wavelength of the steel plate develops approximately along the 45° direction, which results from the principal compressive stress. A global inelastic buckling takes place in the infill steel plate. According to the numbering of the headed studs plotted in Fig. 5 and referring to the curves in Figs. 3 and 4 illustrating the representative studs with relatively large tensile forces and bending moments, it is known that the critical tensile studs are concentrated in the middle of the buckling half-wave on the one side of the infill steel plate; the critical bending studs are at the boundary of buckling half-wave on both sides of the infill steel plate. These tensile forces on the "B" side and bending moments on the "A" side at the drift ratio of 3.3% are expressed using vectors in Fig. 6. The magnitudes of the vectors indicate that the tensile forces and bending moments of the critical studs have almost identical values, respectively. The direction of stud tension is in contrast to that of the out-of-plane displacement of the infill steel plate in the middle of the buckling half-wave. The direction of the stud bending moment is contrary to that of the out-of-plane rotation of the infill steel plate at the boundary of the buckling half-wave. The bending studs at each end of the buckling half-wave have directions consistent with reverse moments.

The relevant interactions between the headed studs, infill steel plate and concrete panels after the global inelastic buckling of the infill steel plate can therefore be deduced from Figs. 7. As displayed in Fig. 7 (a), the tensile force in the headed stud transferred through the concrete panel on side "B" at the peak of the buckling half-wave is the largest, resulting from the significant out-of-plane displacement of the infill steel plate. As displayed in Fig. 7 (b), the bending moments of the headed studs transferred through the concrete panel on both sides at the boundary of the buckling half-wave are the largest due to the relatively significant out-of-plane rotation of the infill steel plate at the same location. It is important to note that at the location of the critical tensile stud, i.e., the peak of the half-wave, the bending moment transfer is tiny attributed to the insufficient rotation; in contrast, at the location of the critical bending stud, i.e., the boundary of the half-wave, the tensile force transfer is weak owing to the slight displacement. Consequently, the coupling effects of the tensile force and bending moment of the headed stud can be neglected, and studies of the stud tension and bending moment in C-SPW design can be performed independently.

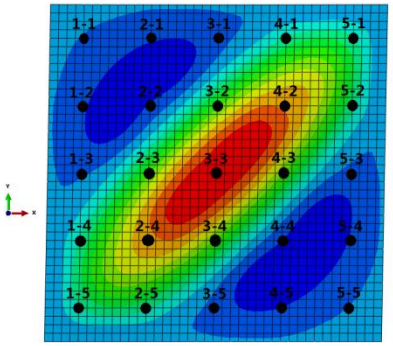

Fig. 5 Out-of-plane deformation of N5-B

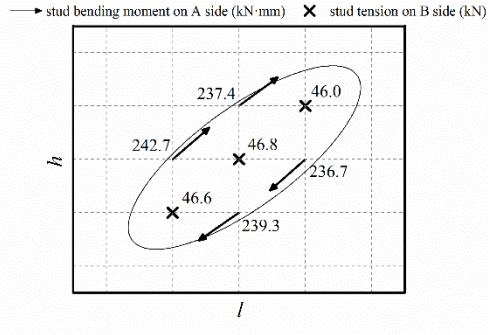

Fig. 6 Distributions of stud tension and bending moment in N5-B

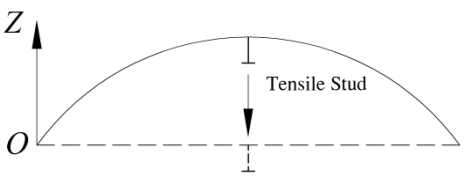

(a) Tensile stud

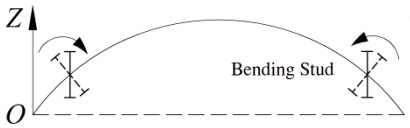

(b) Bending studs

Fig. 7 Schematics of tensile and bending studs

4. Parametric study on tensile force and bending moment of stud

The effects of stud diameter, number of headed studs, steel plate thickness, concrete panel thickness and panel aspect ratio on the stud tension and bending moment are analysed, respectively. Since the tensile forces and bending moments in the critical studs are almost identical, the tensile force and bending

moment developments in the headed studs are analysed using the largest results for each case individually. The development stages as well as the maximums of stud tension and bending moment corresponding to the drift ratio of 2.5%, which is the limitation required by ASCE [32], are recorded for formula fitting. The relationships between the internal force of the infill steel plate and the tensile force and bending moment of the headed stud are established to provide the embryonic forms of the final proposed formulas.

4.1. Parameter analysis on stud tension

Stud tension-drift ratio curves are shown in Figs. 8. It is observed that the onset of tensile force development is determined by the critical drift ratio corresponding to the inelastic buckling of the infill steel plate, which is reflected at the second inflection point of each curve. All curves exhibit the same development pattern including the stage before increasing, i.e., the pre-buckling phase of the C-SPW, Increase Stage 1 and Increase Stage 2, referring to Fig. 3. Stud tension is small in the pre-buckling phase; Increase Stage 1 exists transitorily, where the tensile force rapidly increases; and in Increase Stage 2, the rate of increase of the tensile force tends to be slow.

It follows from Fig. 8 that the critical drift ratio increases with the increment of the steel plate thickness, stud spacing and panel aspect ratio as well as with the reduction of the concrete panel thickness. In Increase Stage 1, the stud tension increases with the increment of the panel aspect ratio, the stud spacing and the ratio of infill steel plate thickness to concrete panel thickness. The curve shapes in Increase Stage 2 are approximately straight lines, where the slope increases with the increment of the infill steel plate thickness, panel aspect ratio and stud spacing. Throughout the entire developmental trend, stud tension is independent of stud diameter.

At a certain drift ratio, the magnitude of stud tension depends on three factors: the critical drift ratio corresponding to the beginning of infill steel plate buckling, the development stage where the tensile force is located and the slope of the tensile force-drift ratio curve, i.e., the rate of increase of the tensile force. As a result, the formula for the maximum stud tension when the drift ratio reaches 2.5% can be fitted based on the results of the parameter analysis presented here.

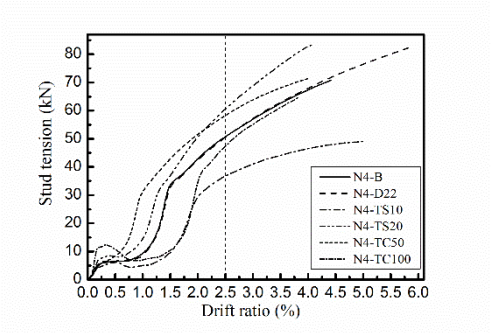

(a) N4 Group

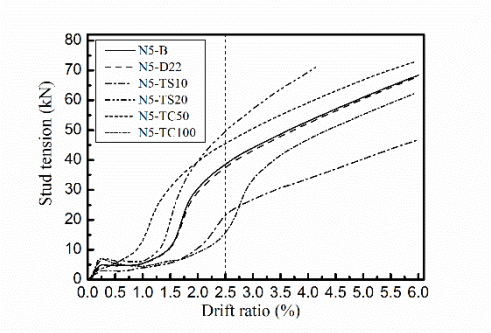

(b) N5 Group

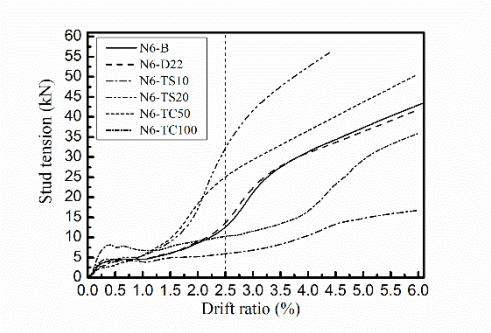

(c) N6 Group

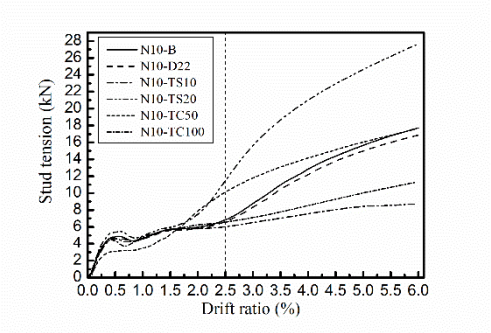

(d) N10 Group

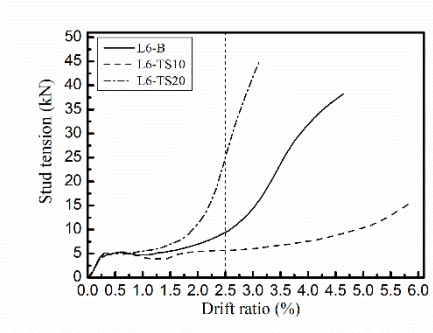

(e) L6 Group

Fig. 8 Tensile force developments of studs

4.2. Parameter analysis on stud bending moment

Stud bending moment-drift ratio curves are illustrated in Figs. 9. The bending moment developments commence at the second inflection points in the curves associated with the buckling of the infill steel plate. All curves exhibit the same development pattern including the stage before infill steel plate buckling, the Increase Stage and the Plateau Stage, as presented in Fig. 4. The stud bending moment is relatively small in the stage before infill steel plate buckling; in the Increase Stage, the stud bending moment increases linearly; and in the Plateau Stage, the curve reaches its maximum and then continues at an approximately constant value.

The commencement of bending moment development corresponds with the onset of tensile force. For the Increase Stage, increasing the infill steel plate thickness, stud spacing, stud diameter and panel aspect ratio and reducing the

concrete panel thickness increase the slope of this curve. It should be noted that the stud diameter and stud length that varies with concrete thickness have correlation with stud bending stiffness which also affects the curve slope. For the Plateau Stage, the maximum value of stud bending moment that can be achieved is largely due to the stud diameter and infill steel plate thickness. In the same specimen group, it can be observed from the curves that the maximum stud bending moments of specimens with an infill steel plate thickness of 10 mm are smaller and the maximum stud bending moments of specimens with a stud diameter of 22 mm are larger, whereas the stud spacing, concrete panel thickness and panel aspect ratio only slightly affect the stud bending moment.

Developing the same conclusion as that for stud tensile force, the stud bending moment at a certain drift ratio is determined by the critical drift ratio, the development stage as well as the slope of the curve. The formula for the maximum stud bending moment when the drift ratio reaches 2.5% can be fitted based on the pertinent parameter analysis results above.

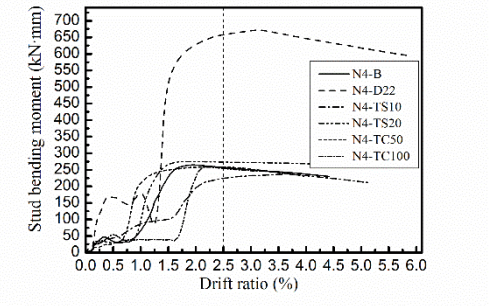

(a) N4 Group

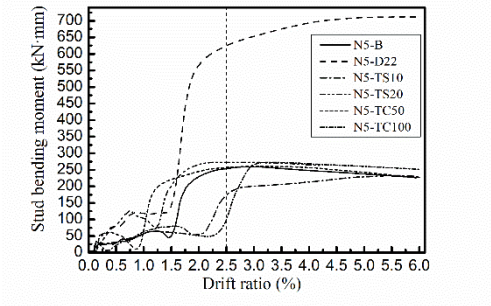

(b) N5 Group

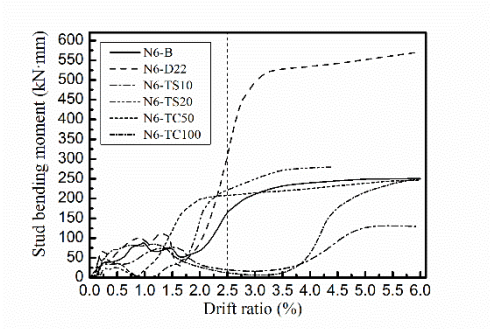

(c) N6 Group

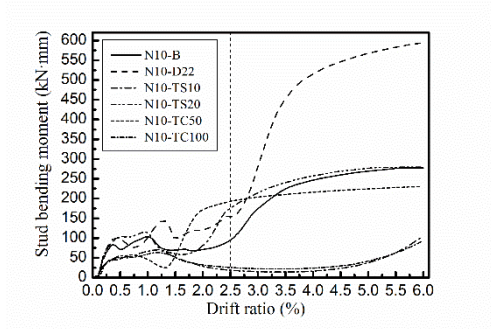

(d) N10 Group

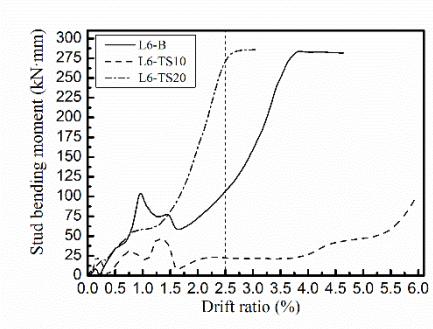

(e) L6 Group

Fig. 9 Bending moment developments of studs

4.3. Interaction between headed stud and infill steel plate

The interaction between the headed stud and infill steel plate in the post-buckling phase is investigated utilizing the vectors of stud tension and bending moment as well as the out-of-plane deformation of the infill steel plate. The finite element analysis results reveal that the stud tension and bending moment exhibit the same distribution pattern indicating that the critical tensile studs are concentrated in the middle of the buckling half-wave of the infill steel plate while the critical bending studs reside at the boundary. However, as the number of studs or panel aspect ratio is varied, the locations and the number of critical studs differ. To illustrate the relationship between the buckling half-wave of the steel plate and locations of the critical studs, representative specimens for the various groups are thus selected: N4-B, N6-B, N10-B and L6-B (analyses of specimen N5-B are presented in Section 3). Accounting for the different critical drift ratios of the specimens, the vectors of the critical headed stud and the out-of-plane deformation of the steel plate are displayed at a relatively large constant drift ratio of 4.0%.

As plotted in Figs. 10-13, the buckling modes imply that all specimens incur global inelastic buckling in the infill steel plate, in which L6-B is characterized by two buckling half-waves. Decreasing the stud spacing increases the buckling half-wavelength, thereby increasing the number of critical tensile and bending studs. The buckling half-waves of specimens N4-B, N6-B and N10-B with a panel aspect ratio of 1.0 incline approximately along the 45° direction, whereas the buckling half-waves in L6-B with a panel aspect ratio of 0.5 develop at a slightly smaller angle than 45°. This finding leads to a larger number of critical studs as the panel aspect ratio is reduced. The magnitudes of the tensile forces and bending moments of the critical studs within the buckling half-wave of the infill steel plate are relatively close to each other. The directions of the tensile forces and bending moments of the critical studs are contrary to that of the out-of-plane deformation of the infill steel plate. The coupling effect of the tensile force and bending moment of the assessed critical stud is minimal.

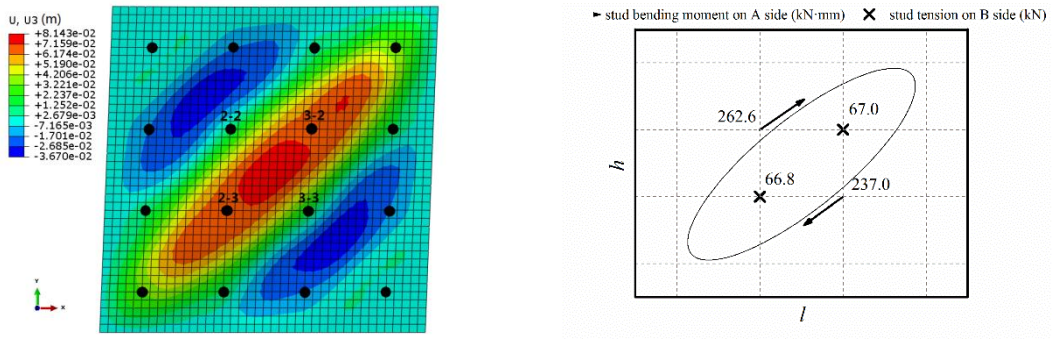

(a) Out-of-plane deformation of steel plate (b) Tensile forces and bending moments of studs

Fig. 10 Relationship between the critical studs and buckling half-wave of N4-B

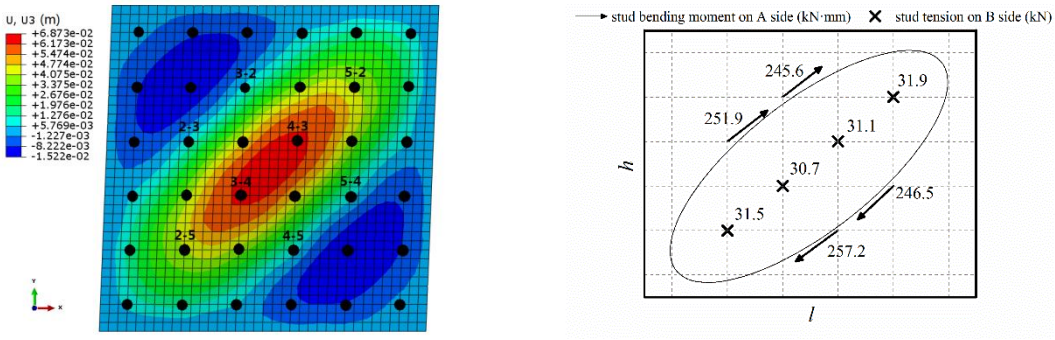

(a) Out-of-plane deformation of steel plate (b) Tensile forces and bending moments of studs

Fig. 11 Relationship between the critical studs and buckling half-wave of N6-B

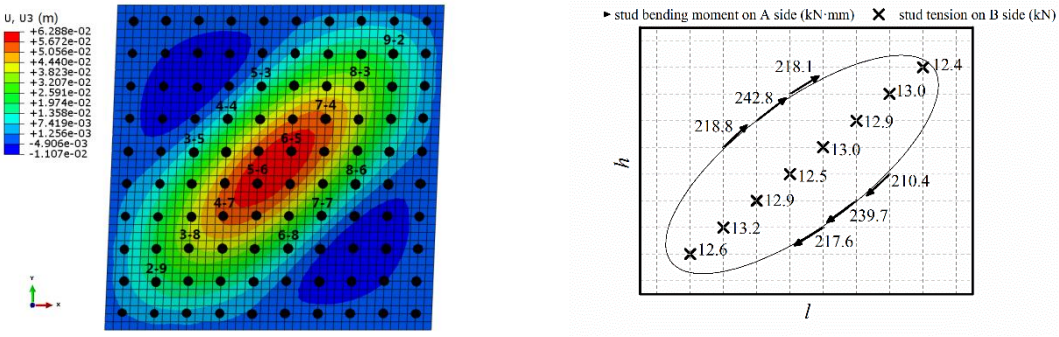

(a) Out-of-plane deformation of steel plate (b) Tensile forces and bending moments of studs

Fig. 12 Relationship between the critical studs and buckling half-wave of N10-B

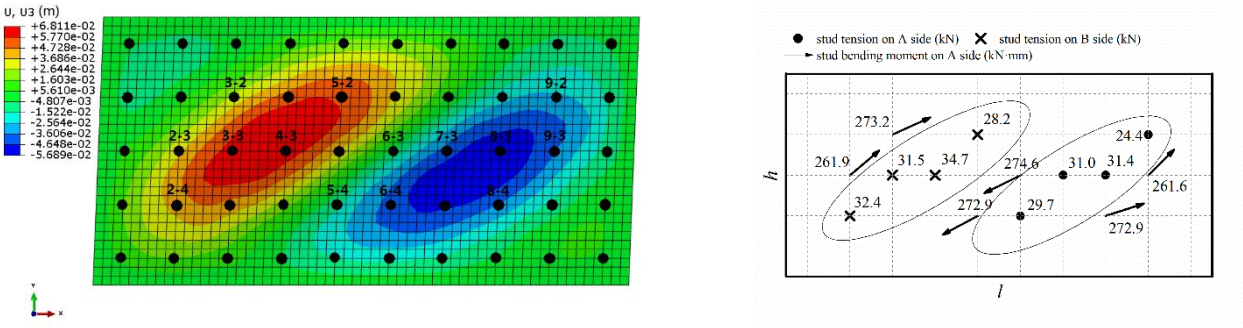

(a) Out-of-plane deformation of steel plate (b) Tensile forces and bending moments of studs

Fig. 13 Relationship between the critical studs and buckling half-wave of L6-B

According to the distribution of the critical tensile and bending studs analysed above, the interaction among structural elements after the onset of global inelastic buckling of the infill steel plate can be inferred. As shown in Fig. 14 (a), the critical tensile and bending studs are analysed in two independent plate strips of infill steel plate, respectively, where w is the half-wavelength (plate strip length), and s is the diagonal stud spacing along the 45° direction

(plate strip width). In one plate strip, one headed stud on a single side in the middle of the buckling half-wave is covered to analyze the tension in the stud. In another plate strip, four headed studs on both sides at the boundary of the buckling half-wave are covered to analyze the stud bending moment. The width of the assigned plate strip *s* reduces with the decrease of stud spacing and panel aspect ratio due to the different numbers of studs located in the buckling half-wave as well as the area in which the buckling half-wave develops.

The responses of headed studs after infill steel plate buckling in each plate strip are illustrated in Fig. 14 (b). Based on static equilibrium, the tensile force of stud F_b is determined by the transverse component of the axial forces at both ends of the analysed plate strip; the bending moments M_s at both ends of the plate strip cancel each other out. Because infill steel plate buckling occurs after shear yielding, this axial force can be deduced to be ηF_{sy}, where $F_{sy}= st_sf_{sy}$ is the axially yield strength of the plate strip (f_{sy} is the yield strength of the steel and t_s is the thickness of the steel plate or plate strip), and η is the proportion of F_{sy} that axial force achieves throughout the development of the buckling half-wave. Taking into account the effects of the stud spacing s_{st} and panel aspect ratio α on the plate strip width *s* as well as the axial force ηF_{sy} in direct proportion to its transverse component, the relationship between the tensile force in the stud after steel plate buckling and the internal force of the infill steel plate is established as Eq. (1), where F_b is the stud tension in kN; f_{sy} is the infill steel plate yield strength in MPa; t_s is the infill steel plate thickness in mm; s_{st} is the stud spacing in mm; α is the panel aspect ratio; and β_f is the dimensionless modification factors for tensile force demand on the headed stud, which is obtained by fitting the results from the finite element analysis.

$$F_b = \beta_f \alpha s_{st} t_s f_{sy} \times 10^{-3} \tag{1}$$

From Fig. 14 (b), it can be concluded that a bending stud is able to be equivalent to a cantilever beam with the analysed plate strip taken as its support, which limits the bending moment of the stud to half of the plastic bending strength of the steel plate strip (0.5 M_{sp}) after the inelastic buckling of the infill steel plate. The plastic bending strength of the steel plate strip is calculated as $M_{sp} =0.25st_s^2f_{sy}$. Accounting for the proportion between the stud bending moment M_b and 0.5 M_{sp} as well as the effects of stud spacing s_{st} and the panel aspect ratio α on the plate strip width *s*, a relationship between the stud bending moment and internal force of the infill steel plate is established as in Eq. (2), where M_b is the stud bending moment in kN·mm; f_{sy} is the infill steel plate yield strength in MPa; t_s is the infill steel plate thickness in mm; s_{st} is the stud spacing in mm; α is the panel aspect ratio; and β_m is the dimensionless modification factors for tensile force demand on the headed stud, which is obtained by fitting the results from the finite element analysis.

$$M_b = \frac{1}{4} \beta_m \alpha s_{st} t_s^2 f_{sy} \times 10^{-3} \tag{2}$$

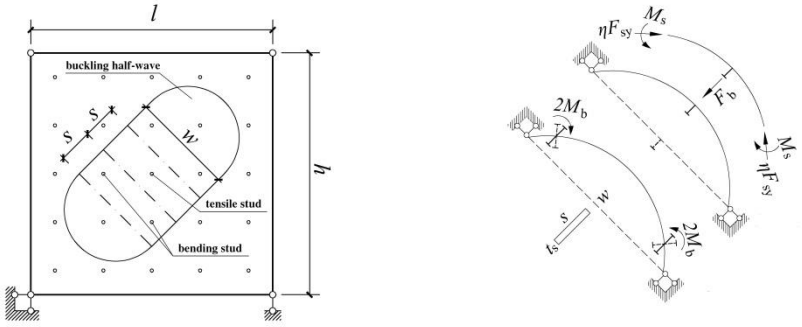

(a) Plane (b) Details

Fig. 14 Schematics of the interaction between stud and infill steel plate

5. Tensile force and bending moment demands on stud

The tensile force and bending moment demands on a stud are proposed following the criterion that the tensile or bending failure of a headed stud in a C-SPW shall not appear until the drift ratio achieves the drift limit of 2.5%. To propose the formulas for the demands on stud tension and bending moment in the design of the C-SPW, the established relationship between the internal forces of the headed stud and infill steel plate in the post-buckling phase is calibrated through fitting modification factors β_f and β_m according to the predicted relevant maximum values from finite element analysis up to the drift ratio of 2.5%. The predicted maximums of the tensile force and bending moment of the stud are denoted as F_{eb} and M_{eb}, respectively.

5.1. Formula for tensile force demand on stud

At the drift ratio of 2.5%, the development stage in which stud tension occurs varies. The earlier that the infill steel plate buckles, the greater the tensile force that develops in the stud. Based on the parametric study on the drift ratio of θ_b, referring to Fig. 8, and considering the extent of influence, the development stage is can be distinguished using Eq. (3), where δ is the dimensionless variable factor; t_s is the infill steel plate thickness; t_c is the concrete panel thickness; s_{st} is the stud spacing; and α is the panel aspect ratio. When δ ranges from 1.11 to 1.53, stud tension development is in the stage before Increase Stage 1; when δ ranges from 1.53 to 2.53, stud tension development is in the Increase Stage 1; and when δ ranges from 2.53 to 5.07, stud tension development is in the Increase Stage 2. The stage of development of stud tension and the corresponding variable factor δ are tabulated in Table 2.

$$\delta = t_s^{0.1} s_{st}^{0.9} \alpha^{0.25} / t_c \tag{3}$$

Substituting F_{eb} for F_b in Eq. (1) yields the modification factor β_f, as listed in Table 2. Because the slope of the stud tension-drift ratio curve is directly proportional to the stud spacing s_{st}, steel plate thickness t_s and panel aspect ratio α is reflected in Eq. (1), the factor β_f is introduced to deal with the influence of the critical drift ratio that determines the stage of development of stud tension. Hence, β_f can be converted into a function of δ and is linearly fitted as Eqs. (4) and (5) for the stage before Increase Stage 2 and Increase Stage 2, respectively.

$$\beta_f = 0.004 + 0.002\delta \quad 1.11 \le \delta < 2.53 \tag{4}$$

$$\beta_f = 0.003 + 0.009\delta \quad 2.53 \le \delta < 5.07 \tag{5}$$

Substituting β_f and Eq. (3) into Eq. (1), the formula for tensile force demand on stud F_b in kN is yielded as Eqs. (6) and (7), where α, f_{sy}, t_s, s_{st} and t_c are stated in the preceding sections.

$$F_b = s_{st} t_s f_{sy} (0.004\alpha + 0.002\alpha^{1.25} \frac{t_s^{0.1} s_{st}^{0.9}}{t_c}) \times 10^{-3}$$

$$1.11 \le \delta < 2.53 \tag{6}$$

$$F_b = s_{st} t_s f_{sy} (0.009\alpha + 0.003\alpha^{1.25} \frac{t_s^{0.1} s_{st}^{0.9}}{t_c}) \times 10^{-3}$$

$$2.53 \le \delta < 5.07 \tag{7}$$

The results of Eq. (3) with regard to the calibration and finite element analysis results are illustrated in Fig. 15, where the F_{eb} is represented as a point,

and the calculations using Eqs. (6) and (7) produce a solid line. It can be observed that the minimum, maximum and average of the differences between the finite element analysis results and the results of Eq. (3) are 0.01%, 25% and 3%, respectively, where the predicted data (F_{eb}) with relatively large differences are almost below the solid line. This demonstrates that Eqs. (6) and (7) for the tensile force demand on a stud can be used to estimate the maximum stud tension of the C-SPW up to a 2.5% drift ratio with reasonable accuracy and conservatism.

Table 2
Calibration of stud tensile force from FEM

Specimens	Development stage	δ	F_{eb} (kN)	$\beta_f \times 10^{-3}$	F_b (kN)
N4-B	Increase Stage 2	3.62	50.7	19.2	52.5
N4-D22	Increase Stage 2	3.62	50.5	19.1	52.5
N4-TS10	Increase Stage 2	3.48	36.8	20.9	34.3
N4-TS20	Increase Stage 2	3.73	60.5	17.2	71.1
N4-TC50	Increase Stage 2	5.06	58.2	22.0	64.0
N4-TC100	Increase Stage 2	2.54	47.3	17.9	43.9
N5-B	Increase Stage 2	2.96	38.5	18.2	37.8
N5-D22	Increase Stage 2	2.96	37.4	17.7	37.8
N5-TS10	Increase Stage 2	2.84	21.3	15.1	24.7
N5-TS20	Increase Stage 2	3.05	49.5	17.6	51.2
N5-TC50	Increase Stage 2	4.15	45.5	21.5	45.3
N5-TC100	Increase Stage 1	2.07	15.7	7.4	17.2
N6-B	Increase Stage 1	2.51	14.4	8.2	15.9
N6-D22	Increase Stage 1	2.51	13.8	7.8	15.9
N6-TS10	Increase Stage 1	2.42	13.4	11.4	10.4
N6-TS20	Increase Stage 2	2.59	32.1	13.7	39.4
N6-TC50	Increase Stage 2	3.52	25.7	14.6	34.5
N6-TC100	Increase Stage 1	1.76	10.3	5.8	13.3
N10-B	Increase Stage 1	1.59	6.8	6.4	7.6
N10-D22	Increase Stage 1	1.59	6.6	6.3	7.6
N10-TS10	Pre-buckling	1.52	5.9	8.5	5.0
N10-TS20	Increase Stage 1	1.63	11.5	8.2	10.3
N10-TC50	Increase Stage 1	2.22	10.2	9.6	8.9
N10-TC100	Pre-buckling	1.12	5.3	6.2	6.6
L6-B	Increase Stage 1	2.49	9.3	8.8	9.5
L6-TS10	Increase Stage 1	2.39	5.6	7.9	6.2
L6-TS20	Increase Stage 2	2.57	25.1	17.7	23.5

5.2. Formula for stud bending moment demand

At the drift ratio of 2.5%, the stud bending moment development stage can also be distinguished using Eq. (3). When δ ranges from 1.11 to 1.53, the stud bending moment development is in the stage before Increase Stage; when δ ranges from 1.53 to 2.53, the stud bending moment development is in the Increase Stage; and when δ ranges from 2.53 to 5.07, the stud bending moment development is in the Plateau Stage.

Substituting the maximum stud bending moment M_{eb} obtained from finite element analysis for M_b in Eq. (2), the modification factor β_m is obtained as listed in Table 3. For the Increase Stage of stud bending, the effects of stud spacing s_{st}, infill steel plate thickness t_s and panel aspect ratio α are contained in Eq. (2). Therefore, the modification factor for stud bending moment β_m is employed to capture the effects of stud diameter d_{st} and overall thickness of the concrete panels t_c on the maximum stud bending moment M_{eb}. According to the parameter analysis on stud bending moment and fitting β_m by the variable d_{st}^2/t_c^2, formulas for β_m in the stage before Increase Stage and Increase Stage are shown in Eqs. (8) and (9), respectively. Substituting Eqs. (8) and (9) into Eq. (2), the bending moment demands on the headed stud M_b in kN·mm in the stage before the Plateau Stage are yielded in Eqs. (10) and (11), where α, f_{sy}, t_s, s_{st}, t_c and d_{st} are stated previously.

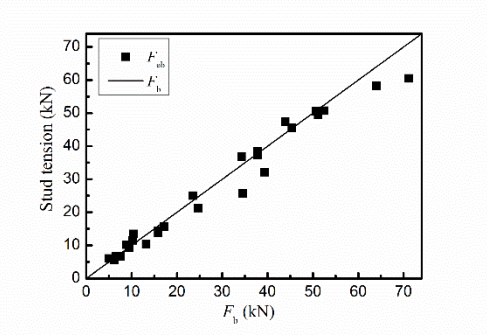

Fig. 15 Calibration of the tensile force demand on stud

$$\beta_m = 2.8\frac{d_{st}^2}{t_c^2} \qquad 1.11 \le \delta < 1.53 \tag{8}$$

$$\beta_m = 1.9\frac{d_{st}^2}{t_c^2} \qquad 1.53 \le \delta < 2.53 \tag{9}$$

$$M_b = 0.7\alpha s_{st} t_s^2 f_y \frac{d_{st}^2}{t_c^2} \times 10^{-3} \qquad 1.11 \le \delta < 1.53 \tag{10}$$

$$M_b = 0.475\alpha s_{st} t_s^2 f_y \frac{d_{st}^2}{t_c^2} \times 10^{-3} \qquad 1.53 \le \delta < 2.53 \tag{11}$$

From the results of the parameter analysis, it is known that the bending moment of a stud in the Plateau Stage is mainly determined by stud diameter d_{st} as well as infill steel plate thickness t_s. The roles that β_m plays include introducing the influences of d_{st}, abating the extent of influence of t_s and eliminating the influences of s_{st} as well as α. Fitting β_m by the variable of $d_{st}^{2.8}/(\alpha s_{st} t_s^{1.8})$ yields Eq. (12). In the Plateau Stage, the bending moment demand on a stud in kN·mm is proposed by substituting Eq. (12) into Eq. (2), as shown in Eq. (13).

$$\beta_m = 1.08\frac{d_{st}^{2.8}}{\alpha s_{st} t_s^{1.8}} \qquad 2.53 \le \delta < 5.07 \tag{12}$$

$$M_b = 0.27 d_{st}^{2.8} t_s^{0.2} f_{sy} \times 10^{-3} \qquad 2.53 \le \delta < 5.07 \tag{13}$$

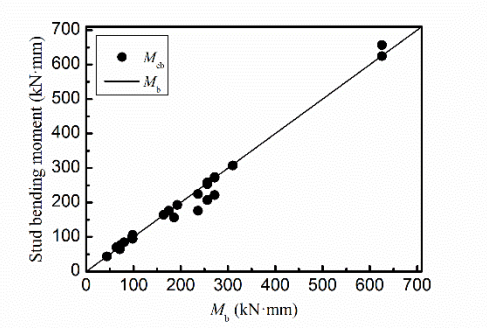

Fig. 16 Calibration of the bending moment demand on stud

The results obtained from calibrating Eq. (3) and the finite element

analysis results are displayed in Fig. 16, where the M_{eb} is represented as a point and the calculations of Eqs. (10) and (11) and (13) produce a solid line. It can be observed that the minimum, maximum and average of the differences between the finite element analysis and Eq. (3) are 0.01%, 29% and 2.6%, respectively, where the predicted data (M_{eb}) with relatively large differences are below the solid line. This indicates that Eqs. (10), (11) and (13) for the bending moment demand on a stud can estimate the maximum stud bending moment of a C-SPW up to a 2.5% drift ratio with reasonable accuracy and conservatism.

Table 3
Calibration of stud bending moment from FEM

Specimens	Development stage	δ	M_{eb} (kN·mm)	$\beta_m \times 10^{-3}$	M_b (kN·mm)
N4-B	Plateau Stage	3.62	257.0	25.9	256.6
N4-D22	Plateau Stage	3.62	657.0	66.2	625.8
N4-TS10	Plateau Stage	3.48	224.2	50.9	236.6
N4-TS20	Plateau Stage	3.73	273.2	15.5	271.8
N4-TC50	Plateau Stage	5.06	258.0	26.0	256.6
N4-TC100	Plateau Stage	2.54	254.2	25.6	256.6
N5-B	Plateau Stage	2.96	253.0	31.9	256.6
N5-D22	Plateau Stage	2.96	624.7	78.8	625.8
N5-TS10	Plateau Stage	2.84	176.0	49.9	236.6
N5-TS20	Plateau Stage	3.05	272.2	19.3	271.8
N5-TC50	Plateau Stage	4.15	257.0	32.4	256.6
N5-TC100	Increase Stage	2.07	100.0	12.6	97.5
N6-B	Increase Stage	2.51	164.0	24.8	164.4
N6-D22	Increase Stage	2.51	307.0	46.4	310.1
N6-TS10	Increase Stage	2.42	76.5	26.0	72.9
N6-TS20	Plateau Stage	2.59	221.3	18.8	271.8
N6-TC50	Plateau Stage	3.52	207.2	31.3	256.6
N6-TC100	Increase Stage	1.76	84.3	12.8	80.4
N10-B	Increase Stage	1.59	94.5	23.8	98.4
N10-D22	Increase Stage	1.59	156.2	39.3	186.1
N10-TS10	Pre-buckling	1.52	70.2	39.7	64.5
N10-TS20	Increase Stage	1.63	175.8	24.9	175.0
N10-TC50	Increase Stage	2.22	192.7	48.6	192.9
N10-TC100	Pre-buckling	1.12	63.7	16.1	71.1
L6-B	Increase Stage	2.49	105.9	26.7	98.4
L6-TS10	Increase Stage	2.39	43.1	24.5	43.7
L6-TS20	Plateau Stage	2.57	271.8	38.6	271.8

6. Conclusions

The objective of this paper was to propose formulas for the tension and bending moment demands on headed studs in the design of C-SPWs. The tensile forces and bending moments of studs in a C-SPW subjected to a lateral load are researched using the finite element method. The development and distributions of stud tension and bending moment as well as the interaction between studs and infill steel plates are analysed with five varying design parameters including concrete panel thickness, infill steel plate thickness, panel aspect ratio (the ratio of height to width) and number of studs. Based on the analysis results, available fitting formulas for the demands on stud tension and bending moment in the design of C-SPWs are proposed.

The conclusions produced in this paper are presented as follows:

Stud tension and bending moment become marked in the post-buckling phase of the infill steel plate resulting from significant, relative out-of-plane deformation between the steel plate and concrete panel.

The critical tensile studs are concentrated in the middle of buckling half-wave, whereas the critical bending studs are located at the boundary of the buckling half-wave. The coupling effect between the tensile force and bending moment is minimal.

Stud tension development is divided into two stages, which incorporate the transitory and rapidly increasing phases of tension as well as the linearly increasing. Stud bending moment development is divided into two stages: linearly increasing and approximately constant.

At the required drift ratio of 2.5% per ASCE, the maximum values of stud tension and bending moment are determined by the critical drift ratio corresponding to the onset of infill steel plate buckling, the development stages in which these values are located as well as their rate of development.

The rate of development of stud tension and bending moment transferred through the concrete panel are determined by the transverse component of axial forces along the buckling half-wave of the infill steel plate and the plastic moment at both ends of the buckling half-wave.

The formulas for the tensile force and bending moment demands on headed studs when the drift ratio of a C-SPW is limited to 2.5% are proposed with reasonable accuracy and conservatism. These formulas can be used in the seismic design of C-SPWs.

Acknowledgement

This research is funded by the National Natural Science Foundation of China (grant number 51678382), which is gratefully acknowledged.

References

[1] Astaneh-Asl A., “Seismic behavior and design of composite steel plate shear walls”. Steel Tips Report, Structural Steel Educational Council, USA, 2002.
[2] Zhao Q.H, and Astaneh-Asl A., “Cyclic behavior of traditional and innovative composite shear walls”, Journal of Structural Engineering, 130(2), 271-284, 2004.
[3] Arabzadeh A., Soltani M. and Ayazi A., “Experimental investigation of composite shear walls under shear loadings”, Thin-Walled Structures, 49, 842-854, 2011.
[4] Rassouli B., Shafaei S., Ayazi A., et al., “Experimental and numerical study on steel-concrete composite shear wall using light-weight concrete”, Journal of Constructional Steel Research, 126, 117-128, 2016.
[5] Seismic provisions for structural steel buildings (ANSI/AISC 341), American Institute of Steel Construction, Chicago, IL, USA, 2010.
[6] Rahai A. and Hatami F., “Evaluation of composite shear wall behavior under cyclic loadings”, Journal of Constructional Steel Research, 65, 1528-1537, 2009.
[7] Shafaei S., Ayazi A. and Farahbod F., “The effect of concrete panel thickness upon composite steel plate shear walls”, Journal of Constructional Steel Research, 117, 81-90, 2016.
[8] Rahnavard R., Hassanipour A. and Mounesi A., “Numerical study on important parameters of composite steel-concrete shear walls”, Journal of Constructional Steel Research, 121, 441-456, 2016.
[9] Dey S. and Bhowmick A.K., “Seismic performance of composite plate shear walls”, Structures, 6, 59-72, 2016.
[10] Simith S.T., Bradford M.A. and Oehlers D.J., “Elastic buckling of unilaterally constrained rectangular plates in pure shear”, Engineering Structures, 21, 443-453, 1999.
[11] Arabzade A., Moharami H. and Ayazi A., “Local elastic buckling coefficients of steel plates in composite steel plate shear walls”, Scientia Iranica, 18(1), 9-15, 2011 (A).
[12] Guo L.H., Li R., Rong Q., et al., “Cyclic behavior of SPSW and CSPSW in composite frame”, Thin-Walled Structures, 51, 39-52, 2012.
[13] Dong Q.L. and Guo Y.L, “Ultimate shear capacity of buckling-restrained steel plate shear walls, Pacific Structural Steel Conference, Steel Structures in Natural Hazarrds, Wairakei, New Zealand, 335-340, 2007.
[14] Guo Y.L., Dong Q.L., “Static behavior of buckling-restrained steel plate shear walls”, The 6th International Conference on Tall Buildings, The University of Hong Kong, Hong Kong, China, 666-670, 2005.
[15] Jin S.S., Ou J.P. and Richard J.Y., “Stability of buckling-restrained steel plate shear walls with inclined-slots: Theoretical analysis and design recommendations”, Journal of Constructional Steel Research, 117:13-23, 2016.
[16] Wei M.W., Richard Liew J.Y. and Fu X.Y., “Panel action of novel partially connected buckling-restrained steel plate shear walls”, Journal of Constructional Steel Research, 128, 483-497, 2017.
[17] Pallarés L. and Hajjar J.F., “Headed steel stud anchors in composite structures, Part II: Tension and interaction”, Journal of Constructional Steel Research, 66, 213-228, 2010.
[18] Lin Z.F., Liu Y.Q. and Roeder C.W., “Behavior of stud connections between concrete slabs and steel girders under transverse bending moment”, Engineering Structures, 117, 130-144, 2016.
[19] Building code requirements for structural concrete (ACI 318), American Concrete Institute, Farmington Hills, Michigan, USA, 2011.
[20] Code requirements for nuclear safety related concrete structures (ACI 349), American Concrete Institute, Farmington Hills, Michigan, USA, 2006.
[21] PCI design handbook: Precast and prestressed concrete, Precast/Prestressed Concrete Institute, Chicago (IL), USA, 2004.

[22] Qi Y., Gu Q., et al., “Shear force demand on headed stud for the design of composite steel plate shear wall”, Engineering Structures, 148, 780-792, 2017. http://dx.doi.org/10.1016/j.engstruct.2017.07.023.
[23] Qi Y., Gu Q., et al., “Concrete panel thickness demand for the design of composite steel plate shear wall”, The Structural Design of Tall and Special Buildings, 28(8) , 2019. http://doi.org/ /10.1002/tal.1605.
[24] Hibbitt K., Sorensen., “ABAQUS/Standard User's Manual (Version 6.12)”, RI: HKS Inc., Pawtucket, USA, 2012.
[25] Lubiner J., Oliver J., Oller S., et al., “A plastic-damage model for concrete”, International Journal of Solids and Structures, 25(3), 399-326, 1989.
[26] Lee B.J., Fenves G.L., Member, ASCE, “Plastic-damage model for cyclic loading of concrete structures”, Journal of Engineering Mechanics, 124(8), 892-990 , 1998.
[27] Zhang K., Varma A.H., Malushte S.R., et al., “Effect of shear connectors on local buckling and composite action in steel concrete composite walls”, Nuclear Engineering and Design, 269, 231-239, 2014.
[28] Cho S.G., Park W.K., So G.H., et al., “Seismic capacity estimation of steel plate concrete (SC) shear wall specimens by nonlinear static analyses”, KSCE Journal of Civil Engineering, 19(3), 698-709, 2015.
[29] Epackachi S., Whittaker A.S., Varma A.H., et al., “Finite element modeling of steel-plate concrete composite wall piers”. Engineering Structures. 100, 369-384. 2015.
[30] Epackachi S., Whittaker A.S. and Aref A., “Seismic analysis and design of steel-plate concrete composite shear wall piers”, Engineering Structures, 133, 105-123, 2017.
[31] Nguyen N.H. and Whittaker A.S., “Numerical modeling of steel-plate concrete composite shear walls”, Engineering Structures, 150, 1-11, 2017.
[32] Minimum Design Loads for Buildings and Other Structures (SEI/ASCE 7), American Society of Civil Engineers, Virginia, USA, 2010.

Advanced Steel Construction – Vol. 15 No. 4 (2019) 349–363
DOI:10.18057/IJASC.2019.15.4.6

MODIFICATIONS TO THE GLOBAL AND INTERACTIVE SHEAR BUCKLING ANALYSIS METHODS OF TRAPEZOIDAL CORRUGATED STEEL WEBS FOR BRIDGES

Su-mei Liu [1, 2], Han-shan Ding [1, *], Luc Taerwe [2, 3] and Wouter De Corte [2]

[1] *School of Civil Engineering, Southeast University, Nanjing, 211189, China*
[2] *Department of Structural Engineering, Faculty of Engineering and Architecture, Ghent University, Ghent, 9000, Belgium*
[3] *College of Civil Engineering, Tongji University, Shanghai, 200092, China*
** (Corresponding author: E-mail: hsding@seu.edu.cn)*

ABSTRACT

The value of the global shear buckling coefficient k_g and the formula for the interactive shear buckling stress of corrugated steel webs (CSWs) are still the subject of debate. In this study, firstly, the analytical formulas for the global and interactive shear buckling stresses of CSWs are deduced by the Galerkin method. Simplified formulas for the global shear buckling coefficient k_g for a four-edge simple support, for a four-edge fixed support, for two edges constrained by flanges fixed and the other two edges simply supported, and an interactive shear buckling coefficient table are given. Secondly, an elastic finite element analysis is carried out to verify the analytical formulas and to study the influence of geometric parameters on the shear buckling stress of CSWs. Finally, a design formula for the shear strength of CSWs which adopts the formulas for the global and interactive shear buckling stresses proposed in this paper is assessed. From a comparison between the shear strength calculated by this design formula, calculated by four previous design formulas and measured in a series of published test results, it is found that the considered design formula provides good predictions for the shear strength of CSWs and can be recommended.

ARTICLE HISTORY

Received: 15 January 2019
Revised: 07 June 2019
Accepted: 13 June 2019

KEYWORDS

Corrugated steel web;
Global shear buckling;
Interactive shear buckling;
Shear strength;
Galerkin method;
Finite element analysis

1. Introduction

The steel-concrete composite girder with corrugated steel webs (CSWs) (see Fig. 1) is known as a new type of bridge structure to overcome the weight problem of common concrete box girders. Compared with concrete webs, CSWs have low longitudinal stiffness due to the accordion effect, so CSWs mainly carry the shear forces and barely carry axial forces [1]. Because of this characteristic, CSWs fail due to shear buckling or yielding [2]. Therefore, the shear buckling stability of CSWs is one of the most important considerations in the design of this kind of composite girder bridges.

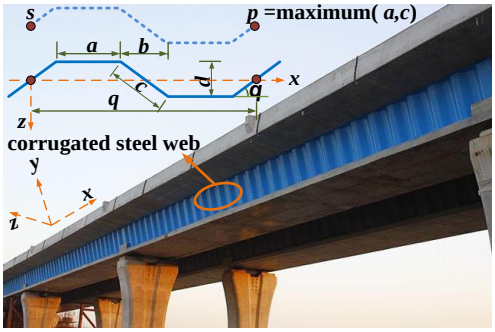

Fig. 1 Composite girder with CSWs

It is widely accepted that local buckling is the primary failure mode in coarse corrugations, whereas global buckling becomes the primary failure mode in dense corrugations and interactive shear buckling mode becomes primary when the density is in between of the two above scenarios [3].

The local shear buckling of CSWs is solved by analyzing a single flat panel constrained by adjacent panels and girder flanges. For this, the shear buckling stress formula of isotropic rectangular plates [4] can be applied. Aggarwal et al. [5] numerically investigated the local shear buckling of CSWs and found that the edge conditions between the CSWs and the girder flanges were close to fixed, while those between the flat and inclined panels lied between simply supported and fixed.

The global shear buckling of CSWs for straight girder bridges is analyzed by treating the whole corrugated steel web (CSW) as an orthotropic rectangular plate constrained by concrete flanges and diaphragms, and has been studied by various researchers. Easley and McFarland [6] investigated the global shear buckling behavior of corrugated metal diaphragms by assuming them as orthotropic plates and developed the formula for the shear buckling load by the Ritz and the Energy method. Then, Easley [7] made a comparative analysis of the Bergmann-Reissner formula [8], the Hlavacek formula [9] and the Easley-McFarland formula [6], and proposed a more comprehensive and applicable global shear buckling formula of corrugated plates. As application of corrugated plates, initially used for aircrafts, was gradually extended to civil engineering, the formula $\tau_g^e = k_g \dfrac{(D_x)^{1/4}(D_y)^{3/4}}{th^2}$ was accepted to calculate the global shear buckling stress of CSWs, where k_g is the global shear buckling coefficient depending on the edge conditions. For a four-edge simple support, Easley [7] suggested k_g=36, Peterson [10] and Bergfelt et al. [11] suggested k_g=32.4, while the Guide to Stability Design Criteria for Metal Structures [12] adopts k_g=31.6. For a four-edge fixed support, Easley [7] suggested k_g=68.4, Peterson [10] and Bergfelt, et al. [11] suggested k_g=60.4, while the Guide to Stability Design Criteria for Metal Structures [12] adopts k_g=59.2. El Metwally and Loov [13] suggested k_g=50 for composite girders with CSWs. From the studies mentioned above, it is clear that although a global shear buckling formula of CSWs has been proposed, researchers hold different views on the value of the global shear buckling coefficient k_g. Many adjustments of the coefficient k_g are based on FEA only, and lack theoretical support. Machimdamrong et al. [14] presented the transition curves of the elastic global shear buckling capacity with the boundary conditions from a four-edge simple support to a four-edge fixed support using the Rayleigh-Ritz method, but only the curves for the plate dimensions (l×h) of 1m×1m and 2m×1m were provided. Therefore, it is necessary to investigate the global shear buckling of CSWs with different boundary conditions theoretically.

Finally, the formula for the interactive shear buckling is determined by the local and global shear buckling stresses, and the yield stress of the plate material [15], but the way these parameters are to be combined is still the subject of debate. Important work has been done by Bergfelt and Leiva-Aravena [16], El Metwally [17], Abbas et al. [18], Shiratani et al. [19], Sayed-Ahmed [20] and Yi et al. [15], etc., and various interactive shear buckling formulas of CSWs were proposed. All the formulas might be not accurate enough since their forms were too simple [21], and are based on the relationship between the local and global shear buckling stresses, and the yield stress only. All the elastic interactive formulas show that the interactive shear buckling stress is the minimum value of the three shear buckling modes, which is not reasonable and lacks theoretical support. Therefore, it is necessary to investigate the interactive shear buckling of CSWs from a theoretical point of view.

For practical applications, Elgaaly et al. [22] recommended that the

capacity of CSWs was controlled by the minimum value of local and global buckling stresses, and a semiempirical formula for the inelastic buckling stress was proposed. Driver et al. [23] suggested a lower bound formula by combining local and global shear buckling formulas. Moon et al. [24] proposed a shear buckling parameter formula for trapezoidal CSWs based on the relationship between local, global and interactive shear buckling stresses. Eldib [3] proposed a shear buckling parameter formula for curved CSWs. Nie et al. [21] carried out eight H-shape steel girders with CSWs and suggested a formula for the shear strength prediction of trapezoidal CSWs. Hassanein et al. studied the shear behavior of linearly tapered girder bridges with CSWs [25], and girders with high-strength CSWs [26]. Leblouba and Barakat [2] experimentally and numerically investigated the shear stress distribution in trapezoidal CSWs.

In this study, the whole CSW is treated as an orthotropic plate constrained by flanges and diaphragms for the global shear buckling analysis, and the folded plate composed of two adjacent panels is treated as an isotropic shallow shell for the interactive shear buckling analysis. Firstly, the analytical formulas for the global and interactive shear buckling stresses are derived by the Galerkin method. Then, an elastic finite element analysis (FEA) is carried out to verify the analytical formulas and to study the influence of geometric parameters on the shear buckling stress of CSWs. Finally, a design formula for the shear strength of CSWs which adopts the formulas for the global and interactive shear buckling stresses proposed in this paper is assessed.

2. Elastic shear buckling stress of CSWs

2.1. Physical equivalent parameters of CSWs

For trapezoidal CSWs that are commonly used in actual girder bridges, when treated as an orthotropic plate, the equivalent flexural stiffnesses D_x, D_y and the torsional stiffness D_{xy} per unit length of a CSW can be expressed as Eqs. (1)-(3) [6].

$$D_x = \frac{q}{s}\frac{Et^3}{12} = \frac{Et^3(2a+2d.\cot\theta)}{12(2a+2d.\csc\theta)} \tag{1}$$

$$D_y = \frac{Etd^2(3a+c)}{6q} = \frac{Etd^2(3a+d.\csc\theta)}{6(2a+2d.\cot\theta)} \tag{2}$$

$$D_{xy} = \frac{s}{q}\frac{Et^3}{6(1+\mu)} = \frac{Et^3(2a+2d.\csc\theta)}{6(1+\mu)(2a+2d.\cot\theta)} \tag{3}$$

where E is the elastic modulus of the original steel plate; μ is the Poisson's ratio; t is the web thickness. As shown in Fig. 1, a is the flat panel width; c is the inclined panel width; d is the corrugation depth; θ is the corrugation angle; q is the horizontal projection length of one periodic corrugation; s is the total folded panel length of one periodic corrugation.

2.2. Elastic local shear buckling

The shear buckling stress formula of isotropic rectangular plates Eq. (4) [4] can be applied to calculate the elastic local shear buckling stress of CSWs.

$$\tau_l^e = k_l\frac{\pi^2 E}{12(1-\mu^2)}\left(\frac{t}{p}\right)^2 \tag{4}$$

where k_l is the elastic local shear buckling coefficient of CSWs; p is the maximum value of the flat panel width a and the inclined panel width c.

The elastic local shear buckling coefficient k_l can be expressed as Eqs. (5)-(7).

For a four-edge simple support:

$$k_{l,s} = 5.34 + 4(p/h)^2 \tag{5}$$

For a four-edge fixed support:

$$k = 8.98 + 5.6(p/h) \tag{6}$$

For the two edges constrained by flanges fixed and the other two edges simply supported:

$$k_{l,fs} = 5.34 + 2.31(p/h) - 3.44(p/h)^2 + 8.39(p/h)^3 \tag{7}$$

2.3. Elastic global shear buckling

2.3.1. Critical buckling stress under pure shear

A CSW with dense corrugations can be treated as an orthotropic plate (Fig. 2) for the global shear buckling analysis.

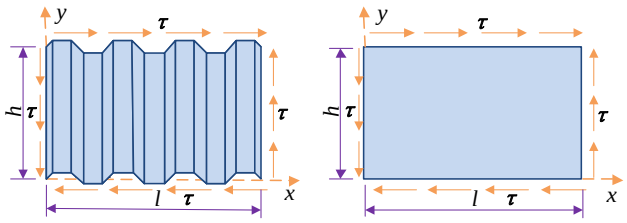

（a）CSW (b) Equivalent orthotropic plate

Fig. 2 CSW and its equivalent orthotropic plate

According to the stability theory of plates, the equilibrium equation of an orthotropic plate subjected to a shear force can be expressed as Eq. (8) [27].

$$\frac{1}{t}\left(D_x\frac{\partial^4}{\partial x^4} + D_{xy}\frac{\partial^4}{\partial x^2\partial y^2} + D_y\frac{\partial^4}{\partial y^4}\right)w = 2\tau\frac{\partial^2 w}{\partial x\partial y} \tag{8}$$

where w is the out of plane deflection of the plate, τ is the shear stress.

It can be assumed that the boundary conditions of CSWs satisfy a four-edge simple support, a four-edge fixed support, or two edges constrained by flanges fixed and the other two edges simply supported (the edges x=0 and x=l are simply supported, the edges y=0 and y=h are fixed supported). The functions of deflection can be expressed respectively as Eqs. (9)-(11).

For a four-edge simple support [4]:

$$w = \sum_{m=1}^{\infty}\sum_{n=1}^{\infty} C_{mn}\sin\frac{m\pi x}{l}\sin\frac{n\pi y}{h} \tag{9}$$

For a four-edge fixed support [28]:

$$w = \sum_{m=1}^{\infty}\sum_{n=1}^{\infty} C_{mn}\left(\frac{1}{m}\sin\frac{m\pi x}{l} - \frac{1}{m+2}\sin\frac{(m+2)\pi x}{l}\right)\left(\frac{1}{n}\sin\frac{n\pi y}{h} - \frac{1}{n+2}\sin\frac{(n+2)\pi y}{h}\right) \tag{10}$$

For the edges x=0 and x=l simply supported, and the edges y=0 and y=h fixed:

$$w = \sum_{m=1}^{\infty}\sum_{n=1}^{\infty} C_{mn}\sin\frac{m\pi x}{l}\left(\frac{1}{n}\sin\frac{n\pi y}{h} - \frac{1}{n+2}\sin\frac{(n+2)\pi y}{h}\right) \tag{11}$$

where h is the web height equal to the clear distance between the top and bottom concrete flanges, l is the web length equal to the distance between the two adjacent diaphragm plates.

Given λ=l/h, α=D_x/D_y and β=D_{xy}/D_y, Eq. (8) can be simplified as Eqs. (12)-(14) according to the Galerkin method.

For the four-edge simple support:

$$\frac{\pi^4 D_y}{4th^2\lambda^3}\left(\alpha m^4 + \beta m^2 n^2\lambda^2 + n^4\lambda^4\right)C_{mn} - 8\tau\sum_{i=1}^{\infty}\sum_{j=1}^{\infty} C_{ij}\frac{mnij}{\left(m^2-i^2\right)\left(n^2-j^2\right)} = 0 \tag{12}$$

$(m \pm i = \text{odd number},\ n \pm j = \text{odd number})$

For the four-edge fixed support:

$$\frac{D_y}{th^2}\frac{\pi^4}{4\lambda^3}\left\{\begin{array}{l}C_{mn}\left\{\begin{array}{l}\alpha\left[m^2+(m+2)^2\right]\left[n^{-2}+(n+2)^{-2}\right]+4\beta\lambda^2\\+\lambda^4\left[m^{-2}+(m+2)^{-2}\right]\left[n^2+(n+2)^2\right]\end{array}\right\}\\-C_{m,n+2}\left\{\alpha\left[m^2+(m+2)^2\right](n+2)^{-2}+2\beta\lambda^2+\lambda^4\left[m^{-2}+(m+2)^{-2}\right](n+2)^2\right\}\\-C_{m,n-2}\left\{\alpha\left[m^2+(m+2)^2\right]n^{-2}+2\beta\lambda^2+\lambda^4\left[m^{-2}+(m+2)^{-2}\right]n^2\right\}\\-C_{m+2,n}\left\{\alpha(m+2)^2\left[n^{-2}+(n+2)^{-2}\right]+2\beta\lambda^2+\lambda^4(m+2)^{-2}\left[n^2+(n+2)^2\right]\right\}\\+C_{m+2,n+2}\left[\alpha(m+2)^2(n+2)^{-2}+\beta\lambda^2+\lambda^4(m+2)^{-2}(n+2)^2\right]\\+C_{m+2,n-2}\left[\alpha(m+2)^2n^{-2}+\beta\lambda^2+\lambda^4(m+2)^{-2}n^2\right]\\-C_{m-2,n}\left\{\alpha m^2\left[n^{-2}+(n+2)^{-2}\right]+2\beta\lambda^2+\lambda^4m^{-2}\left[n^2+(n+2)^2\right]\right\}\\+C_{m-2,n+2}\left[\alpha m^2(n+2)^{-2}+\beta\lambda^2+\lambda^4m^{-2}(n+2)^2\right]\\+C_{m-2,n-2}\left[\alpha m^2n^{-2}+\beta\lambda^2+\lambda^4m^{-2}n^2\right]\end{array}\right.$$

$$-8\tau\sum_{i=1}^{\infty}\sum_{j=1}^{\infty}A_{ij}\left\{\begin{array}{l}\left[\dfrac{1}{m^2-i^2}-\dfrac{1}{(m+2)^2-i^2}-\dfrac{1}{m^2-(i+2)^2}+\dfrac{1}{(m+2)^2-(i+2)^2}\right]\\\times\left[\dfrac{1}{n^2-j^2}-\dfrac{1}{(n+2)^2-j^2}-\dfrac{1}{n^2-(j+2)^2}+\dfrac{1}{(n+2)^2-(j+2)^2}\right]\end{array}\right\}=0 \quad (13)$$

$(m\pm i=\text{odd number},\ n\pm j=\text{odd number})$

For the edges x=0 and x=l simply supported, and the edges y=0 and y=h fixed:

$$\frac{D_y}{th^2}\frac{\pi^4}{4\lambda^3}\left\{\begin{array}{l}C_{mn}\left\{\alpha m^4\left[n^{-2}+(n+2)^{-2}\right]+2\beta\lambda^2m^2+\lambda^4\left[n^2+(n+2)^2\right]\right\}\\-C_{m,n+2}\left[\alpha m^4(n+2)^{-2}+\beta\lambda^2m^2+\lambda^4(n+2)^2\right]\\-C_{m,n-2}\left[\alpha m^4n^{-2}+\beta\lambda^2m^2+\lambda^4n^2\right]\end{array}\right\}$$

$$-8\tau\sum_{i=1}^{\infty}\sum_{j=1}^{\infty}A_{ij}\frac{mi}{m^2-i^2}\left[\begin{array}{l}\dfrac{1}{n^2-j^2}-\dfrac{1}{(n+2)^2-j^2}-\dfrac{1}{n^2-(j+2)^2}\\+\dfrac{1}{(n+2)^2-(j+2)^2}\end{array}\right]=0 \quad (14)$$

$(m\pm i=\text{odd number},\ n\pm j=\text{odd number})$

By assigning values to m and n in Eqs. (12)-(14), a series of linear algebraic equations with C_{ij} as unknowns can be obtained. Then the critical shear buckling stress can be derived by assuming the coefficient determinant of the linear algebraic equations equals zero. (i. e. a linear bifurcation analysis).

According to Eqs. (12)-(14), the elastic global shear buckling stress of CSWs can be expressed as Eq. (15).

$$\tau_g^e=k_g\frac{D_y}{h^2t} \quad (15)$$

where k_g is the elastic global shear buckling coefficient of CSWs. The detailed solution process of the coefficient $k_{g,s}$ for a four-edge simple support, $k_{g,f}$ for a four-edge fixed support, $k_{g,fs}$ for the edges x=0 and x=l simply supported, and the edges y=0 and y=h fixed is given below.

2.3.2. Calculation of the global shear buckling coefficient k_g

(1) Comparison with isotropic plate

Based on "Theory of elastic stability" [4], the elastic shear buckling stress of isotropic rectangular plates can be expressed as Eq. (16).

$$\tau_{cr}^e=k\frac{\pi^2D}{h^2t} \quad (16)$$

where D is the flexural stiffness, and k is the elastic shear buckling coefficient of isotropic rectangular plates. The coefficients k_s for the four-edge simple support, k_f for the four-edge fixed support, k_{fs} for the edges x=0 and x=l simply supported, and the edges y=0 and y=h fixed are given in Timoshenko [4].

When D_x/D_y=1 and D_{xy}/D_y=2, The Eq. (15) for the elastic global shear buckling stress of CSWs derived in this paper can be also applied to calculate isotropic plates. The global shear buckling coefficient k_g in Eq. (15) should be divided by π^2 to meet the needs of comparison with Timoshenko [4]. The shear buckling coefficient k from Timoshenko [4] and k_g/π^2 derived in this paper are given in Table 1.

As can be seen from Table 1, the average difference between k_g/π^2 derived in this paper, which takes 900 trigonometric series (m=30, n=30), and k from Timoshenko [4] is 1.2% (the maximum being 4.4%) showing the accuracy of the solution method proposed in this paper.

Table 1

Elastic shear buckling coefficient of isotropic rectangular plates

Coefficient	Boundaries	l/h									
		1	1.2	1.4	1.5	1.6	1.8	2	2.5	3	4
$k_{g,s}/\pi^2$	Four-edge simply	9.32	7.98	7.29	7.07	6.91	6.69	6.55	6.08	5.84	5.62
k_s		9.34	8	7.3	7.1	7	6.8	6.6	6.1	5.9	5.7
$k_{g,f}/\pi^2$	Four-edge fixed	15.04	—	—	11.77	—	—	10.52	—	—	—
k_f		14.71	—	—	11.5	—	—	10.34	—	—	—
$k_{g,fs}/\pi^2$	x=0, x=l simply,	12.82	—	—	11.01	—	—	10.26	9.88	9.73	—
k_{fs}	y=0, y=h fixed	12.28	—	—	11.12	—	—	10.21	9.81	9.61	—

Note: "—" expresses the value of k is not given in Timoshenko [4].

Table 2

Geometry of CSWs in actual bridges [3, 15, 24, 26, 29]

Bridges	a	b	c	d	h	t_{min}	t_{max}	$\frac{a}{t_{min}}$	$\frac{a}{t_{max}}$	$\frac{3a+c}{q}$	Based on t_{min}		Based on t_{max}	
	mm	mm	mm	mm	mm	mm	mm				α	β	α	β
Cognac	353	319	353	150	1771	8	8	44.1	44.1	1.05	0.0013	0.0022	0.0013	0.0022
Maupre	284	241	284	150	2650	8	8	35.5	35.5	1.08	0.0012	0.0022	0.0012	0.0022
Dole	430	370	430	220	1800~4010	8	12	53.8	35.8	1.08	0.0006	0.0010	0.0013	0.0023
Shinkai	250	200	250	150	1183	9	9	27.8	27.8	1.11	0.0015	0.0028	0.0015	0.0028
Miyukibashi	300	260	300	150	2210	8	12	37.5	25.0	1.07	0.0012	0.0022	0.0028	0.0049
Katsutegawa	430	370	430	220	2080~5300	9	12	47.8	35.8	1.08	0.0007	0.0013	0.0013	0.0023
Hondani	330	270	336	200	1025~5095	9	14	36.7	23.6	1.11	0.0008	0.0016	0.0020	0.0038
Koinumarukawa	430	370	430	220	1580~3600	9	16	47.8	26.9	1.08	0.0007	0.0013	0.0023	0.0041
Shimoda	430	370	430	220	1140~5360	12	16	35.8	26.9	1.08	0.0013	0.0023	0.0023	0.0041
Nakano Viaduct	330	270	336	200	1010~3100	9	19	36.7	17.4	1.11	0.0008	0.0016	0.0037	0.0070
Kurobekawa Railway	400	350	400	200	2500~3400	12	25	33.3	16.0	1.07	0.0016	0.0028	0.0069	0.0120
Altwipfergrund	360	288	360	220	1633~2674	10	22	36.0	16.4	1.11	0.0008	0.0016	0.0041	0.0077
Juancheng-Huanghe	430	370	430	220	1729~4253	10	18	43.0	23.9	1.08	0.0009	0.0016	0.0029	0.0051
Henan-Pohe	250	200	250	150	1305	8	8	31.3	31.3	1.11	0.0012	0.0022	0.0012	0.0022
Wei River	330	270	336	200	1000~1350	8	12	41.3	27.5	1.11	0.0007	0.0012	0.0015	0.0028
Nanjing-Chuhe	430	370	430	220	2420~4900	10	18	43.0	23.9	1.08	0.0009	0.0016	0.0029	0.0051

Note: t_{max} and t_{min} are the maximum and minimum thicknesses of CSWs respectively when an actual bridge has more than one thickness value.

(2) Calculation of k_g

According to Eqs. (12)-(15), the global shear buckling coefficient k_g is associated with the length to height ratio λ (l/h), and the rigidity ratios α (D_x/D_y) and β (D_{xy}/D_y). A statistical analysis of available bridges with CSWs (as shown in Table 2) shows that the rigidity ratio α varies from 0.0006 to 0.0069, whereas β is about (1.67~2.0)α. The following parametric study considers α ranging from 0.0005 to 0.0070, and β equal to 1.6α, 1.8α, 2.0α respectively.

Theoretically, the more numbers used in the trigonometric series (as shown in Eqs. (9)-(11)), the more precise the solution is. If m and n increase toward infinity, exact results of shear buckling stress can be obtained. However, the calculation effort increases with the increasing numbers m and n in the trigonometric series. In the case of the CSW with a length to height ratio l/h less than 5, the deviation between the results with m=30, n=30 and the results with m=25, n=25 is less than 1%. So, adopting m=30 and n=30 for further calculation will not only ensure the accuracy of the calculation but also reduce the calculation effort.

Table 3 shows the values of $k_{g,s}$ calculated for various values of D_x/D_y and l/h, and for β=1.6α, β=1.8α and β=2.0α respectively for a four-edge simple support. The results for β=1.6α and β=2.0α, compared to for β=1.8α, deviate less than 0.6%. The results show that the parameter β/α has little effect on the coefficient k_g for common bridges with CSWs. From an engineering application point of view, the deviations can be ignored. In addition, the conclusion remains unchanged for a four-edge fixed support, and for two edges constrained by flanges fixed and the other two edges simply supported. As a result, β=1.8α is used further in this paper.

Tables 4-6 list the values of the global shear buckling coefficient k_g for length to height ratios l/h varying from 1 to 5, a rigidity ratio D_x/D_y varying from 0.0005 to 0.0070, and a fixed value of β=1.8α. As shown in Tables 4 to 6, global shear buckling coefficients $k_{g,s}$, $k_{g,f}$, and $k_{g,fs}$ for an equal web length to height ratio l/h and rigidity ratio D_x/D_y exhibit relationships: $k_{g,f}/k_{g,s}$=1.84~1.90, $k_{g,fs}/k_{g,s}$=1.83~1.89, $k_{g,f}/k_{g,fs}$=1~1.013. This shows that the global shear buckling stress for the four-edge fixed support is only slightly higher than for two edges constrained by flanges fixed and the other two edges simply supported, the difference is less than 1.5%.

Table 3

The effect of β/α on the global shear buckling coefficient $k_{g,s}$ for the four-edge simple support

D_x/D_y		l/h				
		1	2	3	4	5
0.0005	β=1.6α	5.016	4.947	4.933	4.929	4.927
	β=1.8α	5.024	4.954	4.940	4.936	4.934
	β=2.0α	5.031	4.962	4.948	4.944	4.942
0.0015	β=1.6α	6.729	6.593	6.562	6.550	6.545
	β=1.8α	6.747	6.610	6.579	6.567	6.562
	β=2.0α	6.765	6.627	6.597	6.585	6.579
0.0025	β=1.6α	7.741	7.561	7.509	7.492	7.485
	β=1.8α	7.767	7.586	7.534	7.517	7.510
	β=2.0α	7.793	7.611	7.559	7.542	7.535
0.0035	β=1.6α	8.508	8.269	8.215	8.195	8.185
	β=1.8α	8.543	8.302	8.248	8.227	8.217
	β=2.0α	8.577	8.335	8.280	8.259	8.249
0.0050	β=1.6α	9.526	9.113	9.047	9.020	9.006
	β=1.8α	9.568	9.155	9.090	9.062	9.048
	β=2.0α	9.610	9.198	9.132	9.104	9.090
0.0070	β=1.6α	10.392	10.031	9.919	9.885	9.870
	β=1.8α	10.449	10.085	9.973	9.939	9.924
	β=2.0α	10.507	10.139	10.028	9.993	9.977

Table 4

Global shear buckling coefficient $k_{g,s}$ for a four-edge simple support

l/h	D_x/D_y											
	0.0005	0.001	0.0015	0.002	0.0025	0.003	0.0035	0.004	0.0045	0.005	0.006	0.007
1	5.024	6.047	6.747	7.335	7.767	8.165	8.543	8.903	9.249	9.568	10.025	10.449
1.5	4.975	5.964	6.647	7.186	7.639	8.017	8.371	8.705	9.002	9.255	9.728	10.172
2	4.954	5.937	6.610	7.134	7.586	7.958	8.302	8.624	8.899	9.155	9.638	10.085
2.5	4.945	5.924	6.589	7.113	7.552	7.929	8.268	8.579	8.853	9.112	9.596	10.005
3	4.940	5.914	6.579	7.100	7.534	7.911	8.248	8.553	8.829	9.090	9.556	9.973
4	4.936	5.906	6.567	7.085	7.517	7.893	8.227	8.528	8.806	9.062	9.527	9.939
5	4.932	5.903	6.562	7.079	7.510	7.884	8.217	8.517	8.794	9.048	9.510	9.924

Table 5

Global shear buckling coefficient $k_{g,f}$ for a four-edge fixed support

l/h	D_x/D_y											
	0.0005	0.001	0.0015	0.002	0.0025	0.003	0.0035	0.004	0.0045	0.005	0.006	0.007
1	9.454	11.352	12.654	13.666	14.533	15.297	15.946	16.546	17.109	17.642	18.616	19.428
1.5	9.392	11.242	12.502	13.494	14.314	15.039	15.669	16.247	16.785	17.273	18.153	18.954
2	9.370	11.204	12.451	13.427	14.240	14.950	15.573	16.143	16.662	17.140	18.016	18.784
2.5	9.360	11.187	12.428	13.397	14.207	14.909	15.529	16.093	16.606	17.083	17.942	18.712
3	9.357	11.178	12.415	13.382	14.188	14.887	15.505	16.065	16.577	17.051	17.908	18.668
4	9.354	11.170	12.409	13.368	14.171	14.865	15.482	16.039	16.548	17.020	17.871	18.628
5	9.352	11.165	12.402	13.359	14.163	14.856	15.473	16.029	16.538	17.007	17.856	18.610

Table 6
Global shear buckling coefficient $k_{g,fs}$ for two edges constrained by flanges fixed and the other two edges simply supported

l/h	D_x/D_y											
	0.0005	0.001	0.0015	0.002	0.0025	0.003	0.0035	0.004	0.0045	0.005	0.006	0.007
1	9.442	11.308	12.590	13.614	14.447	15.170	15.841	16.469	16.989	17.470	18.371	19.214
1.5	9.386	11.227	12.483	13.464	14.296	14.996	15.636	16.212	16.725	17.210	18.113	18.878
2	9.366	11.198	12.445	13.419	14.229	14.930	15.558	16.121	16.636	17.121	17.979	18.753
2.5	9.359	11.183	12.423	13.391	14.199	14.898	15.521	16.080	16.595	17.070	17.928	18.691
3	9.356	11.176	12.413	13.378	14.183	14.881	15.500	16.057	16.571	17.041	17.897	18.658
4	9.353	11.168	12.408	13.368	14.170	14.863	15.479	16.036	16.545	17.016	17.866	18.623
5	9.351	11.164	12.401	13.358	14.162	14.855	15.472	16.028	16.537	17.006	17.854	18.607

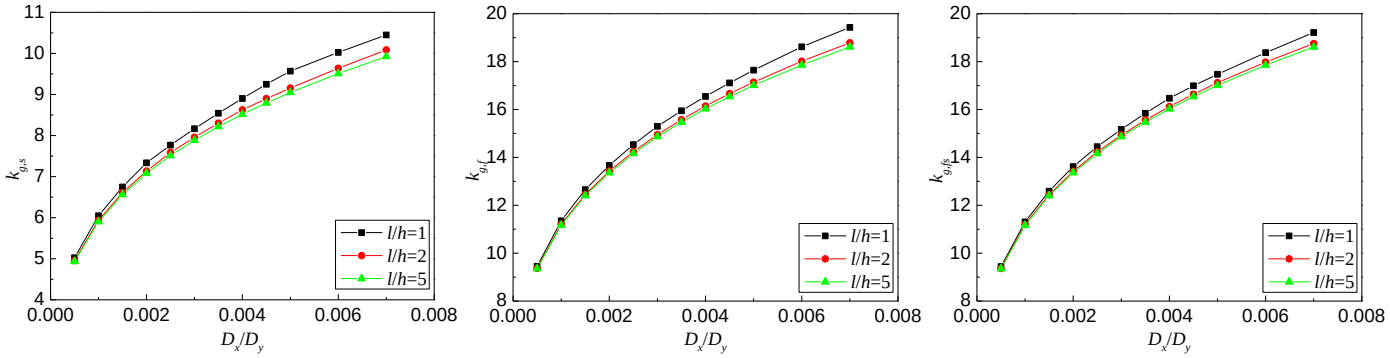

（a）Four-edge simply support (b) Four-edge fixed support (c) Two edges constrained by flanges fixed and the other two edges simply supported

Fig. 3 The effect of the rigidity ratio D_x/D_y on the global shear buckling coefficient k_g

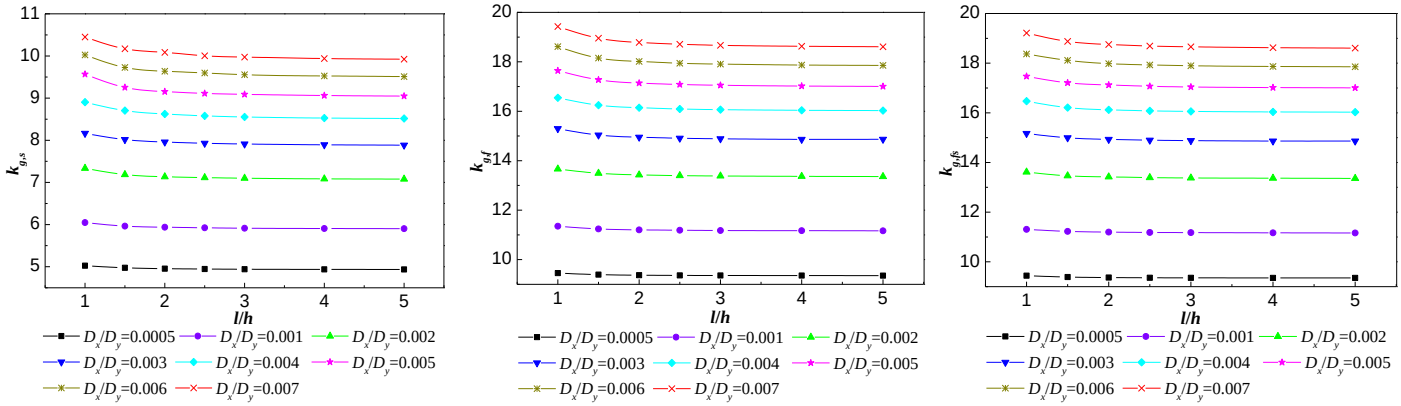

（a）Four-edge simply support (b) Four-edge fixed support (c) Two edges constrained by flanges fixed and the other two edges simply supported

Fig. 4 The effect of the length to height ratio l/h on the global shear buckling coefficient k_g

Table 7
Values of the global shear buckling coefficient k_g for l/h=5

k_g	D_x/D_y													
	0.0005	0.001	0.0015	0.002	0.0025	0.003	0.0035	0.004	0.0045	0.005	0.0055	0.006	0.0065	0.007
$k_{g,s}$	4.932	5.903	6.562	7.079	7.510	7.884	8.217	8.517	8.794	9.048	9.288	9.510	9.722	9.924
$k_{g,f}$	9.352	11.165	12.402	13.359	14.163	14.856	15.473	16.029	16.538	17.007	17.444	17.856	18.242	18.610
$k_{g,fs}$	9.351	11.164	12.401	13.358	14.162	14.855	15.472	16.028	16.537	17.006	17.443	17.854	18.240	18.607

(3) The effect of the rigidity ratio D_x/D_y and the length to height ratio l/h on the global shear buckling coefficient k_g

According to the values of k_g given in Tables 4 to 6, for common bridges with CSWs, Figs. 3-4 show the effect of the web rigidity ratio D_x/D_y and the length to height ratio l/h on the global shear buckling coefficient k_g. As we can see from Figs. 3-4, the global shear buckling coefficient k_g increases with the increase of the rigidity ratio D_x/D_y, and decreases with the increase of the length to height ratio l/h but only very little. When l/h is larger than 2, which is common for CSW bridges, the change of k_g is minimal and the values of k_g show a converging trend.

2.3.3. Elastic global shear buckling stress of CSWs

Substituting Eq. (2) into Eq. (15), the elastic global shear buckling stress of CSWs can be expressed as Eq. (17).

$$\tau_g^e = k_g \frac{E(3a+c)d^2}{6qh^2} = k_g \frac{Ed^2(3a+d.\csc\theta)}{6h^2(2a+2d.\cot\theta)} \tag{17}$$

Because the values of k_g show a converging trend when l/h is larger than 2, we assume l/h=5 for further calculation. This will not only ensure the accuracy of the calculation but also meet the engineering requirements of design simplicity. Table 7 lists the values of k_g for l/h=5.

Through fitting of the data in Table 7, for CSWs with $0.0005 \leqslant \alpha \leqslant 0.0070$, the global shear buckling coefficients $k_{g,s}$, $k_{g,f}$, and $k_{g,fs}$ can be estimated respectively as Eqs. (18) and (19).

For a four-edge simple support:

$$k_{g,s} = 36.8\alpha^{0.2648} \tag{18}$$

For a four-edge fixed support, or for two edges constrained by flanges fixed and the other two edges simply supported:

$$k_{g,f} = k_{g,fs} = 67.7\alpha^{0.2608} \tag{19}$$

For trapezoidal CSWs that are commonly used in actual bridges, the rigidity ratio α can be expressed as Eq. (20).

$$\alpha = \frac{D_x}{D_y} = \frac{q^2t^2}{2s(3a+c)d^2} = \left(\frac{t}{d}\right)^2 \frac{(2a+2d.\cot\theta)^2}{2(2a+2d.\csc\theta)(3a+d.\csc\theta)} \tag{20}$$

2.4. Elastic interactive shear buckling

2.4.1. Critical buckling stress under pure shear

For the interactive shear buckling analysis, folded plate theory is used. A folded plate structure is a spatial thin wall system with several long and thin plates intersecting. Since interactive shear buckling represents the buckling of a few panels, several panels of CSWs can be treated as a folded plate. For simplicity, the folded plate composed of two adjacent panels shown in Fig. 5 is studied here. According to the theory of thin plates and shells, if $l_3/l_* \leq 0.2$, the folded plate can be analyzed as a shallow shell. CSWs general meet this condition.

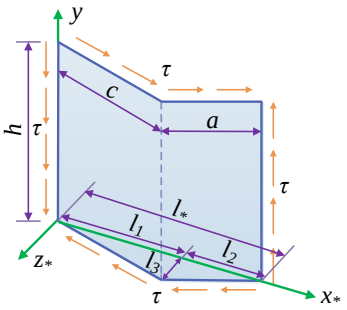

Fig. 5 Shear transfer of interactive shear buckling

In the coordinate system as shown in Fig. 5, the equation for the surface of the shell can be expressed as Eq. (21).

$$z = \frac{l_3}{l_1}x\left[1-u\left(x-l_1\right)\right] + \frac{l_3}{l_2}\left[\left(l_1+l_2\right)-x\right]u\left(x-l_1\right) \tag{21}$$

where $u(x-l_1)$ is the step function and can be expressed as $u(x-l_1)=\begin{cases}0 & x<l_1\\ 1 & x\geq l_1\end{cases}$.

The equilibrium equation and the deformation compatibility equation of a shallow shell under pure shear force can be expressed respectively as Eqs. (22) and (23) [30].

$$\frac{D}{t}\nabla^4 f + \left(k_x\frac{\partial^2}{\partial y^2} - 2k_{xy}\frac{\partial^2}{\partial x\partial y} + k_y\frac{\partial^2}{\partial x^2}\right)\Phi = 2\tau\frac{\partial^2 f}{\partial x\partial y} \tag{22}$$

$$\frac{1}{E}\nabla^4\Phi - \left(k_x\frac{\partial^2}{\partial y^2} - 2k_{xy}\frac{\partial^2}{\partial x\partial y} + k_y\frac{\partial^2}{\partial x^2}\right)f = 0 \tag{23}$$

where f is the out of plane deflection of the shell, Φ is the stress function, $k_x = -\frac{\partial^2 z}{\partial x^2}$, $k_y = -\frac{\partial^2 z}{\partial y^2}$, $k_{xy} = -\frac{\partial^2 z}{\partial x\partial y}$.

It can be conservatively assumed that the boundary conditions of CSWs for the interactive shear buckling analysis satisfy four-edge simple support. The deflection function and stress function can be expressed respectively as Eqs. (24) and (25).

$$f = \sum_{m=1}^{\infty}\sum_{n=1}^{\infty} A_{mn}\sin\frac{m\pi x}{l_*}\sin\frac{n\pi y}{h} \tag{24}$$

$$\Phi = \sum_{m=1}^{\infty}\sum_{n=1}^{\infty} B_{mn}\sin\frac{m\pi x}{l_*}\sin\frac{n\pi y}{h} \tag{25}$$

According to the Galerkin method and give $\eta = h/l_*$, Eqs. (24) and (25) can be simplified as Eqs. (26) and (27) respectively.

$$\begin{aligned}&A_{ij}\frac{D\pi^4}{4t\eta^3 l_*^2}\left(\eta^2 i^2 + j^2\right)^2 + \frac{\pi^2 l_3\left(l_1+l_2\right)}{2\eta l_* l_1 l_2}j^2\sin\frac{i\pi l_1}{l_*}\sum_{p=1}^{\infty}B_{pj}\sin\frac{p\pi l_1}{l_*}\\ &-8\tau\sum_{m=1}^{\infty}\sum_{n=1}^{\infty}A_{mn}\frac{mnij}{\left(i^2-m^2\right)\left(j^2-n^2\right)} = 0\\ &(m\pm i = \text{odd},\ n\pm j = \text{odd})\end{aligned} \tag{26}$$

$$B_{ij}\frac{\pi^4}{4E\eta^3 l_*^2}\left(\eta^2 i^2 + j^2\right)^2 - \frac{\pi^2 l_3\left(l_1+l_2\right)}{2\eta l_* l_1 l_2}j^2\sin\frac{i\pi l_1}{l_*}\sum_{m=1}^{\infty}A_{mj}\sin\frac{m\pi l_1}{l_*} = 0 \tag{27}$$

Make $\gamma = l_1/l_*$, then $l_1 = \gamma l_*$, $l_2 = (1-\gamma)l_*$, $l_3^2 = c^2 - \gamma^2 l_*^2$. By substituting Eq. (27) to Eq. (26), Eq. (26) can be simplified as Eq. (28).

$$\begin{aligned}&A_{ij}\frac{\pi^4}{4\eta^3}\frac{D}{tl_*^2}\left(\eta^2 i^2 + j^2\right)^2\\ &+12\eta j^4(1-u^2)\frac{D}{tl_*^2}\frac{\left(c^2-\gamma^2 l_*^2\right)}{t^2\gamma^2(1-\gamma)^2}\sin i\gamma\pi\sum_{p=1}^{\infty}\frac{\left(\sin p\gamma\pi\right)^2}{\left(\eta^2 p^2 + j^2\right)^2}\sum_{q=1}^{\infty}A_{ij}\sin q\gamma\pi\\ &-8\tau\sum_{m=1}^{\infty}\sum_{n=1}^{\infty}A_{mn}\frac{mnij}{\left(i^2-m^2\right)\left(j^2-n^2\right)} = 0\\ &(m\pm i = \text{odd},\ n\pm j = \text{odd})\end{aligned} \tag{28}$$

Table 2 shows that the flat panel width a is almost equal to the inclined panel width c for actual bridges with CSWs. Sayed-Ahmed [20] also proposed $a=c$. When $a=c$, then $l_1 = l_2 = 0.5l_*$, $l_3 = a\sin(\theta/2)$. Eq. (28) can be simplified as Eq. (29).

$$\begin{aligned}&A_{ij}\frac{D}{tl_*^2}\frac{\pi^4}{4\eta^3}\left(\eta^2 i^2 + j^2\right)^2\\ &+192\eta j^4(1-u^2)\sin\frac{i\pi}{2}\frac{D}{tl_*^2}\left(\frac{a}{t}\sin\frac{\theta}{2}\right)^2\sum_{p=1}^{\infty}\frac{\left(\sin\frac{p\pi}{2}\right)^2}{\left(\lambda^2 p^2 + j^2\right)^2}\sum_{q=1}^{\infty}A_{ij}\sin\frac{q\pi}{2}\\ &-8\tau\sum_{m=1}^{\infty}\sum_{n=1}^{\infty}A_{mn}\frac{mnij}{\left(i^2-m^2\right)\left(j^2-n^2\right)} = 0\\ &(m\pm i = \text{odd},\ n\pm j = \text{odd})\end{aligned} \tag{29}$$

By assigning values to i and j in Eq. (28) or (29), a series of linear algebraic equations with A_{mn} as unknowns can be obtained. Then the critical shear buckling stress can be derived by assuming the coefficient determinant of the linear algebraic equations equals zero. (i. e. a linear bifurcation analysis).

According to Eq. (28), the elastic interactive shear buckling stress of CSWs can be expressed as Eq. (30).

$$\tau_i^e = k_i \frac{D}{l_*^2 t} \tag{30}$$

For CSWs with $a=c$, Eq. (30) can be expressed as Eq. (31).

$$\tau_i^e = k_i \frac{Et^2}{12\left(1-\mu^2\right)\left(2a\cos\left(\theta/2\right)\right)^2} \tag{31}$$

where k_i is the elastic interactive shear buckling coefficient of CSWs. The detailed solution process of the coefficient k_i is given below.

2.4.2. Calculation of the interactive shear buckling coefficient k_i

According to Eq. (28) and using some mathematical softwares, the interactive shear buckling coefficient k_i can be calculated easily. According to Eq. (29), the coefficient k_i for CSWs with $a=c$ is associated with the aspect ratio h/l_* and the parameter $\frac{a}{t}\sin\frac{\theta}{2}$.

Table 2 shows that the parameter a/t varies from 16 to 54. For CSWs used in actual bridges, values of θ between 30° and 45° are typical [31], so the parameter $\frac{a}{t}\sin\frac{\theta}{2}$ normally varies from 4 to 21. Table 8 shows the values of k_i in the case of $h/l_* \le 6$ and $0 \le \frac{a}{t}\sin\frac{\theta}{2} \le 30$. The coefficient k_i for CSWs with $a=c$ can be calculated by linear interpolation.

Table 8
The interactive shear buckling coefficient of CSWs k_i

$a\sin(\theta/2)/t$ \ h/l	1	1.5	2	2.5	3	4	6
0	92.0294	69.7779	64.6068	59.5429	57.6401	55.5123	54.0737
0.25	93.1769	70.4358	65.1533	60.1504	58.2841	56.2034	54.7502
0.5	96.4737	72.3623	66.7412	61.6682	59.7653	57.7165	56.2556
0.75	101.5418	75.4292	69.2377	64.1539	62.2492	60.0918	58.6002
1	107.9047	79.4587	72.4772	67.3685	65.4597	63.3175	61.8178
1.25	115.1066	84.2573	76.3023	71.1993	69.2471	67.1066	65.6054
1.5	122.7766	89.6403	80.5822	75.4736	73.5211	71.3398	69.8362
1.75	130.6405	95.4438	85.2126	80.0664	78.1059	75.9049	74.4034
2	138.5077	101.529	90.1107	85.0094	83.0432	80.8299	79.3286
2.25	146.2490	107.7805	95.2084	90.1018	88.1264	85.8974	84.3952
2.5	153.7778	114.1043	100.4489	95.3454	93.3434	91.1428	89.6401
2.75	161.0361	120.4235	105.7836	100.2358	98.1972	96.0022	94.5007
3	167.9851	126.6760	111.1704	104.6219	102.5653	100.3454	98.6773
3.25	174.5993	132.8113	116.5728	109.0573	106.9074	104.6971	102.0138
3.5	180.8631	138.7891	121.9590	113.5325	110.5256	108.2896	105.3762
3.75	186.7687	144.5771	127.3010	118.0361	114.1704	111.9992	108.7868
4	192.3144	150.1502	132.5740	122.5558	117.8456	115.6795	112.2527
4.25	197.5036	155.4890	137.7565	127.0794	121.5508	119.3297	115.7745
4.5	202.3438	160.5796	142.8289	131.5948	125.2828	123.0553	119.3492
4.75	206.8458	165.4126	147.7743	136.0904	129.0371	126.7668	122.9721
5	211.0229	169.9825	152.5772	140.5553	132.8082	129.9071	126.6377
5.5	218.4650	178.3284	161.7019	149.3521	140.3772	135.0183	132.0734
6	224.8047	185.6367	170.1093	157.9097	147.9408	140.2147	137.4093
6.5	230.1828	191.9637	177.7254	166.1610	155.4507	145.4974	142.7003
7	234.7358	197.3909	184.4964	174.0451	162.8600	150.8560	148.1038
7.5	238.5894	202.0147	190.3940	181.5032	170.1220	156.2740	153.4890
8	241.8551	205.9366	195.4237	188.4706	177.1872	161.7319	159.0231
9	246.9941	212.0662	203.1006	197.9587	190.4379	172.6793	169.9498
10	249.6481	216.4745	208.2566	203.1951	196.9761	183.4995	178.9182
12	252.7794	222.0752	214.1494	209.0746	203.8849	193.4008	190.8814
14	254.6094	225.2856	217.2037	212.2282	208.4515	204.5305	202.8039
16	255.7683	227.2733	219.0022	214.6838	211.9712	209.8780	208.0037
18	256.5482	228.5854	220.1599	215.6484	212.9664	210.7748	209.0133
20	257.0984	229.4967	220.9213	216.3216	213.6575	211.4042	209.6595
22	257.5011	230.1558	221.4389	216.8106	214.1583	211.8635	210.0977
24	257.805	230.6483	221.8279	217.1773	214.5333	212.2091	210.4349
26	258.0399	231.0262	222.1278	217.4597	214.8217	212.4759	210.6952
28	258.2253	231.3226	222.3639	217.6818	215.0485	212.6861	210.9005
30	258.3743	231.5596	222.5532	217.8598	215.2300	212.8548	211.0652

2.5. Discussion of the local, global and interactive shear buckling stresses

Three shear buckling modes are discussed theoretically in this paper. Local buckling is the buckling of a panel and solved by analyzing a single flat panel under shear force, whereas global buckling is the buckling of the whole CSW and solved by treating the whole CSW as an orthotropic plate. Interactive buckling is the buckling of 2~4 panels and solved by treating the 2~4 panels as a folded plate.

Theoretically, the local shear buckling stress τ_l^e is associated with t/p, p/h which can be seen from Eqs. (4)-(7), whereas the global shear buckling stress τ_g^e is associated with θ, d/h and t/d which can be seen from Eqs. (17)-(20). The interactive shear buckling stress τ_i^e is associated with the geometric dimensioning of CSWs which can be seen from Eqs. (28)-(31). When CSWs have equal d/t, p/h and θ values, they will have an equal t/p ratio which affects the local shear buckling stress τ_l^e, and equal d/h and t/d ratios which affect the global shear buckling stress τ_g^e. In the case of $a=c$, they will have an equal $\eta = h/\left(2a\cos(\theta/2)\right)$ and $t/\left(a\cos(\theta/2)\right)$ which affect the interactive shear buckling stress τ_i^e. For CSWs with equal d/t, a/h and θ values, buckling stresses τ_l^e, τ_g^e, and τ_i^e will theoretically be equal.

3. Finite element analysis

An elastic FEA is carried out in the ANSYS software [32] to study the influence of d/t, a/h and θ on the shear buckling stress of CSWs and to see if the analytical formulas are correct. According to Yi et al. [15], a/h=0.1~0.2 and d/t=10~25 in actual bridges. In this study, conservatively adopting a/h=0.1~0.3 and d/t=10~30, while other geometric parameters are taken as: θ=30°~45° and t=8mm~12mm. The span of the girders is set as 20q. In addition, the width and the thickness of flanges are 8d and 80mm respectively. There are three stiffeners and their behavior is assumed to be rigid.

3.1. Finite element model

A shell element (shell 181) is used to model the girders with CSWs. The finite element model is shown in Fig. 6 and the boundary conditions are given in Table 9. A concentrated load is applied at the midspan (point 2). All models adopt a symmetry boundary condition with roller supports at the intersection nodes of the bottom flange and the end stiffeners, and Point 1 restrained in the longitudinal direction (x direction) [26]. In addition, Point 1 and Point 2 are restrained in the lateral direction (z direction) to avoid lateral-torsion buckling.

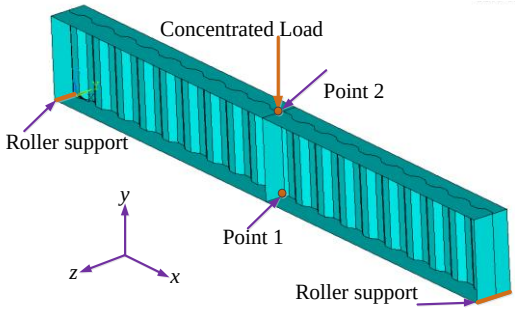

Fig. 6 Load and boundary conditions of a girder with CSWs

Table 9
Boundary conditions of finite element models

Boundary	δ_x	δ_y	δ_z	θ_x	θ_y	θ_z
Roller support	○	●	●	●	●	○
Point 1	●	○	●	○	○	○
Point 2	○	○	●	○	○	○

Note: ○: Free; ●: Restrained.

In this study, the number of elements per sub-panel is 6, as suggested by Eldib [3], and the element mesh size is $a/6$. The elastic modulus and Poisson's ratio of steel are taken as 210000MPa and 0.3 respectively. Fig. 7 represents three shear buckling modes of CSWs.

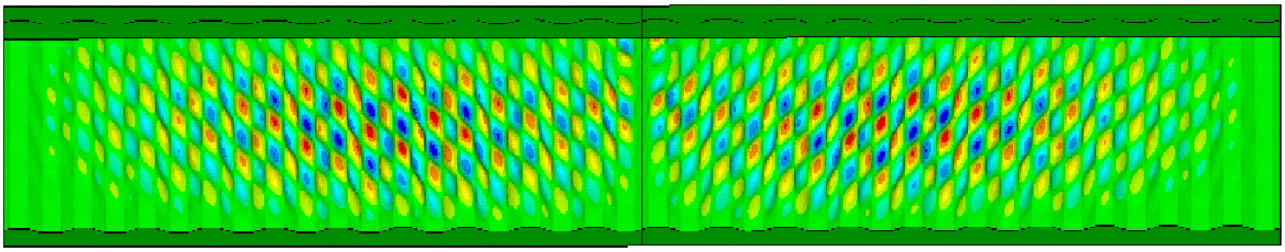

(a) Local shear buckling

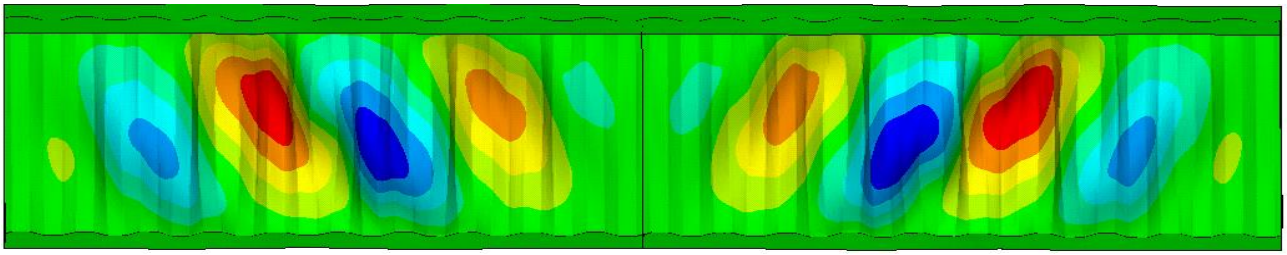

(b) Global shear buckling

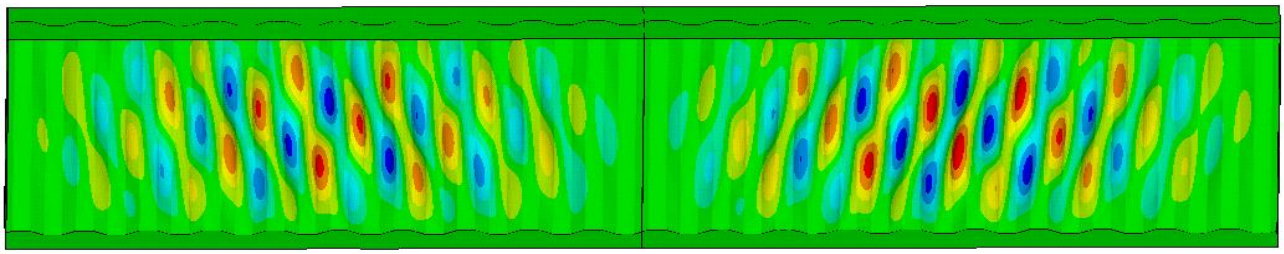

(c) Interactive shear buckling

Fig. 7 Three shear buckling modes

3.2. Parametric analysis

Theoretically, in the case of a=c, and equal d/t, a/h and θ, the elastic local shear buckling stress τ_l^e, global shear buckling stress τ_g^e, and interactive shear buckling stress τ_i^e should be equal. It can be seen from Fig. 8 that for CSWs with different web thicknesses but equal d/t, a/h and θ when a=c, the FEA results τ_{FEA}^e are indeed practically the equal which is in good agreement with the theoretical expectations. τ_{FEA}^e is the maximum shear stress of CSWs from FEA. It is worth mentioning that the d/t, a/h and θ are the determining factors, rather than t. In what follows, t=10mm is adopted.

The influence of d/t, a/h and θ on the elastic shear buckling stress is shown in Tables 10-12 and Figs. 9-10. It can be seen from Tables 10-12 and Figs. 9-10 that, apart from the global shear buckling modes with small d/t and small a/h, the FEA results agree well with the theoretical results τ_{cr}^e. The elastic shear buckling stress of CSWs τ_{cr}^e is controlled by the minimum value of local, global and interactive shear buckling stress, and can be calculated by Eq. (32).

$$\tau_{cr}^e = \text{minimum}\left(\tau_{l,s}^e, \tau_{g,s}^e, \tau_i^e\right) \tag{32}$$

It can be seen from Fig. 9 that the shear buckling stress greatly decreases with the increase of d/t. That is to say, improving the thickness of CSWs is an effective method to improve the shear buckling stress of CSWs. It can be seen from Fig. 10 (a) that the shear buckling stress increases with the increase of a/h. However, with the increase of a/h, the buckling stress τ_{FEA}^e shows a converging trend. It can be seen from Fig. 10 (b) that the shear buckling stress increases with the increase of θ. Though improving θ can improve the shear buckling stress, θ=30°~45° is adopted in actual engineering because larger θ need more steel and is not economic.

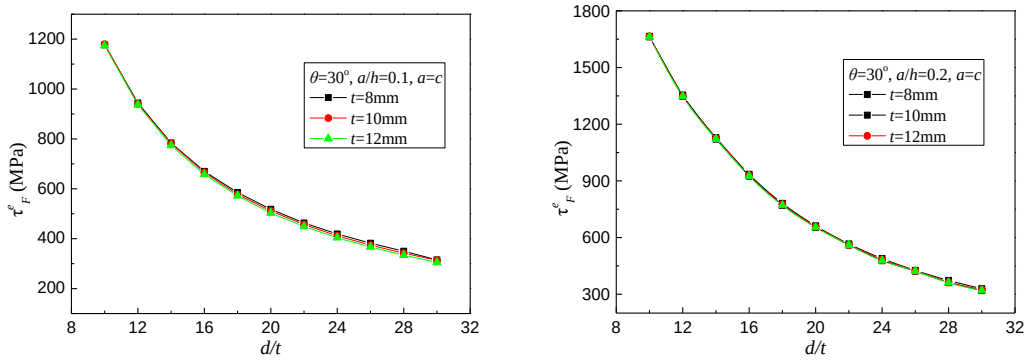

(a) a/h=0.1 (b) a/h=0.2

Fig. 8 Influence of t on the elastic shear buckling stress τ_{FEA}^e

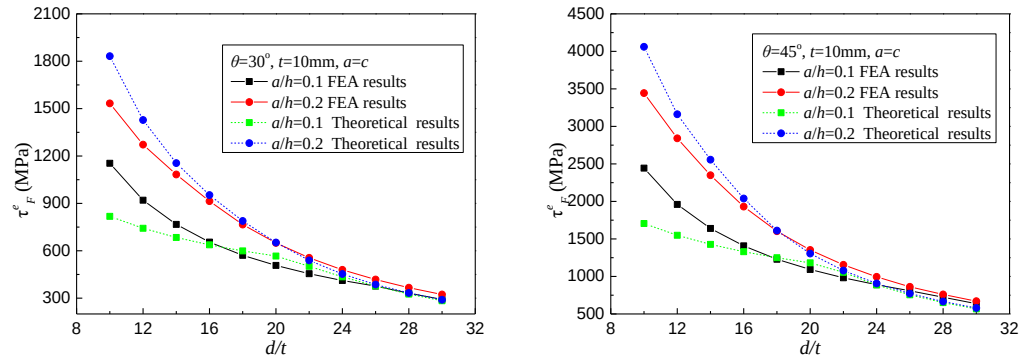

(a) θ=30° (b) θ=45°

Fig. 9 Influence of d/t on the elastic shear buckling stress

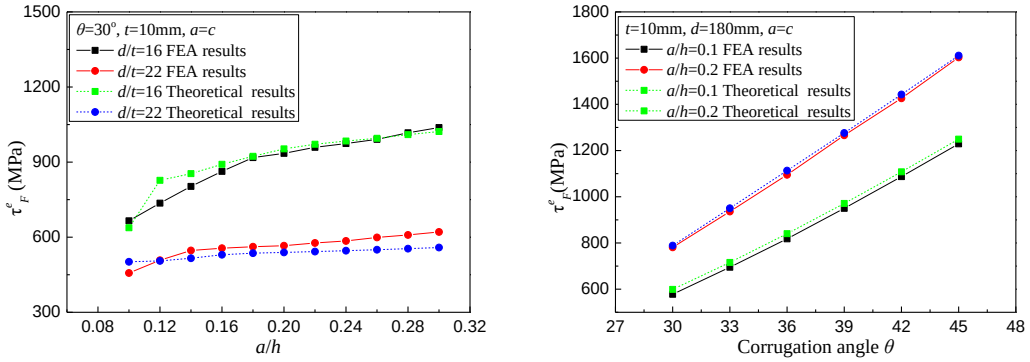

(a) a/h (b) θ

Fig. 10 Influence of a/h and θ on the elastic shear buckling stress

Table 10
Elastic shear buckling stress of CSWs with different d/t

θ (^{O})	a/h	d/t	a (mm)	b (mm)	d (mm)	h (mm)	$\tau_{l,s}$ (Mpa)	$\tau_{g,s}$ (Mpa)	τ_i (Mpa)	τ_{cr} (Mpa)	τ_{FEA} (Mpa)	τ_{FEA}/τ_{cr}^e	Buckling mode
		10	200	173	100	2000	2553	818	1673	818	1180	1.442	G
		12	240	208	120	2400	1773	743	1260	743	940	1.266	G
		14	280	242	140	2800	1302	684	998	684	782	1.142	G
		16	320	277	160	3200	997	638	821	638	665	1.043	G
		18	360	312	180	3600	788	599	692	599	578	0.965	G
	0.1	20	400	346	200	4000	638	567	589	567	511	0.903	G
		22	440	381	220	4400	527	539	502	502	457	0.910	I
		24	480	416	240	4800	443	514	435	435	412	0.947	I
		26	520	450	260	5200	378	493	382	378	374	0.991	L
		28	560	485	280	5600	326	474	337	326	342	1.050	L
30		30	600	520	300	6000	284	457	297	284	314	1.105	L
		10	200	173	100	1000	2610	3272	1832	1832	1664	0.908	I
		12	240	208	120	1200	1812	2971	1428	1428	1354	0.949	I
		14	280	242	140	1400	1332	2738	1155	1155	1129	0.977	I
		16	320	277	160	1600	1019	2551	953	953	935	0.981	I
		18	360	312	180	1800	805	2396	789	789	781	0.990	I
	0.2	20	400	346	200	2000	652	2266	654	652	662	1.015	L
		22	440	381	220	2200	539	2155	549	539	566	1.050	L
		24	480	416	240	2400	453	2058	467	453	489	1.079	L
		26	520	450	260	2600	386	1972	401	386	426	1.103	L
		28	560	485	280	2800	333	1897	349	333	373	1.121	L
		30	600	520	300	3000	290	1828	306	290	329	1.135	L
		10	141	100	100	1414	5106	1706	3717	1706	2444	1.433	G
		12	170	120	120	1697	3546	1549	2806	1549	1960	1.266	G
		14	198	140	140	1980	2605	1427	2229	1427	1640	1.149	G
		16	226	160	160	2263	1994	1330	1837	1330	1408	1.059	G
	0.1	18	255	180	180	2546	1576	1249	1546	1249	1229	0.984	G
		20	283	200	200	2828	1276	1182	1302	1182	1093	0.925	G
		22	311	220	220	3111	1055	1124	1112	1055	982	0.931	L
		24	339	240	240	3394	886	1073	965	886	890	1.004	L
		26	368	260	260	3677	755	1028	848	755	809	1.071	L
		28	396	280	280	3960	651	989	741	651	723	1.110	L
45		30	424	300	300	4243	567	953	653	567	637	1.123	L
		10	141	100	100	707	5220	6823	4061	4061	3444	0.848	I
		12	170	120	120	849	3625	6195	3162	3162	2841	0.899	I
		14	198	140	140	990	2663	5709	2556	2556	2349	0.919	I
		16	226	160	160	1131	2039	5320	2102	2039	1931	0.947	L
		18	255	180	180	1273	1611	4998	1731	1611	1603	0.995	L
	0.2	20	283	200	200	1414	1305	4727	1431	1305	1353	1.037	L
		22	311	220	220	1556	1078	4494	1202	1078	1155	1.071	L
		24	339	240	240	1697	906	4292	1021	906	995	1.098	L
		26	368	260	260	1838	772	4114	878	772	862	1.116	L
		28	396	280	280	1980	666	3955	763	666	760	1.142	L
		30	424	300	300	2121	580	3813	669	580	670	1.155	L
Average												1.054	
Coefficient of variation												0.122	
Average (G)												1.131	
Coefficient of variation (G)												0.165	
Average (I and L)												1.024	
Coefficient of variation (I and L)												0.083	

Table 11
Elastic shear buckling stress of CSWs with different *a*/*h*

θ (°)	*d*/*t*	*a*/*h*	*a* (mm)	*b* (mm)	*d* (mm)	*h* (mm)	$\tau_{l,s}$ (Mpa)	$\tau_{g,s}$ (Mpa)	τ_i (Mpa)	τ_{cr} (Mpa)	τ_{FEA} (Mpa)	τ_{FEA}/τ^e_{cr}	Buckling mode
		0.1	320	277	160	3200	997	638	821	638	665	1.043	G
		0.12	320	277	160	2667	1000	918	827	827	736	0.890	I
		0.14	320	277	160	2286	1004	1250	854	854	803	0.940	I
		0.16	320	277	160	2000	1009	1632	891	891	863	0.968	I
		0.18	320	277	160	1778	1014	2066	923	923	918	0.994	I
	16	0.2	320	277	160	1600	1019	2551	953	953	935	0.981	I
		0.22	320	277	160	1455	1026	3086	971	971	959	0.987	I
		0.24	320	277	160	1333	1032	3673	984	984	974	0.990	I
		0.26	320	277	160	1231	1040	4311	995	995	991	0.996	I
		0.28	320	277	160	1143	1048	4999	1010	1010	1017	1.007	I
30		0.3	320	277	160	1067	1057	5739	1022	1022	1038	1.016	I
		0.1	440	381	220	4400	527	539	502	502	457	0.911	I
		0.12	440	381	220	3667	529	776	505	505	508	1.005	I
		0.14	440	381	220	3143	531	1056	516	516	547	1.060	I
		0.16	440	381	220	2750	534	1379	530	530	556	1.049	I
		0.18	440	381	220	2444	536	1745	541	536	562	1.048	L
	22	0.2	440	381	220	2200	539	2155	549	539	566	1.050	L
		0.22	440	381	220	2000	542	2607	556	542	577	1.064	L
		0.24	440	381	220	1833	546	3103	561	546	585	1.071	L
		0.26	440	381	220	1692	550	3642	566	550	599	1.089	L
		0.28	440	381	220	1571	554	4224	572	554	609	1.099	L
Average												1.012	
Coefficient of variation												0.055	

Table 12
Elastic shear buckling stress of CSWs with different θ

d/*t*	*a*/*h*	θ (°)	*a* (mm)	*b* (mm)	*d* (mm)	*h* (mm)	$\tau_{l,s}$ (Mpa)	$\tau_{g,s}$ (Mpa)	τ_i (Mpa)	τ_{cr} (Mpa)	τ_{FEA} (Mpa)	τ_{FEA}/τ^e_{cr}	Buckling mode
		30	360	312	360	3600	788	599	692	599	578	0.965	G
		33	330	277	330	3305	935	716	824	716	695	0.971	G
	0.1	36	306	248	306	3062	1089	840	964	840	818	0.974	G
		39	286	222	286	2860	1248	971	1110	971	950	0.978	G
		42	269	200	269	2690	1411	1108	1260	1108	1087	0.981	G
18		45	255	180	255	2546	1576	1249	1414	1249	1229	0.984	G
		30	360	312	360	1800	805	2396	789	789	781	0.990	I
		33	330	277	330	1652	956	2863	950	950	936	0.985	I
	0.2	36	306	248	306	1531	1113	3361	1126	1113	1095	0.984	L
		39	286	222	286	1430	1276	3885	1315	1276	1266	0.992	L
		42	269	200	269	1345	1443	4432	1516	1443	1426	0.989	L
		45	255	180	255	1273	1611	4998	1729	1611	1603	0.995	L
Average												0.982	
Coefficient of variation												0.009	

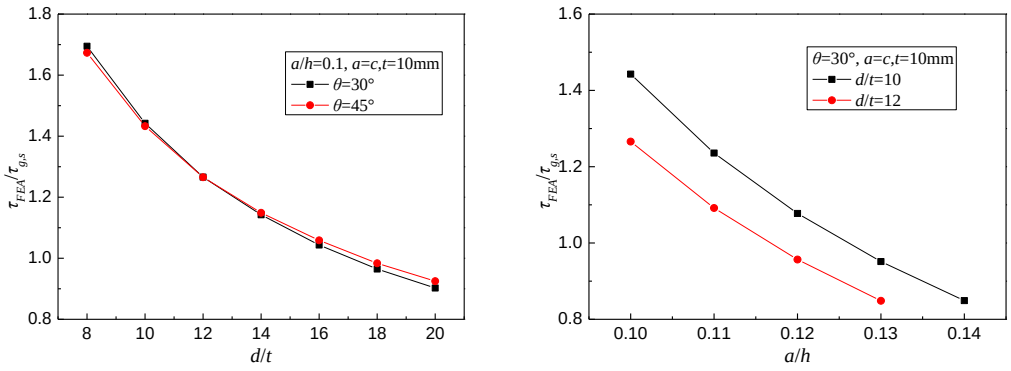

(a) *d*/*t* (b) *a*/*h*

Fig. 11 Influence of *d*/*t* and *a*/*h* on $\tau^e_{FEA}/\tau^e_{g,s}$

The boundary condition of the global buckling mode is complicated. Fig. 11 shows the ratios of τ^e_{FEA} to $\tau^e_{g,s}$ varies with *d*/*t* and *a*/*h* in the case of $\tau^e_{g,s} < minimum\left(\tau^e_{l,s}, \tau^e_i\right)$ which the global buckling becomes the primary failure mode. It can be seen from Fig. 11 that $\tau^e_{FEA}/\tau^e_{g,s}$ decreases with the increase of *d*/*t* and *a*/*h*. That is to say, the constraint effect of flanges on CSWs gradually decreases with the increase of *d*/*t* and *a*/*h*. Although the ratios of τ^e_{FEA} to $\tau^e_{g,s}$ are high for small *d*/*t* and *a*/*h*, the simple support boundary condition is adopted for conservative consideration.

4. Shear design of CSWs

Considering material nonlinearity and yielding, the formula for the elastic shear buckling stress cannot keep up with the actual. So a formula which can reflect the actual shear strength needs to be proposed. Important work has been done by Elgaaly [22], Driver [23], El Metwally [17], Yi et al. [15], Sause [31], Nie et al.[21]. The previous design formulas may be not precise because adopting the interactive shear buckling stress formula which based on the relationship between the local and global shear buckling stresses, and the yield stress only. All the previous elastic interactive formulas adopt $\left(1/\tau_i^e\right)^n=\left(1/\tau_l^e\right)^n+\left(1/\tau_g^e\right)^n$, n=1~4 [15], show that the interactive shear buckling stress is the minimum value of the three shear buckling modes, which is not reasonable and lacks theoretical support. Unlike the past, in this study, the formulas for the elastic global and interactive shear buckling stresses proposed in section 2 are used in the design formula.

Eq. (33) was provided to calculate the ultimate shear strength of CSWs in the design manual for PC bridges with CSWs [33].

$$\tau_{cr}=\tau_y\times\begin{cases}1 & \lambda_{cr}\le 0.6\\ 1-0.614\left(\lambda_{cr}-0.6\right) & 0.6\le\lambda_{cr}\le\sqrt{2}\\ 1/\lambda_{cr}^2 & \lambda_{cr}>\sqrt{2}\end{cases} \tag{33}$$

$$\lambda_{cr}=\sqrt{\tau_y/\tau_{cr}^{e*}} \tag{34}$$

For conservative consideration, τ_{cr}^{e*} adopts Eq. (32) introducing a modification factor.

$$\tau_{cr}^{e*}=\text{minimum}\left(0.85\tau_{l,s}^e,\tau_{g,s}^e,0.85\tau_i^e\right) \tag{35}$$

where τ_y is the shear yield stress and can be calculated by $\tau_y=f_y/\sqrt{3}$, f_y is the uniaxial yield stress.

Eq. (33) is verified by using published experimental results of 102 specimens obtained by Elgaaly et al. [22], Lindner et al. [34], Peil [35], Gil et al. [36], Abbas et al. [18], Moon et al.[24]. Tables 13-18 show a comparison between the shear strength calculated by Eq. (33) and four previous design methods and experimental results τ_e [31]. In Tables 13-18, $\tau_{n,A}$, $\tau_{n,B}$, $\tau_{n,M}$, $\tau_{n,Y}$ are the shear strength of CSWs calculated by the four previous design methods proposed by Driver [23], Sause [31], El Metwally [17], Yi et al. [15]. Fig. 12 shows the normalized shear capacity τ_e/τ_y and τ_e/τ_{cr} versus λ_{cr}. It can be seen that all the tests have a ratio $\tau_e/\tau_{cr}\ge 0.8$.

Table 13
Comparison between the shear strength calculated by the proposed design formulas and the test results obtained by Elgaaly et al.[22]

Specimen	*e*/*h*	*a* (mm)	*b* (mm)	*θ* (°)	*h* (mm)	*t* (mm)	τ_y (Mpa)	τ_e (Mpa)	λ_{cr}	τ_{cr} (Mpa)	τ_e/τ_{cr}	$\tau_e/\tau_{n,A}$	$\tau_e/\tau_{n,B}$	$\tau_e/\tau_{n,M}$	$\tau_e/\tau_{n,Y}$
V-PILOTA	1	38.1	25.4	45	304.8	0.7823	358	346.54	1.03	262.5	1.320	1.404	1.349	1.316	1.363
V-PILOTB	1	38.1	25.4	45	304.8	0.7849	368	347.54	1.05	267.4	1.300	1.177	1.132	1.109	1.149
V121216A	1	38.1	25.4	45	304.8	0.6375	389.8	257.3	1.32	216.4	1.189	1.159	1.132	1.178	1.194
V121216B	1	38.1	25.4	45	304.8	0.7645	383.8	375.8	1.10	267.0	1.408	1.464	1.41	1.405	1.452
V181216B	0.67	38.1	25.4	45	457.2	0.6096	356.8	334.9	1.33	197.0	1.700	1.649	1.64	1.768	1.993
V181216C	0.67	38.1	25.4	45	457.2	0.7595	391.5	343.9	1.12	267.1	1.288	1.325	1.316	1.385	1.539
V181816A	1	38.1	25.4	45	457.2	0.635	341.3	257.2	1.25	205.5	1.252	1.22	1.228	1.311	1.449
V181816B	1	38.1	25.4	45	457.2	0.7366	354.2	285.4	1.10	246.3	1.159	1.203	1.185	1.232	1.359
V241216A	0.5	38.1	25.4	45	609.6	0.635	341.3	195.1	1.25	205.2	0.951	0.996	1.01	1.129	1.374
V241216B	0.5	38.1	25.4	45	609.6	0.7874	339.2	277.7	1.03	250.1	1.110	1.238	1.252	1.343	1.523
V121221A	1	41.9	23.4	55	304.8	0.6299	383.8	240.8	1.46	179.8	1.339	1.27	1.226	1.277	1.236
V121221B	1	41.9	23.4	55	304.8	0.7849	383.8	302.9	1.17	248.9	1.217	1.227	1.194	1.202	1.189
V122421A	2	41.9	23.4	55	304.8	0.6756	358	210	1.32	200.7	1.046	1.023	0.998	1.028	0.996
V122421B	2	41.9	23.4	55	304.8	0.7823	368	256.5	1.15	243.3	1.054	1.073	1.04	1.041	1.031
V181221A	0.67	41.9	23.4	55	457.2	0.6096	333.4	221.7	1.41	167.1	1.327	1.274	1.236	1.302	1.356
V181221B	0.67	41.9	23.4	55	457.2	0.762	349.6	280.7	1.16	230.0	1.220	1.236	1.204	1.23	1.29
V181821A	1	41.9	23.4	55	457.2	0.635	318.3	194.4	1.32	176.6	1.101	1.07	1.046	1.095	1.13
V181821B	1	41.9	23.4	55	457.2	0.7366	343.9	277.2	1.19	219.9	1.260	1.26	1.234	1.268	1.326
V241221A	0.5	41.9	23.4	55	609.6	0.6096	351.7	207.8	1.45	166.7	1.247	1.177	1.159	1.26	1.468
V241221B	0.5	41.9	23.4	55	609.6	0.762	368.5	272.6	1.19	235.1	1.159	1.157	1.165	1.248	1.399
V121232A	1	49.8	26.4	62.5	304.8	0.6401	383.8	210.8	1.70	132.2	1.594	1.83	1.781	1.831	1.803
V121232B	1	49.8	26.4	62.5	304.8	0.7798	369.9	257.1	1.37	194.4	1.323	1.594	1.536	1.596	1.499
V121832A	1.5	49.8	26.4	62.5	304.8	0.6401	405.8	176.6	1.75	132.2	1.336	1.526	1.488	1.526	1.511
V121832B	1.5	49.8	26.4	62.5	304.8	0.9195	324.2	190.3	1.09	226.7	0.840	0.963	0.947	0.964	0.906
V122432A	2	49.8	26.4	62.5	304.8	0.6401	411.8	159.5	1.76	132.2	1.206	1.376	1.343	1.377	1.365
V122432B	2	49.8	26.4	62.5	304.8	0.7772	366	206.4	1.37	192.9	1.070	1.289	1.242	1.29	1.211
V181232A	0.67	49.8	26.4	62.5	457.2	0.5969	318.2	188.9	1.67	113.7	1.661	1.895	1.842	1.899	1.921
V181232B	0.67	49.8	26.4	62.5	457.2	0.7493	347.5	233.6	1.39	178.4	1.309	1.563	1.507	1.569	1.545
V181832A	1	49.8	26.4	62.5	457.2	0.6096	397.8	189.8	1.83	118.6	1.600	1.797	1.757	1.801	1.854
V181832B	1	49.8	26.4	62.5	457.2	0.7493	334.6	229.4	1.37	177.2	1.295	1.547	1.49	1.552	1.518
V241232A	0.5	49.8	26.4	62.5	609.6	0.6223	388.5	182	1.78	123.1	1.478	1.662	1.622	1.674	1.798
V241232B	0.5	49.8	26.4	62.5	609.6	0.762	337.1	218.3	1.35	181.6	1.202	1.43	1.38	1.447	1.496
V121809A	1.5	19.8	11.9	50	304.8	0.7061	330.2	293.3	0.79	291.1	1.007	1.256	1.163	1.066	1.119
V121809C	1.5	19.8	11.9	50	304.8	0.6325	385.8	285.9	0.88	318.9	0.896	1.048	1.003	0.97	1.04
V122409A	2	19.8	11.9	50	304.8	0.7137	338.1	265.6	0.80	296.6	0.895	1.111	1.03	0.947	0.994
V122409C	2	19.8	11.9	50	304.8	0.6629	358	286	0.84	305.4	0.937	1.13	1.062	1.001	1.063
V181209A	0.67	19.8	11.9	50	457.2	0.5588	397.8	316.7	1.39	205.2	1.544	1.672	1.621	1.722	1.883
V181209C	0.67	19.8	11.9	50	457.2	0.6096	341.6	318.3	1.26	203.7	1.563	1.694	1.65	1.73	1.779
V181809A	1	19.8	11.9	50	457.2	0.6096	356.7	295	1.28	206.7	1.427	1.551	1.507	1.584	1.637
V181809C	1	19.8	11.9	50	457.2	0.6223	322.4	272.6	1.21	200.7	1.358	1.468	1.436	1.495	1.525
V241209A	0.5	19.8	11.9	50	609.6	0.6223	349.6	186.4	1.69	122.9	1.517	1.553	1.505	1.565	1.654
V241209C	0.5	19.8	11.9	50	609.6	0.635	358	204.8	1.70	124.2	1.649	1.686	1.635	1.698	1.792
Average											1.270	1.363	1.326	1.367	1.422
Coefficient of variation (C.V.)											0.175	0.182	0.182	0.194	0.198

Table 14
Comparison between the shear strength calculated by the proposed design formulas and the test results obtained by Lindner et al. [34]

Specimen	e/h	a (mm)	b (mm)	θ (°)	h (mm)	t (mm)	τ_y (Mpa)	τ_e (Mpa)	λ_{cr}	τ_{cr} (Mpa)	τ_e/τ_{cr}	$\tau_e/\tau_{n,A}$	$\tau_e/\tau_{n,B}$	$\tau_e/\tau_{n,M}$	$\tau_e/\tau_{n,Y}$
L1A	0.98	140	50	45	994	1.94	169	145.5	1.00	127.1	1.144	1.259	1.210	1.190	1.235
L1B	0.99	140	50	45	994	2.59	193	194.5	0.80	168.9	1.152	1.426	1.316	1.202	1.266
L2A	1.04	140	50	45	1445	1.94	163	120.3	0.99	124.1	0.970	1.069	1.050	1.072	1.178
L2B	1.04	140	50	45	1445	2.54	183	153.7	0.80	160.5	0.958	1.187	1.120	1.080	1.180
L3A	1	140	50	45	2005	2.01	162	111.9	1.07	115.7	0.967	1.065	1.080	1.165	1.324
L3B	1	140	50	45	2005	2.53	173	152.6	1.04	126.7	1.204	1.338	1.312	1.361	1.484
B1	1.33	140	50	45	600	2.1	197	165.1	0.99	150.0	1.100	1.225	1.174	1.136	1.122
B4	1.33	140	50	45	600	2.11	210	144.9	1.02	156.4	0.926	1.022	0.981	0.958	0.944
B4b	1.33	140	50	45	600	2.11	210	171.8	1.02	156.4	1.098	1.212	1.163	1.136	1.120
B3	1.33	140	50	45	600	2.62	183	156.5	0.76	164.6	0.950	1.209	1.105	0.976	0.974
B2	1.17	140	50	45	600	2.62	182	173.8	0.76	164.0	1.060	1.350	1.234	1.088	1.086
M101	1	70	15	45	600	0.99	109	89.2	0.79	96.2	0.927	1.156	1.086	1.039	1.133
M102	1	70	15	45	800	0.99	110	100.0	1.00	83.0	1.205	1.354	1.326	1.370	1.500
M103	1	70	15	45	1000	0.95	123	88.4	1.34	67.4	1.313	1.443	1.413	1.526	1.748
M104	1	70	15	45	1200	0.99	109	87.4	1.49	48.9	1.789	1.922	1.862	1.975	2.200
L1	1.5	106	86.6	30	1000	2.1	237	181.1	0.83	203.0	0.892	1.081	1.013	0.962	1.039
L1	1.49	106	86.6	30	1000	3	260	203.6	0.65	251.3	0.810	1.107	1.003	0.884	0.931
L2	1.44	106	86.6	30	1498	2	217	200.3	0.98	166.5	1.203	1.354	1.336	1.384	1.531
L2	1.43	106	86.6	30	1498	3	232	201.4	0.91	188.0	1.071	1.229	1.186	1.145	1.201
No.1	1.33	102	85.5	33	850	2	205	161.7	0.78	182.0	0.889	1.116	1.024	0.921	0.960
No.2	1.33	91	71.5	38.2	850	2	201	155.6	0.69	189.6	0.820	1.094	0.990	0.861	0.890
V1/1	9.46	144	102	45	298	2.05	172	111.3	0.92	138.7	0.803	0.938	0.899	0.863	0.821
V1/2	6.71	144	102	45	298	2.1	163	111.7	0.87	136.0	0.821	0.968	0.930	0.876	0.838
V1/3	3.36	144	102	45	298	2	172	135.9	0.94	136.2	0.997	1.161	1.113	1.077	1.020
V2/3	2.75	144	102	45	600	3	161	130.4	0.64	156.8	0.832	1.146	1.031	0.869	0.833
Average											1.036	1.217	1.158	1.125	1.182
C.V.											0.206	0.164	0.173	0.225	0.269

Table 15
Comparison between the shear strength calculated by the proposed design formulas and the test results obtained by Gil et al. [36]

Specimen	e/h	a (mm)	b (mm)	θ (°)	h (mm)	t (mm)	τ_y (Mpa)	τ_e (Mpa)	λ_{cr}	τ_{cr} (Mpa)	τ_e/τ_{cr}	$\tau_e/\tau_{n,A}$	$\tau_e/\tau_{n,B}$	$\tau_e/\tau_{n,M}$	$\tau_e/\tau_{n,Y}$
L1	NA	450	300	33.7	1500	4.8	144.3	103.8	1.174	93.4	1.111	1.188	1.167	1.188	1.103
L2	NA	550	300	32.2	1500	4.8	144.3	87	1.413	72.2	1.205	1.328	1.280	1.328	1.214
L3	NA	450	300	9.4	1500	4.8	144.3	74	1.192	91.9	0.806	0.847	0.836	0.870	0.905
L4	NA	550	300	10.6	1500	4.8	144.3	66	1.413	72.2	0.914	1.007	0.972	1.018	1.043
G1	NA	200	180	14.2	2000	4.8	144.3	114.4	0.917	116.2	0.985	1.133	1.090	1.053	1.092
G2	NA	160	50	33.4	2000	3.8	144.3	120.4	1.143	96.2	1.252	1.366	1.346	1.384	1.388
G3	NA	160	100	15.1	2000	3.8	144.3	122.7	1.391	74.2	1.653	1.852	1.786	1.866	1.871
I1	NA	320	100	24.0	2000	4.8	144.3	137.1	0.862	121.1	1.132	1.343	1.321	1.338	1.480
I2	NA	350	100	16.0	2000	3.8	144.3	74.6	1.265	85.4	0.874	1.054	1.038	1.174	1.481
Average											1.103	1.235	1.204	1.247	1.286
C.V.											0.233	0.234	0.229	0.230	0.231

Note: NA-Not available

Table 16
Comparison between the shear strength calculated by the proposed design formulas and the test results ob-tained by Peil [35]

Specimen	e/h	a (mm)	b (mm)	θ (°)	h (mm)	t (mm)	τ_y (Mpa)	τ_e (Mpa)	λ_{cr}	τ_{cr} (Mpa)	τ_e/τ_{cr}	$\tau_e/\tau_{n,A}$	$\tau_e/\tau_{n,B}$	$\tau_e/\tau_{n,M}$	$\tau_e/\tau_{n,Y}$
SP1	2.19	146	104	45	800	2	177	140.7	1.03	129.9	1.083	1.189	1.143	1.120	1.080
SP2	2.19	170	80	45	800	2	172	134.3	1.18	110.6	1.214	1.274	1.254	1.277	1.209
SP3	2.19	185	65	45	800	2	168	130.7	1.27	99.2	1.317	1.397	1.358	1.400	1.322
SP4	2.25	117	83	45	800	2	172	144.5	0.82	148.8	0.971	1.188	1.097	0.988	0.986
SP5	2.25	136	64	45	800	2	168	138.1	0.94	133.0	1.038	1.163	1.118	1.059	1.059
SP6	2.25	148	52	45	800	2	169	137.1	1.02	125.1	1.096	1.204	1.156	1.134	1.135
SP2-2-400 1	2.5	170	80	45	400	2	152	100.6	1.06	109.1	0.922	1.029	1.001	1.001	0.934
SP2-2-400 2	2.5	170	80	45	400	2	152	110.5	1.06	109.1	1.013	1.130	1.099	1.099	1.026
SP2-2-800 1	1.25	170	80	45	800	2	157	111.8	1.13	106.0	1.054	1.119	1.094	1.100	1.049
SP2-2-800 2	1.25	170	80	45	800	2	157	111.0	1.13	106.0	1.047	1.112	1.087	1.093	1.042
SP2-3-600 1	1.67	170	80	45	600	3	170	167.8	0.77	151.9	1.104	1.396	1.280	1.134	1.109
SP2-3-600 2	1.67	170	80	45	600	3	170	171.7	0.77	151.9	1.130	1.429	1.310	1.161	1.135
SP2-3-1200 1	0.83	170	80	45	1200	3	170	170.0	0.79	150.2	1.132	1.415	1.298	1.161	1.188
SP2-3-1200 2	0.83	170	80	45	1200	3	170	173.9	0.79	150.2	1.158	1.447	1.327	1.188	1.215
SP2-4-800 1	1.25	170	80	45	800	4	188	188.0	0.62	186.0	1.011	1.415	1.269	1.063	1.033
SP2-4-800 2	1.25	170	80	45	800	4	188	188.6	0.62	186.0	1.014	1.419	1.273	1.066	1.036
SP2-4-1600 1	0.63	170	80	45	1600	4	189	189.6	0.63	185.9	1.020	1.418	1.278	1.104	1.147
SP2-4-1600 2	0.63	170	80	45	1600	4	189	191.3	0.63	185.9	1.029	1.432	1.290	1.114	1.158
SP2-8-800 1	1.25	170	80	45	800	8	156	205.0	0.28	156.0	1.314	1.858	1.656	1.319	1.314
SP2-8-800 2	1.25	170	80	45	800	8	156	215.4	0.28	156.0	1.381	1.952	1.739	1.385	1.381
Average											1.102	1.349	1.256	1.148	1.128
C.V.											0.110	0.173	0.145	0.100	0.104

Table 17
Comparison between the shear strength calculated by the proposed design formulas and the test results ob-tained by Abbas et al.[18]

Specimen	e/h	a (mm)	b (mm)	θ (°)	h (mm)	t (mm)	τ_y (Mpa)	τ_e (Mpa)	λ_{cr}	τ_{cr} (Mpa)	τ_e/τ_{cr}	$\tau_e/\tau_{n,A}$	$\tau_e/\tau_{n,B}$	$\tau_e/\tau_{n,M}$	$\tau_e/\tau_{n,Y}$
G8A	3	300	200	36.9	1500	6.3	268	228.6	0.88	221.9	1.030	1.207	1.12	1.017	1.023
G7A	3	300	200	36.9	1500	6.3	268	243.1	0.88	221.9	1.095	1.282	1.188	1.077	1.084
SC1	3	300	200	36.9	1500	6.3	268	213.3	0.88	221.9	0.961	1.126	1.045	0.949	0.955
Average											1.029	1.205	1.118	1.014	1.021
C.V.											0.065	0.065	0.064	0.063	0.063

Table 18.
Comparison between the shear strength calculated by the proposed design formulas and the test results obtained by Moon et al. [24]

Specimen	e/h	a (mm)	b (mm)	θ (°)	h (mm)	t (mm)	τ_y (Mpa)	τ_e (Mpa)	λ_{cr}	τ_{cr} (Mpa)	τ_e/τ_{cr}	$\tau_e/\tau_{n,A}$	$\tau_e/\tau_{n,B}$	$\tau_e/\tau_{n,M}$	$\tau_e/\tau_{n,Y}$
MI2	0.803	250	220	17.2	2000	4	170.9	109.2	0.93	136.1	0.803	0.904	0.889	0.9	0.996
MI3	0.728	220	180	14.6	2000	4	170.9	105.4	1.01	127.6	0.826	0.872	0.837	0.822	0.899
MI4	0.887	220	180	18.7	2000	4	170.9	131.6	0.84	146.2	0.900	1.089	1.013	0.955	1.036
Average											0.843	0.955	0.913	0.892	0.977
C.V.											0.061	0.123	0.099	0.075	0.072

Table 19
Comparison between test results and theoretical results

Specimen	Num.	τ_e/τ_{cr}		$\tau_e/\tau_{n,A}$		$\tau_e/\tau_{n,B}$		$\tau_e/\tau_{n,M}$		$\tau_e/\tau_{n,Y}$	
		Mean	C.V.	Mean	C.V.	Mean	C.V.	Mean	C.V.	Mean	C.V.
All	102	1.146	0.199	1.297	0.188	1.242	0.187	1.230	0.214	1.269	0.231
e/h>1 and $\theta\geq30^o$	46	1.028	0.138	1.221	0.165	1.151	0.151	1.086	0.145	1.083	0.148

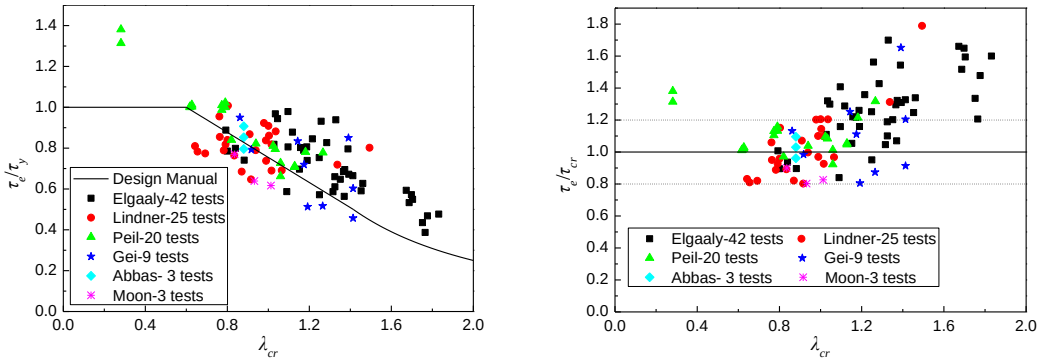

(a) τ_e/τ_y *versus* λ_{cr} (b) τ_e/τ_{cr} *versus* λ_{cr}

Fig. 12 Comparison between the shear strength calculated by Eq. (33) and the test results

For actual bridges, the distance between two adjacent stiffeners is much larger than the web height h, and θ always meets $\theta\geq 30^o$ [37], so the experimental results for the 46 specimens with e/h>1 and $\theta\geq30^o$ are selected. e/h is the shear span ratio[31]. The comparison between test results and theoretical results is given in Table 19. It can be seen that Eq. (33) which adopts the formulas for the elastic global and interactive shear buckling stresses proposed in this study provides on average much more accurate predictions of the shear strength of CSWs for the 102 specimens, and provides much more accurate predictions with the best average value and smallest coefficient of variation for the 46 specimens. So Eq. (33) is recommended to calculate the shear strength of CSWs.

It is worth mentioning that in Table 18, Reference [31] adopted the design corrugation depth of CSWs, however according to Reference [24], the negative error between the design corrugation depth and the measured corrugation depth can reach to 20%. Because the buckling will initiate at the area that has the minimum measured corrugation depth [24], the minimum measured corrugation depth is adopted in this paper.

5. Conclusions

In this paper, the shear capacity of CSWs is theoretically and numerically studied, and the following main conclusions can be drawn:

(1) The whole CSW is assumed as an orthotropic plate, and the analytical formula for the global shear buckling stress of CSWs is derived by the Galerkin method. Simplified formulas of the global shear buckling coefficient k_g for a four-edge simple support, for a four-edge fixed support, and for two edges constrained by flanges fixed and the other two edges simply supported are given.

(2) The folded plate composed of two adjacent panels is treated as an isotropic shallow shell, and the analytical formula for the interactive shear buckling stress of CSWs is derived by the Galerkin method. The interactive shear buckling coefficient table for CSWs with the same flat panel and inclined panel width is given.

(3) An elastic FEA is carried out to verify the analytical formulas and to study the influence of geometric parameters on the shear buckling stress of CSWs. Results show that the shear buckling stress greatly decreases with the increase of d/t, while increases with the increase of a/h and θ.

(4) A design formula for the shear strength of CSWs which adopts the formulas for the global and interactive shear buckling stresses proposed in this paper is assessed. From a comparison between the shear strength calculated by this design formula, calculated by four previous design formulas and measured in a series of published test results, it is found that the considered design formula provides good predictions for the shear strength of CSWs and can be recommended.

Acknowledgments

The supports from the National Natural Science Foundation of China (grant no.51378106) and the China Scholarship Council are gratefully acknowledged.

References

[1] Hamilton R.W., "Behavior of welded girders with corrugated webs", Ph.D. Thesis, University of Maine, Orono, USA, 1993.

[2] Leblouba, M., Junaid, M.T., Barakat, S., Altoubat, S. and Maalej, M., "Shear buckling and stress distribution in trapezoidal web corrugated steel beams", Thin-Walled Structures, 113, 13-26, 2017.

[3] Eldib M.H., "Shear buckling strength and design of curved corrugated steel webs for bridges", Journal of Constructional Steel Research, 65(12), 2129-2139, 2009.

[4] Timoshenko S.P. and Gere J.M., Theory of Elastic Stability 2nd ed., McGraw-Hill Book Company, New York, USA, 1961.

[5] Aggarwal K., Wu S.and Papangelis J., "Finite element analysis of local shear buckling in corrugated web beams", Engineering Structures, 162, 37-50, 2018.

[6] Easley J.T. and McFarland D.E., "Buckling of light-gage corrugated metal shear diaphragms", Journal of the Structural Division, 95(7), 1497-1516, 1969.

[7] Easley J.T., "Buckling formulas for corrugated metal shear diaphragms", Journal of the Structural Division, 101(7), 1403-1417, 1975.

[8] Bergman S. and Reissner H., "Neuere probleme aus der flugzeugstatik–über die knickung von wellblechstreifen bei schubbeanspruchung", Zeitschrift für Flugzeugtechnik und Motorluftschiffahrt, 20(18), 475-481, 1929.

[9] Hlavacek V., "Shear instability of orthotropic panels", Acta Technica CSAV, 1, 134-158, 1968.

[10] Peterson J.P., Investigation of the Buckling Strength of Corrugated Webs in Shear, National Aeronautics and Space Administration, New York, 1960.

[11] Bergfelt A., Edlund B. and Leiva L., "Trapezoidally corrugated girder webs: shear buckling, patch loading", Ing. et Arch. Suisses, 111, 22-27, 1985.

[12] Ziemian R.D., Guide to Stability Design Criteria for Metal Structures, 6th ed., John Wiley & Sons, New York, USA, 2010.

[13] El Metwally A. and Loov R.E., "Corrugated steel webs for prestressed concrete girders", Materials and Structures, 36(2), 127-134, 2003.

[14] Machimdamrong C., Watanabe E. and Utsunomiya T., "Shear buckling of corrugated plates with edges elastically restrained against rotation", International Journal of Structural Stability and Dynamics, 4(1), 89-104, 2004.

[15] Yi J., Gil H., Youm K. and Lee H., "Interactive shear buckling behavior of trapezoidally corrugated steel webs", Engineering Structures, 30(6), 1659-1666, 2008.

[16] Bergfelt A. and Leiva-Aravena L., "Shear buckling of trapezoidally corrugated girder webs", Division of Steel and Timber Structures, Chalmers University of Technology, Gothenburg, Publication S, 84(2), 1984.

[17] El Metwally A.S., "Prestressed composite girders with corrugated steel webs", Ph.D.Thesis, University of Calgary, Calgary, 1998.

[18] Abbas H., Sause R. and Driver R., "Shear strength and stability of high performance steel corrugated web girders", SSRC Conference, Seattle, USA, 361-387, 2002.

[19] Shiratani H., Ikeda H., Imai Y. and Kano K., "Flexural and shear behavior of composite bridge girder with corrugated steel webs around middle support", Doboku Gakkai Ronbunshu, 2003(724), 49-67, 2003.

[20] Sayed-Ahmed E.Y., "Plate girders with corrugated steel webs", Engineering Journal, 42(1), 1-13, 2005.

[21] Nie J.G., Zhu L., Tao M.X. and Tang L., "Shear strength of trapezoidal corrugated steel webs", China Civil Engineering Journal, 67(2), 223-236, 2013.

[22] Elgaaly M., Hamilton R.W. and Seshadri A., "Shear strength of beams with corrugated webs", Journal of Structural Engineering, 122(4), 390-398, 1996.

[23] Driver R.G., Abbas H.H. and Sause R., "Shear behavior of corrugated web bridge girders", Journal of Structural Engineering, 132(2), 195-203, 2006.

[24] Moon J., Yi J., Choi B.H. and Lee H.E., "Shear strength and design of trapezoidally corrugated steel webs", Journal of Constructional Steel Research, 65(5), 1198-1205, 2009.

[25] Hassanein M.F. and Kharoob O.F., "Shear buckling behavior of tapered bridge girders with steel corrugated webs", Engineering Structures, 74, 157-169, 2014.

[26] Hassanein M.F., Elkawas A.A., El Hadidy A.M. and Elchalakani M., "Shear analysis and design of high-strength steel corrugated web girders for bridge design", Engineering Structures, 146, 18-33, 2017.

[27] Lekhnitskii S.G., Anisotropic Plates, Gordon and Breach Science Publishers, New York, USA, 1968.

[28] Batdorf S.B., A Simplified Method of Elastic-Stability Analysis for Thin Cylindrical Shells I: Donnell's Equation, Technical Report Archive Image Library, Langley Memorial Aeronautical Laboratory, Langley Field, USA, 1947.

[29] Xu Q. and Wan S., Design and Application of PC Composite Box Girder Bridges with Corrugated Steel Webs, China Communication Press, Beijing, China, 2009.

[30] Li S.M., Stability Theory, China Communications Press, Beijing, China,1989.

[31] Sause R. and Braxtan T.N., "Shear strength of trapezoidal corrugated steel webs", Journal of Constructional Steel Research, 67(2), 223-236, 2011.

[32] ANSYS, ANSYS User's Manual Revision 12.1, ANSYS Inc., Canonsburg, USA, 2012.

[33] Design Manual for PC Bridges with Corrugated Steel Webs., Research Committee for Hybrid Structures with Corrugated Steel Webs, 1998.

[34] Lindner J. and Aschinger R. "Biegetragfähigkeit von I-trägern mit trapezförmig profilierten stegen", Stahlbau, 57(12), 1988.

[35] Peil, U., "Statische versuche an trapezstegtragern untersuchung der querkraftbeanspruchbarkeit, Institut fur Stahlbau", Braunschweig (Germany): Technischen Universitat Braunschweig, 1998.

[36] Gil H., Lee S., Lee J. and Lee H., "Shear buckling strength of trapezoidally corrugated steel webs for bridges", Transportation Research Record Journal of the Transportation Research Board, CD11-S, 473-480, 2005.

[37] Lindner J. and Huang B., "Beulwerte fur trapezformig profilierte bleche unter schubbeanspruchung", Stahlbau, 64(12), 370-373, 1995.

Advanced Steel Construction – Vol. 15 No. 4 (2019) 364–376
DOI:10.18057/IJASC.2019.15.4.7

MODELING THE LOCAL BUCKLING FAILURE OF ANGLE SECTIONS WITH BEAM ELEMENTS

Farshad Pourshargh[1], Frederic P. Legeron[2,4] and Sébastien Langlois[3,*]

1 Ph.D. candidate at Université de Sherbrooke, Sherbrooke, Canada
2 Eng., Ph.D. Formerly Professor, Civil Engineering Department, Université de Sherbrooke, Sherbrooke, Canada
3 Eng., Ph.D. Assistant professor, Civil Engineering Department, Université de Sherbrooke, Sherbrooke, Canada
4 Present affiliation: Vice President, Parsons, Dubai, UAE
**(Corresponding Author: Email address: Sebastien.Langlois@USherbrooke.ca)*

A B S T R A C T

Slender steel sections are widely used in the construction of steel structures such as lattice structures for transmission line and telecommunication towers. Local buckling may be the observed failure mode under compression loads for these slender sections, and many experimental studies have been conducted to evaluate their resistance. All steel design codes include equations to account for local buckling. In numerical models, local buckling can be reproduced using 2D shell or 3D elements. Nonlinear numerical models have been developed in the last decades that can capture the complex behavior of lattice structures up to failure. These models typically use beam elements that consider correctly the global buckling and yielding of sections but do not consider the local buckling of angles due to geometrical limitations. This article proposes a method that modifies the material behavior of sections to involve the local buckling failure in the analysis. Forty-two experimental tests were conducted on short angles and a general stress-strain formula was defined based on the test results. The formula relates the local buckling slenderness ratio of the members to a material constitutive law that accounts for the local buckling. To evaluate the method, the numerical results were compared to those of four x-braced frame configurations using slender angle sections. The results demonstrate that the proposed method can accurately model the local buckling failure of fiber beam elements.

ARTICLE HISTORY

Received: 11 January 2019
Revised: 26 February 2019
Accepted: 17 July 2019

K E Y W O R D S

Lattice steel tower;
Angle section;
Local buckling;
Finite element model;
Nonlinear behavior;
Fiber beam element

1. Introduction

Angle steel members are widely used in steel lattice structures for transmission lines and telecommunications. Lattice towers that are made of angle members exhibit complex structural behavior, which is mainly due to connection eccentricity, bolt slippage, local buckling and their impacts on failure modes. The standard procedure for designing tower members is to build a simple linear model of the structure for determining the forces in each member and to evaluate the resistance using design code equations. This type of analysis may not be correct because the buckling resistance should be verified as an integrated part of the design and not as an independent stage [1, 2]. To overcome the limitations of this simple analysis, transmission line lattice towers are typically tested under various load conditions in full-scale field tests prior to mass production.

Prasad Rao [3] reported that 32 towers out of 138 full-scale tests at the Structural Engineering Research Centre [CSIR-SERC] experienced various types of premature failures, which demonstrates the limitations of the design method that is used in practice. To study the failure in detail, they modeled three towers and analyzed them using the NE-Nastran nonlinear finite element software. The option for geometric and material nonlinearity in the software was used to obtain the behavior and limit loads. The entire tower was modeled using beam-column elements. However, to capture more details, the failed compression bracings were modeled as plate elements. The test failure pattern coincided with the analysis failure pattern for both beam and plate modeling. However, nonlinear finite element analysis predicted a failure load that was 7 to 14 percent higher than the test results.

Another study was performed by the same researchers [4] on five prematurely failed towers. They encountered overprediction of the strength by nonlinear analysis and concluded that finite element analysis is still not a fully reliable method for predicting tower strength and the tests remain necessary for this objective. However, it is indicated that the nonlinear analysis is essential for understanding the behavior, load carrying capacity, design deficiencies, and instability in the structure. This type of nonlinear model aims at capturing the complex and nonlinear behavior of steel lattice structures. It is not a practical design method because it does not rely on design code equations or more advanced methods such as the direct strength method (DSM) [5, 6, 7] to evaluate the resistance of sections. It provides a one-step numerical model for representing the pre- and post-buckling behaviors of the structure. This type of model is useful as an alternative or complement to full-scale tests for understanding the behavior and evaluating the resistance of lattice towers. Recent works showed that depending on the objective of the modeling, the following characteristics of lattice behavior might need to be considered: joint eccentricity [8, 9], bolt slippage [10], and residual stresses [11], among others. However, in this type of model, which normally simulates the elastoplastic buckling of angle members, the potential local buckling of members is neglected. This article will focus on developing an efficient method to account for local buckling in nonlinear models of lattice structures.

Currently, most research on the modeling of angle members uses either beam elements or 2D shell elements. Angle sections may undergo global or local buckling instability under a compression load, depending on the slenderness and the width-to-thickness ratios. Shell elements can represent the full three-dimensional behavior of angle sections and local buckling with high accuracy if the mesh is sufficiently refined. However, for large and complex structures such as lattice towers, the high number of members render the use of shell elements impractical. For example, Shan et al. [12], proposed modeling angle members by nonlinear plate elements. They included both material and geometric nonlinearities in the study; however, the analysis procedure was computation-intensive and time-consuming. They concluded that 2D elements can only be used for small structures and as a research tool. This conclusion has been supported by other researchers [13]. In slender angle sections with a high width-to-thickness ratio, the global buckling deformation is accompanied by local buckling of leg plates [14] and this effect should be incorporated into the finite element model of the structure. Lee and McClure [13] developed an L-section beam finite element for elastoplastic large deformation analysis. In terms of the computational time, the beam element is 2.4 times more efficient than shell modeling if the member length is equal to 4 meters.

The fiber beam element is a highly effective element that is used with success to model angle sections. This element can properly incorporate the stress and yielding effects in the member. Kitipornchai et al. [19, 20] reported an analysis with nonlinear fiber elements of angle sections under axial and bending loads. Numerical studies were conducted on various structures and the angle members were modeled as fiber elements. Several examples were presented to demonstrate the satisfactory performance of the fiber element model in predicting the ultimate behavior of imperfect angle columns. The results that were obtained from the study were compared to experimental tests on two pairs of angle trusses with web members.

Vieira et al. [21] and Carrera et al. [22] proposed a 1D beam element for modeling the buckling of beams using analytical formulas. The results accorded with finite element models. Several limitations in capturing the local buckling behavior were reported. According to the authors, additional tests and experiments are needed for extending the method.

Other computational methods for calculating the buckling loads of thin-walled sections were studied. Huang et al. [23] developed a mathematical formulation. They considered the angle section as an example and conducted a numerical analysis of the elastic and inelastic buckling using finite element models. The results from beam and shell elements were compared with the theoretical results. It was concluded that the mathematical solution of higher order differential equations is complicated and for members with complicated deflections another method should be applied. Considering other research and experiments in this field, the approach with fiber elements is well adapted analytically for modeling the transmission tower structures; however, a full local buckling behavior that covers the pre- and post-buckling behaviors is not well defined.

The objective of this paper is to propose a method for incorporating the local buckling behavior in the finite element model of structures using fiber beam elements by developing a stress-strain behavior curve of steel. Forty-two slender section angle members were tested and full force-deflection curves were extracted. Then, a local buckling slenderness ratio was defined via the direct strength method [5] and equations were developed to relate the slenderness ratio to two specified points on the stress-strain curve. Considering these two points, full stress-strain equations were defined by using curve fitting techniques to model the compressive behavior of a slender angle with a specified slenderness ratio. Finally, the proposed method was evaluated by comparing its results to the test results on four full-scale X-braced frames of angle slender members that were obtained by Morissette [24].

2. Short angle specimens

2.1. Local buckling slenderness

The experimental program consists of testing 42 short angle members under pure compression. These tests were conducted to evaluate the global stress-strain behavior of angles that are failing due to local buckling. To characterize the sections that are undergoing local buckling, Table 1 introduces the local buckling slenderness ratio, which is denoted as λ_p and is defined in Equation 1. This ratio is used in the direct strength method [31] and was found to be useful for relating the properties of the angle to the stress-strain behavior.

$$\lambda_p = \sqrt{\frac{F_y}{\sigma_{cr}}} \tag{1}$$

In this equation, F_y stands for the yielding stress of steel and σ_{cr} is the critical elastic local buckling stress for the member, which can be calculated using finite element software such as Code_Aster, ANSYS or ABAQUS. In this study, a finite strip software, namely, CUFSM, which is developed by Schafer [32], will be used to perform critical elastic buckling load calculations. CUFSM, which has been developed to accompany the direct strength method, is a finite strip elastic buckling analysis application. In the first step, the geometry of the member is modeled either manually or using a built-in cross-section library. Then, general end boundary conditions and loading are applied to the member and the section is meshed automatically with finite strips. Finally, the analysis provides the buckling mode shapes of the member and the critical elastic buckling load for each mode. This software is freely available.

In practice, FE analysis is time-consuming for engineers. However, as a simplification, a mathematical relation can be developed between the local buckling stress and the width-to-thickness ratio b/t, where b is the width of the angle leg and t is the thickness of the leg. Based on all the angle members that are reported in Table 1, a formula is presented that relates σ_{cr} and ratio (b/t):

$$\left(\frac{b}{t}\right) = \frac{\alpha}{\sqrt{\sigma_{cr}}} \tag{2}$$

where the value of α is calculated to be 323 according to the curve fitting analysis that is shown in Fig. 1. In this work, the modulus of elasticity of steel was assumed to be 200,000 MPa. This simplification can be used when the boundary conditions of the angle member are fixed translation and free rotation. However, as shown in Fig. 1, the discrepancy in the local buckling stress can be important, especially at low b/t values. Therefore, for higher precision, the full procedure that is presented in the next sections, which involves a finite element model, is recommended.

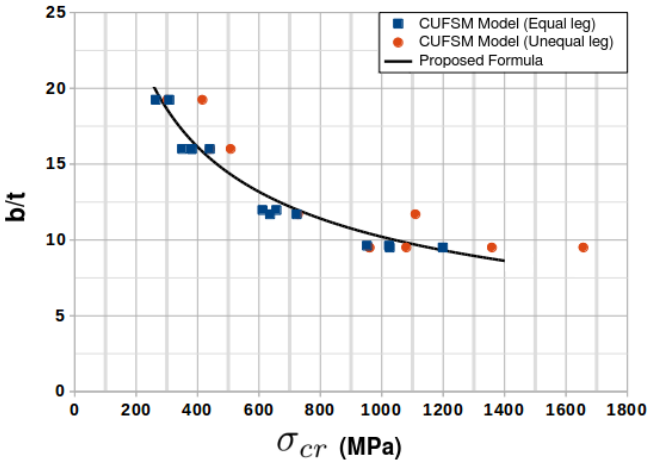

Fig.1 Calculated curve that relates σ_{cr} and (b/t) values

2.2. Experimental program

The objective of the experimental program is to provide test results on local buckling behavior from specimens of various geometries. Forty-two short angle specimens, which are listed in Table 1, were tested under pure compression and the force-deformation behavior was measured. The leg width-to-thickness ratio, namely, (b/t), of the specimens ranged from 9.5 to 19. According to (CSA-S16) [25] and Eurocode 3 [27], all specimens are classified as class 4 sections, which are subject to local buckling prior to yielding under compression. The steel grade of the specimens is ASTM-A36 [28] and their material properties are listed in Table 1.

The lengths of specimens were selected to avoid global buckling instability. Most configurations were tested on two identical specimens to evaluate the repeatability of results. The average result of these identical tests was considered the final result to better represent the types of sections that are available in the market. Since the specimens are short and they fail under the local buckling mode, the effects of geometrical imperfections and residual stresses are not considered. These effects are more important on global buckling mode, which is outside the scope of this article. Taking the discussed effects in consideration adds additional parameters to the prediction, which renders finding a solution highly complicated; hence, these effects are not investigated further in this article.

To provide continuous and uniform end conditions throughout the tests, the extremities of all specimens were accurately milled flat and strictly perpendicular to the axis of the angle. The specimens were supported by a thick steel plate without a hinge for the test. The alignment of the centroid of the angle with the line of action of the force was secured by top and bottom adjustment plates (Fig. 2) that were bolted to the thick plates. To avoid any eccentric moment, the center of the force that was applied by the machine coincided with the center of gravity of the section. The angle-shaped opening in each set of adjustment plates provided the required end constraints: fixed translation and free rotation.

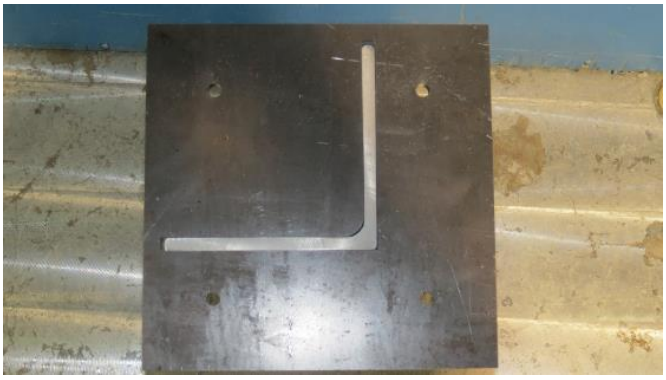

Fig. 2 Adjustment plate in the supports

Table 1
Properties of the short angle test specimens

Test	Section	Length (mm)	b/t	F_y (MPa)	F_u (MPa)	E (MPa)	σ_{cr} (MPa)	λ_p
1	L152x152x7.9	600	19.2	339	519	178000	264	1.13
2	L152x152x7.9	600	19.2	339	519	178000	264	1.13
3	L152x152x7.9	400	19.2	339	519	178000	308	1.05
4	L152x152x7.9	400	19.2	339	519	178000	308	1.05
5	L152x152x9.5	600	16	390	543	207000	381	1.01
6	L152x152x9.5	600	16	390	543	207000	381	1.01
7	L152x152x9.5	400	16	390	543	207000	440	0.94
8	L152x152x9.5	400	16	390	543	207000	440	0.94
9	L152x152x16	600	9.5	395	514	188281	1026	0.62
10	L152x152x16	600	9.5	395	514	188281	1026	0.62
11	L152x152x16	400	9.5	395	514	188281	1199	0.57
12	L152x152x16	400	9.5	395	514	188281	1199	0.57
13	L152X102X9.5	433	16	373	495	206297	508	0.86
14	L152X102X9.5	437	16	373	495	206297	508	0.86
15	L152X102X16	438	9.5	375	564	212700	1359	0.53
16	L152X102X16	439	9.5	375	564	212700	1359	0.53
17	L152X102X16	680	9.5	375	564	212700	1080	0.59
18	L152x152x9.5	598	16	392	541	201000	381	1.01
19	L152x152x9.5	597	16	392	541	201000	381	1.01
20	L152x152x9.5	598	16	392	541	201000	381	1.01
21	L152X102X9.5	718	16	371	492	208000	440	0.92
22	L152x152x9.5	850	16	380	526	210000	350	1.04
23	L152X102X16	800	9.5	375	563	212700	960	0.63
24	L152X102X16	300	9.5	375	563	212700	1657	0.48
25	L152X102X16	800	9.5	375	563	212700	960	0.63
26	L152x152x13	850	11.7	388	547	202626	636	0.78
27	L152x152x13	850	11.7	388	547	202626	636	0.78
28	L152x152x13	500	11.7	388	547	202626	723	0.73
29	L152x102x13	800	11.7	407	587	193387	727	0.75
30	L152x102x13	800	11.7	407	587	193387	727	0.75
31	L152x102x13	300	11.7	407	587	193387	1110	0.61
32	L152x102x7.9	800	19.2	405	557	204017	302	1.16
33	L152x102x7.9	800	19.2	405	557	204017	302	1.16
34	L152x102x7.9	300	19.2	405	557	204017	416	0.99

35	L76x76x6.35	400	12	379	526	203000	612	0.79
36	L76x76x6.35	400	12	379	526	203000	612	0.79
37	L76x76x6.35	300	12	379	526	203000	657	0.76
38	L76x76x6.35	300	12	379	526	203000	657	0.76
39	L76x76x7.9	400	9.6	388	555	203000	952	0.64
40	L76x76x7.9	400	9.6	388	555	203000	952	0.64
41	L76x76x7.9	300	9.6	388	555	203000	1024	0.62
42	L76x76x7.9	300	9.6	388	555	203000	1024	0.62

The compression jig was set up for performing the tests as shown in Fig. 3 in a 500-kN hydraulic testing machine. The loading was displacement-controlled at rates that ranged from 0.12 to 0.3 mm/min according to the length of the specimen to reach the maximum load within 5 to 10 minutes. The test was continued up to the occurrence of a substantial nonlinear behavior. The relative displacement of the specimens was measured by a displacement transducer that was attached to the adjustment plate from the bottom to the top (Fig. 3).

2.3. Material property tests

Two or three coupons were cut and prepared from each batch of steel material and tested under tension according to the ASTM A370-02 [29] standard. The values of F_y that were provided by the coupon tests were used to calculate λ_p for each specimen. The values are listed in Table 1.

3. Definition of material stress-strain behavior

Based on the force-deflection results from the short angle tests, 42 stress-strain material behaviors were extracted. Each material behavior is related to the corresponding λ_p value of the specimen. The values of σ(stress) and ε(strain) are calculated by assuming homogeneous behavior as σ = P/A and ε = δ/L, where P is the applied force (N); A is the cross-sectional area (mm^2); δ is the vertical deflection of the specimen (mm); and L is the length of the specimen (mm).

Fig. 4 plots the measured behaviors of six specimens. To characterize the behavior of a member under compression, it is assumed that the full stress-strain curve can be characterized by 2 points: A(ε_A,σ_A), which denotes the first peak in the curve, and B(0.01,σ_B). Table 2 reports the ε_A, σ_A, and σ_B values. Other points were also considered; however, based on the accuracy of the fitted curve, the two points that are specified above were selected. Using the short angle test results (Table 2) and a curve fitting technique, Equations 3 to 5 were developed for calculating the coordinates of points A and B based on the value of λ_p. Since the number of tested specimens was limited, the range of values of λ_p for which the equations apply was limited to 0.57-1.20. This also affected the calculated values of σ_A in terms of the material yield stress. Fig. 5 plots the equations and the distribution of the test points.

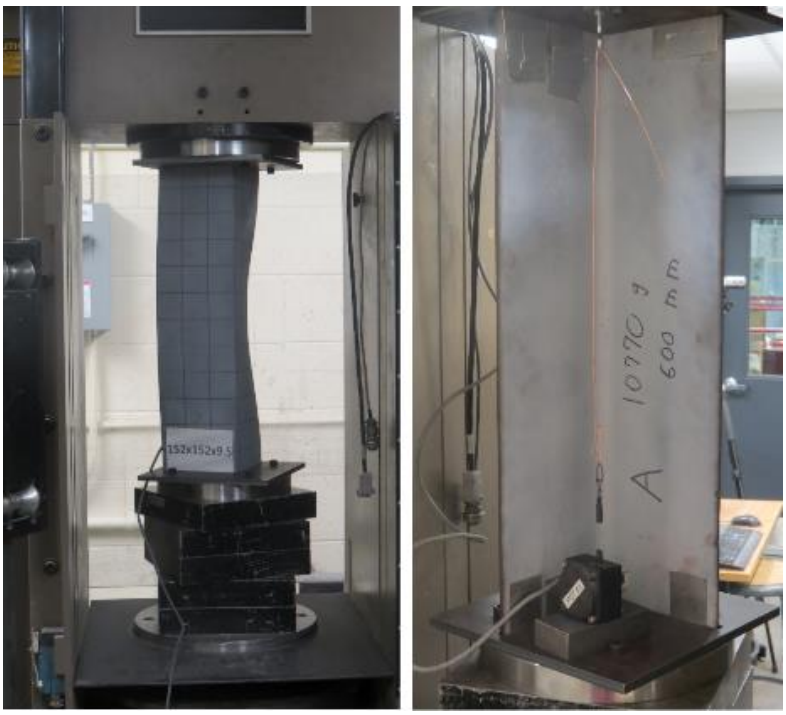

Fig. 3 Test setup and displacement transducer

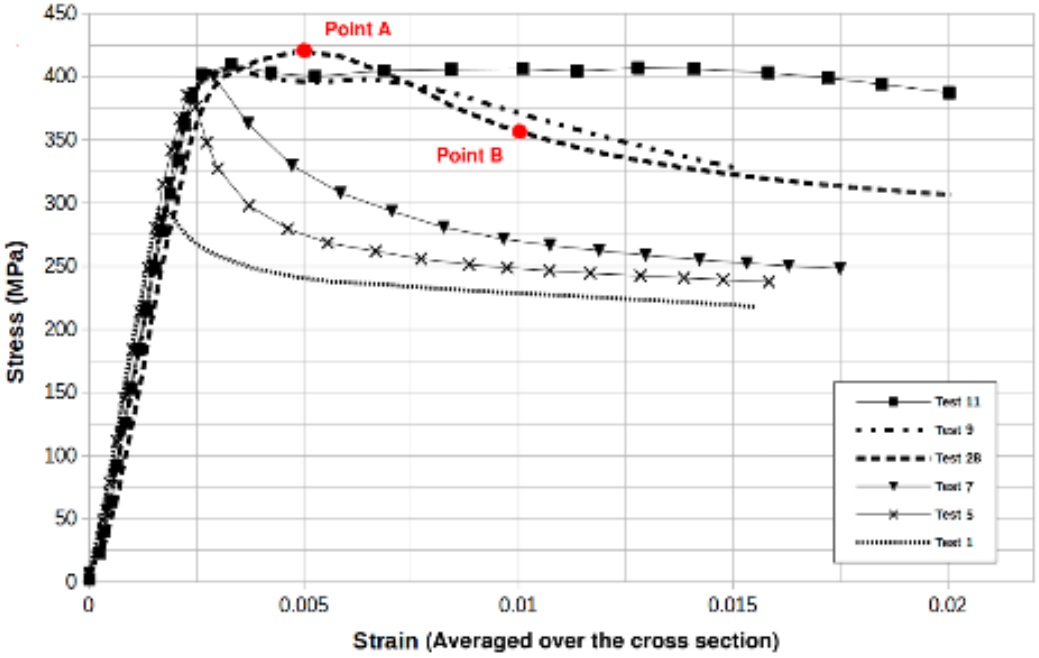

Fig. 4 Measured stress-strain behaviors of six test specimens

$$\varepsilon_A = 0.0004965 \times (1 + \lambda_p{}^{-11.6})^{\frac{1}{5.8}} + 0.001521 \qquad 0.57 < \lambda_p < 1.20 \qquad (3)$$

$$\sigma_A = 407.9 \times (1 + \lambda_p^{20})^{-\frac{1}{10}} \qquad 0.57 < \lambda_p < 1.20 \qquad (4)$$

$$\sigma_B = 350.1 \times \lambda_p{}^2 - 903.9 \times \lambda_p + 809.1 \qquad 0.57 < \lambda_p < 1.20 \qquad (5)$$

Table 2
Results of the short angle tests

Test	λ_p	ε_A	σ_A (MPa)	σ_B (MPa)
1	1.13	0.0017	298	228
2	1.13	0.0018	288	229.9
3	1.05	0.0022	313	234
4	1.05	0.0035	297	242
5	1.01	0.0023	389	248
6	1.01	0.0021	379	250
7	0.94	0.0028	401	269.7
8	0.94	0.0028	400	267.8
9	0.62	0.0032	407	371.2
10	0.62	0.0027	406	398.7
11	0.57	0.0032	409	406.6
12	0.57	0.0032	410	406.3
13	0.86	0.0029	367	271.7
14	0.86	0.0031	367	270.8
15	0.53	0.0035	350	374
16	0.53	0.0049	353	376
17	0.59	0.0022	350	350.7
18	1.01	0.0025	390	256.9
19	1.01	0.0026	384	254.8

20	1.01	0.0024	377	256.2
21	0.92	0.0024	371	254
22	1.04	0.0022	356	241.6
23	0.63	0.003	422	376
24	0.48	0.005	423	436.7
25	0.63	0.0035	425	392
26	0.78	0.0034	413	305
27	0.78	0.0032	413	301.8
28	0.73	0.0048	420	356.8
29	0.75	0.0036	414	332.2
30	0.75	0.0035	413	334
31	0.61	0.007	450	453
32	1.16	0.0021	336	234.6
33	1.16	0.0021	319	245.1
34	0.99	0.0031	404	285.7
35	0.79	0.0029	418	292.6
36	0.79	0.003	419	293
37	0.76	0.0034	411	329
38	0.76	0.0038	415	324.3
39	0.64	0.0031	431	406.8
40	0.64	0.0027	429	422
41	0.62	0.003	432	427
42	0.62	0.0031	429	423.6

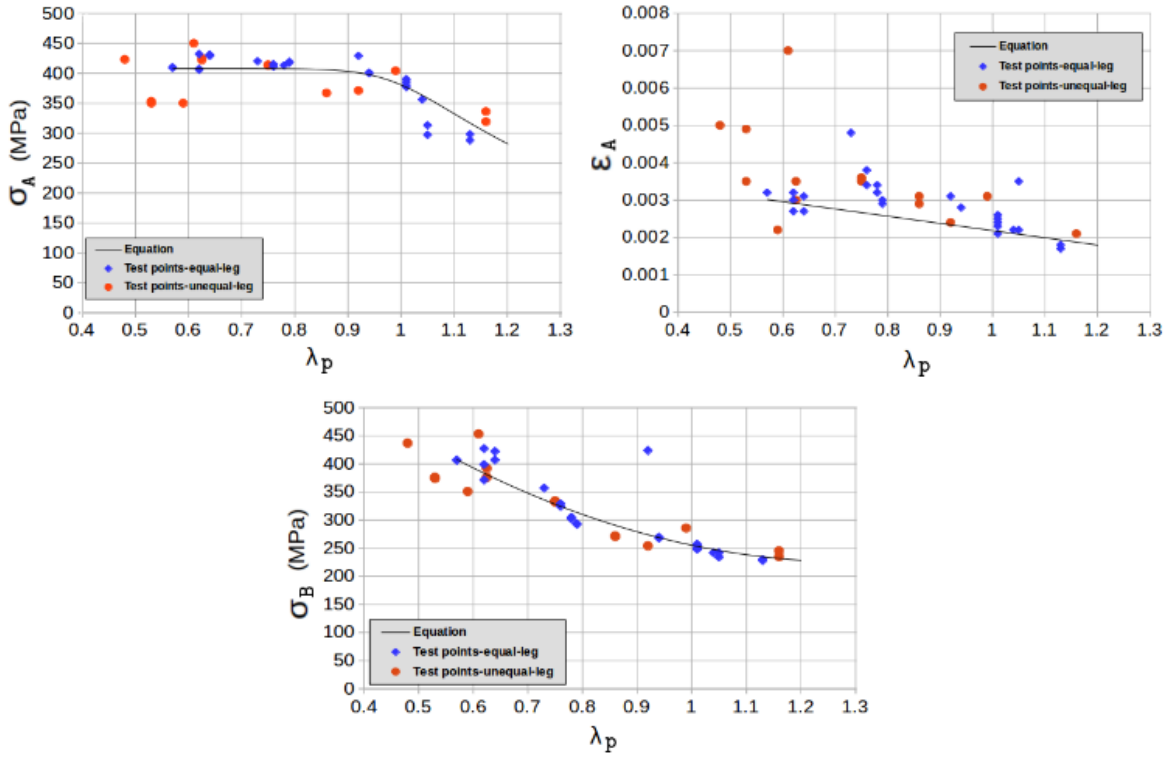

Fig. 5 Plots of equations 3 to 5 and the distribution of the test points

The coordinates of points A and B are used to calculate the three unknown parameters (C, D, and k) that are used to define the stress-strain equation (6). Since the behavior of steel in the first steps of loading is completely elastic, the third criterion that is used to calculate the parameters of the equation is the slope of standard steel stress-strain material in elastic range, which is assumed to be 200,000 MPa (Young's modulus). The main stress-strain equation is expressed as follows:

$$\sigma = \begin{cases} 200000 \times \varepsilon & \varepsilon \leq 0.0005 \\ C \times \varepsilon_m \times (\varepsilon_m + D \times \varepsilon_m{}^{(-k)})^{(-k)} & \varepsilon > 0.0005 \end{cases} \quad (6)$$

$$\varepsilon_m = 1000 \times \varepsilon \quad (7)$$

Equations 3 to 5 relate the λ_p value of any class 4 member to two characteristic points, namely, A and B, of the stress-strain curve. Then, Equation 6 relates these two points to a complete and modified stress-strain curve that can be included in a beam element as a material behavior. The values of the unknown parameters in the equation (C, D, and k) were obtained via trial and error. A simple script was developed for inputting the λ_p value. The script calculates the coordinates of points A and B based on Equations 3 to 5. Then, points A and B are substituted into Equation 6, which yields the full stress-strain behavior. Table 3 lists the values of parameters C, D and k that are calculated based on points A and B for each specimen and λ_p value. The output of Equation 6 can be entered as a nonlinear material behavior into any finite element software. An alternative simplified solution is to define the material as a bilinear stress-strain relation without using Equation 6. The bilinear behavior could be defined by using σ_A as F_y and the slope of the line that connect points A and B (AB) as E_t (the tangent modulus of the material). Fig. 6 compares the stress-strain curve that was calculated via Equation 6 with the test results from short angle specimens for six λ_p values.

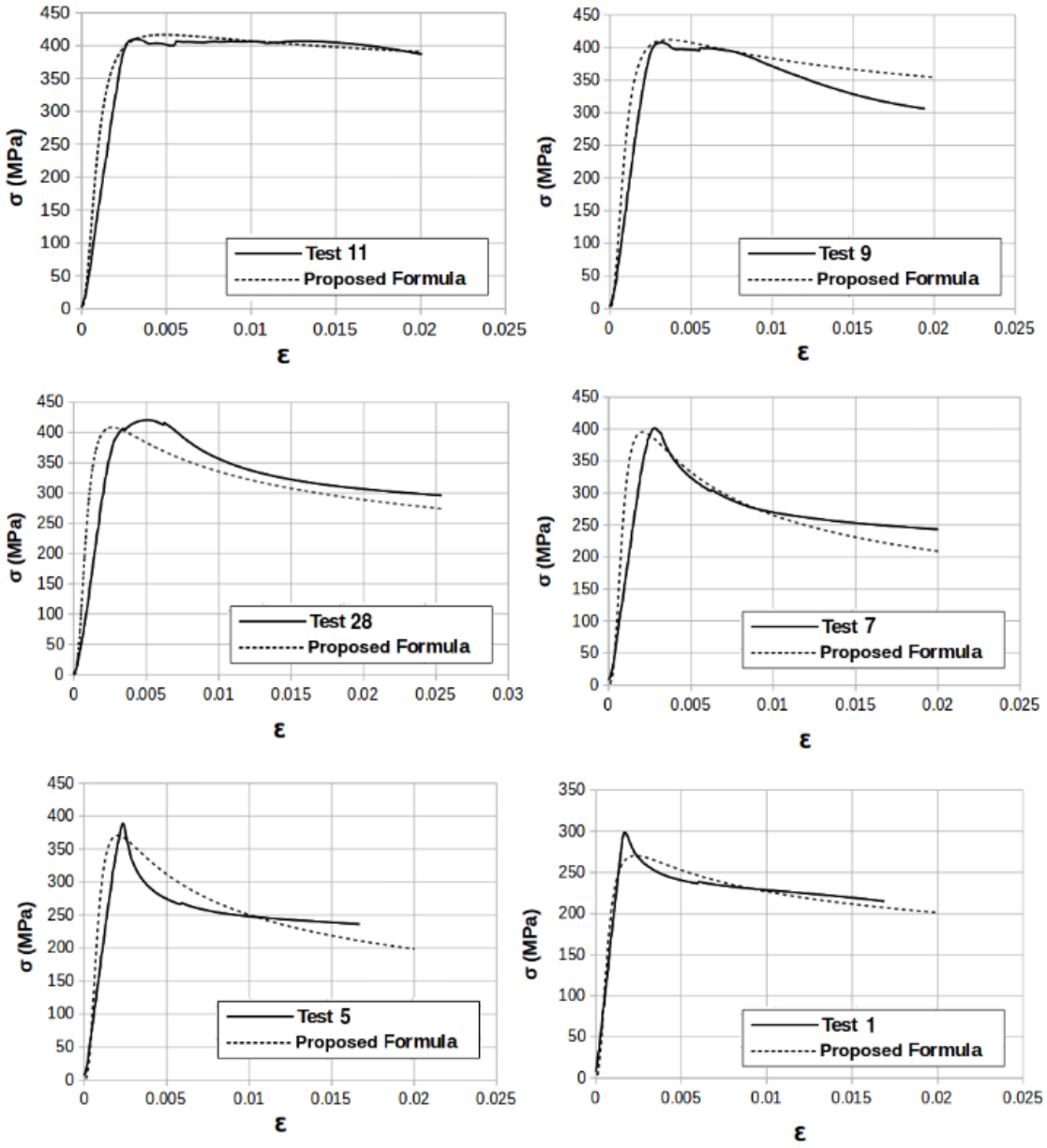

Fig. 6 Comparison of the stress-strain relationship between the test results and Equation 6

Table 3
Calculated values of parameters for Equation 6

Tests	λ_p	C	D	k
1,2	1.13	440.289	0.563	1.272
3,4	1.05	526.022	0.625	1.329
5, 6, 18, 19, 20	1.01	563.891	0.653	1.346
7, 8	0.94	601.782	0.692	1.349
9, 10	0.62	512.091	0.831	1.123
11, 12	0.57	479.906	0.844	1.068
13, 14	0.86	602.713	0.729	1.315
15, 16	0.53	449.86	0.848	1.018
17	0.59	493.722	0.84	1.091
21	0.92	605.266	0.702	1.343
22	1.04	536.673	0.633	1.334
23, 25	0.63	517.363	0.827	1.133
24	0.48	441.128	0.847	1.004
26, 27	0.78	583.226	0.764	1.263
28	0.73	565.003	0.786	1.224
29, 30	0.75	572.487	0.777	1.24
31	0.61	506.351	0.834	1.113
32, 33	1.16	409.118	0.538	1.246
34	0.99	578.983	0.665	1.351
35, 36	0.79	585.562	0.76	1.269
37, 38	0.76	575.722	0.773	1.247
39, 40	0.64	523.266	0.824	1.143
41, 42	0.62	512.091	0.831	1.123

According to Fig. 6, the calculated curves are comparable to the experimental results and they have an acceptable accuracy. This is also demonstrated in Table 4, which compares the values of ε_A, σ_A and σ_B from Equation 6 and experimental work on short angles. The mean value of the differences is very close to 1.0 and the COV values are reasonable for parameters σ_A and σ_B. The strain at the peak is always difficult to capture in angles showing close to elasto-perfectly plastic behavior. As a consequence, the COV value for parameter ε_A is relatively high. Despite the statistical comparisons in Table 4, the trend of the stress-strain curve that was calculated via the formula accords with the experimental results and the inaccuracy of ε_A does not impact the close agreement of the predicted curve with the experimental results.

Table 4
Comparison of parameters that were calculated via Equation 6 with test values for parameters ε_A, σ_A, and σ_B

Test	ε_A (T)	σ_A (T)	σ_B (T)	ε_A (F)	σ_A (F)	σ_B (F)	ε_A (F/T)	σ_A (F/T)	σ_B (F/T)
1	0.0017	298	228	0.0021	317	234	1.24	1.06	1.03
2	0.0018	288	230	0.0021	317	234	1.17	1.1	1.02
3	0.0022	313	234	0.002	358	245	0.91	1.14	1.05
4	0.0035	297	242	0.002	358	245	0.57	1.21	1.01
5	0.0023	389	248	0.002	376	252	0.87	0.97	1.02
6	0.0021	379	250	0.002	376	252	0.95	0.99	1.01
7	0.0028	401	270	0.0019	397	269	0.68	0.99	1
8	0.0028	400	268	0.0019	397	269	0.68	0.99	1
9	0.0032	407	371	0.0036	412	383	1.13	1.01	1.03
10	0.0027	406	399	0.0036	412	383	1.33	1.01	0.96
11	0.0032	409	407	0.0046	416	402	1.44	1.02	0.99
12	0.0032	410	406	0.0046	416	402	1.44	1.01	0.99
13	0.0029	367	272	0.0022	406	291	0.76	1.11	1.07

14	0.0031	367	271	0.0022	406	291	0.71	1.11	1.07
15	0.0035	350	374	0.0042	418	428	1.2	1.2	1.14
16	0.0049	353	376	0.0042	418	428	0.86	1.19	1.14
17	0.0022	350	351	0.0042	414	397	1.91	1.18	1.13
18	0.0025	390	257	0.002	373	251	0.8	0.96	0.98
19	0.0026	384	255	0.002	376	252	0.77	0.98	0.99
20	0.0024	377	256	0.002	376	252	0.83	1	0.98
21	0.0024	371	254	0.0021	401	274	0.88	1.08	1.08
22	0.0022	356	242	0.0019	363	247	0.86	1.02	1.02
23	0.003	422	376	0.0034	411	379	1.13	0.97	1.01
24	0.005	423	437	0.0046	421	433	0.92	1	0.99
25	0.0035	425	392	0.0034	411	379	0.97	0.97	0.97
26	0.0034	413	305	0.0024	408	317	0.71	0.99	1.04
27	0.0032	413	302	0.0024	408	317	0.75	0.99	1.05
28	0.0048	420	357	0.0026	409	336	0.54	0.97	0.94
29	0.0036	414	332	0.0025	408	328	0.69	0.99	0.99
30	0.0035	413	334	0.0025	408	328	0.71	0.99	0.98
31	0.007	450	453	0.0038	412	388	0.54	0.92	0.86
32	0.0021	336	235	0.0021	302	231	1	0.9	0.98
33	0.0021	319	245	0.0021	302	231	1	0.95	0.94
34	0.0031	404	286	0.002	384	257	0.65	0.95	0.9
35	0.0029	418	293	0.0024	408	314	0.83	0.98	1.07
36	0.003	419	293	0.0024	408	314	0.8	0.97	1.07
37	0.0034	411	329	0.0025	408	323	0.74	0.99	0.98
38	0.0038	415	324	0.0025	408	323	0.66	0.98	1
39	0.0031	431	407	0.0033	411	374	1.06	0.95	0.92
40	0.0027	429	422	0.0033	411	374	1.22	0.96	0.89
41	0.003	432	427	0.0036	412	383	1.2	0.95	0.9
42	0.0031	429	424	0.0036	412	383	1.16	0.96	0.9
Average							0.93	1.02	1
COV (%)							30.29	7.56	6.53

Note: (T: Test, F: Formula) – The stress values are specified in MPa.

4. Evaluating the method with experimental results

4.1. Experimental Program

To evaluate the accuracy of the method, the numerical results were compared to the results of experimental tests that were performed at Université de Sherbrooke [24] on four X-bracing frame configurations. The test setup is a two-dimensional frame than can include angle members that act as X-braces. Fig. 7 and Fig. 8 present a sketch and a photograph of the test set-up. A lateral load was applied to the frame, which introduces compression and tension forces into the angles. The maximum capacity of the jack is 500 kN and it is mounted horizontally to a rigid supporting system. The frame was restrained by steel cables to avoid out-of-plane deflections. The beam-to-column connections were designed as pinned joints using a single bolt such that no bending moment was applied to the frame members and the lateral force induced direct axial tension and compression into the angles.

To measure the applied force to the angles, strain gauges were placed on end connection plates. Fig. 9 presents the geometry of the end plates. The end plates were of thickness 25.4 mm and two sets of plates were prepared for bolt sizes of 12.7 mm and 15.9 mm. To ensure the accuracy of the measured force, all assemblies of end plates and strain gauges were calibrated separately. Then, the recorded data from the strain gauges that were mounted on the end plates could be transformed to the applied force. In addition, displacement transducers were used to measure the lateral and out-of-plane deformations of the frame and braces. The load was applied based on the displacement control principle with a rate of 0.5 mm/min.

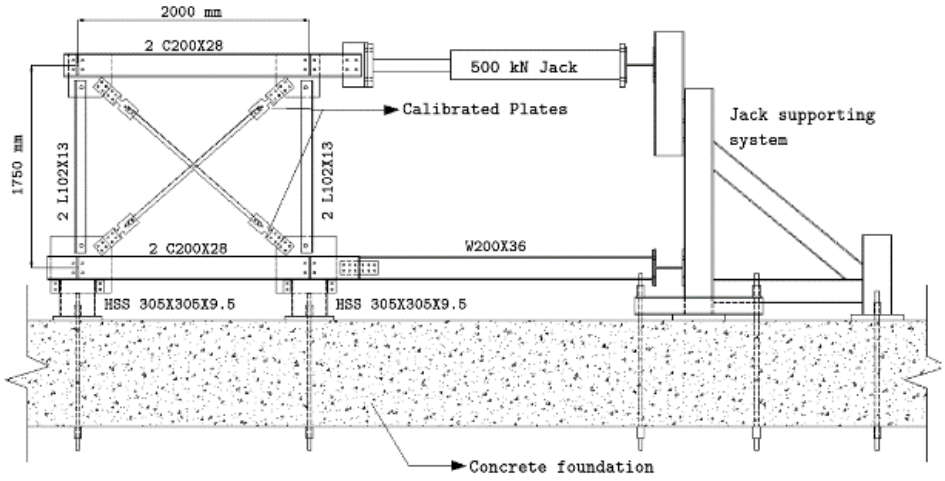

Fig. 7 Schematics of the test setup [24]

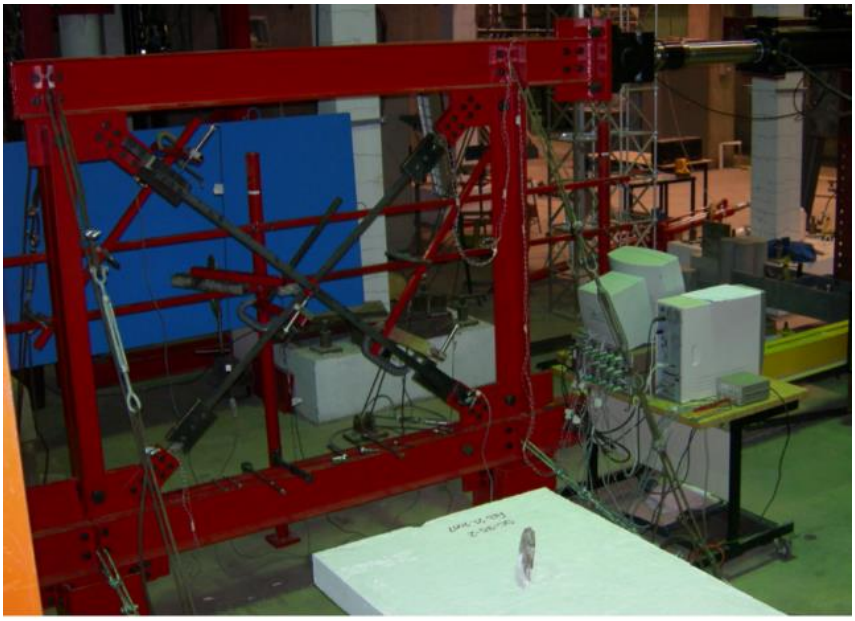

Fig. 8 X-bracing test setup [24]

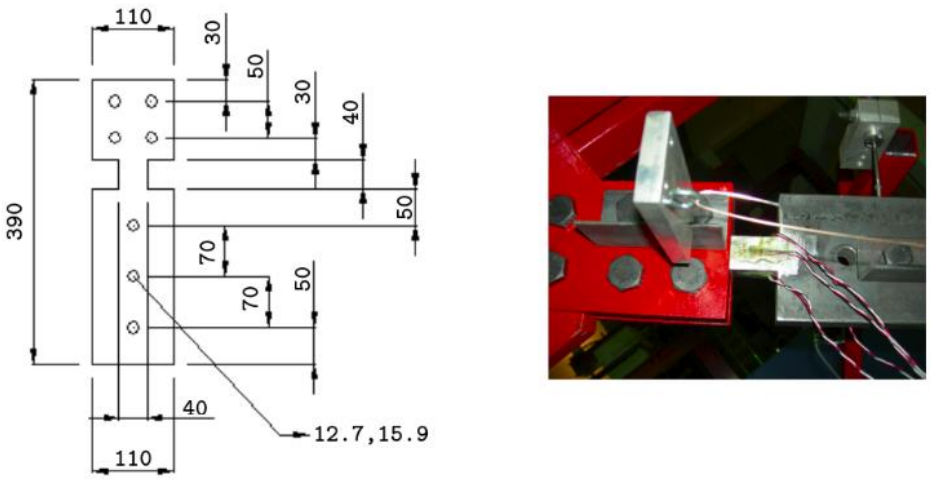

Fig. 9 Geometry of the end plates and locations of the strain gauges (dimensions in millimeters) [24]

4.2. Test Specimens

The X-bracing configuration involves two single angle sections under tension and compression. The target member is the angle under compression. Each angle is connected to the end plates using three bolts on one leg. The same leg is restrained in the middle of the member by a single bolt that is connected to the other bracing member, which is under tension. A filler plate was provided to fit the space between two angles in the middle and to ensure sufficient lateral support at the point of attachment (Fig. 10). The two configurations were L38X38X3.2 and L44X44X3.2 angle sections. The repeatability of results was assessed by testing two specimens for each configuration. Table 5 lists the specimens and their properties, which are based on tests that were conducted on coupons.

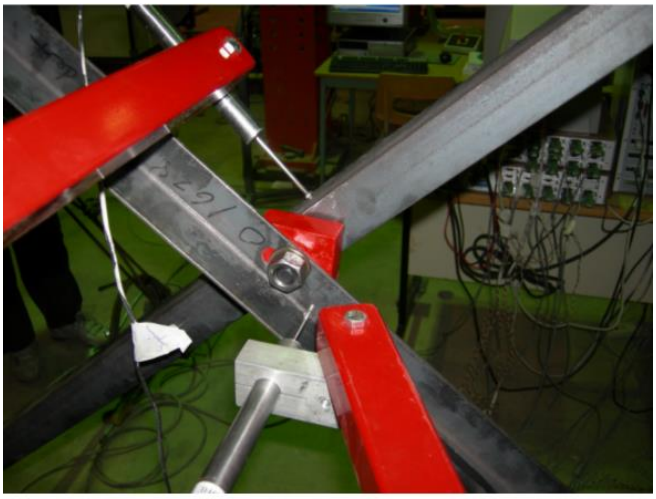

Fig. 10 Lateral support of the angles in the middle [24]

Table 5
Details of the X-bracing test specimens

Test	Section	D (mm)	F_y (MPa)
1	L38X38X3.2	12.7	370
2	L38X38X3.2	12.7	392
3	L44X44X3.2	15.9	393
4	L44X44X3.2	15.9	393

Note: (D: Bolt diameter)

4.3. Finite Element Modeling of the Specimens

The four angle specimens of the previous section were modeled using the Code_Aster software. Fiber beam elements are considered, and the optimum element size was evaluated to be 100 mm after conducting preliminary tests. To simplify the analysis, only the bracing angle members and the end connection plates are included in the model. A preliminary deflection value of Length/1000 [30] at the mid-length of the braces is applied to the weak bending axis as a global geometrical imperfection. It is assumed that the outside frame members are rigid in comparison to the angle members. Therefore, the end connection plates on top are supported by fixed supports with only unrestrained lateral displacement. The bottom supports are assumed to be fixed. The angle members are connected to these supports via two elements: a rigid beam element, which is used to include the member eccentricity, and a nonlinear spring, which is used to model the three-bolt-connection behavior. The properties of the spring element depend on the slippage and the bolted connection behavior according to the formulas that are presented by Rex et al. [33]. To model the single bolt that attaches the members at the middle of the bracing system, it is assumed that the middle nodes have identical displacement. However, the relative rotational displacement is free at this point.

The proposed method was applied to the analysis. First, σ_{cr} was calculated for each specimen using Code_Aster (Fig. 11). Since the boundary conditions of the members are not as described in Section 2.1, Equation 2 cannot be used and finite element modeling is implemented instead. In the X-bracing tests, the angle member needed to be restrained at the middle for modeling the pinned connection. Since CUFSM could not apply this type of restraint to the member, Code_Aster was used to perform the calculation. The bracing member under compression was modeled in Code_Aster using plate elements and mesh refinement was optimized via several trials. Each element had four corner nodes with six degrees of freedom and the maximum element size was 4 mm. Fixed boundary conditions were applied to the nodes on one leg of the member on each end. To model the constraint in the middle of the brace member, a hinged support was applied to a node on the same supported leg (Fig. 7). Then, the elastic buckling analysis was performed and the σ_{cr} value was calculated for the brace member.

The next step was to calculate the λ_p value for each specimen via Equation 1. Table 6 summarizes the calculated σ_{cr} and λ_p values for each specimen. Then, the stress-strain curve is calculated using the two steps that were specified earlier: first, Equations 3 to 5 were used to calculate two points, namely, A and B, on the curve for the specified value of λ_p; second, the parameters in Equations 6 and 7 were calculated such that the stress-strain curve passes through points A and B. In the final step, the calculated curve is applied as a material behavior to the fiber elements of the specimens. The nonlinear analysis phase is completed by Code_Aster and the assumptions of nonlinear material and large displacements are included in the procedure.

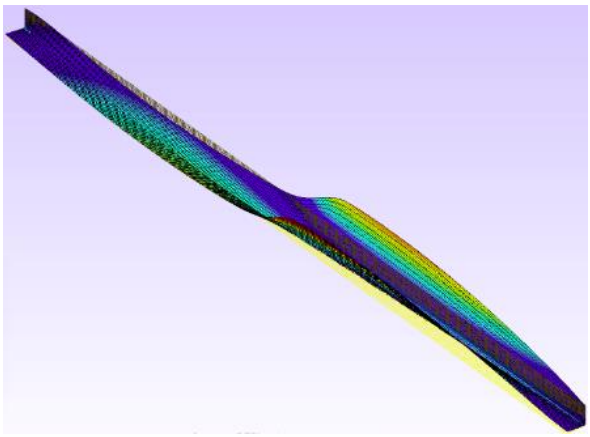

Fig. 11 Local buckling mode of a specimen (Test 3)

Table 6
Calculated σ_{cr} and λ_p values for the test specimens

Test	σ_{cr} (MPa)	λ_p
1	295	1.11
2	295	1.15
3	234	1.29
4	234	1.29

4.4. Results comparison and discussion

The experimental specimens failed due to local buckling phenomena. Fig. 12 shows the final deflection for four of the test specimens. Fig. 13 compares the failure stresses of the experimental tests to those of the finite element models and the member capacity based on ASCE 10-97 [34] and EC3 [27]. To evaluate the performance of the presented method, another set of analyses is performed without applying the proposed method to account for local buckling in the model. According to the comparisons, neglecting the local buckling failure in the analysis results in very high failure stresses. In the class

4 sections of this study, the local buckling failure controls the member capacity. Although the global buckling effect is included in the analysis due to large displacement option, it cannot take into account local failures which results in very high values of failure stress.

According to Table 7, the results of failure stress ($\sigma_{failure}$) for the finite element model are much more accurate and consistent with the tests when the presented method is applied. The mean value of FEA to Test results is 1.02 when the modification of material behavior is involved in the model. Despite the use of large displacement analysis, the above value increases dramatically to 1.54 if the effect of local buckling is ignored. Hence, the procedure that is presented in this study offers an appropriate solution for modeling the local buckling behavior of slender sections by beam elements.

Comparing the results of the presented method and the design capacity of the specimens that is based on ASCE 10-97 and EC3, the proposed method yields results that are similar to ASCE 10-97 and that are consistent with (but less conservative than) EC3. The coefficient of variation (COV) is slightly less than for design codes. For test 4, the discrepancy between the finite element model and the experimental test reaches a maximum of 15 percent. This is also consistent with the maximum error that is obtained with ASCE 10-97. This error could be due in part to the loading and boundary conditions that are used in the bracing tests, which are not perfectly represented in the model and in the codes.

Fig. 12 Local failure of test specimens (2 and 3) [24]

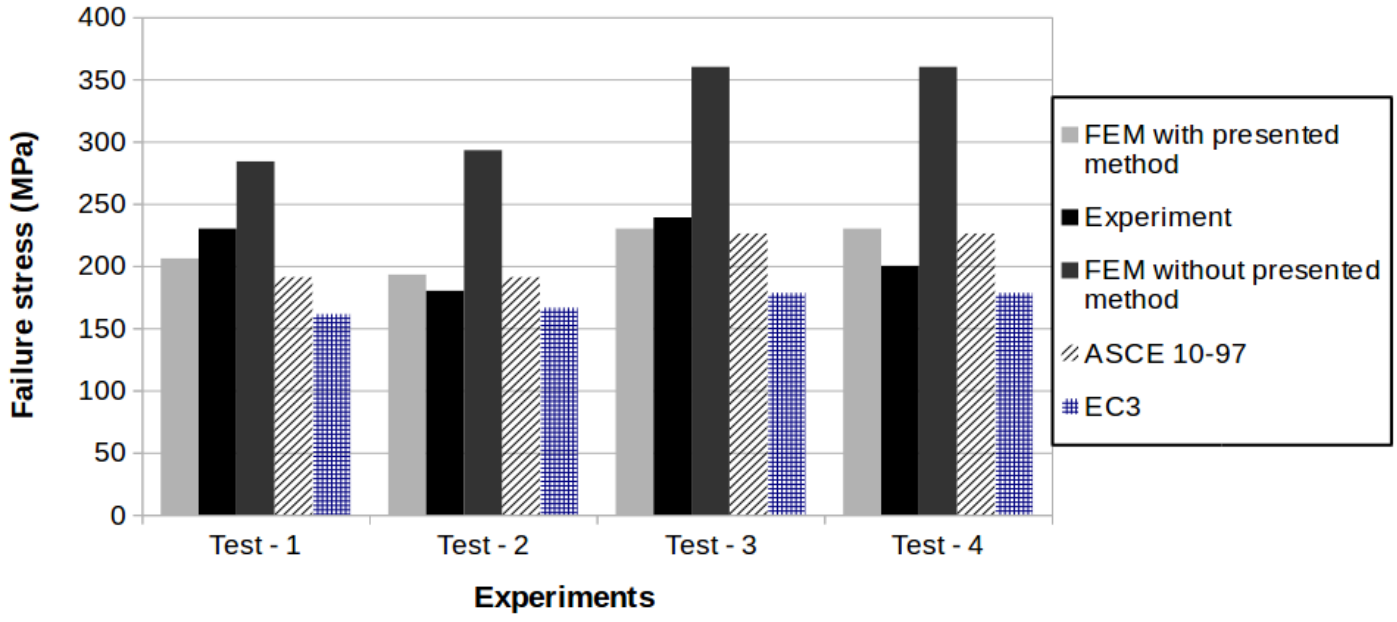

Fig. 13 Comparison of failure stress results

Table 7
Accuracy of the analysis with and without utilization of the presented method

Test	$\sigma_{failure}$ FEA (MPa)		$\sigma_{failure}$ test (MPa)	$\sigma_{capacity}$ ASCE (MPa)	$\sigma_{capacity}$ EC3 (MPa)	$\sigma_{failure}$ (FEA/test) ratio		ASCE / test	EC3/test
	w-lb	w/o-lb				w-lb	w/o-lb		
1	206	284	230	191	162	0.89	1.23	0.83	0.7
2	193	293	180	191	167	1.07	1.62	1.06	0.92
3	230	360	239	226	179	0.96	1.5	0.94	0.75
4	230	360	200	226	179	1.15	1.8	1.13	0.89
Average						1.02	1.54	0.99	0.82
COV (%)						11	15.4	13.2	13.3

Note: (w-lb: with local buckling and w/o-lb: without local buckling)

5. Conclusions

This article presented a new method for including the local buckling failure of class 4 members that are modeled by fiber beam finite elements. To consider this phenomenon, the stress-strain material behavior of the member was modified in the finite element model. A stress-strain curve formula was provided for each class 4 member that is based on the local buckling slenderness value (λ_p) of the member. Forty-two short angle specimens with λ_p values between 0.57 and 1.20 were tested and the force-deflection behavior of each specimen was recorded. Then, the stress-strain behavior was calculated for each of the λ_p values of the tests. Based on the above stress-strain behaviors and curve fitting technique, a general formula was presented that relates the λ_p value to a stress-strain material behavior.

To apply the method to a full-scale model, each class 4 member is recognized and the corresponding λ_p value is calculated. In the next step, the modified stress-strain curve is generated via the presented formula. Finally, the curve is assigned to the corresponding member as the material behavior in the finite element software.

To evaluate the feasibility and accuracy of the method, it was implemented for four cross-braced frame structures that were tested at Université de Sherbrooke. For the two studied configurations, class 4 angle sections were used as bracing members. The results were compared to two fiber element models, with and without using the proposed method. It was observed that when utilizing the proposed method in the models, the mean ratio of the model-to-test failure stress is 1.02, whereas this ratio increases to 1.54 when the method is not utilized. Additionally, comparing the proposed method to the design capacity that is calculated based on Eurocode and ASCE standards demonstrated that the new method provides more consistent results. Although the proposed method is not a practical design procedure, it may be used to improve nonlinear beam models of lattice towers that aim at complementing and reducing the need for full-scale transmission tower tests.

The presented method for modifying the material stress-strain behavior is only valid for the $\lambda_p$values interval of 0.57 to 1.20. Future research is needed for expanding this interval to cover more versatile class 4 sections such as unequal leg angles. Additionally, the method was validated with only four bracing tests. Further investigations should be conducted to validate the proposed method on more complex structures and field test results.

Acknowledgements

The authors gratefully acknowledge the financial support from the National Sciences and Engineering Research Council of Canada (NSERC), RTE and Hydro-Québec.

References

[1] Chan S. and Cho S., Second order analysis and design of angle trusses part i: Elastic analysis and design, Engineering Structures, 30, 616–625, 2008.
[2] Cho S. and Chan S., Second order analysis and design of angle trusses part ii: Plastic analysis and design, Engineering Structures, 30, 626–631, 2008.
[3] Prasad Rao, N. and Samuel K.G.M., Lakshmanan N. and Nagesh, R.I., Failure analysis of transmission line towers, Journal of Performance of Constructed Facilities, 25(3), 231–240, 2011.
[4] Prasad Rao N., Samuel K.G.M., Lakshmanan N., Nagesh R.I., Investigation of transmission line tower failures, Journal of Engineering Failure Analysis, 17, 1127–1141, 2010.
[5] Schafer B., Advances in direct strength design of thin-walled members, Advanced Structures, 1, 333–339, 2003.
[6] Silvestre N., Camotim D. and Dinis P.B., Post-buckling behaviour and direct strength design of lipped channel columns experiencing local/distortional interaction, Journal of Constructional Steel Research, 73, 12–30, 2012.
[7] Martins A.D., Camotim D. and Dinis P.B., On the distortional-global interaction in cold-formed steel columns: Relevance, post-buckling behaviour, strength and DSM design, Journal of Constructional Steel Research 145, 449–470, 2018.
[8] Bouchard P.-L., Calcul de la capacité de pylônes à treillis avec une approche stabilité. Mémoire de maîtrise. Université de Sherbrooke, 2013.
[9] Sad Saoud K., Langlois S., Loignon A. and Lamarche C.P., Failure analysis of transmission line steel lattice towers subjected to extreme loading. Annual Conference of the Canadian Society for Civil Engineering, June 13-16, Fredericton, Canada, 2018.
[10] Prasad Rao N., Samuel K.G.M., Lakshmanan N. and Nagesh R.I., Effect of bolt slip on tower deformation, Practice Periodical on Structural Design and Construction, 17(2), 65–73, 2012.
[11] Gravel G, Bouchard P.L., Prud'homme S., Sad Saoud K. and Langlois S., Assessment of the effect of residual stresses on the mechanical behavior of steel lattice transmission towers. Annual Conference of the Canadian Society for Civil Engineering, June 13-16, Fredericton, Canada, 2018.
[12] Shan L. and Peyrot A.H., Plate element modeling of steel angle members, Journal of Structural Engineering (ASCE), 114(4), 821–840, 1988.
[13] Lee P.-S. and McClure G., A general three-dimensional l-section beam finite element for elastoplastic large deformation analysis, Computers and Structures, 84, 215–229, 2006.
[14] Park Y.-S., Iwai S., Kameda H. and Nonaka T., Very low cycle failure process of steel angle members, Journal of structural engineering, 122(2), 133–141, 1996.
[15] Becque J. and Rasmussen K.J., Experimental investigation of local-overall interaction buckling of stainless steel lipped channel columns, Journal of Constructional Steel Research, 65(8-9), 1677–1684, 2009.
[16] Rasmussen K.J., Design of slender angle section beam-columns by the direct strength method, Journal of Structural Engineering, 132(2), 204–211, 2006.
[17] Haidarali M. and Nethercot D., Local and distortional buckling of cold-formed steel beams with edge-stiffened flanges, Journal of Constructional Steel Research, 73, 31–42, 2012.
[18] Haidarali M., Nethercot D. and Ashraf M., Local buckling of cold-formed steel lipped z section beams under pure bending, 5th International Conference on Advances in Steel Structures, ICASS 2007, 3, 474–480, 2007.
[19] Kitipornchai S. and Chan S., Nonlinear finite-element analysis of angle and tee beam-columns, Journal of Structural Engineering (ASCE), 113(4), 721–739, 1987.
[20] Kitipornchai S., Albermani F. and Chan S., Elastoplastic finite-element models for angle steel frames, Journal of Structural Engineering, (ASCE), 116 (10), 2567–2581, 1990.
[21] Vieira R.F., Virtuoso F.B.E., Pereira E.B.R., Buckling of thin-walled structures through a higher order beam model, Computers and Structures, 180, 104–116, 2017.
[22] Carrera E., Pagani A. and Petrolo M., Refined 1D Finite Elements for the Analysis of Secondary, Primary, and Complete Civil Engineering Structures, Journal of Structural Engineering, 141(4), 2015.
[23] Huang L., Li B. and Wang Y., Computation Analysis of Buckling Loads of Thin-Walled Members with Open Sections, Mathematical Problems in Engineering Volume 2016, Article ID 8320469.
[24] Morissette E., Évaluation des normes de calcul et du comportement des cornières simples en compression utilisées comme contreventements dans les pylônes à treillis en acier, Masters Degree Thesis, Université de Sherbrooke, 2008.
[25] Handbook of Steel Construction - Ninth Edition, Canadian Institute of Steel Construction - ISBN : 0-88811-114-2, 2006.
[26] Steel construction manual, American Institute of Steel Construction, 2005.
[27] Eurocode 3: Design of steel structures, European Committee for Standardization (CEN), Brussels., EN 1993-1-1, 2005.
[28] ASTM A36 / A36M-14, Standard Specification for Carbon Structural Steel, ASTM International, West Conshohocken, PA, 2014.
[29] ASTM A370-02, Standard Test Methods and Definitions for Mechanical Testing of Steel Products, ASTM International, West Conshohocken, PA, 2001
[30] A. Beyer, N. Boissonnade, A. Khelil, A. Bureau, Influence of assumed geometric and material imperfections on the numerically determined ultimate resistance of hot-rolled U-shaped steel members, Journal of Constructional Steel Research, 147, 103–115, 2018.
[31] Schafer B., Review: The direct strength method of cold-formed steel member design, Journal of Constructional Steel Research, 64, 766–778, 2008.
[32] Schafer B. and Adany S., Buckling analysis of cold-form steel members using cufsm: conventional and constrained finite strip methods, Proceedings of the 18th International Specialty Conference on Cold-formed Steel Structures, Florida, USA, 2006.
[33] Rex C.O. and Easterling W.S., Behavior and modeling of a bolt bearing on a single plate, Journal of Structural Engineering, 129(6), 792–800, 2003.
[34] Design of Latticed Steel Transmission Structures. ASCE 10-97, American Society of Civil Engineers, 1998.

Advanced Steel Construction – Vol. 15 No. 4 (2019) 377–385
DOI:10.18057/IJASC.2019.15.4.8

ANTI-COLLAPSE ANALYSIS OF UNEQUAL SPAN STEEL BEAM–COLUMN SUBSTRUCTURE CONSIDERING THE COMPOSITE EFFECT OF FLOOR SLABS

Wei-hui Zhong[1, 2, *], Zheng Tan[1], Xiao-yan Song[1] and Bao Meng[1]

[1] *School of Civil Engineering, Xi'an University of Architecture & Technology, Xi'an 710055, China*
[2]*Key Lab of Structural Engineering and Earthquake Resistance, Ministry of Education, Xi'an University of Architecture and Technology, Xi'an 710055, China*
(Corresponding author: E-mail:zhongweihui1980@163.com)

ABSTRACT

Based on the alternate load path method and considering the composite effect of floor slabs, a beam–column frame with unequal spans was studied to derive the equations for the load–deformation relationship at five different stages (elastic, elastic–plastic, plastic, transient, and catenary) during progressive collapse. The anti-collapse mechanism of the composite beam–column frame and the influence of arch action were carefully analyzed. A numerical model was established using ABAQUS for the relevant model, and the model was verified by comparison with experimental data. Further, the theoretical equations were compared with the results of numerical simulations for different span ratios. The results show that the theoretical equations possess good generality and high accuracy for analyzing progressive collapse of a composite beam–column frame with unequal spans.

ARTICLE HISTORY

Received: 25 December 2018
Revised: 05 August 2019
Accepted: 11 August 2019

KEYWORDS

Composite beam–column frame;
Anti-collapse mechanism;
Progressive collapse;
Arch action;
Unequal spans

1. Introduction

A fundamental aim of structural design is to ensure the safety of a structure; specifically, to prevent progressive collapse of the structure. Once progressive collapse occurs, it is often catastrophic and can cause serious loss of life and property. Therefore, methods to prevent the progressive collapse of structures are an important part of the theoretical and experimental practice of structural engineering. When vertical load-bearing components (columns) in a structure are destroyed, the remaining structure will redistribute the internal forces. With increasing vertical deformation, the internal force in the horizontal members (beams) gradually changes from flexural to tensile to carry the vertical loads, forming what is called a catenary mechanism. At this stage, the catenary mechanism is the last line of defense against progressive collapse of the structure, and therefore, it is a key component in the anti-collapse design of a structure.

Research regarding anti-collapse mechanisms of beam–column frames currently focuses on pure steel frame beam–column structures with equal spans. Studies using unequal spans are rare, and the composite effect between supported concrete slabs and the steel beams is usually not considered. Demonceau and Jaspart[1] conducted static loading tests on a single-story frame and proposed a mechanical model of the substructure considering the composite beam effect in different stages, where the load–displacement formula was deduced and verified. Izzuddin et al.[2-4], Arash and Fereidoon[5], and Vlassis et al.[6] theoretically analyzed the behavioral changes of steel beams with equal spans during the failure of the middle column, and proposed formulas for the anti-collapse bearing capacity. Li et al.[7,8] proposed a model of steel beams subjected to axial and rotational spring constraints under distributed loads. The constrained coefficient method and rigid plastic hinge model were used to derive the load–span deflection formula of constrained steel beams in different stages. The reliability of the formula was verified using finite element analysis. In our previous report [9], we analyzed the entire process of a beam–column substructure of a steel frame resisting external loads using the alternate load path method and deduced the formula for the anti-collapse bearing capacity and displacement of the beam–column substructure. The accuracy of the formula was verified using numerical examples.

Based on the alternate load path method[10] and the constraint coefficient method[11], a concrete slab and steel composite beam–column frame was considered in this study. The bearing capacity–deformation equations of the composite beam–column frame with unequal spans were derived for different stages of the process. The influence of arch action was also considered. A numerical analysis model was established using ABAQUS, and then validated by comparison with relevant test results. In addition, the results of the derived equations were compared with those of the numerical simulation for different span ratios. The results of the comparison indicate that the theoretical equations provide good versatility and high calculation accuracy for anti-collapse analysis of a composite beam–column frame with unequal spans.

2. Analysis model of the composite beam–column substructure

2.1. Analysis model

In the anti-collapse analysis of a frame structure, the floors above the failure column and the two spans connected to the failure column are usually defined as being in the direct influence area, while other parts are within the indirect influence area [3], as shown in Fig. 1. The direct influence area is the focus of anti-collapse research and design as it must directly bear the load resulting from the failure of the vertical load-bearing component in order to prevent progressive collapse, while the indirect influence area provides reliable boundary conditions for the direct influence area.

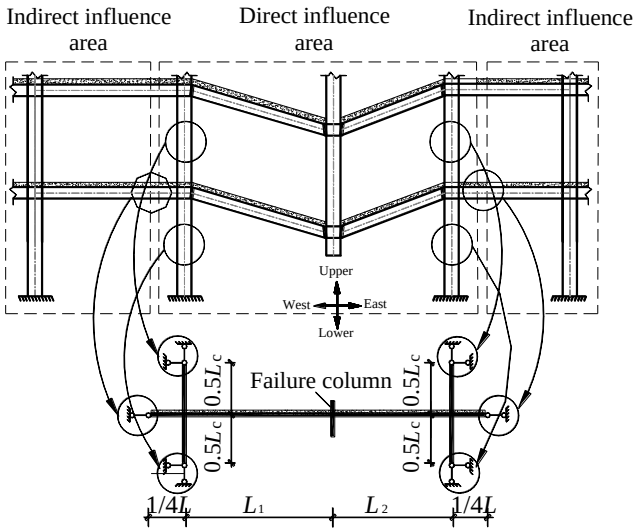

Fig. 1. Diagram defining the direct and indirect influence areas of the composite beam–column frame mode

The alternate load path method is currently the most commonly used method for analyzing and designing the collapse resistance of a frame structure. This method does not consider the cause of failure or the failure process of the column; it only considers the change in the behavior of the main components connected to the failure column under load. In the frame, the inflection point of the side column is approximately located in the middle of the story height. The quarter point (L_0) of the beam in the panel adjacent to the failure column, between two intact column joints, is taken as the location of the boundary condition to simulate the constraint of the peripheral members.

A composite frame model [12] consisting of two beams and three columns is shown in Fig. 1. When the middle column of this structure fails, the beams on each side of the column are subjected to an increasingly large deformation, and the resistance mechanism gradually transforms from beam action to catenary action.

As shown in Fig. 1, the joints of the composite beam–column frame model have both axial and rotational constraints. If the model is further simplified by applying an axially constrained spring and a rotationally constrained spring (corresponding to spring stiffnesses K_R and K_r, respectively) at the joint, a simplified analysis model of the composite beam–column frame can be obtained, as shown in Fig. 2, in which the failure column allows only vertical movement and no rotation.

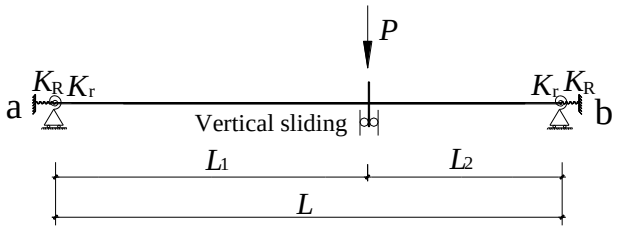

Fig. 2. Simplified analysis model of the composite beam–column frame direct influence area

2.2. Analytical assumptions and response of a composite beam

2.2.1. Assumptions

To obtain the bearing capacity–deformation equation of the composite beam–column frame, the following simplifications and assumptions were made:(1) The beam and column sections are all I-shaped sections, and the material is an ideal elastic-plastic material;(2) Rigid plastic hinges only appear on the beam;(3) The tensile strength of the concrete is negligible;(4) The slip between the steel beam and the concrete slab is not considered as the composite beam is assumed to contain a complete shear connection, while the differential deformation of the steel beam members and buckling of the flange plate are ignored.(5) The correlation between the axial force and bending moment of the composite beam section followed Eq. (1) [11,13]. (6) The joint has sufficient rotational deformation capability to allow the catenary effect to be fully developed and employed.

$$\frac{M}{M_p}+\frac{N}{N_p}=1 \tag{1}$$

Here, M_p is the plastic limit bending moment of the composite beam section and N_p is the plastic limit axial force of the composite beam section.

2.2.2 Response of composite beam under concentrated load

A typical vertical bearing capacity (P) vs. deformation (V)curve (load–displacement curve) is used to describe the force in the joint and the tensilebending of the composite beam–column frame during progressive collapse, as shown in Fig. 3. Five clear stages are defined:the (1) elastic (OA), (2) elastic–plastic (AB), (3) plastic (BC), (4) transient (CD), and (5) catenary (DE) stages. The load–displacement curve in each stage is approximately linear.

In the elastic phase and the elastic–plastic phase (① and ②, respectively in Fig. 3), the joint mainly relies on the bending moment of the section to resist the external force; the axial force is insignificant at this stage. The structure mainly resists collapse via the beam mechanism. The tensile-bending correlation curve mainly moves vertically from the origin to the plastic positive yielding moment M_{p+} and to the plastic negative yielding moment M_{p-} of the composite beam, as shown in Fig. 4a. When the structure enters the plastic stage (③ in Fig. 3), the axial force is still insignificant. The joint reaches its plastic bending capacity and the load does not change over this defined range of displacement. In the tensile-bending correlation curve, the composite beam reaches the plastic bending yield moment M_{p+} at the mid-span and reaches the plastic negative yield bending moment M_{p-} at the beam end, as shown in Fig. 4b. When the plastic phase ends, the structure enters the transition stage (④ in Fig. 3), and significant axial force is generated in the composite beam. At this time, the composite beam–column structure begins to transform from being supported by the bending mechanism
to being supported by the catenary mechanism, and the axial force causes astate transformation of the joint. The tensile-bending correlation curve mainly moves linearly from the plastic yield bending moment to the plastic tensile bearing capacity, as shown in Fig. 4c. When the structure enters the catenary stage (⑤ in Fig. 3), the beam mechanism is no longer active; only axial tension exists in the composite beam, and the joint has yielded due to tensile stress, as shown in Fig. 4d.

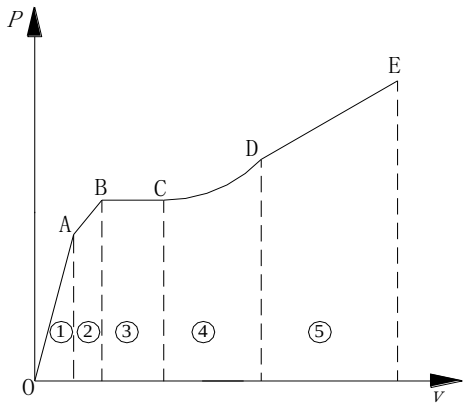

Fig. 3. Typical load–deformation curve for the composite beam–column substructure

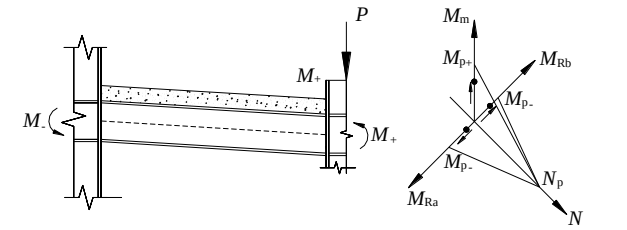

(a) Before joint yielding (elastic stage and elastic-plastic stage)

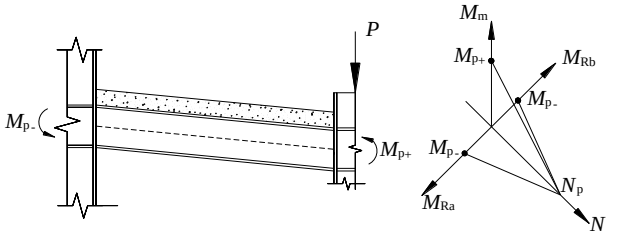

(b) Formation of plastic hinges (plastic stage)

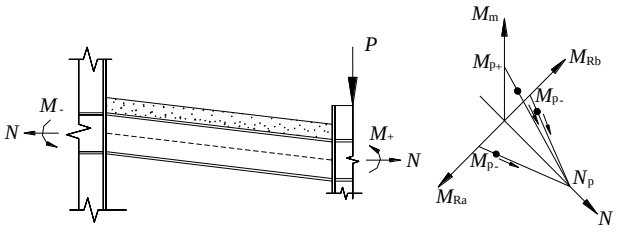

(c) Transformation from the beam mechanism to the catenary mechanism (transition stage)

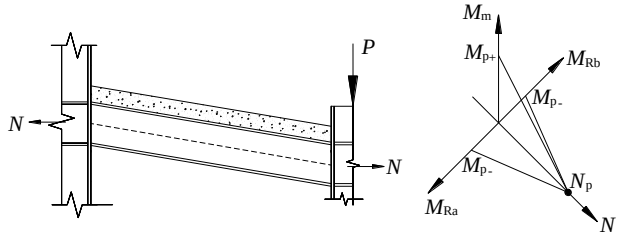

(d) Catenary mechanism (catenary stage)

Fig. 4. Behavior of the frame joints during different stages of progressive collapse

3. Theoretical background of collapse stages

Among the stages of progressive collapse of the composite beam–column frame defined in Fig. 3., the elastic–plastic stage reflects the process of forming plastic hinges at the end of the composite beam at the failure column and the side columns. This stage is a complex nonlinear process with too

many influencing factors to accurately capture. To simplify the analysis, the behavior in this stage was approximated as a straight line. The various stages of the process are described here in detail.

3.1. Elastic stage

In the elastic stage, the beam–column frame mainly relies on the bending moment resistance of the section to resist the external force; as the axial force is ignored, only the action of the rotationally constrained spring is considered. The corresponding model of the elastic stage is shown in Fig. 5.

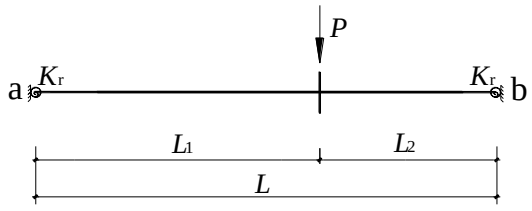

Fig. 5. Analysis model for the elastic stage

If ends a and b of the beam are considered to be hinged ($K_r = 0$), then the bending moment M_{sm} at the beam end and vertical deformation v_s at the failure column are given by:

$$M_{sm} = \frac{PL_1L_2}{L}, \quad v_s = \frac{PL_1^2L_2^2}{3EI_+L} \tag{2}$$

where, E is the elastic modulus of the steel and I_+ is the section moment of inertia of the composite beam, converted into steel under the positive bending moment [14]. If the beam ends a and b are fixed ($K_r \to \infty$), then the bending moment M_{fm} of the beam ends at the failure column, the vertical deformation v_f at the failure column, and the bending moments M_{fa} and M_{fb} of the beam ends at the side columns are given by:

$$M_{fm} = \frac{2PL_1^2L_2^2}{L^3}, \quad v_f = \frac{PL_1^3L_2^3}{3EI_+L^3} \tag{3}$$

$$M_{fa} = \frac{PL_1L_2^2}{L^2}, \quad M_{fb} = \frac{PL_1^2L_2}{L^2} \tag{4}$$

The actual state of the rotational constraint is a mixture of the hinged and fixed conditions. To simplify the analysis, the constraint coefficient method was adopted, introducing the rotational constraint coefficients c_f and c_s as follows:

$$c_f = \frac{K_{er}}{K_{rm}} = \frac{K_{rs}}{2K_{rm}+K_{rs}}, \quad c_s = 1-c_f = \frac{2K_{rm}}{2K_{rm}+K_{rs}} \tag{5}$$

$$K_{er} = \frac{1}{\frac{2}{K_{rs}}+\frac{1}{K_{rm}}} \tag{6}$$

where K_{er} is the equivalent line stiffness of the composite beam; K_{rs} is the negative rotational stiffness of the composite beam corresponding to the negative bending moment; and K_{rm} is the positive rotational stiffness of the composite beam corresponding to the positive bending moment, as follows:

$$K_{rm} = \frac{EI_+}{L}, \quad K_{rs} = \frac{EI_-}{L'} \tag{7}$$

where I_- is the section moment of inertia of the composite beam converted into steel under the negative bending moment [14] and L' is the length of the rotational spring, calculated as follows [15]:

$$L' = L\left(\sqrt{(I_-/I_+)^2 + I_-/2I_+} - I_-/I_+\right) \tag{8}$$

For the calculation model of the composite beam–column substructure in the elastic stage shown in Fig. 5, the vertical deformation v at the failure column and the beam bending moments at the failure column M_m and at the side columns M_{Ra} and M_{Rb} were determined as follows:

$$v = c_s v_s + c_f v_f = \frac{PL_1^2L_2^2}{3EI_+L}\left(\frac{L_1L_2}{L^2}c_f + c_s\right) \tag{9}$$

$$M_m = c_s M_{sm} + c_f M_{fm} = \frac{PL_1L_2}{L^3}(L^2c_s + 2L_1L_2c_f) \tag{10}$$

$$M_{Ra} = c_f M_{fa} = \frac{PL_1L_2^2}{L^2}c_f \tag{11}$$

$$M_{Rb} = c_f M_{fb} = \frac{PL_1^2L_2}{L^2}c_f \tag{12}$$

According to Eq. (9), the equation for the bearing capacity at the failure column of the composite beam–column substructure in the elastic stage is written as:

$$P① = \frac{3EI_+L^3v}{L_1^2L_2^2(L_1L_2c_f + L^2c_s)} \tag{13}$$

It is easy to observe that the rotational constraint coefficient c_f determines where the plastic hinge appears earliest in the failure column and side column. In the case where $L_1 > L_2$ and $M_{Ra} < M_{Rb}$, the plastic hinge might appear on the right side of the failure column or at end b of the composite beam.

If the right side of the failure column yields earlier than end b of the composite beam, then:

$$P_{fm} = \frac{M_{p+}L^3}{L_1L_2(L^2c_s + 2L_1L_2c_f)} \tag{14}$$

However, if end b of the composite beam yields earlier than the right side of the failure column, then:

$$P_{fb} = \frac{M_{p-}L^2}{L_1^2L_2c_f} \tag{15}$$

Note that:

1) When,

$$P_{fm} \le P_{fb} \Rightarrow c_f \le \frac{M_{p-}L^2}{M_{p+}LL_1 + M_{p-}L^2 - 2M_{p-}L_1L_2},$$

the right side of the failure column yields earlier than end b of the composite beam, and

$$P_A = P_{fm}, \quad v_A = \frac{P_AL_1^2L_2^2}{3EI_+L}\left(\frac{L_1L_2}{L^2}c_f + c_s\right) \tag{16}$$

2) When,

$$P_{fm} > P_{fb} \Rightarrow c_f > \frac{M_{p-}L^2}{M_{p+}LL_1 + M_{p-}L^2 - 2M_{p-}L_1L_2},$$

end b of the composite beam yields earlier than the right side of the failure column, and

$$P_A = P_{fb}, \quad v_A = \frac{P_AL_1^2L_2^2}{3EI_+L}\left(\frac{L_1L_2}{L^2}c_f + c_s\right) \tag{17}$$

Here, P_A and v_A are the values corresponding to Point A on the load–deformation curve of the failure column (Fig. 3).

3.2. Elastic–plastic stage

The elastic–plastic stage occurs between the elastic and plastic stages. To simplify analysis, a linear transition between the stages was adopted, so the equation for the bearing capacity at the failure column of the composite beam–column frame is as follows:

$$P② = \frac{P_B - P_A}{v_B - v_A}(v - v_A) + P_A \tag{18}$$

where P_B and v_B are the values corresponding to Point B in Fig. 3. The end of the elastic–plastic stage is marked by the development of plastic hinges on both sides of the failure column and at beam ends a and b. The calculation model at this time is shown in Fig. 6, where θ_1 and θ_2 are the beam end angles opposite the failure column, ignoring the bending deformation of the composite beam. According to the principle of virtual work (excluding the axial force and axial deformation in the composite beam), and referring to the calculation method of the deflection of a simply supported composite beam[16], the corresponding bearing capacity and deformation can be obtained as follows:

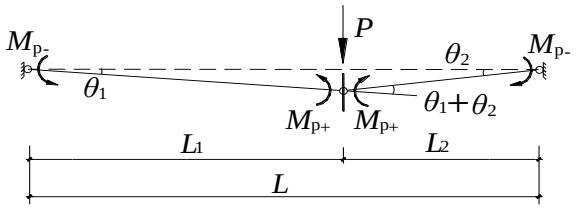

Fig.6. Analysis model in the plastic stage

$$\Sigma M \times \theta = P\Delta \Rightarrow P_B = (M_{p-} + M_{p+})\frac{L}{L_1 L_2} \tag{19}$$

$$v_B = \frac{PL_2(L^2 - L_2^2)^{\frac{3}{2}}}{9\sqrt{3}EI_+ L} \tag{20}$$

By substituting these expressions for P_B and v_B into Eq. (18), the correlation between bearing capacity and deformation at the failure column in the elastic–plastic stage can be obtained.

3.3. Plastic stage

In the plastic stage, plastic hinges appear on both sides of the failure column and at beam ends a and b, and the resistance of the frame no longer increases. In this case,$P③=P_C=P_B$ and the axial tension in the composite beam remains small. As the deformation increases, the internal force in the composite beam changes from primarily a bending moment to a combined bending moment and axial force. The catenary mechanism then gradually becomes dominant and the structure enters the transient stage. The final vertical deformation of the plastic stage $v_C$was analyzed using the conversion process from the plastic hinge mechanism to the catenary mechanism. The detailed derivation process is shown in section 3.4.

3.4. Transient stage

In the transient stage, due to the presence of axial force in the composite beam, the axially constrained spring at the beam ends begins to participate in the work. To simplify analysis, we assumed that the axial forces in the left and right span beams are equal [9,17] and that there is no eccentricity. The equivalent axial stiffness K_e of the composite beam can then be given by:

$$K_e = \frac{1}{1/K_{ac} + 1/K_{as} + 1/K_R} \tag{21}$$

where K_{ac} is the axial stiffness of the composite beam;A_c is the sum of the cross-sectional area of the steel beam and the area of the steel bars in the concrete slab; $K_{as} = 48EI_c/L_c^3$is the axial stiffness provided by the side column, where I_c is the section moment of inertia of the column; and K_R is the axial restraint stiffness provided by the perimeter members of the beam–column joint.

The calculation model of the composite beam–column frame in the transient stage is shown in Fig. 7. As the deformation increases, the axially constrained spring at the composite beam end is continuously elongated. If the left span is analyzed, the geometric relationship can be approximated as follows:

$$L_1^2 = v^2 + (L_1 - D_a)^2 \tag{22}$$

$$D_a = v^2 / 2L_1 \tag{23}$$

$$\partial D_a = v\partial v / L_1 \tag{24}$$

where D_a is the horizontal deformation of composite beam end a. Similar relationships can be written with D_b:

$$D_b = v^2 / 2L_2 \tag{25}$$

$$\partial D_b = v\partial v / L_2 \tag{26}$$

According to the rigid plastic hinge model, the horizontal deformation of the beam end includes the axial spring deformation and plastic hinge deformation.

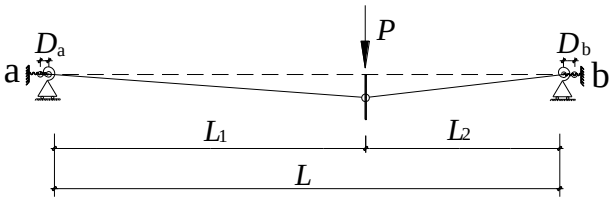

Fig.7. Analysis model in the transient stage

Hence, the total elastic elongation of the equivalent axial spring of the composite beam is as follows:

$$D_e = D_a + D_b - D_{pm+} - D_{pa-} - D_{pb-} \tag{27}$$

whereD_{pm+}, D_{pa-}, and D_{pb-} are the positive bending moment of the plastic hinge at the failure column of the composite beam, and the negative bending moment of the plastic hinges at the composite beam ends a and b, respectively. The axial tension provided by the axial spring is:

$$N = K_e D_e \tag{28}$$

With the differential of Eq. (28) given by:

$$\partial N = K_e \partial D_e \tag{29}$$

Substituting Eq. (27) into Eq. (29):

$$\partial N = K_e(\partial D_a + \partial D_b - \partial D_{pm+} - \partial D_{pa-} - \partial D_{pb-}) \tag{30}$$

According to the plastic yield flow criterion,

$$\partial D_p N_p = \partial \theta_p M_p \tag{31}$$

where N_p is the plastic axial force of the composite beam section. M_p/N_p is defined as r_p, where positive and negative bending moments in the plastic hinge corresponds to r_{p+} and r_{p-}, respectively. Ignoring the bending deformation of the beam, for a rigid plastic hinge, the plastic angular increment is approximated by:

$$\partial\theta_{pa-} = \partial v / L_1, \quad \partial\theta_{pb-} = \partial v / L_2, \quad \partial\theta_{pm+} = L\partial v / L_1 L_2 \tag{32}$$

Substituting Eq. (31) and (32) into Eq. (30):

$$\partial N = K_e\left(\frac{v\partial v}{L_1} + \frac{v\partial v}{L_2} - \frac{L\partial v}{L_1 L_2} r_{p+} - \frac{\partial v}{L_1} r_{p-} - \frac{\partial v}{L_2} r_{p-}\right) \tag{33}$$

The plastic stage (Phase ③ in Fig. 3) was assumed to have no axial tension, where v_C of the failure column at the end of the plastic stage (the beginning of the transient stage) was determined using Eq. (32) as:

$$v_C = r_{p+} + r_{p-} \tag{34}$$

Integrating Eq. (32), the axial force N is obtained as follows:

$$N = \frac{K_e L}{2L_1 L_2}(v - r_{p+} - r_{p-})^2 \tag{35}$$

The force in the composite beam–column frame under progressive collapse in the transient stage is thus as shown in Fig. 8 (considering the left span for analysis).

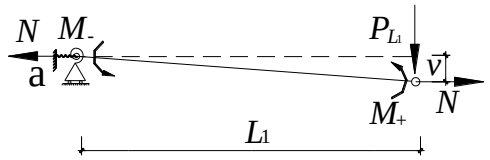

Fig.8. Force diagram of the composite beam in the transient stage

According to the relevant equation for bending moment and axial force (Eq. (1)), combined with the torque balance condition shown in Fig.9:

$$M_- + M_+ + Nv = P_{L_1} L_1 \tag{36}$$

$$M_{p-} + M_{p+} + N[v - (r_{p+} + r_{p-})] = P_{L_1} L_1 \tag{37}$$

The equation for bearing capacity of the failure column in the transient stage is thus:

$$P④ = \frac{L}{L_1 L_2}(M_{p-} + M_{p+}) + \frac{K_e L^2}{2L_1^2 L_2^2}(v - r_{p+} - r_{p-})^3 \tag{38}$$

At the end of the transient stage, the axial tension causes the composite beam to reach full-section yield (in which the bending moment in the beam is zero and the beam mechanism has ceased to function altogether). Then, the deformation of Point D in Fig. 3 is obtained from Eq. (35) as:

$$v_D = r_{p+} + r_{p-} + \sqrt{\frac{2N_p L_1 L_2}{K_e L}} \tag{39}$$

By substituting v_D from Eq. (39) into Eq. (38), the corresponding bearing capacity P_D at Point D can be obtained.

3.5.Catenary stage

In the catenary stage, the axial force in the composite beam section reaches N_p and then remains unchanged. As the deformation increases, the effect of the catenary mechanism becomes increasingly significant. At this time, the bending moment in the beam is ignored, and the composite beam represents the tensile force of the two-bar system. Therefore, the bearing capacity at the failure column is written as:

$$P⑤ = \frac{L}{L_1 L_2} N_p v \tag{40}$$

Related studies [18] have shown that when the relative v of the failure column exceeds one-fifth of the short beam span, frame failure can be considered as the collapse failure criterion of the structure.

4. Analysis of anti-collapse mechanism

4.1. Experimental tests

Previously, a progressive collapse test of a 1/3-scale composite beam–column frame consisting of four spans connected by rigid joints was conducted [19]. The dimensions and joint details of the specimen are shown in Figs. 9a and 9b.The steel columns and beams were H200×200×8×12 (mm) and H200×100×5.5×8 (mm) sections, respectively, of Q235B Chinese grade material. The concrete strength grade was C30, the thickness of the concrete slab was 100 mm, the concrete cube compressive strength was 24.5 MPa, and its elastic modulus was 2.65 × 10^4 MPa. The steel bars in the concrete slab wereHPB235 and were arranged in the slab as shown in Fig. 9c. A summary of the material properties of the steel components are listed in Table 1.

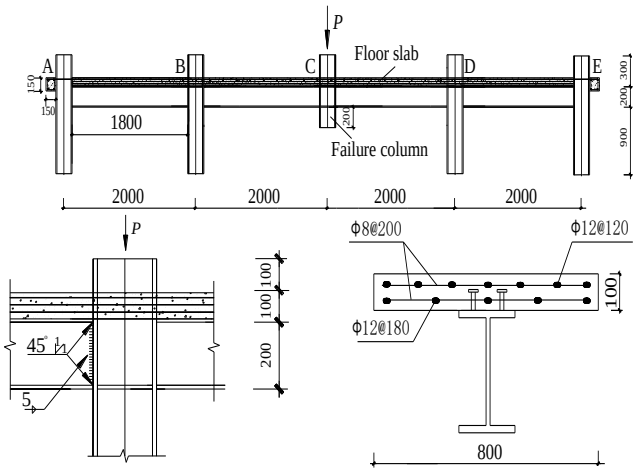

(a) Dimensions of the test specimen (b) Connection details (c) Layout of the rebar in the RC slab

Fig. 9. Composite beam–column frame test specimen (dimensions in mm)

Table 1
Material properties of the steel used in the test specimens

Components	Yield strength f_y (MPa)	Tension strength f_u (MPa)	Elastic modulus $E \times 10^5$(MPa)
Column flange	269	401	1.96
Column web	275	411	2.09
Beam flange	247	396	2.00
Beam web	276	415	1.98
ϕ 8	325	487	1.96
ϕ 12	331	464	1.95

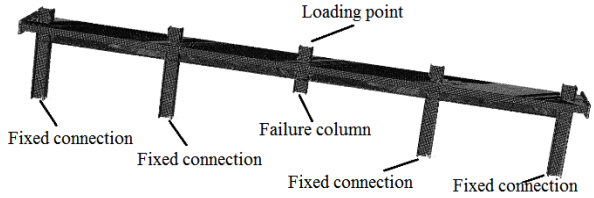

Fig. 10. Numerical analysis model of composite beam–column frame

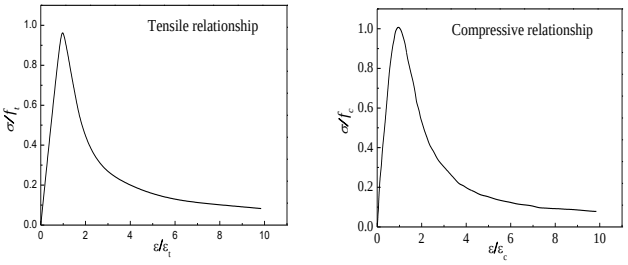

(a) Tensile relationship (b) Compressive relationship

Fig. 11. Stress–strain relationship of concrete

4.2. Numerical simulation

The numerical analysis model of the composite beam–column frame established in ABAQUS in a previous study [19] was used here, as shown in Fig.10. The beam–column members and the concrete slab were all constructed using C3D8R solid elements, and the steel bars in the concrete slab were constructed using T3D2 truss elements. The steel material was represented by the double-fold line constitutive model; its Poisson's ratio was 0.3 and the material properties shown in Table 1were used as input data. The concrete material was represented by the stress–strain relationship of C30 concrete as recommended in Appendix C of the Concrete Structure Design Code GB50010-2010 [20], as shown in Fig.11. The modeling method is described in detail in Section 6.2.

4.3. Numerical simulation and experimental results

A comparison of the bearing capacity–deformation curves determined using the numerical simulation (FE1) and experiments (Test) at the failure

column is shown in Fig.12. In general, the results of the numerical simulation agreed well with those of the experiment. However, because the arch action is not fully described in the numerical simulation, the first bearing capacity peak (around point B') was not obvious in the modeled curve. Overall, the numerical analysis model established here simulates the collapse resistance of composite beam–column frames after the failure of the middle column quite well, and can be used for analysis of progressive collapse of similar substructures.

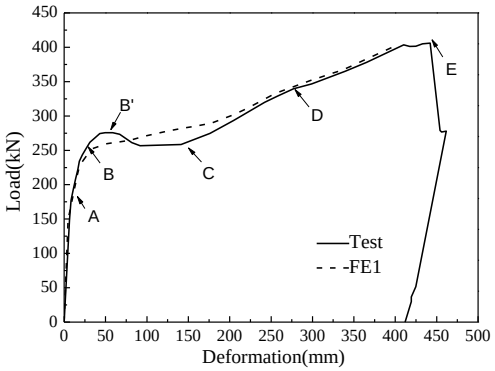

Fig. 12. Comparison between load-deformation curves from the numerical simulation (FE1)and experiments (Test). Points A–E are as defined in Fig. 3, while point B' is the point of peak load.

4.4. Verification of theoretical equation

Figure 13 shows a comparison of the load–deformation curves of the test results, numerical simulations, and theoretical equation (SM1). The theoretical curve better matched that of the experimental results in the initial stages compared to the numerical simulation curve, although the stiffness was greatly overestimated by the theoretical equation in the catenary stage compared to the other curves. This was mainly due to the fact that the side span of the frame selected in the physical test cannot provide sufficient axial constraint for the failure span; hence, the horizontal restraint stiffness of the composite beam of the failure span was too small to fully develop the catenary effect.

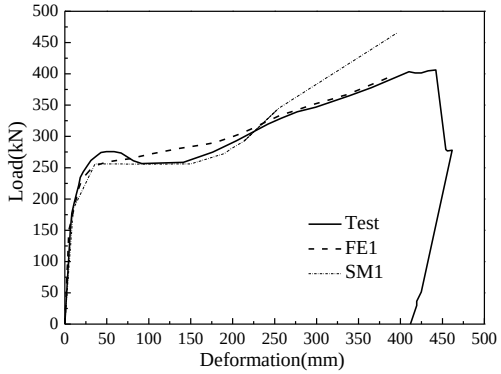

Fig.13. Load–displacement curves produced using the theoretical equation (SM1), numerical simulation (FE1), and experimental results (Test)

We applied an effective axial lateral constraint to both ends of the model (ends A and E shown in Fig.9a), which resulted in curve FE2 from the numerical simulation, as shown in Fig.14.Although the lateral constraint boundary condition has little effect on the initial stage of collapse, when the frame enters the transient stage, the ultimate anti-collapse bearing capacity of the structure significantly increased and its deformation significantly reduced. The FE2 curve matched that of the theoretical equation (SM1) extremely well in the catenary stage; hence, the axial constraint applied at the beam ends provided a more accurate description of the actual catenary mechanism of the structure in the late stage of collapse.

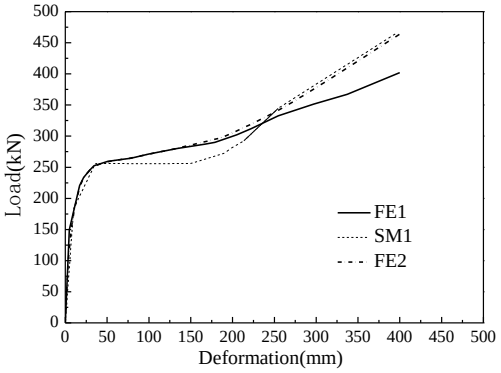

Fig. 14. Comparison of the load–displacement curves using the theoretical equations (SM1) compared to numerical simulations with (FE2) and without (FE1) axial constraints.

5. Analysis of arch action

5.1. Calculation of arch action

The application of a concentrated load at the failure column causes the beam ends at the side column to be subjected to a negative bending moment. As the applied load increases, the crack developed in the upper tension zone of the composite beam section near the side column will continue to develop, resulting in the neutral axis (bending axis) moving downward. However, the beam end section at the failure column is subjected to a positive bending moment, where the neutral axis is biased toward the concrete slab. Therefore, the curved neutral axis of the cross-section at both ends of the composite beam is not in a horizontal plane, but rather in the form of an arch, which results in a load distribution referred to as the arch action, as shown in Fig.15.Under the arch action of the composite beam shown in Fig.15, the rotating end sections of the composite beams at the failure column form the crown of the arch, and the rotating end sections of the composite beams at the side column form the haunches of the arch, resulting in an arch rib in the oblique direction with a height ofΔ.

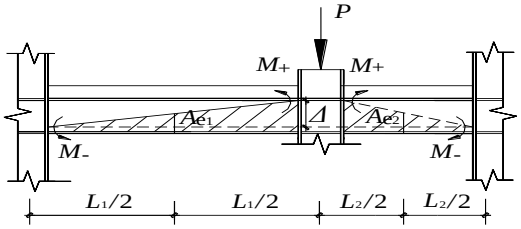

Fig. 15. Arch action of beams under applied load

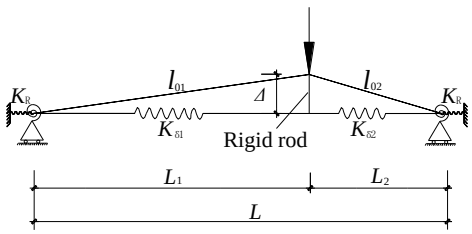

Fig. 16. Arch spring model of a beam under applied load

If the axial constraint of the composite beam is simplified to a spring constraint with stiffness K_R, the arch spring model shown in Fig.16 is obtained [19]. In this model, in addition to the diagonal arch rib members, the lower flange and a portion of the web are considered as spring-loaded members. The oblique arch rib member and the spring rod member are connected by an incompressible rigid rod member (in which the beam–column joint at the failure column is considered to be a rigid body). Here, l_{01} and $l_{02}$are defined as the lengths of the ribs, where$l_{01}=(L_1^2+\Delta^2)0.5$ and $l_{02}=(L_2^2+\Delta^2)\text{^}0.5$.

Under the applied vertical load at the failure column, the horizontal deformations of the beam ends at the side columns are d_1 and d_2, and the spring deformation elongations are$\delta_1$andδ_2, respectively, as shown in Fig.17.

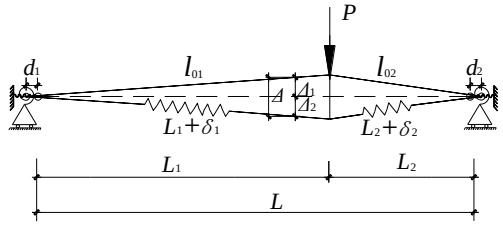

Fig.17. Deformation of the arch spring model

For$\Delta_2=v$,then:

$$\Delta_1 = \Delta - v \tag{41}$$

For the left half of the span:

$$d_1 = \sqrt{{l_{01}}^2 - {\Delta_1}^2} - L_1 = \sqrt{{l_{01}}^2 - (\Delta - v)^2} - L_1 \tag{42}$$

$$\delta_1 = \sqrt{v^2 + {l_{01}}^2 - {\Delta_1}^2} - L_1 = \sqrt{v^2 + {l_{01}}^2 - (\Delta - v)^2} - L_1 \tag{43}$$

For the right half of the span:

$$d_2 = \sqrt{{l_{02}}^2 - {\Delta_1}^2} - L_2 = \sqrt{{l_{02}}^2 - (\Delta - v)^2} - L_2 \tag{44}$$

$$\delta_2 = \sqrt{v^2 + {l_{02}}^2 - {\Delta_1}^2} - L_2 = \sqrt{v^2 + {l_{02}}^2 - (\Delta - v)^2} - L_2 \tag{45}$$

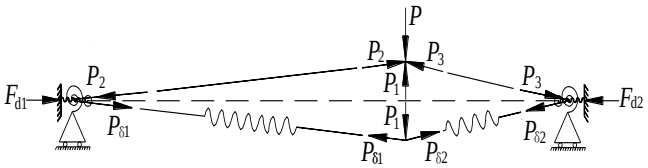

Fig.18. Force diagram of the composite beams under arch action

The forces in the composite beams under the conditions of arch action are shown in Fig. 18. According to the equilibrium condition, this force can be obtained as follows:

$$P_1 = P_{\delta 1}\frac{v}{L_1 + \delta_1} + P_{\delta 2}\frac{v}{L_2 + \delta_2} \tag{46}$$

$$P_2\frac{L_1}{l_{01}} = K_{\mathrm{d}} d_1 + P_{\delta 1}\frac{L_1}{L_1 + \delta_1} \tag{47}$$

$$P_3\frac{L_2}{l_{02}} = K_{\mathrm{d}} d_2 + P_{\delta 2}\frac{L_2}{L_2 + \delta_2} \tag{48}$$

$$P_{\delta 1} = K_{\delta 1} \times \delta_1, \quad P_{\delta 2} = K_{\delta 2} \times \delta_2 \tag{49}$$

$$P = P_1 + P_2\frac{\Delta - v}{l_{01}} + P_3\frac{\Delta - v}{l_{02}} \tag{50}$$

where $K_\delta$is the axial spring stiffness of the rod, calculated by:

$$K_{\delta 1} = \frac{EA_{\mathrm{e}1}}{L_1}, \quad K_{\delta 2} = \frac{EA_{\mathrm{e}2}}{L_2} \tag{51}$$

A_{e1} and A_{e2} are the areas of the steel beams on each side of the failure column below the mid-span oblique rib line prior to column failure[19], as shown in Fig. 15.Substituting Eqs. (46)–(49) into Eq. (50) yields:

$$P_{\Delta} = \left(\frac{K_{\delta 1}\delta_1}{L_1 + \delta_1} + \frac{K_{\delta 2}\delta_2}{L_2 + \delta_2}\right)v + (\Delta - v) \times \left[\frac{K_{\mathrm{d}}(L_2 d_1 + L_1 d_2)}{L_1 L_2} + \frac{K_{\delta 1}\delta_1}{L_1 + \delta_1} + \frac{K_{\delta 2}\delta_2}{L_2 + \delta_2}\right] \quad (v \le \Delta) \tag{52}$$

When the vertical deformation of the failure column is $v=\Delta$, the extrapolated horizontal displacements of the beam ends will reach their maximum value. As the vertical deformation of the failure column continues to increase, the horizontal displacements of the beam ends begin to decrease (pulling inward). At this point, the arch effect fails, and Eq. (52) is no longer applicable. To simplify analysis, the symmetric curve $v=\Delta$is used to represent the entire arch action phase. When$\Delta<v\le 2\Delta$:

$$P_{\Delta} = \left(\frac{K_{\delta 1}\delta_1}{L_1 + \delta_1} + \frac{K_{\delta 2}\delta_2}{L_2 + \delta_2}\right)(2\Delta - v) + (v - \Delta) \times \left[\frac{K_d(L_2 d_1 + L_1 d_2)}{L_1 L_2} + \frac{K_{\delta 1}\delta_1}{L_1 + \delta_1} + \frac{K_{\delta 2}\delta_2}{L_2 + \delta_2}\right] \quad (\Delta < v \le 2\Delta) \tag{53}$$

It should be noted that arch action mainly occurs during the small deformation stage; therefore, it usually functions in the first three stages of progressive collapse, especially during the initial collapse resistance of the plastic stage. According to the superposition principle combined with the theoretical equations of the different collapse stages, the equations for the bearing capacity of the composite beam–column frame considering arch action were obtained:

$$P(v) = \begin{cases} P① + P_{\Delta} \\ P② + P_{\Delta} \\ P③ + P_{\Delta} \\ P④ + P_{\Delta} \\ P⑤ + P_{\Delta} \end{cases} \tag{54}$$

When $v\le\Delta$, $P_\Delta$is calculated using Eq. (52); when $\Delta<v\le2\Delta$, P_Δ is calculated using Eq. (53); and when $v>2\Delta$, $P_\Delta = 0$.

5.2. Experimental verification of arch action

A comparison between the theoretical calculation results and experimental curves with and without arch action is shown in Fig.19. The theoretical results considering arch action (SM2) better matched the experimental curve (Test). Therefore, it is necessary to consider the influence of arch action in the analysis of the anti-collapse behavior of a structure in the early stages.

A numerical comparison ofexperimental and theoretical results at key points is shown in Table 2. The theoretical results consideringarch action (SM2) were more similar to the experimental ones (Test) than the results that did not consider arch action(SM1). The deviations in the force and deformation

between the theoretical and experimental results were no more than 4%. It can also be observed that the superposition of the calculated arch action upon each stage met the accuracy requirements of engineering calculations.

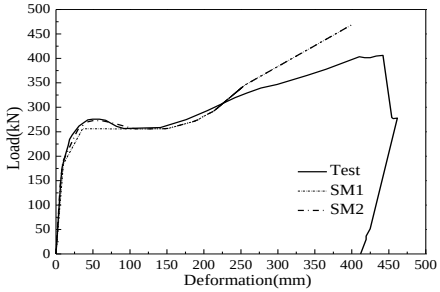

Fig. 19. Comparison of load–displacement curves from theoretical calculations with (SM2) and without (SM1) considering arch action and experimental results (Test)

It is known from error analysis that arch action can delay the time at which a structure enters the plastic stage, providing conditions for deformation development of the structure. This effect can significantly increase the peak load of the structure so that the initial bearing capacity of the structure is improved, but has almost no effect on the collapse resistance in later stages. In general, arch action has a positive effect on the collapse resistance of the structure.

6. Numerical analysis

6.1. Specimen design

To verify the reliability of the theoretical equations for the anti-collapse analysis of a composite beam-column frame with unequal spans, several specimens with different span ratios were evaluated. The span ratio of the left-to-right beam (L_1:L_2) was set to 1:1, 1:1.5, and 1:2, where the length of the right span L_2 was 3000 mm, 4500 mm, and 6000 mm, respectively, the length of the left span L_1 was 3000 mm (standard span), and the length of column L_c was 3000 mm. The dimensions of the steel column and beam were HW300×300×10×16 (mm) and HW300×200×8×12 (mm), respectively. The concrete strength grade was C30, the thickness of the concrete slab was 100 mm, and the effective width of the slab was 1200 mm. Longitudinal HPB300 steel bars were arranged on the top and bottom of the concrete slab and attached to the beam end baffles. The upper row of longitudinal steel bars and the distributed steel bars formed a steel mesh, and the reinforcement ratio was calculated to meet the design requirements. The composite floor slab and steel beams were connected by shear studs with a diameter of 19 mm and a length of 80 mm. The studs were arranged in a double row with a spacing of 210 mm. The dimensions of the concrete slab and slab reinforcement are shown in Fig.20.

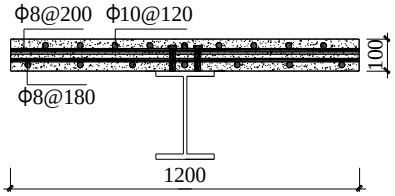

Fig. 20. Arrangement of steel bars in the concrete floor slabs (in mm)

6.2. Numerical model

In the numerical model, the steel was considered an ideal elastic–plastic material with a yield strength of 235 MPa, an elastic modulus of 2.06×10^5 MPa and a Poisson's ratio of 0.3. The concrete was modeled using the stress–strain relationship of C30 concrete as recommended in Appendix C of the Concrete Structure Design Code GB50010-2010 [20], as shown in Fig.11. The numerical model used the three-dimensional truss unit T3D2 to simulate the steel bars in the slab, while the eight-node reduced integral solid element C3D8R was used to model the other components.

The welds between the beam and column sections were simulated by a tie constraint. The steel bars and studs in the concrete slab were treated as embedded units. The interfaces between the bolts, webs, and shear tabs were defined as general contacts. Friction was represented by an isotropic Coulomb model, with an assumed friction coefficient of 0.3, as commonly used for steel-to-steel contact. Considering the influence of large deformations in the calculation, displacement control was used, and the corresponding amplitude was applied in a smooth analysis step. It should be noted that the middle position of the side column must be connected to the fixed connecting plate by establishing an axial connecting unit to simulate the pair of peripheral members, capturing the effects of the frame on the collapse resistance, in which the axial restraint stiffness is K_R. The boundary conditions and the mesh division of the numerical model of the composite beam–column substructure are shown in Fig.21.

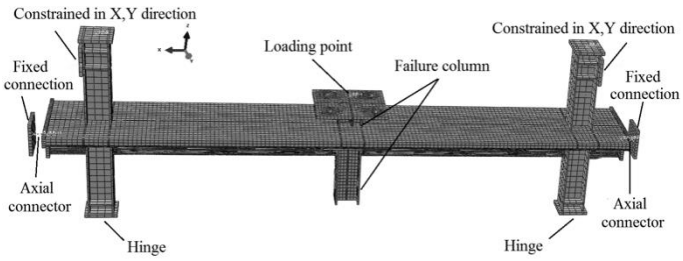

Fig. 21. Numerical model of composite beam–column substructure with unequal spans

6.3. Validation of the model

Figure 22 compares the results of the numerical simulations with the theoretical results for the composite beam–column frames with different span ratios. With increasing span ratio, the initial stiffness of the composite beam–column frame decreased, and the catenary effect is postponed, providing conditions for the development of structural deformation. However, the different span ratios had a significant influence on the bearing capacity of the rigid-joint composite beam–column frame. For the same standard span, the geometry with unequal spans had lower resistance to structural collapse. Notably, the composite beam–column frame is subjected to vertical loads. Because of the high stiffness of the short-span beam, it is subjected to a large load as the internal force is redistributed, resulting in the short-span beam yielding earlier than the long-span beam and subsequent destruction of the structure. Finally, the catenary effect of the long-span beam was not fully developed, and the vertical bearing capacity of the structure decreasedwith increasing span ratio. The main reason for the mismatch between the theoretical and numerical results in the transient stage may be due to the theoretical modelnot considering the role of stud tightening, while the *M–N* relationship (Eq. (1)) used in the transient stage does not fully reflect the bending–tensile performance of the composite joint.

Table 2. Comparison of the key points of the *P–v* curves of the composite beam–column frame

Key points	Test[19]		SM1		SM2		Deviation			
	P (kN)	v (mm)	P_1 (kN)	v_1 (mm)	P_2 (kN)	v_2 (mm)	P/P_1	P/P_2	v/v_1	v/v_2
A	183	10	184	10	184	10	0.99	0.99	1.00	1.00
B	252	31	256	36	256	31	0.98	0.98	0.86	1.00
B’	278	55	256	-	274	55	1.09	1.01	-	1.00
C	252	157	256	163	256	163	0.98	0.98	0.96	0.96
D	338	274	345	268	345	268	0.98	0.98	1.02	1.02

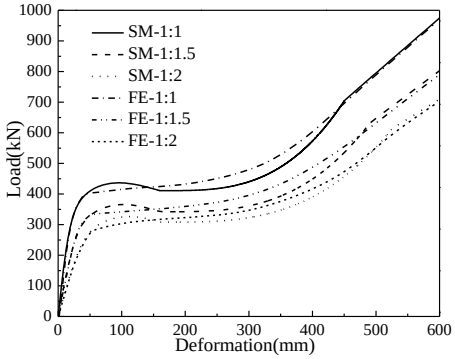

Fig. 22. Load–deformation curves from theoretical calculations (SM) andthe numerical model (FE) for different span ratios

In general, the theoretical and numerical results for structures with different span ratios agreed well, indicating that the theoretical equations provide a high degree of accuracy and meet engineering design requirements. Therefore, the proposed equations can be confidently used as the basis for the evaluation of the anti-collapse resistance of steel-frame structures. It should be pointed out that this work mainly considers the collapse resistance of steel frames connected by rigid joints. When evaluating the more popular semi-rigid joints, due to the diversity of forms, there will be a significant difference in the initial rotational stiffness and the resistance mechanisms of the composite joints under positive and negative bending moments, which will have a large impact on the overall force distribution within the structure. Therefore, the determination and verification of an accurate and reliable evaluation method for the collapse resistance of steel frames connected by semi-rigid joints requires further analysis of systematic test data.

7. Conclusion

An anti-collapse calculation model supported by both axial and rotational spring constraints was proposed to investigate a composite beam–column frame with unequal spans.According to the different stress states, the progressive collapse of the structure was divided into five resistance stages and the anti-collapse mechanism was analyzed. The load–deformation curves of the composite beam–column frame at different stages under unequal spans wereanalyzed in detail, and the influence of arch action was fully considered. The entire progressive collapse process was analyzed, indicating that the stress state changed from predominantly bending, to mixed bending–tensile, and finally to a tensile-dominated mechanism resisting the external load. The major conclusions of this study are as follows:

1) The arch action and catenary effect were generated under axial and rotational constraints at the beam ends of the composite beam–column frame. This arch action effectively increased the peak load of the structure in the plastic stage.

2) The theoretical relationship considering arch action described the corresponding experimental results well, indicating that this equation has a high degree of credibility.

3) The numerical analysis and theoretical calculations of the structural behavior with unequal spans showed that with increasing the left-to-right spanratio, the initial stiffness and ultimate bearing capacity of the composite beam–column frame decreased. Hence, unequal spans are not conducive to the development of arch action. Therefore, a structure with equal spans is preferable for improving anti-collapse bearing capacity.

4) The versatility of the theoretical equations derived here was verified by numerical examples with various unequal spans, where the theoretical equations satisfied the accuracy requirements of engineering calculations.

Acknowledgments

This work was supported by the National Natural Science Foundation of China (Grant No. 51678476). Any opinions, findings, conclusions, and recommendations expressed in this paper are those of the authors and do not necessarily reflect the views of the sponsors.

References

[1] Demonceau JF, Jaspart JP. Experimental and analytical investigations on the response of structural building frames further to a column loss. Proceedings of the 2009 Structures Congress, 2009: 1801–1810.

[2] Izzuddin BA, Vlassis AG, Nethercot DA. Progressive collapse of multi-storey buildings due to sudden column loss—Part I: Simplified assessment framework. Eng. Struct., 30(5), 1308–1318, 2008.

[3] Izzuddin BA. A simplified model for axially restrained beams subject to extreme loading. Int. J. Steel Struct., 5(5), 421–429, 2005.

[4] Vlassis AG., Izzuddin BA., Nethercot DA., Progressive collapse of multi-storey buildings due to sudden column loss-Part II: application[J]. Eng. Struct., 30(5), 1424-1438, 2008.

[5] Arash N, Fereidoon I. Progressive collapse analysis of steel frames: Simplified procedure and explicit expression for dynamic increase factor. Int. J. Steel Struct., 12(4), 537–549, 2012.

[6] Vlassis AG, Izzuddin BA, Elghazouli AY, et al. Progressive collapse of multi-storey buildings due to sudden column loss—Part II: Application. Eng. Struct., 30(5), 1424–1438, 2008.

[7] Kaiqiang W, Guoqiang L, Taochun Y. A study of re-strained steel beams with catenary action under distributed load—Part I: Theoretical model. China Civil Eng. J., 43(1), 1–7, 2010.

[8] Guoqiang L, Kaiqiang W, Taochun Y. A study of re-strained steel beams with catenary action under distributed load—Part II: Numerical verification. China Civil Eng. J., 43(1), 8–12, 2010.

[9] Weihui Z, Bao M, Jiping H. Analysis of anti-collapse of steel frame beam-column substructure with asymmetric spans. Eng. Mech., 34(5), 125–131, 2017.

[10] GSA 2003. Progressive collapse analysis and design guidelines for new federal office buildings and major modernization projects. Washington, DC: United States General Services Administration, 2003.

[11] Yin YZ, Wang YC. Analysis of catenary action in steel beams using a simplified hand calculation method, Part 1: Theory and validation for uniform temperature distribution. J. Constr. Steel Res., 61(2), 183–211, 2005.

[12] Yang B, Tan KH, Xiong G, et al. Experimental study about composite frames under an internal column-removal scenario. J. Constr. Steel Res., 121, 341–351, 2016.

[13] Gao S, Guo LH. Capacity of semi-rigid composite joints in accommodating column loss. J. Constr. Steel Res., 139(139), 288–301, 2017.

[14] Hongtie Z, Sumei Z. Composite structure design principle. Higher Education Press, 2005.

[15] Sucuoglu H, Çitipoglu E, Altin S. Resistance mechanisms in RC building frame subject to column failure. J. Struct. Eng., 120(3), 765–782, 1994.

[16] Xuezhong W, Yazhen S. A simple method for calculating the maximum deflection of simply-supported beams. Mech. Eng., 35(4), 63–64, 2013.

[17] Ying W, Xianglin G, Feng L. Vertical bearing capacity of RC two-bay beams considering compressive arch action. J. Build. Struct., 34(4), 32–42, 2013.

[18] DOD (Department of Defense). Design of Buildings to Resist Progressive Collapse, Unified Facilities Criteria, UFC 4-023-03, USA, 2013.

[19] Guo L, Gao S, Fu F, et al. Experimental study and numerical analysis of progressive collapse resistance of composite frames. J. Constr. Steel Res., 89(5), 236–251, 2013.

[20] GB50010-2010. Code for design of concrete structures. Beijing, China: Architecture & Building Press, 2010.

Advanced Steel Construction – Vol. 15 No. 4 (2019) 386-397
DOI: 10.18057/IJASC.2019.15.4.9

STUDY OF SEISMIC RESISTANCE OF KIEWIT-8 DOME CONSIDERING KEY STRUCTURAL DESIGN PARAMETERS

Ming Zhang[1, *], Yao-Peng Liu[2], Zhi-Xiang Yu[1] and Gerry Parke[3]

[1] *School of Civil Engineering, Southwest Jiaotong University, Chengdu 610031, China (corresponding author)*
[2] *Department of Civil and Environmental Engineering, The Kong Kong Polytechnic University, Hong Kong, China*
[3] *Department of Civil and Environmental Engineering, University of Surrey, Guildford, Surrey GU2 7XH, UK*
** (Corresponding author: E-mail: zhangming@home.swjtu.edu.cn)*

ABSTRACT

A new seismic failure criterion is proposed for the Kiewit-8 (K8) dome subjected to earthquakes based on key structural parameters. Firstly, the K8 dome models were built in the finite-element package ANSYS after considering the key structural design parameters. Secondly, the incremental dynamic analysis was undertaken resulting in a typical structural damage index D_s. These were introduced to undertake the nonlinear dynamic response history analyses at each increased level of seismic records intensity and permitted the calculation of collapse loads of domes. Three hundred three-dimensional seismic records based on the main influential factors of ground motion were selected as input seismic waves. Thirdly, the lognormal distribution was selected to appraise collapse loads to gain the dynamic collapse fragility curves for domes after comparing three maximum likelihoods. Then, the lower bound collapse loads with 95% probability of non-exceedance changing with structural parameters were determined. Finally, relationships between lower bound collapse loads and five key structural parameters were separated out by using numerical matching methods, followed by a new seismic failure criterion for all the relationships including the five key structural parameters and a safety factor of 1.5. The new seismic failure criterion will contribute to the safe design and construction of these excellent space structures worldwide, particularly in the countries which are prone to earthquakes.

ARTICLE HISTORY

Received: 22 April 2019
Revised: 12 August 2019
Accepted: 15 August 2019

KEYWORDS

Domes;
New seismic failure criterion;
Collapse loads;
Key structural parameters;
95% probability of non-exceedance

1. Introduction

Single-layer domes are adopted worldwidely as long-span roofs in recent decades [1-3] because of their advantages, such as their good aesthetic appearance, large space coverage capability and sound structural performance. Current research work is mainly focused on the structural response [4-10], collapse [11-13] of the steel structure under different loads through experiment and numerical simulation analysis [14-18], considering stability and buckling [19-22]. Only few reports have investigated the structural dynamic failure modes [17, 19, 23, 24] and the seismic failure loads when the single-layer reticulated shells are subject to earthquakes. Especially in countries prone to earthquakes (or tremor), design methods considering not only static but also dynamic behavior are required. In the technical manual for designing and analyzing the space structures [25], the maximum displacement is restricted to 1/400 of the shortest span of the single-layer domes under the action of static loads and frequent tremors. But there are no design guidelines at present to deal with the design of single-layer domes subjected to severe tremors. Currently, the design process for single-layer domes under strong earthquakes are mainly referring to general steel structure guidelines and the engineer's experience [26-28]. In these circumstances, Zhi [23] empirically proposed two different criteria for predicting the failure loads of Kiewit-8 (K8) domes and cylindrical reticulated shells by determining the maximum nodal displacement and structural plastic deformation. However, the existing dynamic criteria need to be determined by undertaking a series of numerical analyses using finite element software, which is complicated and time consuming for the structural engineer. Therefore, there is a need to develop a systematic, practical and fast method to estimate the limit load of these shell structures.

In this paper, typical single-layer dome models of the K8 domes [23] were built in the finite-element package ANSYS [29]. This was undertaken after considering key structural factors, which have a great effect on the dynamic failure loads of these kind of structures. Secondly, an incremental dynamic analysis (IDA) [30] with a typical structural damage index D_s [23] were used to conduct nonlinear dynamic response history analyses (RHAs) at each increased level of seismic records intensity. This was used to determine the collapse loads of the domes whose failure modes were dynamic strength failure. For considering the action of the properties of earthquake waves on the failure loads, three hundred three-dimensional seismic records from the database of the COSMOS [31] on the basis of the main influential factors of ground motion, such as earthquake magnitude, distance, focal mechanism and site class, were selected as input seismic waves to obtain collapse fragility curves for the domes. Thirdly, the lognormal distribution [32] was selected to fit the collapse loads to obtain the collapse fragility curves for the domes under the action of seismic waves after comparing the results from lognormal, Weibull [33], and Gamma distributions [34, 35]. The lower bound collapse loads with 95% probability of non-exceedance [28, 36-38] changing with structural roof weights, spans, rise to span ratios and tube sections were determined based on the collapse fragility curves. Finally, relationships between the lower bound collapse loads and five key structural design parameters were separately selected out by numerical matching methods, followed by a new seismic failure criterion, a general equation, for all the relationships including the five key structural parameters and a safety factor of 1.5 [39]. The reason for the relatively higher safety factor is that the value of the statistical life [40-42] is significantly higher comparing with the cost of dome construction, which could increase the safety of the dome structures and reduce the risk of death.

2. Factors to be considered in the ultimate load evaluation and the dome models

2.1 Factors

The domes should be safely and properly designed not to buckle or collapse under design loads. The calculation of the critical load corresponding to the collapse stage under the action of earthquakes should consider several factors, such as membrane action, structural configuration, boundary conditions, materials, members, nodes, connections between members and nodes, geometric imperfections, load distribution, peak ground motion and the duration as well as the frequency of the ground motions. The following gives a short explanation of the key factors considered in the ultimate load evaluation.

The membrane action is the membrane stresses prevailing in the shell-like structures. The domes generally resist external loads through membrane action with relatively low bending moments, in a similar way to continuous shells. Accordingly, the K8 domes used in this paper were designed and modeled as thin shell-like forms. To comply with this assumption, the shape and boundary conditions should be compatible with the membrane action, leading to a state of small bending moments. In these types of thin structures, appropriate measures are required for avoiding shell-like collapse.

The support types greatly influence the behaviour of the domes. In general, the buckling failure load or collapse load is higher in the case of pin-support where the supports are fixed against translation but free for rotation, than in the case of simple-support where the supports are fixed against only vertical translation. The failure load is higher in the case of simple-support conditions than that in the case of free edges if the form and members are the same for each particular dome.

The members used in the reticulated shell were considered to be fabricated from high strength, ductile steel. The ultimate load should be evaluated taking into consideration the effects of Young's modulus, yield stress, and residual

stress in the fabricated members.

The members and nodes are the fundamental elements of domes. The member slenderness ratio, subtended half angle and the arrangement of members are regarded as the key factors for the ultimate load of the dome.

The connection between members mainly refers to the rigidity and strength provided at the connections. It is well known that when the bending stiffness at a connection is high enough, the ultimate loads can be increased on account of the full rigidity at the connection, while the ultimate load will be reduced if the joint rigidity is low.

Geometric imperfections are classified roughly into global geometrical imperfections associated with nodal deviations and member crookedness. In the case of the domes, the geometric imperfections should be considered when evaluating ultimate loads, and the magnitude of real imperfections should be as small as possible.

The load distribution includes uniform loads, asymmetric snow accumulation, and combined loads of uniform and concentrated areas over a local region.

The peak ground motion and the duration, as well as the frequency, are the three fundamental parameters of ground motions. All of them can change the ultimate load of the domes subjected to earthquakes.

2.2. Single-layer dome models

In view of the above factors, the K8 dome [23] and its classification, the members and the material of the members are presented in Figs 1a, b, c and d, respectively. The RHAs was carried out for the dome models with all the supports fixed against translation but free for rotation. The joints between the members were taken as rigid, which is in accordance with most of the constructed structures. The span L and rise f could control the shape of the dome. The PIPE20 [29] element was chosen to simulate the structural members which yield stress and Young's modulus are 235 MPa and 2.06×10^5 MPa, respectively. The bilinear isotropic hardening model for all of the elements was adopted. The roof weight including cladding is equivalent to the surface area supported and the lumped masses applied to the nodes are described by the point elements MASS21 [29]. The dead load distributions are all uniform loads for all domes selected in this paper. Rayleigh damping was assumed here, whose damping ratio was empirically set to be 0.02. The consistent mode imperfection method was adopted to consider the geometric imperfections referring to the technical manual [25], and the maximum value of the consistent mode was 1/300 of the span L. Other parameters of the selected domes were designed to meet the technical manual [25], such as tube slenderness ratio, subtended half angle and the arrangement of members. The basic configurations of the domes are listed in Table 1, other cases with changed parameters complying with the basic configurations, such as different uniform roof weight, spans, rise to span ratios and cross sections, are shown in Appendix Table 1.

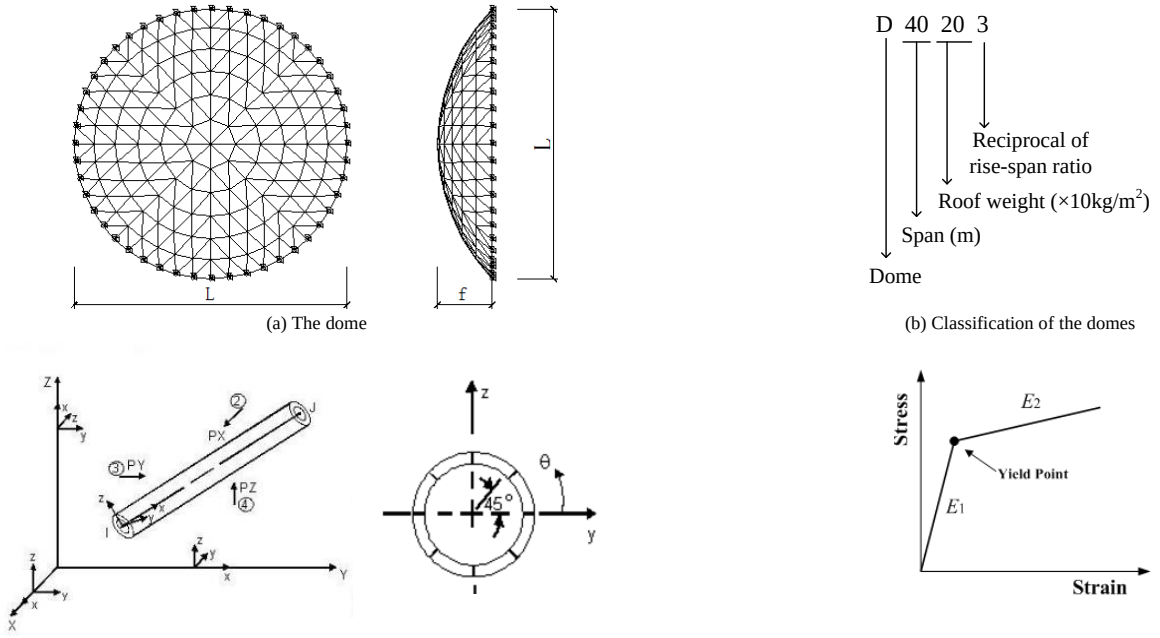

(a) The dome

(b) Classification of the domes

(c) The PIPE20 geometry [29]

(d) The material of the members

Fig. 1. The K8 dome system

The pipe20 [29] element can resist axial force, bending moment, shear, torque, etc. Meanwhile, the element has plastic, creep and swelling capabilities, and by using it, it is possible to output nodal displacements (including the nodal displacements in three directions at a node), member forces for nodes, shear strains, strain energy, and so on. In addition, there were eight integration points distributed uniformly around the cross-section of the pipe20 element presented in Fig.1c, which can output all the data information mentioned above.

Table 1

Labels and parameters of the K8 system

Dome label	Span (m)	Roof weight including cladding (kg/m²)	Rise to span ratio	Cross section (mm)	
				radial and hoop members	oblique members
D40203	40	200	1/3	146×5	140×6
D40205	40	200	1/5	146×5	140×6
D40207	40	200	1/7	146×5	140×6
D50063	50	60	1/3	168×6	152×5
D50065	50	60	1/5	168×6	152×5
D50067	50	60	1/7	168×6	152×5
D60063	60	60	1/3	194×6	168×6
D60065	60	60	1/5	194×6	168×6
D60067	60	60	1/7	194×6	168×6

3. The failure load (PGA), seismic records, and the lower bound failure load as well as its safety factor

3.1. The failure loads (PGA) of the domes

To obtain the collapse load of these structures, Ibarra and Krawinkler [43, 44] proposed using IDA method [30] to estimate the collapse load of the selected dome for each seismic record. Obtaining the dynamic collapse loads is a time-consuming job. In this study, the collapse states of the dome include dynamic instability and dynamic strength failure according to the definition of Zhi [23]. It is easy to judge the failure modes and failure loads for the dynamic instability as described in the literature [23]. However, it is difficult to discriminate its failure mode accurately for the dynamic strength failure because of the terrible plastic deformation and overall displacements before structures topple down. Here a failure criterion proposed in literature [23] is used to calculate failure loads of the domes whose failure modes are dynamic strength failure. The equation of the index D_s can be defined as:

$$D_s = 3.2\sqrt{(H/L)\left(100\left(\left(\frac{D-D_e}{L}\right)^2+\left(\frac{\varepsilon_a}{\varepsilon_u}\right)^2\right)+R_{1p}^2+R_{\theta p}^2}} \quad (1)$$

where D_s is the structural damage index; H and L are the height and span of the dome, respectively; D refers to the nodal displacement, whose value is the largest comparing with other nodes in the selected dome; D_e accounts for the largest elastic displacement before entering plastic state; ε_a means the average strain for the global dome; ε_u equals the strain of steel when the failure occurred; R_{1p} and $R_{\theta p}$ are the plastic ratios of the members.

3.2. The seismic records

It is known to all that all the information contained in the seismic records, such as PGAs, durations and frequencies, can affect the structural dynamic response. In order to consider these factors as far as possible, three hundred seismic records from the database of the COSMOS [31] were selected as input seismic waves. In this paper, three hundred three-dimensional seismic records were selected from seven earthquakes on the basis of the main influential factors of ground motion mentioned above. The ratio of the PGAs along the three directions, X, Y and Z, was modulated into 1: 0.85 : 0.65 for all the seismic waves according to the technical manual [25], and the 90% energy duration T_d ($T_d = T_2 - T_1$, $\triangle E = E(T_2) - E(T_1) = 90\% E_a$, where E_a is the total energy) was adopted to calculate the durations of the input seismic waves.

3.3. Three probability distributions and the lower bound collapse load of the dome

Here, three hundred seismic records were selected to obtain the failure fragility curve based on three probability distributions, namely lognormal, Weibull and Gamma distributions, whose PDF and CDF are given by [32 - 35], presented in Eq. (2) – Eq. (8):

$$f_X(x) = \frac{1}{x\sigma\sqrt{2\pi}}\exp\left(-\frac{(\ln x-\mu)^2}{2\sigma^2}\right) \quad (2)$$

$$F_X(x) = \Phi\left(\frac{\ln x-\mu}{\sigma}\right) \quad (3)$$

$$f(x;\lambda,k) = \begin{cases}\frac{k}{\lambda}\left(\frac{x}{\lambda}\right)^{k-1}\exp\left(-\left(\frac{x}{\lambda}\right)^k\right) & x\geq 0\\ 0 & x<0\end{cases} \quad (4)$$

$$F(x;\lambda,k) = \begin{cases}1-\exp\left(-\left(\frac{x}{\lambda}\right)^k\right) & x\geq 0\\ 0 & x<0\end{cases} \quad (5)$$

$$f(x;k,\theta) = \frac{x^{k-1}e^{-\frac{x}{\theta}}}{\theta^k\Gamma(k)} \quad \text{for } x>0 \text{ and } k,\theta>0 \quad (7)$$

$$F(x;k,\theta) = \int_0^x f(u;k,\theta)du = \frac{\gamma\left(k,\frac{x}{\theta}\right)}{\Gamma(k)} \quad (8)$$

where $f_X(x)$ and $F_X(x)$ denote the PDF and CDF of the Lognormal distribution, X is the log-normally distributed random variable, x is the failure load PGA, μ and σ account for the mean value and standard deviation, Φ is the CDF of the standard normal distribution; $f(x; \lambda, k)$ and $F(x; \lambda, k)$ are the PDF and CDF of the Weibull distribution, $k > 0$ and $\lambda > 0$ refer to the shape parameter and the scale parameter; $f(x; k, \theta)$ and $F(x; k, \theta)$ equal the PDF and CDF of the Gamma distribution.

In addition, in this paper the Kolmogorov-Smirnov test [34, 35] was used to calculate the confidence level for the three probability distributions. It quantificationally analyzes the deviations between the hypothesized CDF $F_X(x)$ and the measured cumulative histogram, which can be given by

$$D = \max_{i=1}^{n}\left[\left|F^*\left(X^{(i)}\right)-F_X\left(X^{(i)}\right)\right|\right] = \max_{i=1}^{n}\left[\left|\frac{i}{n}-F_X\left(X^{(i)}\right)\right|\right] \quad (9)$$

where $X^{(i)}$ is the ith largest observed value in the random sample of size n.

After this, the PDF and CDF for the collapse loads of D40205 under the action of the three hundred ground motions are presented in Fig. 2 that have been fitted to the simulation results by lognormal, Weibull, and Gamma method. It can be seen from Fig. 2 that the lognormal distribution is the best fit to the dynamic failure loads and approximately satisfies the above test method with 95% confidence interval in agreement with these figures in Zhong's doctoral dissertation [45]. Hence, the lognormal distribution will be adopted to analyzing the dynamic failure fragility curves in this paper. The dome D40205 has a median dynamic failure load of 22.10m/s^2, whose logarithmic standard deviation is 0.2084. This dispersion only considered the uncertainty of ground motion, not included modeling uncertainty.

In practical engineering, a 95% probability of non-exceedance [28, 52, 36, 37] was the most commonly used to obtain a design value with credible and confidence intervals. In this paper the 95% confidence limit was also adopted to discriminate the lower bound collapse loads for domes subjected to the selected seismic records. In other words, the structural collapse loads for all the selected seismic waves would be larger than the lower bound collapse loads with 95% probability.

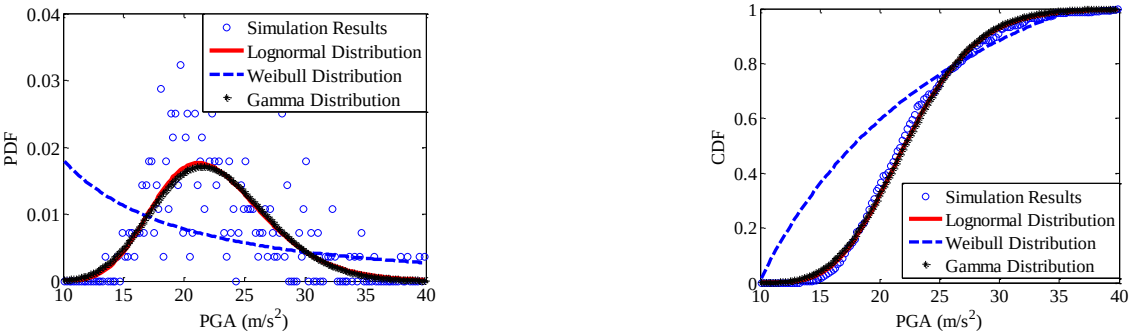

Fig. 2 The distributions for D40205 subjected to different seismic records

3.4. The safety factor and its rational

A dome should have sufficient capability to carry limit loads/design loads, as shown in Fig. 3, without large deformation detrimental to its serviceability state and load-bearing state. The ultimate load here is the load on the structure corresponding to ultimate point in Fig. 3, namely, corresponding to the collapse state. The ultimate loads of the domes can be calculated using FEA software. However, there is not a reasonable method to evaluate the limit loads/design loads for domes subjected to strong earthquakes at present. In the field of aircraft structures, the limit loads/design loads can be estimated by dividing the ultimate loads by, a factor of safety, 1.5, and the failure probability of the aircraft can be accepted. Because of the significance of domes, the same factor of uncertainty of 1.5 has been used to evaluate the limit loads/design loads, which can be obtained approximately using equation (10).

$$D_L = \frac{U_L}{1.5} \quad (10)$$

where the U_L is the ultimate loads and the D_L is the limit loads/design loads.

To confirm the rationality of the safety factor, the PGA-Displacement curve

for D40205 is shown in Fig. 3. In Fig. 3 the structural yield point denotes that the structure enters the plastic stage as shown in Fig. 4a; the design state (as shown in Fig. 4b) denotes the limit loads/design load and its corresponding displacement; and the ultimate point (as shown in Fig. 4c) denotes the structural maximum load and displacement followed by the structure collapse as shown in Fig. 4d.

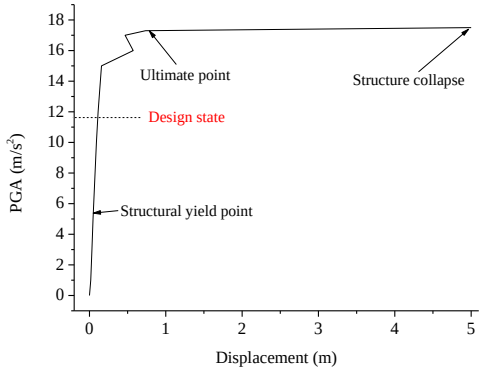

Fig. 3 The PGA-Displacement curve of D40205

As shown in Fig. 3, the PGA corresponding to the design state, of 11.53m/s^2, exceeds the PGA associated with the structural yield point, which indicates that the plastic yielding ability of the material has been partly used. Importantly, the displacement 0.11 m, nearly equals 1/400 of the structural span, and is less than 1/100 of the span of the domes which was proposed as the ultimate value of the critical displacement in reference [43] based on the statistical data and consideration of the practical factors related to design, construction, service, maintenance and restoration. In order to further verify the safety factor, Table 2 gives the collapse load, design load/limit load and ratio of the displacement corresponding to the design load/limit load to structure span for nine domes including D40205 under the action of the Taft wave recorded by station of USGS station 1095 in Kern County earthquake in 1952. In most cases the ratios of the displacement to the structural span are less than 1/100 as shown in Table 2. Only two of the nine displacements are a little larger than 1/100, but they are both very close to 1/100. These displacements can verify the sensibility of using a safety factor of 1.5, to a certain extent.

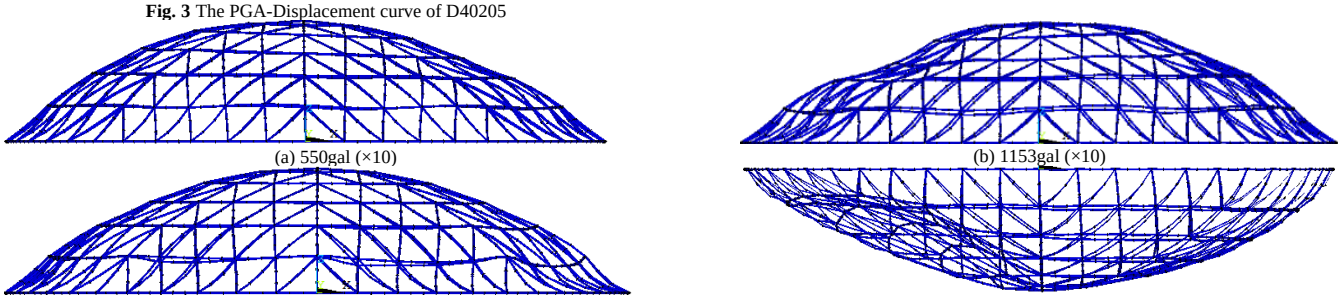

(a) 550gal (×10) (b) 1153gal (×10)

(c) 1730gal (×1) (d) 1750gal (×1)

Fig. 4 The deformation of D40205 subjected to the Taft wave at four critical stages.

Table 2
The dynamic failure stage of nine typical domes subjected to Taft wave

Dome	earthquake	Collapse load (m/s2)	Design load (m/s^2)	Displacement/span
D40203	Taft wave	12.00	8.00	0.93/400
D40205		17.30	11.53	1.00/400
D40207		16.50	11.00	3.42/400
D50203		43.00	28.67	1.41/400
D50065		64.50	43.00	2.95/400
D50207		57.30	38.20	4.58/400
D60063		48.30	32.20	2.67/400
D60065		64.30	42.87	3.15/400
D60067		52.70	35.13	4.44/400

Note: the Collapse load and Design load are the peak ground acceleration (m/s^2).

4. Relationship between the lower bound collapse load and key structural parameters

Table 3
Twenty seismic waves selected from the three hundred seismic records

Number	Stations	Number	Stations
1	CSMIP station 24272	11	CSMIP station 13879 Chino
2	CSMIP station 24401	12	MWD station 0709
3	CSMIP station 24399	13	CSMIP station 14828 Chino
4	CSMIP station 24207	14	CSMIP station 13095 Chino
5	CSMIP station 128	15	CSMIP station 23138 Chino
6	CSMIP station 24402	16	USGS station 0117
7	USC station 5361	17	TCU station 078
8	CSMIP station 23525 Chino	18	TCU station 116
9	USC station 0047	19	WNT station
10	CSMIP station 23842 Chino	20	USGS station 1095

Empirically, the ultimate loads of the domes have a close relation with the key structural factors like, dome spans, rise to span ratios, roof weights and member cross section sizes. Hence, numerical simulations for the ultimate loads of the domes with these key structural parameters mentioned above subjected to earthquakes were performed. To attain the collapse fragility curves of the ultimate loads and to reduce the computational effort, twenty seismic records with different frequencies and durations were selected as input seismic waves as shown in Table 3. Similarly, the IDA method was used to determine the collapse load for each seismic record. After this, the CDF distributions for the domes could be obtained based on the collapse loads, and the lower bound collapse load for each dome could be simultaneously discriminated with 95% probability. The relationships between each key structural parameter would then be analyzed independently, and an equation could be proposed to calculate the lower bound collapse load for the domes based on the five structural parameters. In this study, the prime target was to look for the relationship between the ultimate loads and the key structural parameters.

4.1. Relationship between lower bound collapse loads and roof weights

For buildings the relationship between the roof weights including cladding and the lower bound collapse loads, the RHAs were performed in the ANSYS software for a dome, whose span is 50 m and rise to span ratio is 1/5, with roof weights 60 kg/m^2, 100 kg/m^2, 160 kg/m^2, 200 kg/m^2, 260 kg/m^2, 300 kg/m^2, 360 kg/m^2, 400 kg/m^2 and 460 kg/m^2, which covered all cases in engineering applications [46], subjected to the twenty seismic records listed in Table 3. The collapse loads for the domes with different roof weights subjected to twenty seismic records are listed in Table 4, and their collapse fragility curves are presented in Fig. 5.

Table 4
The collapse loads for the domes with different roof weights subjected to twenty seismic records

Number	Collapse loads (m/s^2)								
	60 kg/m^2	100 kg/m^2	160 kg/m^2	200 kg/m^2	260 kg/m^2	300 kg/m^2	360 kg/m^2	400 kg/m^2	460 kg/m^2
1	120.60	76.00	39.00	27.40	17.00	11.80	6.00	5.20	3.00
2	100.50	58.60	31.00	20.60	14.00	9.60	6.40	5.20	2.80
3	136.80	79.60	42.80	31.40	18.20	13.40	8.00	5.60	3.00
4	138.80	86.60	46.00	29.80	22.00	14.00	9.00	7.20	4.00
5	97.40	64.00	35.80	25.60	17.20	12.60	7.60	5.60	3.00
6	124.60	76.80	44.60	31.00	19.40	12.80	9.00	5.80	3.80
7	118.20	35.80	42.40	31.20	19.80	15.00	9.20	6.80	4.00
8	92.40	59.80	35.80	25.60	16.80	13.00	7.80	5.60	3.20
9	61.40	36.00	18.00	12.00	7.00	4.80	3.20	2.40	1.20
10	111.80	73.80	43.60	30.80	19.60	14.40	8.40	6.40	3.40
11	105.60	66.80	41.40	31.40	20.40	14.60	8.80	6.40	3.40
12	123.80	88.80	44.00	30.00	23.00	15.00	10.80	8.40	3.40
13	159.40	95.80	49.80	32.40	19.40	15.60	10.40	7.20	4.40
14	133.80	82.00	51.60	35.00	19.80	14.00	7.40	5.80	3.20
15	118.60	79.80	47.00	32.00	21.60	16.00	10.40	8.20	4.60
16	70.80	42.60	23.60	16.40	9.20	6.60	4.00	3.20	1.60
17	65.40	35.40	18.40	12.60	7.60	5.20	3.60	2.80	1.40
18	55.40	31.60	16.40	12.00	7.00	5.00	3.40	2.40	1.40
19	88.60	52.60	29.80	21.40	13.80	10.40	6.60	5.00	2.80
20	64.50	38.00	20.40	13.40	8.20	5.60	3.20	2.80	1.80

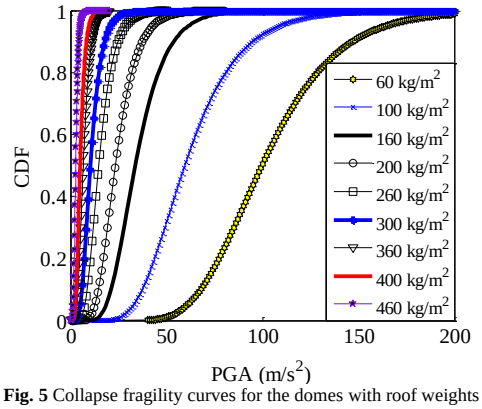

Fig. 5 Collapse fragility curves for the domes with roof weights

The lower bound collapse loads with 95% probability of non-exceedance changing with roof weights are given in Table 5 according to the failure fragility curves shown in Fig. 5.

On the basis of Table 5, the relationship between logarithmic lower bound collapse loads and roof weights are shown in Fig. 6. It demonstrates that there is a strongly statistically significant trend between logarithmic lower bound collapse loads (LPGA) and roof weights (RW) with a very small variance 0.12.

Empirically, the response variable *LPGA* can be written as a linear function of the predicator variable *RW* plus an error term. The linear prediction function has slope β and intercept α

$$\log(PGA)=\alpha+\beta RW+\varepsilon \quad (11)$$

where ε is an independent random variable, and its distribution has mean 0 and standard deviation σ.

Table 5
Lower bound collapse loads changing with roof weights

Dome	RW* (kg/m^2)	Lower bound Collapse load (m/s^2)
D50065	60	60.50
D50105	100	32.50
D50165	160	18.26
D50205	200	11.45
D50265	260	7.20
D50305	300	4.89
D50365	360	3.28
D50405	400	2.53
D50465	460	1.38

*Roof Weight

For these data, the least-squares method estimates of slope, intercept and error term were β=-0.009, α=4.4055 and σ=0.12, respectively. Therefore, the linear prediction function (11) can be rewritten as

$$\log(PGA) = -0.009RW + 4.4055 \pm 0.12 \quad (12)$$

where $RW \in$ [60 kg/m^2, 460 kg/m^2] is the roof weight including cladding.

4.2. Relationship between lower bound collapse loads and structural spans

In this section, the dome, whose roof weight is 60 kg/m^2 and rise to span ratio is 1/5, with spans 90 m, 85 m, 80 m, 75 m, 70 m, 65 m, 60 m, 50 m and 40 m were firstly selected as typical cases. Then the RHAs were performed in the ANSYS software for these typical cases subjected to the twenty seismic records listed in Table 3. The collapse loads for the domes with different spans subjected to twenty seismic records are listed in Table 6, and their collapse fragility curves, lognormal distributions, are shown in Fig. 7.

The lower bound collapse loads with 95% probability of non-exceedance changing with spans are then listed in Table 7 on the basis of the collapse fragility curves shown in Fig. 7.

On the basis of Table 7, the relationship between logarithmic lower bound collapse loads and spans is shown in Fig. 8. It demonstrates that there is also a strongly statistically significant trend between LPGA and spans with a very small variance 0.2788.

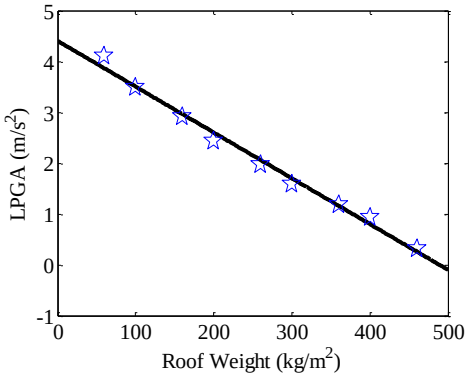

Fig. 6 Relationship between lower bound collapse loads and roof weights. (Note: the natural logarithm LPGA=log (Lower bound collapse load))

Table 6
The collapse loads for the domes with different spans subjected to twenty seismic records

Number	Collapse loads (m/s^2)								
	90 m	85 m	80 m	75 m	70 m	65 m	60 m	50 m	40 m
1	2.70	7.00	11.60	18.00	24.80	33.20	50.20	120.60	240.00
2	1.60	5.20	9.80	14.80	21.80	29.80	43.00	100.50	169.80
3	4.00	13.80	21.60	29.60	37.80	48.40	64.80	136.80	226.80
4	3.50	8.00	14.00	19.00	25.00	35.00	56.00	138.80	208.40
5	3.20	8.20	12.00	17.60	22.40	31.00	44.80	97.40	165.00
6	2.70	7.80	13.80	18.80	27.60	38.60	55.60	124.60	239.20
7	3.40	9.80	16.60	21.20	31.60	44.00	57.60	118.20	192.60
8	1.50	4.80	10.00	15.40	22.80	32.80	46.80	92.40	166.00
9	0.88	2.80	4.40	8.20	11.00	14.60	22.60	61.40	119.80
10	1.70	6.60	12.00	18.60	28.00	39.00	55.60	111.80	204.00
11	2.20	7.00	12.20	17.40	26.80	34.60	39.80	105.60	184.60
12	4.60	9.80	15.60	19.60	29.00	36.00	56.00	123.80	256.00
13	3.50	10.40	16.60	24.40	34.20	47.80	68.60	159.40	317.80
14	3.00	7.80	13.60	19.60	30.00	42.00	62.00	133.80	250.00
15	3.10	11.00	17.60	23.00	30.60	39.40	58.00	118.60	196.00
16	1.06	3.20	5.60	9.00	14.00	20.80	30.00	70.80	141.40
17	0.80	2.80	5.40	7.80	10.60	16.20	23.20	65.40	134.00
18	0.70	2.60	4.40	7.40	11.40	17.00	23.40	55.40	110.40
19	1.70	4.60	8.00	12.40	19.20	28.20	41.20	88.60	166.00
20	0.96	3.00	5.80	8.60	12.00	16.60	24.40	64.50	130.20

Table 7
Lower bound collapse loads changing with spans

Dome	Span (m)	Lower bound Collapse load (m/s2)
D90065	90	0.782
D85065	85	2.60
D80065	80	4.72
D75065	75	7.85
D70065	70	11.40
D65065	65	11.74
D60065	60	23.90
D50065	50	60.50
D40065	40	117.30

Referring to Equation (11), the relationship between lower bound collapse loads and spans could be given by:

$$\log(PGA) = -0.0923L + 8.6673 \pm 0.2788 \quad (13)$$

where $L \in$ [40m, 90m] is the structural span.

4.3 Relationship between lower bound collapse loads and rise to span ratios

Here, the domes, whose span is 50 m and roof weight is 60 kg/m^2, with rise to span ratios 0.10, 0.15, 0.20, 0.25, 0.30, 0.35, 0.40, 0.45 and 0.5 were firstly selected as typical cases. Then the RHAs were carried out in the ANSYS software for these typical cases subjected to the twenty seismic records listed in Table 3. The collapse loads for the domes with nine rise to span ratios subjected to twenty seismic records are given in Table 8, and their collapse fragility curves, lognormal distributions, are shown in Fig. 9.

The lower bound collapse loads with 95% probability of non-exceedance changing with rise to span ratios are presented in Table 9 based on the failure fragility curves shown in Fig. 9. Based on Table 9, the relationship between

logarithmic lower bound collapse loads and rise to span ratios is presented in Fig. 10. According to the LPGA changing to the cubic curve model is the best model among several different models of curve estimation with a very small variance 0.1122.

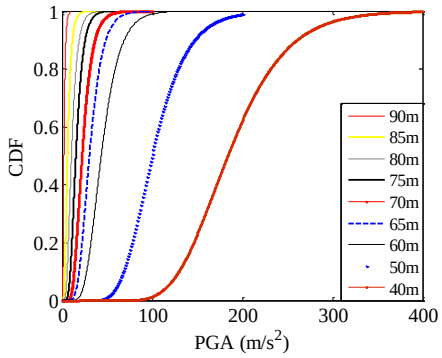

Fig. 7 Collapse fragility curves for the domes with different spans

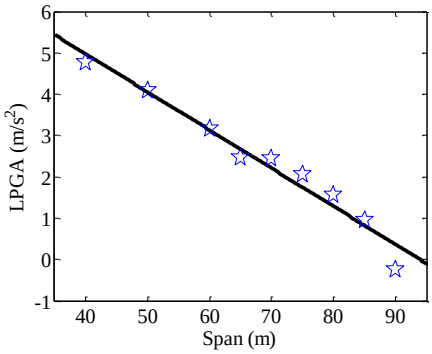

Fig. 8 Relationship between lower bound collapse loads and spans

Table 8
The collapse loads for the domes with nine rise to span ratios subjected to twenty seismic records

Number	Collapse loads (m/s^2)								
	0.10	0.15	0.20	0.25	0.30	0.35	0.40	0.45	0.5
1	73.00	115.60	120.60	123.00	112.20	110.10	118.80	96.60	83.60
2	64.20	94.40	100.50	36.60	66.00	75.00	87.60	73.40	58.80
3	106.80	99.80	136.80	140.80	94.40	49.80	103.80	104.00	118.20
4	97.60	125.80	138.80	116.00	105.80	91.80	78.80	71.60	68.80
5	68.40	94.40	97.40	118.40	119.00	87.60	150.20	99.80	97.80
6	99.40	119.80	124.60	153.60	130.20	129.40	152.40	127.40	113.00
7	94.00	108.80	118.20	115.80	155.40	153.60	170.00	140.20	123.20
8	72.20	94.80	92.40	79.00	69.60	63.40	55.60	49.00	42.00
9	36.60	54.60	61.40	48.40	41.80	39.40	42.60	30.60	26.20
10	78.60	117.00	111.80	100.60	90.60	86.40	82.20	69.20	57.40
11	94.60	112.60	105.60	93.60	86.00	87.40	90.80	83.40	74.00
12	102.00	128.00	123.80	119.20	122.20	130.60	201.60	156.60	140.40
13	123.60	155.80	159.40	158.60	139.80	136.80	149.00	116.40	105.00
14	106.60	144.00	133.80	136.60	166.00	158.20	140.20	127.40	107.60
15	88.80	117.00	118.60	114.00	108.00	108.60	103.00	90.60	78.80
16	57.40	77.60	70.80	52.00	45.00	41.00	37.80	31.00	24.90
17	36.80	56.20	65.40	54.80	49.00	43.80	49.60		31.40
18	29.00	54.40	55.40	42.20	34.60	28.00	21.80	17.60	14.00
19	45.20	81.20	88.60	83.00	76.00	68.80	66.60	52.80	46.20
20	40.40	60.00	64.50	50.20	48.60	42.40	47.20	32.60	26.80

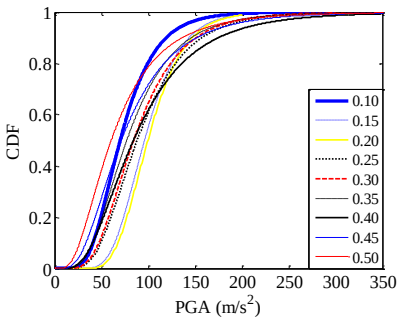

Fig. 9 Collapse fragility curves of the domes with different rise to span ratios

Table. 9
Lower bound collapse loads changing with rise to span ratios

Ratio	Lower bound Collapse load (m/s^2)
0.10	35.35
0.15	57.20
0.20	60.50
0.25	41.88
0.30	40.00
0.35	33.92
0.40	32.93
0.45	26.94
0.50	21.25

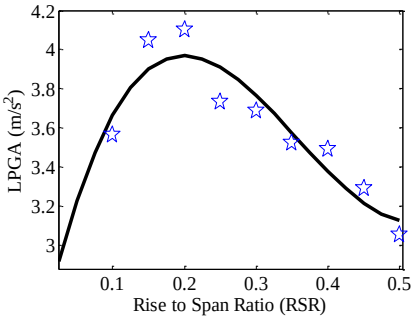

Fig. 10 Relationship between lower bound collapse loads and rise to span ratio

Referring to Equation (11), the relationship between the lower bound collapse loads and rise to span ratios could be given by:

$$\log(PGA) = 53.5354RSR^3 - 57.3447RSR^2 + 16.4657RSR + 2.5404 \pm 0.1122 \quad (14)$$

where $RSR \in [0.1, 0.5]$ is the rise to span ratio.

4.4 Relationship between lower bound collapse loads and tube member thicknesses

In this section, the dome spans D50065 with tube member thicknesses A, B, C, D, E and F were firstly selected as typical cases as shown in Table 11. Then the RHAs were performed in ANSYS software for these typical cases subjected to the twenty seismic records listed in Table 3. The collapse loads for D50065 with different tube thicknesses subjected to twenty seismic records are listed in Table 10, and their failure fragility curves, lognormal distributions, are shown in Fig. 11.

Table 10
The collapse loads for D50065 with different tube thicknesses subjected to twenty seismic records

Number	Collapse loads (m/s²)					
	A	B	C	D	E	F
1	106.00	120.60	127.20	150.40	162.80	149.80
2	86.00	100.50	103.60	121.20	119.60	135.60
3	118.00	136.80	146.00	159.80	220.00	215.80
4	117.20	138.80	140.00	160.20	164.00	149.60
5	86.60	97.40	99.20	122.00	119.80	144.60
6	107.60	124.60	126.60	152.40	171.60	186.80
7	101.20	118.20	120.00		156.60	166.20
8	81.00	92.40	93.40	109.40	114.40	128.00
9	50.40	61.40	62.40	76.60	74.60	84.80
10	96.80	111.80	113.00	133.20	141.20	157.80
11	87.20	105.60	106.60	123.40	130.60	144.40
12	104.60	123.80	124.60		154.60	169.60
13	131.60	159.40	159.80	192.60	212.80	243.60
14	112.60	133.80	136.00	159.60	177.60	196.20
15	104.60	118.60	121.00		147.00	163.00
16	58.60	70.80	71.80	85.60	85.20	96.80
17	53.60	65.40	66.40	79.40	77.60	89.60
18	46.40	55.40	56.40	68.00	70.20	80.40
19	77.20	88.60	90.00	105.00	119.60	133.20
20	54.80	64.50	65.60	80.40	81.80	

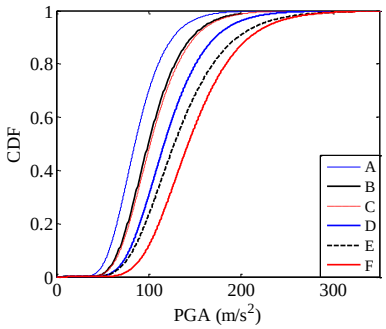

Fig. 11 Collapse fragility curves for D50065 with different tube thicknesses

The lower bound collapse loads with 95% probability of non-exceedance changing with tube thicknesses are presented in Table 11 on the basis of the failure fragility curves given in Fig. 11. Based on Table 11, the relationship between logarithmic lower bound collapse loads and member tube wall thicknesses is shown in Fig. 12. It demonstrates that there is also a strongly statistically significant trend between LPGA and tube wall thicknesses with a very small variance 0.0455.

Referring to Equation (11), the relationship between lower bound collapse loads and rise to span ratios could be given by:

$$LPGA = 0.0629TH + 3.6977 \pm 0.0455 \quad (15)$$

where $TH \in$ [5.0 mm, 12.5 mm] is the tube wall thickness.

Table. 11
Lower bound collapse loads changing with tube thicknesses

	Tube dimensions: outside diameter (mm)×Wall thickness (mm)		Lower bound collapse load (m/s²)
	Radial and Hoop t_1	Oblique t_2	
A	168.00×5.00	152.00×4.00	51.20
B	168.00×6.00	152.00×4.80	60.50
C	168.00×6.30	152.00×5.04	61.93
D	168.00×8.00	152.00×6.40	70.86
E	168.00×10.00	152.00×8.00	73.56
F	168.00×12.50	152.00×10.0	87.37

Note: t_1:t_2=1:0.8

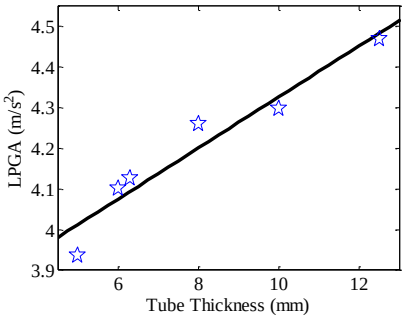

Fig. 12 Relationship between lower bound collapse loads and tube wall thicknesses

4.5 Relationship between lower bound collapse loads and the tube outer diameters

In this section, the dome spans D50065 with tube outer diameters A, B, C, D, E, F, G, H and I (shown in Table 13) were firstly selected as typical cases as shown in Table 12. Then the RHAs were performed in ANSYS software for these typical cases subjected to the twenty seismic records listed in Table 3. The collapse loads for D50065 with different tube outer diameters subjected to twenty seismic records are listed in Table 12, and their collapse fragility curves, lognormal distributions, are shown in Fig. 13.

The lower bound collapse loads with 95% probability of non-exceedance changing with tube outer diameters are also listed in Table 13 based on the collapse fragility curves given in Fig. 13.

On the basis of Table 13, the relationship between logarithmic lower bound collapse loads and logarithmic tube outer diameters is shown in Fig. 14. This demonstrates that there is also a strongly statistically significant trend between LPGA and logarithmic tube outer diameters with a very small variance 0.1645.

The relationship between LPGAs and logarithmic tube outer diameters could be given by:

$$\log(PGA) = 2.3243\log(OD) - 8.0037 \pm 0.1645 \tag{16}$$

where $OD \in$ [114.30 mm, 355.6 mm] is the tube outer diameter, log (OD) is the logarithmic tube outer diameter.

Table 12
The collapse loads for D50065 with different tube outer diameters subjected to twenty seismic records

Number	Collapse loads (m/s²)								
	A	B	C	D	E	F	G	H	I
1	27.60	59.20	127.20	180.80	248.60	306.00	347.40	437.00	450.00
2	27.20	50.60	103.60	140.60	187.60	228.80	254.00	341.60	343.40
3	38.00	73.40	146.00	215.80	269.60	299.80	376.60	486.40	562.20
4	33.20	75.80	140.00	161.20	201.80	262.20	312.00	374.00	445.40
5	24.00	51.60	99.20	149.80	184.60	230.20	270.00	326.00	386.60
6	31.40	67.20	126.60	173.40	243.00	298.40	348.60	490.00	449.00
7	33.40	65.00	120.00	165.60	213.40	259.40	380.60	362.80	485.20
8	30.20	54.60	93.40	121.80	152.20	181.00	211.80	255.40	293.20
9	14.00	27.20	62.40	87.80	116.80	148.60	184.40	270.40	299.40
10	34.80	66.80	113.00	151.80	241.40	239.00	285.00	364.20	386.80
11	29.20	56.80	106.60	143.60	184.60	223.20	278.60	345.80	428.80
12	30.60	65.60	124.60	177.80	245.80	314.20	390.60	485.40	572.00
13	38.60	77.60	159.80	235.00	310.80	395.80	469.00	593.80	681.60
14	32.00	69.00	136.00	195.60	241.40	290.60	346.40	448.80	477.80
15	35.00	70.60	121.00	155.60	193.60	230.40	271.60	346.00	384.40
16	19.20	37.00	71.80	96.60	125.20	154.20	183.40	232.60	273.80
17	15.00	27.60	66.40	93.40	123.00	146.00	180.00	253.00	283.80
18	16.00	30.20	56.40	76.00	95.60	112.20	132.20	169.60	188.60
19	25.80	46.80	90.00	118.00	148.40	186.20	229.00	283.40	307.40
20	15.80	32.00	65.60	90.00	113.80	138.80	171.00	250.20	269.20

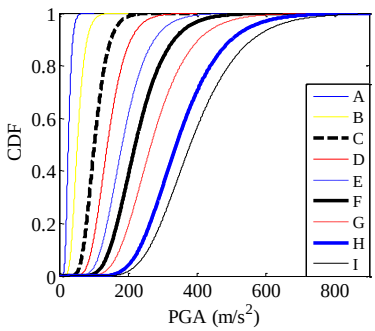

Fig. 13 Collapse fragility curves for D50065 with different tube outer diameters

Table. 13
Lower bound collapse loads changing with tube outer parameters

	Outer parameters (mm×mm)		Lower bound collapse load (m/s²)
	Radial and Hoop D_1	Oblique D_2	
A	114.30×6.30	102.90×5.04	15.60
B	139.70×6.30	125.70×5.04	29.75
C	168.00×6.30	152.00×5.04	61.93
D	193.70×6.30	174.30×5.04	83.60
E	219.10×6.30	197.20×5.04	106.80
F	244.50×6.30	220.05×5.04	129.60
G	273.00×6.30	245.70×5.04	155.60
H	323.90×6.30	291.50×5.04	206.60
I	355.60×6.30	320.00×5.04	230.75

Note: D_1:D_2=1:0.9

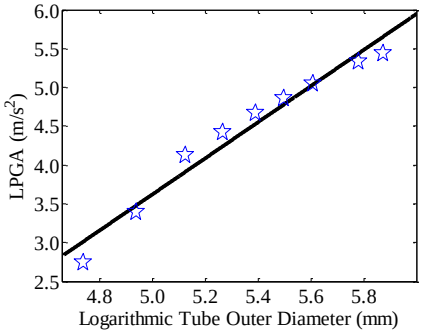

Fig. 14 Relationship between LPGAs and tube outer diameters

4.6 Failure acceleration considering the above key structural design parameters

Based on Eqs. (12) - (16), failure PGA corresponding to the lower bound collapse loads and considering the safety factor in terms of the key structural design parameters is then evaluated as follows.

$$PGA=\frac{1}{1.5}\exp[-0.0090RW-0.0923L+53.5354RSR^3-57.3447RSR^2 +16.4657RSR+0.0629TH+2.3243\log(OD)-4.7194] \quad (17)$$

where $RW \in$ [60 kg, 460 kg] is the roof weight including cladding; $L \in$ [40 m, 90 m] is the structural span; $RSR \in$[0.1, 0.5] is the rise to span ratio; $TH \in$ [5.0 mm, 12.5 mm] is the tube thickness; $OD \in$[114.30 mm, 355.6 mm] is the tube outer diameter.

5. Verification of the fitting formulation and discussion

5.1 Verification

In order to verify the fitting formulation Eq. (17), the domes listed in Table 2 subjected to Taft wave which never participated in obtaining the fitting formulation were selected to compare the failure PGAs. Then, the failure PGAs from different domes calculated separately by using the FEM dynamic response analysis and the fitting formulation Eq. (17) are given in Table 14. Here, PGA_1 denotes the failure PGAs obtained by FEM dynamic response analysis, while PGA_2 the PGAs obtained by the Eq. (17) according to the key structural design parameters.

Table 14
The failure PGAs of nine domes obtained from two methods

Dome	PGA_1 (m/s^2)	PGA_2 (m/s^2)
D40203	12.00	10.81
D40205	17.30	15.01
D40207	16.50	13.72
D50203	43.00	22.35
D50205	64.50	31.03
D50207	57.30	28.37
D60063	48.30	12.40
D60065	64.30	17.22
D60067	52.70	15.75

From Table 14, the failure PGAs, PGA_1, obtained from the FEM dynamic response analysis are all larger than that PGA_2 from the fitting formulation Eq. (17), which proves the rationality of the fitting formulation Eq. (17) based on the key structural design parameters. The reason is that the failure PGAs, PGA_2 corresponding to the lower bound collapse loads, calculated by the fitting formulation Eq. (17) considering the safety factor in terms of the key structural design parameters was obtained from their collapse fragility curves with 95% probability of non-exceedance. While the failure PGAs, PGA_1, from the FEM dynamic response analysis depended solely upon one seismic wave, the TAFT wave. For both cases, the domes with rise to span ratio 1/5 have relatively larger failure PGAs than other rise to span ratios, namely this kind of structure with rise to span ratio 1/5 can resist relatively larger three-dimensional seismic waves comparing with the other cases.

5.2. Discussions on the key structural design parameters

This poses a question about which structural parameter is more efficient for an earthquake resistant structure, such as a large roof weight or small roof weight for domes. (1) Fig. 6 illustrates that the LPGA, roof weight - based fundamental seismic capacity ratio, is a linear decreasing function of structural roof weights. (2) It has the similar tendency that the LPGA decreases linearly depending on the increasing structural span *L* as shown in Fig. 8. (3) As illustrated in Fig. 10 in section 5.3, a dome with rise to span ratio 0.2 would seem superior to a dome with other rise to span ratios subjected to three-dimensional seismic waves. Therefore, it is recommended that a dome with rise to span ratio 0.2 should be considered for the structural design of dome space structures in seismic regions. (4) For the parameter of tube cross section, the failure loads increases following with the increase of tube wall thicknesses and outside diameters as shown in Fig. 12 and Fig. 14. Compare to tube thickness, the outer diameter has higher impact on the structural load bearing capacity, as the LPGA ranges from 3.0 to 6.0 within the tube outer diameter range, while it ranges from 4.0 - 4.5 for the tube wall thickness changes. It is in agreement with the fact that changing the tube outer diameters is more efficient to alter the cross-sectional moment of inertia than changing tube thicknesses, which is a key factor for this type of structure which have to resist substantial bending moments.

6. Conclusion

In this present study a new seismic failure criterion has been developed focusing on domes under seismic loads based on key structural design parameters. The following conclusions are drawn.

(1) In developing the new seismic failure criterion, which has taken into account the functions of five important structural design parameters, roof weights, spans, rise to span ratios, member tube wall thicknesses and tube outside diameters, on the failure loads. Besides the five key structural design parameters, it also considered the influence of the properties of earthquake on failure loads. Hence three hundred three-dimensional seismic records from the database of the COSMOS from seven earthquakes on the basis of the main influential factors of ground motion were selected as input seismic waves to attain the failure fragility curves of the dome structures.

(2) A safety factor 1.5 was introduced to translate the limit load into the design load, which could improve the safety of important large space structures. The reason of the higher safety factor is that the value of the statistical life is significantly higher comparing with the cost of the dome construction, which could increase the safety of the dome structures and reduce the risk of death.

(3) The failure seismic loads estimated by the new seismic failure criterion is the lower bound collapse loads with 95% probability of non-exceeded and considering the safety factor in terms of the five key structural design parameters.

(4) The logarithmic lower bound collapse loads (LPGA) are linear decreasing functions of structural roof weights and span, but increase following with the increase of tube member wall thicknesses and outside diameters within the chosen range. Compare to the tube wall thickness, the outer diameter develops a larger effect on the structural load-bearing capacity. For the rise to span ratio, a cubic curve fits well the relation of the LPGA and the ratios, and a dome with a rise to span ratio 0.2 would seem superior to a dome with other ratios subjected to three-dimensional seismic waves.

(5) Further studies are required for domes with other structure factors, such as membrane action, different configurations, boundary conditions, materials, nodes, connections between members and nodes, geometric imperfection and load distribution.

Acknowledgements

The research work is finished by the financial aid from the NSFC (Grant No. 51508472) and IEC\NSFC\170451- International Exchanges 2017 Cost Share (China). Special thanks to all the staffs in IT services in University of Surrey for providing their many computers.

References

[1] Yu Z. W., Zhi X. D., Fan F. and Chen, L., "Effect of substructures upon failure behavior of steel reticulated domes subjected to the severe earthquake", Thin-Walled Structures, 49, 1160-1170, 2011.
[2] Bai Y., Yang L. and Gong L. F., "Elasto-plastic bearing capacity of four types of single-layer reticulated shell structures under fire hazards", International Journal of Structural Stability and Dynamics, 15(3), 1450051-1-15, 2015.
[3] Liu Y. P., Pan S. J., Leung Simon W. K. and Chan S. L., "Design and construction of long-span single-layer dome structures by direct analysis", HKIE Transactions, 25(1), 29-43, 2018.
[4] Liu C. G. and Li H. J., "A novel method to calculate the dynamic reliability of space structures subjected to multi-dimensional multi-support excitations", International Journal of Space Structures, 25(1), 25-34, 2010.

[5] Zhai X. M. and Wang Y. H., "Modeling and dynamic response of steel reticulated shell under blast loading", Shock and Vibration, 20(1), 19-28, 2013.
[6] Nie G. B., Zhi X. D., Fan F. and Dai J.W., "Seismic performance evaluation of single-layer reticulated dome and its fragility analysis", Journal of Constructional Steel Research, 100, 176-182, 2014.
[7] Kong D. W., Fan F. and Zhi X. D., "Seismic performance of single-layer lattice shells with VF-FPB", International Journal of Steel Structures, 14(4), 901-911, 2014.
[8] Li Y. G., Fan F. and Hong H. P., "Effect of support flexibility on seismic responses of a reticulated dome under spatially correlated and coherent excitations", Thin-Walled Structures, 82, 343-351, 2014.
[9] Fan F., Li Y. G., Zhi X. D. and Li L., "Comparison of seismic response of single-layer reticulated dome under uniform and incoherence three-directional excitations", International Journal of Steel Structures, 14(4), 855-863, 2014.
[10] Ma J. L., Wu C. Q., Zhi X. D. and Fan F., "Prediction of confined blast loading in single-layer lattice shells", Advances in Structural Engineering, 17(7), 1029-1043, 2014.
[11] Ye J. H., Zhang Z. Q. and Chu Y., "Strength failure of spatial reticulated structures under multi-support excitation", Earthquake Engineering and Engineering Vibration, 10(1), 21-36, 2011.
[12] Ye J. H., Zhang Z. Q. and Chu Y., "Strength behavior and collapse of spatial-reticulated structures under multi-support excitation", Science China-Technological Sciences, 54, 1624-1638, 2011.
[13] Liu W. Z. and Ye J. H., "Collapse optimization for domes under earthquake using a genetic simulated annealing algorithm", Journal of Constructional Steel Research, 97, 59-68, 2014.
[14] Zhu N. H. and Ye J. H., "Structural vulnerability of a single-layer dome based on its form", Journal of Engineering Mechanics, 140(1), 112-127, 2014.
[15] Yan R. Z., Chen Z. H., Wang X. D., Xiao X. and Yang Y., "Calculation theory and experimental study of the K6 single-layer reticulated shell", International Journal of Steel Structures, 14(2), 195-212, 2014.
[16] Ma H. H., Fan F., Wen P., Zhang H. and Shen S. Z., "Experimental and numerical studies on a single-layer cylindrical reticulated shell with semi-rigid joints", Thin-Walled Structures, 86, 1-9, 2015.
[17] Yang C., Yu Z. X., Sun Y. P., Zhao L., and Zhao H., "Axial residual capacity of circular concrete-filled steel tube stub columns considering local buckling", Advanced Steel Construction, 14(3), 496-513, 2018.
[18] Zhong J., Zhi X. D. and Fan F., "A dominant vibration mode-based scalar ground motion intensity measure for single-layer reticulated domes", Earthquakes and Structures, 11(2), 245-264, 2016.
[19] Fan F., Wang D. Z., Zhi X. D. and Shen S. Z., "Failure modes of reticulated domes subjected to impact and the judgment", Thin-Walled Structures, 48(2), 143-149, 2010.
[20] Ramalingam R. and Jayachandran S. A., "Postbuckling behavior of flexibly connected single layer steel domes", Journal of Constructional Steel Research, 114, 136-145, 2015.
[21] Bruno L., Sassone M. and Fiammetta V., "Effects of the equivalent geometric nodal imperfections on the stability of single layer grid shells", Engineering Structures, 112, 184-199, 2016.
[22] Yan J. C., Qin F., Cao Z. G., Fan F. and Mo Y. L., "Mechanism of coupled instability of single-layer reticulated domes", Engineering Structures, 114, 158-170, 2016.
[23] Zhi X. D., Fan F. and Shen S. Z., "Failure mechanisms of single-layer reticulated domes subjected to earthquakes", International Association of Shell and Spatial Structures, 48(1), 29-44, 2007.
[24] Yu Z. X., Qiao Y.K., Zhao L., Xu H., Zhao S. C. and Liu Y. P., "A simple analytical method for evaluation of flexible rockfall barrier part 1: working mechanism and analytical solution", Advanced Steel Construction, 14(2), 115-141.
[25] Standardization Administration of China, Technical specification for space frame structures, JGJ 7 -2010, Beijing, China Architecture & Building Press, 2010. (in Chinese).
[26] Architectural Institute of Japan, Dynamic Behavior and Seismic Design of Spatial Structures, Tokyo, Showa Joho Process, 2006.
[27] American Institute of Steel Construction, Seismic Provisions for Structural Steel Buildings, ANSI/AISC 341-10, Chicago, 2010.
[28] British Standards Institution, Eurocode 8: Design of Structures for Earthquake Resistance – Part 1: General Rules, Seismic Actions and Rules for Buildings, CEN. EN 1998-1, 2004.
[29] ANSYS 10.0. Theory reference. ANSYS Inc. 2005.
[30] Vamvatsikos D, Cornel CA, "Incremental dynamic analysis", Earthquake Engineering and Structural Dynamics, 31(3), 491-514, 2002.
[31] COSMOS Virtual Data Center. (http:/db.cosmos-eq.erg/scripts/default.plx).
[32] Johnson Norman L., Kotz Samuel, Balakrishnan N., "14: Lognormal Distributions", Continuous univariate distributions, Vol. 1, Wiley Series in Probability and Mathematical Statistics: Applied Probability and Statistics (2nd ed.), New York: John Wiley & Sons, ISBN978-0-471-58495-7,MR1299979, 1994.
[33] Papoulis A. P., Pillai S. U., "Probability, Random Variables, and Stochastic Processes (4th ed.)". Boston, McGraw-Hill, ISBN 0-07-366011-6, 2002.
[34] http://ocw.mit.edu/courses/mathematics/18-443- statistics -for-applications-fall-2006/lecture-notes/lecture6. pdf.
[35] Benjamin J. R., Cornell C. A., "Probability, Statistics, and Decision for Civil Engineers", McGraw-Hill: New York, NY, 1970; 684.
[36] Soutsos M. N., Breysse D., Garnier V., Goncalves A. and Monteiro A. V., "Estimation of on-site compressive strength of concrete", In Non-Destructive Assessment of Concrete Structures, Reliability and Limits of Single and Combined Techniques, RILEM, Talence, France, 2012.
[37] American Institute of Steel Construction, Specification for Structural Steel Buildings, ANSI/AISC 360-16, Chicago, 2016.
[38] Department of Transportation, Standard Specifications, CalTrans, State of California, 2015.
[39] Department of Defense, J Joint service specification guide: Aircraft structures, SSG – 2006, Washington, U.S, 1998 .
[40] Department of the Prime Minister and Cabinet, Best Practice Regulation Guidance Note: Value of statistical life, Australian Government, 2014.
[41] Ministry of Transport, Social cost of road crashes and injuries 2016 update, New Zealand Government, 2016.
[42] Department of Transportation, Guidance on Treatment of the economic value of a statistical life (VSL) in U.S. department of transportation analyses-2016 adjustment, Office of the Secretary of Transportation, U. S., 2016.
[43] Shen S. Z., Zhi X. D., "Failure mechanism of reticular shells subjected to dynamic actions", the 4th International Conference for Advances in Steel Structures, ShangHai, China, 2005.
[44] Ibarra LF, Krawinkler H, "Global collapse of frame structures under seismic excitations", Report No. 152, The John A. Blume Earthquake Engineering Center, Department of Civil and Environmental Engineering, Stanford University, Stanford, CA, 2005.
[45] Zhong J., "Probabilistic Seismic Fragility Analysis of Reticulated Shells", PhD thesis, Harbin Institute of Technology, Harbin, China, 2016. (in Chinese).
[46] Fan F., Zhi X. D. and Shen S. Z., "Failure mechanism of reticulated shells under earthquake", Science Press, 2014. (in Chinese).

Appendix Table 1. The domes with various structural parameters

	Span (m)	Roof weight (kg/m^2)	Ratio of rise-span	Cross section (mm)	
				radial and hoop members	oblique members
Domes with various roof weights	50	60	0.20	168.00×6.00	152.00×5.00
		100			
		160			
		200			
		260			
		300			
		360			
		400			
		460			
Domes with various spans	40	60	0.20	168.00×6.00	152.00×5.00
	50				
	60				
	65				
	70				
	75				
	80				
	85				
	90				
Domes with various rise to span ratios	50	60	0.10	168.00×6.00	152.00×5.00
			0.15		
			0.20		
			0.25		
			0.30		
			0.35		
			0.40		
			0.45		
			0.50		
Domes with various tube thicknesses	50	60	0.20	168.00×5.00	152.00×4.00
				168.00×6.00	152.00×4.80
				168.00×6.30	152.00×5.04
				168.00×8.00	152.00×6.40
				168.00×10.00	152.00×8.00
				168.00×12.50	152.00×10.00
Domes with various tube outside diameters	50	60	0.2	114.30×6.30	102.90×5.04
				139.70×6.30	125.70×5.04
				168.00×6.30	152.00×5.04
				193.70×6.30	174.30×5.04
				219.10×6.30	197.20×5.04
				244.50×6.30	220.05×5.04
				273.00×6.30	245.70×5.04
				323.90×6.30	291.50×5.04
				355.60×6.30	320.00×5.04

Advanced Steel Construction – Vol. 15 No. 4 (2019) 398-405
DOI:10.18057/IJASC.2019.15.4.10

EXPERIMENTAL ANALYSIS OF SPACE TRUSSES WITH TYPICAL CONNECTIONS REINFORCED WITH STEEL AND SISAL-RESIN SPACERS

Cleirton A. S. Freitas[1,*], Welington V. Silva[2], Luciano M. Bezerra[2], Francisco F. S. M. Júnior[1], Vinícius C. P. Neto[1], and Brenda A. T. Ribeiro[1]

[1]*Research Group on Structural Engineering in Cariri - GPEEC, Federal University of Cariri - http://www.ufca.edu.br, Juazeiro do Norte, Brazil*

[2]*Department of Civil and Environmental Engineering, University of Brasilia - UnB http://www.unb.br, Brasília, Brazil*

**(Corresponding author: E-mail: andre.freitas@ufca.edu.br)*

ABSTRACT

Space trusses are reticulate systems used worldwide because of their advantages in covering roofs with large free spaces. In addition to having a low cost, the self-weight of such trusses is relatively reduced. The limitations on the use of these structures are mainly related to the fragility of the nodes, specifically those classified as typical nodes which may collapse when submitted to service loads due to eccentricities generated by stamped connections. This fact restricts significantly the use of space trusses. Considering this fact, the present research evaluates a reinforcement proposal for the typical connections with a series of eighteen prototypes. The reinforcements tested are made with steel plates and spacers. In this work, spacers are made of steel or sisal with fiber polymer resin. Such spacers are employed to correct part of the eccentricities present at typical nodes. The experimental tests show an increase of about 40% of the resistant capacity of the truss with the proposed reinforcement avoiding the early collapse of typical nodes. In truss prototypes with typical nodes, local abrupt collapses always happened at nodes. In reinforced trusses, collapse took place by buckling of the bars at the top chord of the prototypes, therefore, taking account of the bar full resistance.

ARTICLE HISTORY

Received: 26 May 2019
Revised: 17 August 2019
Accepted: 01 September 2019

KEYWORDS

Space trusses;
Fragility;
Experimental study;
Simple connections;
Spacers reinforcement

1. Introduction

Space trusses are reticulate lightweight structures in 3D geometric pattern made of bars or tubes interlocked at nodes. They are frequently made of steel tubes and used in the construction of roofs over large areas with few interior supports. The reticulate tubes have several interconnections at nodes of the intersections of the tubes, like top and bottom chords, and diagonals. Space trusses are generally made with an assemblage of tetrahedral modules. There is a variety of node connections, some patented, some of the public domain. The simple and most used connection on 3D trusses is named "typical node" where flattened-end tubes are put together with a single trespassing bolt [1].

The design of space trusses is, generally, based on a nodal system that transmits only tensile and compression axial forces. The ideal node connection is not conceived to transmit a bending moment [2], but just axial forces. Therefore, in a real situation, the connection between bars or tubes must always be designed to minimize bending stresses. However, this situation is usually not possible for some connection, especially the typical connection with tubes with flattened ends (Fig. 1). Other examples of connection nodes are pointed out in Souza´s research [3] (Figs. 2 and 3).

Fig. 1 Typical node

Fig. 2 Steel node [3]

Fig. 3 Steel node made with plates [3]

Several patented systems of nodes may be found worldwide [4,5,6], (Figs. 4, 5 and 6). Some node solutions can make the construction work expensive and the execution of the space truss impractical. Usually, the simplest and economical option is the use of the typical nodes. In such a connection the ends of the tubes are stamped, flattened, and put together with a single trespassing bolt (Fig. 1). This system is widely used due to its facilities in the manufacture, transportation, assemblage, and low cost [8].

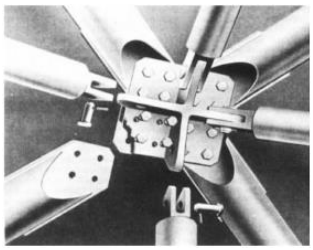

Fig. 4 Rai joint – Holland [5]

Fig. 5 Eco – Italy[5]

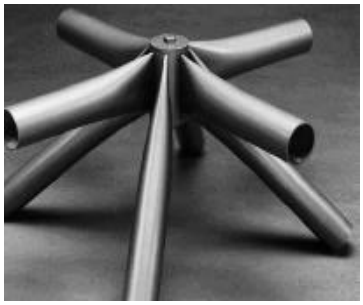

Fig. 6 Triodetic – Canada [5]

This research motivation is related to the fact that the space trusses frequently present local instabilities [8], especially, at the link between the tube ends (Fig. 1). Such nodes present fragility when under stress, showing highly distortions and local collapse before the buckling of the tubes - as can be observed in (Fig. 7) [9]. This problem is explained by the geometric changes generated at the tube ends [10], due to the smashing of the bar ends. This produces eccentricities in the connections [7] reducing the load capacity of the structure [11]. Some collapses of the connections have been reported, such as the ones in Spain [11] and Brazil [12] (Fig. 8) [9]. Other examples of 3D truss collapse in the world, like the dome in Romania, Burcharest, 1963, in Hartford USA, 1978, in Malaysia, 2009, are reported in [13].

Fig. 7 Node failure [9]

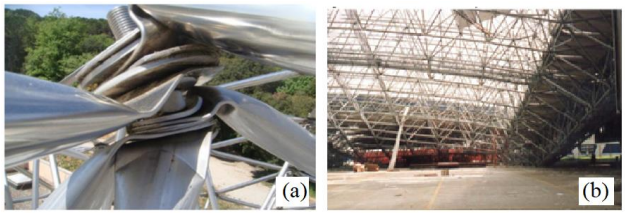

Fig. 8 Collapse of space trusses: (a) In Spain [11], (b) In Manaus [12]

Typical nodes, like the one in Fig. 1, show eccentricities E_1 and E_2 that can be seen in Fig. 9 and such eccentricities contribute to local collapse. The proposal for the solution of early local collapse at the nodes of 3D trusses with typical nodes was to improve the efficiency of such connections. The correction consists of removing, at least one of the eccentricities, E_2, due to the flattened ends of the tubes connected at the node - as shown in Fig. 09 [11]. Such correction can be done with low-cost spacers easy to be applied (Fig. 10). Lab tests show eccentricity E1 does not play an important role [11, 14].

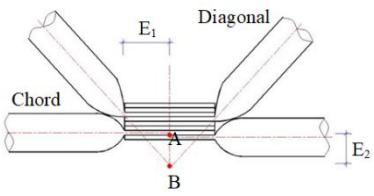

Fig. 7 Eccentricities [14]

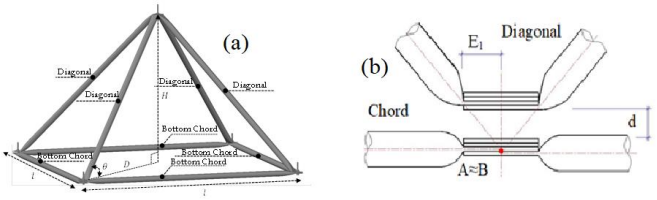

Fig. 8 Correcting eccentricity [14]

Space trusses are made of connections between tetrahedron or pyramids, as shown in Figs. 8b and 10a. The use of spacers aims to reallocate the diagonal bars (as in Fig. 10b) and, consequently, eliminate eccentricity E_2. With a spacer with height d (Fig. 10b), the moments at the typical node can be substantially reduced. This is because normal forces generated by the diagonals can now converge to the central axis of the chords. The distance d is given as a function of the length of the chord l, the height H and the tube thickness t [11] (see Fig. 10a). Given E_1, d can be calculated according to Equation 1:

$$d = \frac{2HE_1}{l\sqrt{2} - 4E_1} - 8t \tag{1}$$

1.1. Preliminary steps in this research

Recent studies carried out in the Structural Laboratory of the Research Group on Civil Engineering Structures (GPEEC) at the Federal University of Cariri (UFCA) in prototypes [11, 14, 15] evaluated the performance of 3D trusses with spacers correcting the typical nodes. Initially, twelve truss specimens were tested in the Structural Lab of the University of Brasilia (UnB). They were divided into groups of three prototypes with the following differences: (1) Typical Connection (LTE), (2) Typical Connection with Steel Spacer (LTDE), and (3) Typical Connection with Steel Spacer and Steel Plate

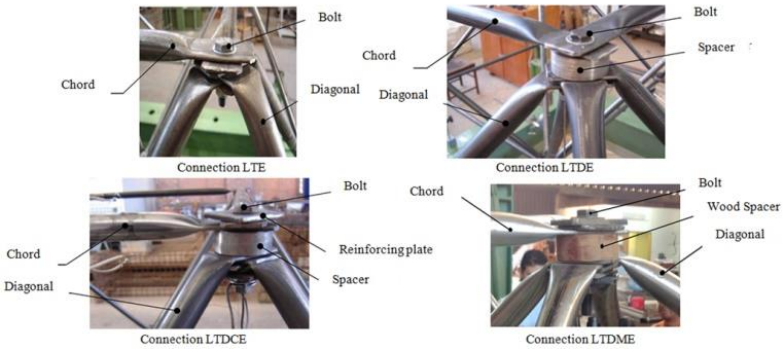

(LTDCE), and (4) Typical Connection with Wood Spacer (LTDME), as shown in Fig. 11 [14].

Fig. 9 Types of prototypes tested in the structural laboratories of UnB and UFCA.

The geometry of the pyramid module (Fig. 10a and 12) has the base and height, respectively, equal to 1000 mm and 707 mm. With the use of steel spacers, the tests in the

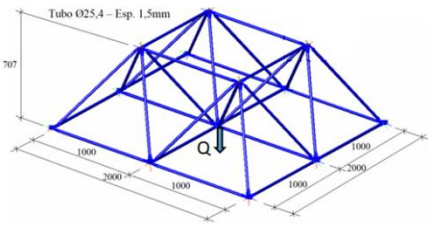

Space Truss LTE (mm)

prototypes indicated a resistance improvement of approximately 40% of the load capacity in comparison with typical node connections, according to the prototypes in Fig. 13.

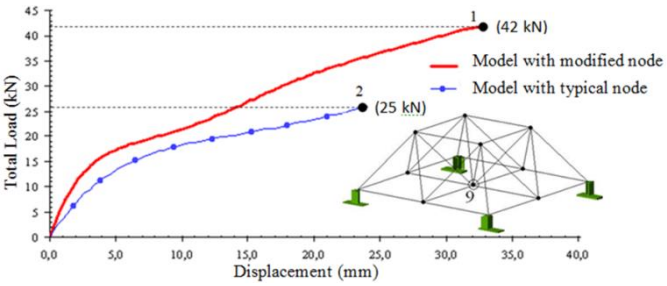

Fig. 10 Geometry of the prototype [15].

The results in Fig. 13 show that the LTE prototype presented local collapse at the node with an average of collapse load of 25 kN and after reaching that value, the truss collapsed globally. The use of typical nodes should be avoided because the collapse of the node was abrupt. In this case, the maximum capacity of the bars was not reached. Moreover, there was a 32.75% increase in deflection compared to the prototypes with spacers. On the other hand, the LTDE prototypes had a 35.9% increase in the resistance capacity compared to LTE connection, with a 35.87 mm overall displacement.

Fig. 11 Average Load vs Displacements for prototypes with typical node and prototypes with spacers (modified node) [1]

It is observed (Fig.14) an increase in stiffness due to eccentricity correction since the mechanism of the collapse was by buckling of the bar. The LTDCE (Fig.16) prototypes truss presented the best behavior. In this case, the resistance gain was 40.77% compared to the LTE prototypes (Fig.15). The 31.75 mm displacement proved the efficiency of the reinforcement plate on the connection,

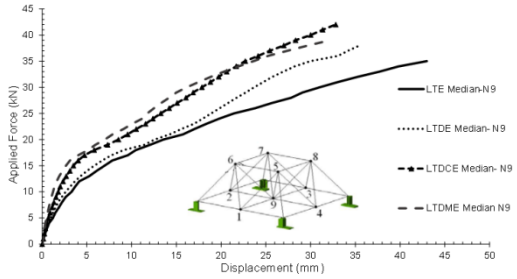

increasing the node stiffness (Fig. 17). Finally, the LTDME (Fig. 18) prototypes also showed better resistance than the LTE prototypes arriving to a collapse load of 39.68 kN. Table 1 reports a summary of the tests.

Fig. 12 Average curves for Loads vs displacements for prototypes tested in [1].

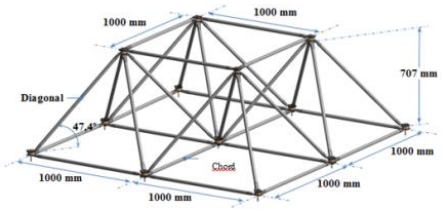

Fig. 13 Collapse for prototypes with LTE (25kN) [1].

Fig. 14 Collapse for prototypes with LTDCE (42kN) [1].

Fig. 15 Collapse of LTDE (38kN) [14]

Table 1
Summary of the LT, LTD, LTDC, and LTME test results

Prototypes	Model of Connection	Dimensions (mm)	Element Chord	Element Diagonal	Element Spacer	Ultimate Load (kN)	Collapse Mode
PROT 1	LT 1	2000x2000	16φ 25 × 1060	16φ 25 × 1076	-----	25,33	Node collapse
PROT 2	LT 2		16φ 25 × 1060	16φ 25 × 1076	-----	25,89	Node collapse
PROT 3	LT 3		16φ 25 × 1060	16φ 25 × 1076	-----	25,78	Node collapse
PROT 1	LTD 1	2000x2000	16φ 25 × 1060	16φ 25 × 1076	13	39,63	Local bar collapse
PROT 2	LTD 2		16φ 25 × 1060	16φ 25 × 1076	13	40,14	Local bar collapse
PROT 3	LTD 3		16φ 25 × 1060	16φ 25 × 1076	13	36,91	Local bar collapse
PROT 1	LTDC 1	2000x2000	16φ 25 × 1060	16φ 25 × 1076	13	42,21	Bar stability
PROT 2	LTDC 2		16φ 25 × 1060	16φ 25 × 1076	13	42,13	Bar stability
PROT 3	LTDC 3		16φ 25 × 1060	16φ 25 × 1076	13	41,74	Bar stability
PROT 1	LTM 1	2000x2000	16φ 25 × 1060	16φ 25 × 1076	13	39,10	Bar stability
PROT 2	LTM 2		16φ 25 × 1060	16φ 25 × 1076	13	39,68	Bar stability
PROT 3	LTM 3		16φ 25 × 1060	16φ 25 × 1076	13	38,80	Bar stability

Fig. 16 Collapse of LTDME (P1 - 39kN)

In the Federal University of Cariri - UFCa, other spacers were developed for applications to space trusses [1]. To tests such spacers, new prototypes in real scale 6000 mm x 9000 mm were built up with pyramids connected through their vertices. Each pyramid had a lateral length l = 1500 mm of square base and height H = 1061 mm. The inclination angles of the diagonals were 45º relative to the base plane of the pyramid. The steel tubes of the space truss were 38 mm (1½ in) in diameter and 1.20 mm (0.047 in) thick.

The tubes were made from the Brazilian steel MR250, with properties equivalent to the ASTM A36. In the reinforced nodes, a 4.76mm thick reinforcement plate was used. Fig. 19 shows the typical node and Fig. 20 shows the node corrected with spacers and reinforced with a superposing round plate [1].

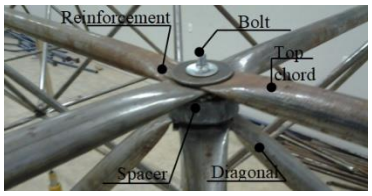

Fig. 17 Typical flat-tened-end tubes connected [1].

Fig. 18 Modified node [1].

The results obtained in the lab experiments (Fig. 21) [1] showed that

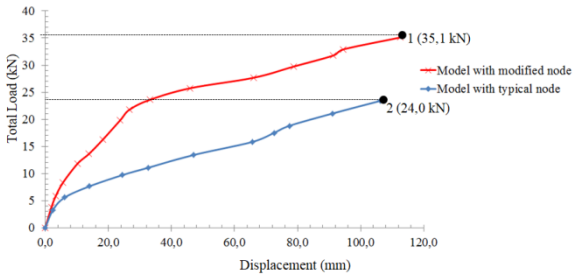

prototypes with typical connections presented excessive deformations of 106 mm at 24 kN collapse load. The LT prototypes collapsed locally at the node, as can be seen in Fig. 22. The use of reinforced nodes with spacers and plate resulted in a significant decrease of the deformations compared to the typical node prototype of about 45 mm, for the same loading conditions. A buckling collapse of the bars at the top chords in the prototype with spacers and reinforcement plates was observed – see Fig. 23.

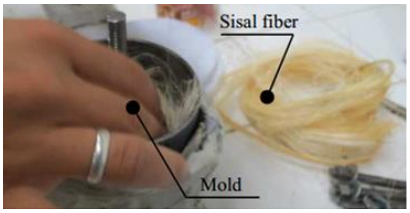

Fig. 19 Loads vs displacements for the experimental tests in [1]

Fig. 20 Collapse in typical node (24kN) [1]

Fig. 21 Collapse in modified typical node prototype (35.1kN) [1]

2. New experimental studies with new spacers

2.1. New materials for spacers used in this research

Although the previous studies [1] have demonstrated the efficiency of the steel spacers in the typical nodes, their use, significantly, increases the cost and the self-weight of the 3D truss. The present research evaluates the performance of the connections with more economical spacers, comparing them with the steel spacers. All prototypes were tested in the Structural Laboratory of the Civil Engineering Department of the Federal University of Cariri.

Fiber-reinforced polymer (FRP) is a composite material made from a fiber-reinforced polymer, widely used in the aerospace, automotive, marine, and construction industries. The polymer is usually developed from a thermosetting epoxy, vinyl ester, polyester resin or phenol-formaldehyde resin and the fibers are generally glass, carbon, basalt, aramid, paper or wood. Based on the worldwide adoption of FRP, a new material was used in the manufacturing of spacers: sisal with resin. Sisal is a natural fiber [16] and together with the resin resulted in a material with a high modulus of elasticity and good mechanical strength [17]. Other advantages of this compound are the low cost, renewable source and easy reachability in Brazil. The northeastern region of Brazil is the world's largest sisal exporter with 52% of the whole production. Brazilian sisal exportation is largely directed to Europe, Asia, and North America [18, 19].

Sisal is a species native to Central America, with the botanical name of Agave Sisalana (Fig. 24). Sisal fiber has traditionally been used in the textile industry but has many other uses. Thus, this research developed a Polymer Reinforced with Sisal Fiber (PRSF) as spacers to correct the typical nodes. The following images show the sisal placed in the steel mold (Fig. 25) and soaked with epoxy resin (Fig. 26), after two hours the spacer is extracted from the mold, see Fig. 27. Finally, the details of the constituent elements of the space truss, as well as their dimensions and specifications are presented in Fig. 28.

Fig. 22 Sisal farm [15]

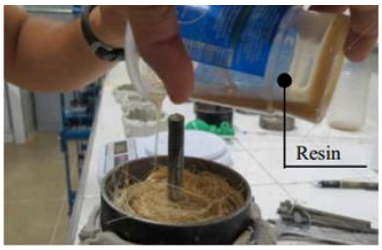

Fig. 23 Steel mold for make as space with PRSF

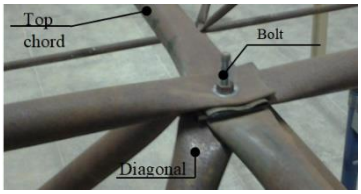

Fig. 24 Mold filled with resin and sisal fibers [15]

Fig. 25 Spacer made with sisal and resin PRSF [15].

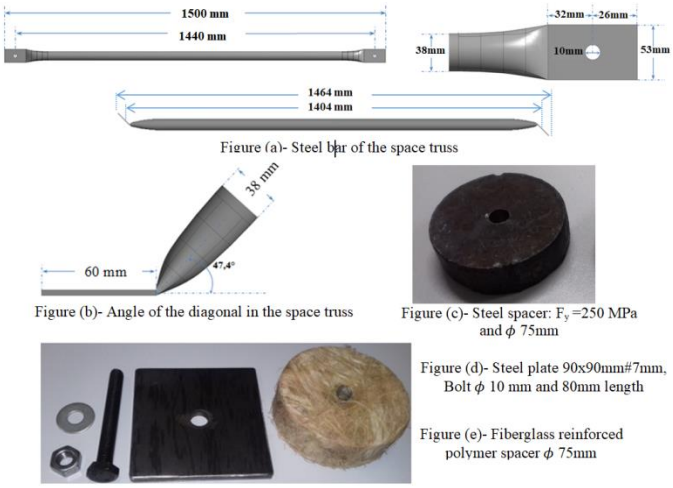

Figure (a)- Steel bar of the space truss

Figure (b)- Angle of the diagonal in the space truss

Figure (c)- Steel spacer: F_y =250 MPa and ϕ 75mm

Figure (d)- Steel plate 90x90mm#7mm, Bolt ϕ 10 mm and 80mm length

Figure (e)- Fiberglass reinforced polymer spacer ϕ 75mm

Fig. 26 Detail of the assembly of prototypes

2.2. Methodology to assemble the space truss

The experimental tests evaluated six prototypes, two for each type of the three connections: (1) Typical Connection without spacer (LT), (2) Typical Connection with Steel Spacer (LTDA), and (3) Typical Connection with Sisal Spacer (LTDS). The prototypes were made of 192 bars, and 56 nodes. Of all bars, 96 were diagonals, 38 top chords, and 58 bottom chords, Fig. 29. The connections were done with bolts, nuts, washers, spacers, and reinforcement plates, depending on the prototype under test – see Figs. 30, 31 and 32. The tests used new tubes for each connection type tested. Tubes were made of MR 250 steel with engineering properties similar to ASTM A36 steel (yielding stress, Fy = 250 MPa) as the twelve initial experiments at UnB. The 3D trusses were assembled in the same way, with different spacers. Table 2 summarizes the prototypes tested and also presents the collapse load of each prototype.

Table 2
Denomination of Prototype

Prototypes	Identification	Designation	Total Load kN	Collapse
PROT 1	LT 01	Typical Connection LT without spacer	30,90	Node Collapse
PROT 2	LT 02		30,4	Node Collapse
PROT 3	LTDA 01	Typical Connection With Steel Spacer	42,4	Bar Buckling
PROT 4	LTDA 02		42,5	Bar Buckling
PROT 5	LTDS 01	Typical Connection with Sisal Spacer	42,0	Bar Buckling
PROT 6	LTDS 02		44,90	Bar Buckling

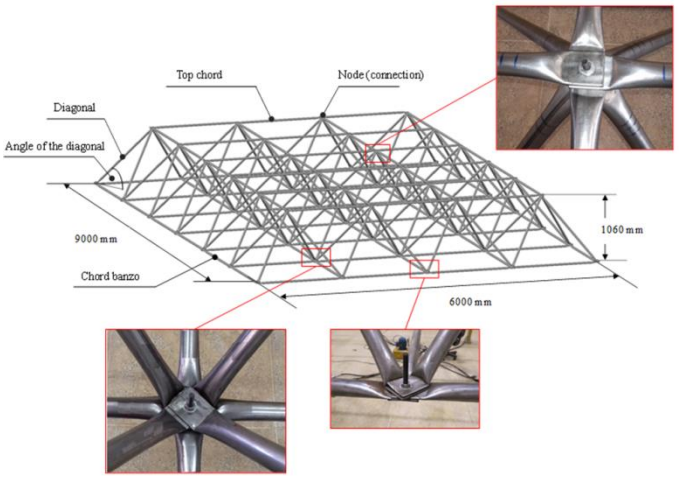

Fig. 27 Prototype of the space truss with typical connection LT

Fig. 28 Example of LT

Fig. 29 Example of LTDA

Fig. 30 Example of LTDS

2.3. Experimental Program

The space trusses were raised as shown in Fig. 33. The instrumentation process began with the placement of load cells, reading panels, analog deflectometers, and steel cables to apply the load to the truss through the hydraulic jacks. After the tests, the data obtained through the load control panels and deflectometers were processed. Results were arranged in graphs to show the behavior of the 3D trusses relative to each type of node tested.

All the space trusses were assembled following a sequential connection of bars keeping the symmetry of the truss. All prototypes were initially prepared on the floor of the laboratory and then lifted by a hydraulic jack up to the top of four steel columns. To standardize the tightening of all connection bolts, the tightness of the bolt was measured with a torque meter with an intensity of 50 Nm - this value was previously calculated [11]. The data were obtained by reading the loads on digital panels connected to load cells and analog deflectometers attached to the connections. Fig. 34 shows the application of the loads. The direction of the load application was in the direction of the gravitational force so that the structure was pulled down by the hydraulic jacks that were attached to the reaction floor of the laboratory.

Fig. 31 Prototypes in the Laboratory at UFCa [1]

The accuracy of the deflectometer was 0.01 mm and the maximum reading was 30 mm. Each load cell had a capacity of 20 kN. Load-measuring panels were installed to monitor the loads applied from the hydraulic jacks. Four nodes were used to transfer the load from the hydraulic jack to the truss prototypes. The load was applied to the four nodes over a wooden block to avoid stress concentration. The pressure of the hydraulic jacks was controlled by the pump controller as shown in Fig. 35. The readings were performed at each 0.25 kN load step. The applied load was gradually increased until the collapse of the 3D

truss. The results were arranged in spreadsheets with the reading loads and the respective displacements obtained from the deflectometers.

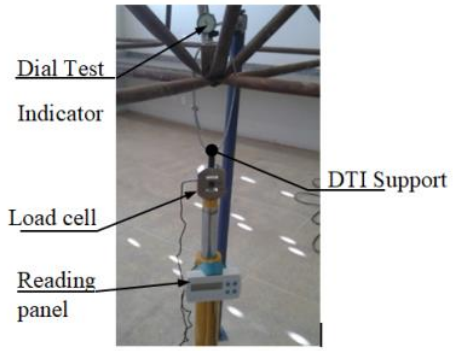

Fig. 32 Measuring system

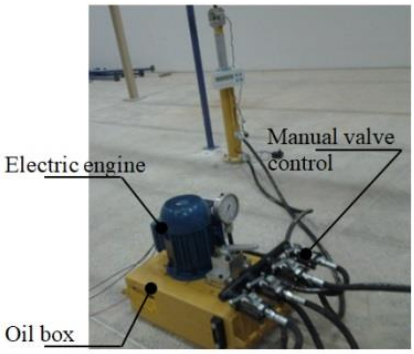

Fig. 33 Hydraulic pump control

3. Results

Load vs displacement data from tests are now presented. Result data shows the behavior of the different prototypes with different types of node connections. The measurements were done during the whole loading process until the overall collapse of the truss prototype is reached. The total applied load is the sum of the loads (Q1, Q2, Q3, Q4) applied individually by the four hydraulic jacks at the points as indicated in Fig. 36. The average displacement is computed from the four reading points where the loads are applied. Thus, X-Y graphs with displacements at the X-axis and loads at the Y-axis express the overall behavior of the 3D trusses.

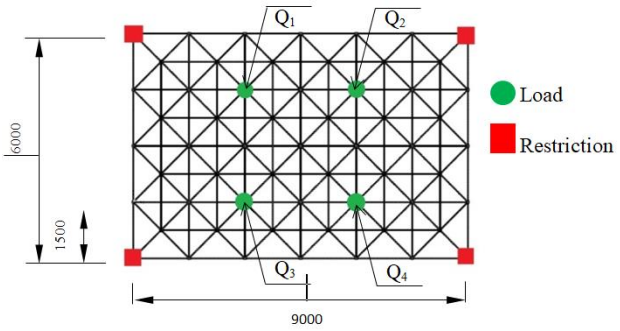

Fig. 34 Top view of the prototype (Units in Millimeter) [1]

3.1. Results of the Typical Node without Spacer

The two tests performed with the prototypes LT-01 and LT-02 presented similar results as expected. The LT-01 prototype test showed the collapse of the truss with an applied total load of 30.9 kN, with a mean displacement of 119.80 mm measured from the nodes of the applied loads - as can be seen in Fig. 37.

The values obtained in the second LT-02 test showed that its collapse occurred at 30.4 kN load and 119.5 mm average deflection, see Figs. 38. This shows the quality of the truss prototypes tested in this research.

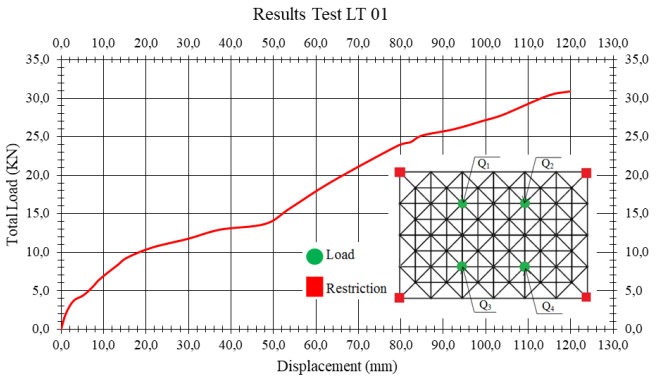

Fig. 35 Load versus Displacement for LT-01

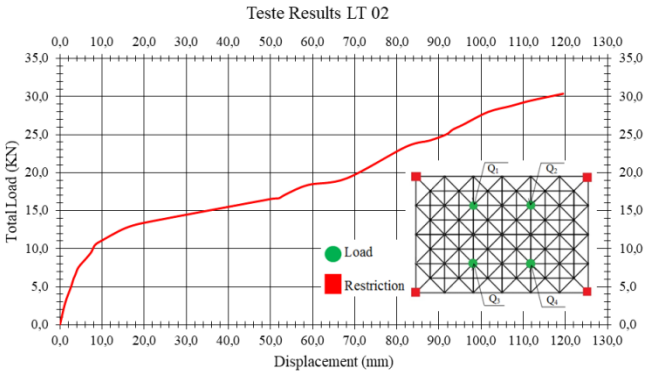

Fig. 36 Load versus displacement for LT-02

In agreement with the results obtained in previous studies [1, 2, 11, 12, 13], when typical nodes are used, collapse happened locally at nodes. The deformed connections at collapse showed significant rotations due to the presence of bending moments. They also show excessive deformation and failure of the top chords in the vicinity of the typical connection - see Figs. 39 and 40.

Fig. 37 Typical node collapse LT-01

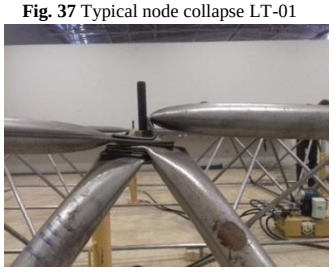

Fig. 38 Typical node collapse LT-02

3.2. Results of the Typical Node with Steel Spacer

The tests with these prototypes using LTDA spacers showed improvement due to the eccentricity correction of the typical node. LTDA brought a substantial decrease of the bending moments at the nodes and took advantage of the maximum strength of the steel bars. LTDA-01 prototype came to rupture at 42.4 kN and 99.8 mm deflection, Fig. 41.

In the LTDA-02 prototype, the rupture was at 42.5 kN at an average displacement of 107.2 mm (Fig. 42). In both prototypes collase took place at the top chord of the trusses.

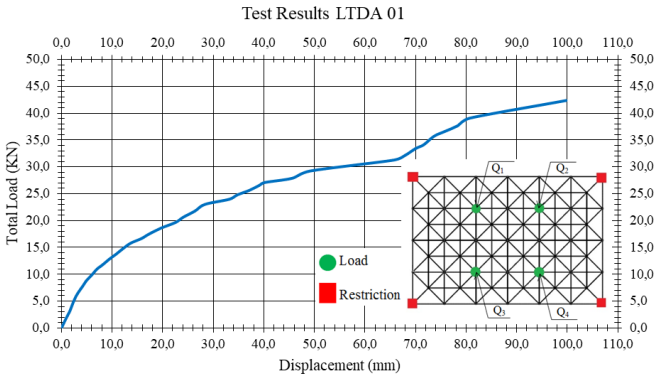

Fig. 39 Load versus displacement for LTDA-01.

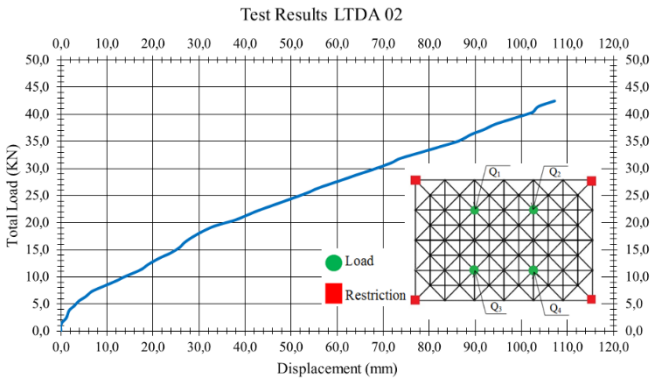

Fig. 40 Load versus displacement for LTDA-02.

The collapse of the two prototypes tested was by buckling of the top chord tubes, at the truss central span, see Fig. 43 and 44. It is observed a linear behavior of the prototype LTDA-01 until reaching the load of 19.70 kN. In prototype LTDA-02, collapse was of approximately at 20,04 kN compared to 10,05 kN of the LT-02 prototype. The distribution of load in the prototypes with spacers resulted in a soft break by the buckling of top chords, and no local distortion at nodes, see Fig. 45 and 46.

Fig. 41 Detail of deformed chord for LTDA-01

Fig. 42 Detail of buckled chord for LTDA-02

Fig. 43 No local collapse of node at chord buckling for LTDA-02

Fig. 44 Detail of nodes for LTDA-02.

3.3. Results of the Typical Node with Sisal-Resin Spacer

Prototype LTDS-01 showed collapse at 42 kN and a respective average displacement of 114.5 mm, see Fig. 47. The LTDS-02 prototype collapsed at 44.9 kN load with an average displacement of 95.00 mm, see Fig. 48.

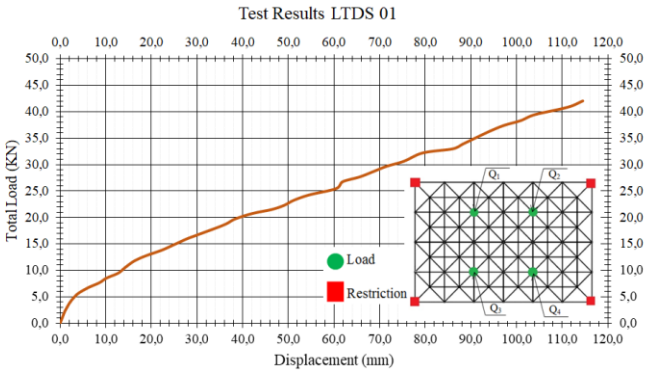

Fig. 45 Load versus Displacement for LTDS-01.

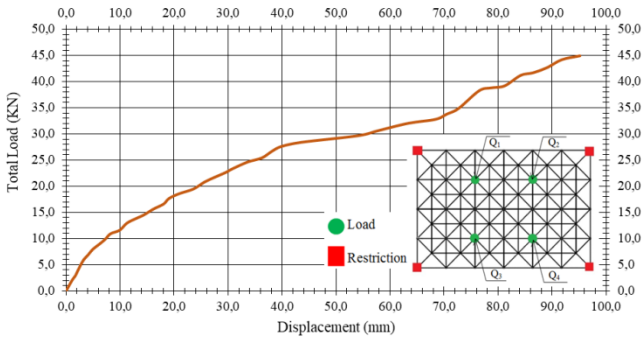

Fig. 46 Load versus Displacement for LTDS-02.

The collapse identified in LTDS prototypes was by buckling due to the compressed bars of the top chords, Fig. 49. All 56 connections were analyzed at the end of the test and no local failure of the node was observed (see Fig. 50). All spacers remained intact too, confirming the node resistance increase (Figs. 51 and 52).

Fig. 47 Buckling of the top cords for LTDS prototypes

Fig. 48 Node after collapsing the Structure

Fig. 49 Lateral deformation

Fig. 50 Lateral Deformation

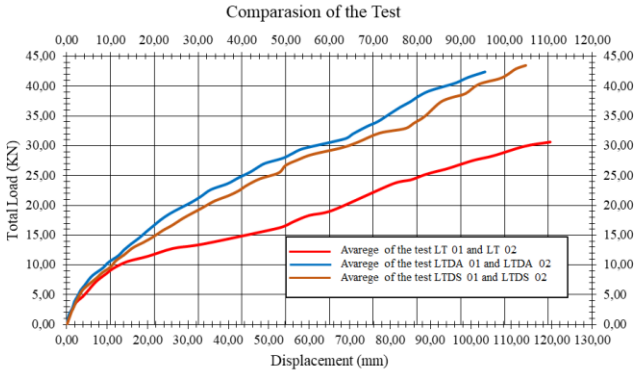

Fig. 51 Average curves comparing prototypes´ performance in this research

3.4. Comparison of all the Tests

The graph in Fig. 53 shows the rates of the load vs displacement during the experimental tests performed with different types of connections. The proposed modifications represented substantial improvement in the strength of the trusses when steel spacers or sisal-resin spacers are used. The increase in load capacity was about 40% in the collapse loads compared to trusses with nodes without spacers, the typical nodes commonly found worldwide. The tests performed with the sisal-resin spacers showed goos performance and strength increase of the truss. Collapse loads were, on average, 6% slightly better than that obtained with the steel spacers. This minor improvement in strength may be explained due to the lower self-weight of the sisal-resin spacers compared to the overload steel spacers produce on trusses.

4. Conclusion

Space trusses with typical nodes made with tubes with flattened-ends trespassed by a single bolt are used worldwide. They are easy to do, but this type of connection may collapse at early load stage due to instabilities at such typical nodes. This research proposed and tested a solution to how typical nodes can gain resistance. Spacers and reinforcement plates were tested in 18 specimens of 3D trusses of two different dimensions. The test results reported in this paper showed that spacers and reinforcement plates provide a significant improvement of the typical nodes of about 40% gains in the load capacity of 3D truss. The results show the effectiveness of spacers in correcting eccentricity in 3D trusses made with typical nodes. Tests done in prototypes with typical nodes showed local instability of the nodes due to eccentricities. Prototypes tested using typical nodes reinforced with steel plates and spacers showed that the bad effect of eccentricities can be removed. With spacers, instead of the local collapse of the nodes, truss collapse achieved the buckling of the compressed tubes. This was observed in the tests of the prototypes with steel spacers (LTDA-01 & LTDA-02) and with sisal-resin spacers (LTDS-01 & LTDS-02). In both, the maximum strength of compressed tubes was reached.

The test results with sisal-resin spacers proved to be equivalent to the results obtained with steel spacers – in fact, slightly better due to less self-weight. Moreover, sisal-resin spacers have a low cost of production; they are lightweight, easy to manufacture, and have high strength and availability. More research is needed to confirm the results here obtained in 3D trusses with other dimensions and geometries.

Acknowledgements

The authors want to express their gratitude to the Research Group in Civil Engineering Structures (GPEEC) of the Federal University of Cariri (UFCA) and to the Post-graduation Program in Structures and Civil Construction (PECC) of the University of Brasilia for the use of their laboratory facilities. The authors are also very thankful to CNPQ, CAPES, and FUNCAP, financial support Brazilian agencies, for providing research funding for this research.

References

[1] Cleirton A.S. Freitas, Luciano M. Bezerra, Rafael M. Araújo, Emanue C. Sousa, Geverson M. Araújo and Édipo A. Bezerra1., New experimental results of the research on Reinforced node in space truss, An International Journal Advanced Steel Construction, 13(1), 30-44, 2017.

[2] Freitas C.A.S., et al., "Polymer Composite with Sisal Fiber Used for Node Reinforce in Space-Truss with Stamped Connection", Applied Mechanics and Materials, 719-720, 202-205, 2015

[3] Souza A.C. and Gonçalves R.M., "Behavior of tubular space truss connections with stamped end bars", International Journal of Space Structures, 5, 337 – 345, 2002.

[4] Malite M., Maiola C. H., Gonçalves R.M. and Souza A.S.C., Experimental analysis of the structural performance of space trusses commonly used in Brazil, International Journal of Space Structures, 16 (4), 253–260, 2001. (ISSN: 0266-3511).

[5] Souza A.S.C., Goncalves R.M., Nardin S.D. and Calado, L., "A Strategy of Numerical Analysis of Space Truss Connections with Stamped Bar Ends," International Journal of Space Structures, 23(3), 143 - 152, 2008.

[6] Subramanian, N. Space structures: Principles and Practice. Multi-Science Publishing. Sussex, 213–280, 2007.

[7] Chan S.L. and Cho S.H., Second-Order P-Δ-δ Analysis and Design of angle Trusses Allowing for Imperfections and Semi-Rigid Connections, , An International Journal Advanced Steel Construction, 1(1), 157-172, 2005.

[8] Hill D.C., Blandford G.E., Wang S.T., Post-buckling analysis of steel space trusses. J. Struct. Eng., 115(4), 900-919, 1989.

[9] Souz, A.S.C., Theoretical and experimental analysis of space trusses. DSc Thesis, School of Engineering of Sao Carlos, EESC/USP, São Paulo, 2003 (in Portuguese).

[10] Grecoa M., Gesualdoa F.A.R., Venturinib W.S. and Codab H.B., Nonlinear positional formulation for, space truss analysis, Finite Elements in Analysis and Design, 42, 1079–1086, 2006.

[11] Alegre V., Ródenas V. and Villalba, S., Collapse of the steel roof of a sports center; singular & current pathologies, 140–156 (in Spanish): doi:http://dx.doi.org/10.21041/ra.v 2i3.33, 2014.

[12] Freitas C.A.S., Cavalcante, O.R.O., Araujo R.M. and Araújo G.M., Numerical Investigation of the Space-Truss with Reinforce of the Stamped Connection After Calibration Model in Experimental Study. In: 10th World Congress on Computational Mechanics, São Paulo. Comp. Mechanics 2012 - Proceedings, 2012-20176, 2012.

[13] Hamid Y.S., Progressive Collapse of Double Layer Space Trusses. PhD Thesis, University of Surrey, UK, 2015.

[14] Bezerra L.M., Freitas, C. A. S., Matias, W. T., Nagato, Y., "Increasing load capacity of steel space trusses with end-flattened connections", Journal of Constructional Steel Research, 65, 2197 – 2206, 2009.

[15] Freitas C.A.S., Bezerra L.M. and Silva, R.S.Y.C., "Numerical and Experimental Study of Steel Space Truss with Stamped Connection", Journal of Civil Engineering and Architecture, 5, 494-504, 2011.

[16] Martin AR, Martins MA, Mattoso LHC, Silva ORRF, Chemical and structural haracterization of sisal fibers from Agave sisalana variety, Polímeros, 19:40–46, 2009.

[17] Bledzki A.K. and Gassan J., Progress Polymere Sci., 24, 221, 1999.

[18] Silva O.R.R. and Beltrão N.R.R.F., "O Agronegócio do Sisal no Brasil", Embrapa, Brasília 1999.

[19] Martins M.A., "Fibra de Sisal: Mercerização, Acetilação e Aplicação em Compósitos de Borracha de Pneu Triturado", Tese de Doutorado, Universidade Estadual de Campinas, Brasil, 2001.